TECHNISCHE UNIVERSITÄT
BERGAKADEMIE FREIBERG

The University of Resources. Since 1765.

Metal Surface Contamination in c-Si Solar Cell Processing

By the Faculty of Chemistry and Physics
of the Technische Universität Bergakademie Freiberg

approved

THESIS

to attain the academic degree of

Doctor rerum naturalium
(Dr. rer. nat.)

submitted by **Florian Buchholz**

born on the 2nd May 1983 in Hamburg

Assessors: **1. Prof. Dr. Edwin Kroke**
Institut für Anorganische Chemie, TU Bergakademie Freiberg
2. Prof. Dr. Johannes Heitmann
Institut für Angewandte Physik, TU Bergakademie Freiberg
Stellungnahme: Dr. Eckard Wefringhaus
International Solar Energy Research Center (ISC) Konstanz e.V.

Date of the award: Freiberg, 23rd May 2016

Versicherung

Hiermit versichere ich, dass ich die vorliegende Arbeit ohne unzulässige Hilfe Dritter und ohne Benutzung anderer als der angegebenen Hilfsmittel angefertigt habe; die aus fremden Quellen direkt oder indirekt übernommenen Gedanken sind als solche kenntlich gemacht.Bei der Auswahl und Auswertung des Materials sowie bei der Herstellung des Manuskripts habe ich Unterstützungsleistungen von folgenden Personen erhalten:

- Markus Reutz, ATU Herrenberg (ICP-MS Messungen)
- Lejo Joseph Koduvelikulathu (Simulationen von Solarzellen).

Weitere Personen waren an der Abfassung der vorliegenden Arbeit nicht beteiligt.

Die Hilfe eines Promotionsberaters habe ich nicht in Anspruch genommen. Weitere Personen haben von mir keine geldwerten Leistungen für Arbeiten erhalten, die nicht als solche kenntlich gemacht worden sind. Die Arbeit wurde bisher weder im Inland noch im Ausland in gleicher oder ähnlicher Form einer anderen Prüfungsbehörde vorgelegt.

23. Mai 2016 Florian Buchholz

Declaration

I hereby declare that I completed this work without any improper help from a third party and without using any aids other than those cited. All ideas derived directly or indirectly from other sources are identified as such.

In the selection and use of materials and in the writing of the manuscript I received support from the following persons:

- Markus Reutz, ATU Herrenberg (ICP-MS measurements)
- Lejo Joseph Koduvelikulathu (simulations of solar cells).

Persons other than those above mentioned did not contribute to the writing of this thesis.

I did not seek the help of a professional doctorate-consultant. Only those persons identified as having done so received any financial payment from me for any work done for me. This thesis has not previously been published in the same or a similar form in Germany or abroad.

23rd May 2016 Florian Buchholz

Contents

1 Introduction **1**
1.1 Motivation . . . 3
1.2 Structure of the work . . . 5

2 Crystalline silicon solar cells **7**
2.1 Properties of crystalline silicon and crystalline silicon wafers . . . 8
2.1.1 Properties of crystalline silicon . . . 8
2.1.2 Production of a silicon wafer . . . 11
2.2 Preparation of the silicon wafer surface . . . 15
2.2.1 Properties of the silicon surface . . . 15
2.2.2 Wet chemical etching . . . 19
2.2.3 Wet chemical cleaning . . . 24
2.2.4 Passivation of silicon surfaces . . . 28
2.3 The *pn*-junction . . . 32
2.3.1 Junction formation . . . 32
2.3.2 Junction parameters in the dark and under illumination . . . 35
2.4 Contact formation . . . 37
2.5 Solar cell structures and processes . . . 38
2.5.1 Full aluminum BSF solar cells . . . 38
2.5.2 PERC solar cells . . . 39
2.5.3 PERT and bifacial solar cells . . . 40

3 Physics of contamination in silicon devices **43**
3.1 Recombination mechanisms of charge carriers . . . 44
3.1.1 Bulk recombination lifetime . . . 44
3.1.2 Emitter recombination . . . 48
3.1.3 Surface recombination . . . 50
3.2 Semiconductor characterisation methods . . . 52
3.2.1 Quasi-steady state photoconductance . . . 52
3.2.2 Quasi-steady state microwave-detected photoconductance decay . . . 56
3.2.3 Measurement of iron concentrations in p-type silicon . . . 58
3.2.4 Corona-charge . . . 59

4 The impact of metal surface contamination on solar cell devices **63**
4.1 Surface contamination . . . 64
4.1.1 Measurement of surface contamination . . . 64
4.1.2 Choice of elements used for further contamination studies . . . 65
4.2 Intentional contamination of silicon surfaces . . . 68
4.2.1 Contamination from diluted HF . . . 69
4.2.2 Contamination from DI water . . . 69
4.3 Processing of p-type substrates . . . 73
4.3.1 Back-side passivation . . . 73
Excursus I: Firing of solar cells . . . 76
4.3.2 Phosphorus diffusion . . . 81
Excursus II: Variation of diffusion parameters and segregation of metals at the PSG/n^+ interface . . . 86
4.4 Processing of n-type substrates . . . 93
4.4.1 Phosphorus and boron diffusion . . . 93
4.5 Simulation of solar cells . . . 102
4.5.1 Injection dependent recombination behaviour of Cu . . . 103
4.5.2 Injection dependent recombination behaviour of Fe . . . 109

4.5.3 Light induced degradation . . . 109
4.5.4 Simulation parameters . . . 111
4.5.5 P-type solar cell simulation results . . . 115
4.5.6 N-type solar cell simulation results . . . 117
4.5.7 Conclusion . . . 119
4.6 Summary and outlook . . . 121

5 Cleaning in solar cell processing 125
5.1 The as-cut wafer and FEOL etching . . . 127
5.1.1 Analysis of sawing residues . . . 127
5.1.2 Alkaline etching . . . 129
5.2 Cleaning in Al-BSF processing . . . 135
5.3 Cleaning in high efficiency solar cell processing . . . 139
5.4 Cleaning before high temperature processes . . . 142
5.5 Development of an industrially feasible ozone-based cleaning process . . . 144
5.5.1 Comparison of different cleaning systems . . . 145
5.6 Optimisation of the HF/ozone cleaning sequence . . . 147
5.6.1 Cleaning of saw damage etched surfaces (flat surfaces) . . . 148
5.6.2 Cleaning of textured surfaces (random pyramids) . . . 154
5.6.3 Conclusion . . . 157
5.7 Testing for high efficiency solar cell processes . . . 159
5.7.1 N-type BiSoN, FEOL vs. BEOL . . . 159
5.7.2 N-type BiSoN, FEOL cleaning . . . 160
5.8 Surface roughness . . . 163
5.8.1 Initial observations . . . 164
5.8.2 Impact of etching and cleaning on micro- and nano-roughness . . . 166
5.8.3 Impact of surface roughness on lifetime samples . . . 169
5.8.4 Impact of surface roughness on solar cell properties . . . 169
5.8.5 Conclusion . . . 172
5.9 Summary and outlook . . . 174

6 Experimental section 177
6.1 Overview runs . . . 178
6.2 Analytical methods . . . 179
6.2.1 Sandwich-etch ICP-MS . . . 179
6.2.2 Spectrophotometric determination of Fe and Cu . . . 183
6.3 Chemicals used in this work . . . 185

7 Simulation models 187
7.1 EDNA 2 simulation of heavily doped regions . . . 187
7.2 Models and input parameters used for consistent simulation . . . 191
7.3 Atlas Simulation . . . 192
7.4 Effective lifetime fits . . . 193

Bibliography 195

Glossary 219

Acknowledgments 223

List of publications by the author 225

1 Introduction

A steep learning curve (cf. **Fig. 1.1**) has allowed silicon solar cells to become a competitive way of energy production [1–4]. With falling module prices the margins for the solar cell manufacturer, however, have strongly shrunk and especially the German solar industry has suffered strongly. With the pressure to decrease module prices current process sequences and process steps have been continually optimised. Yet, in order to further decrease cost per watt-peak, the most promising strategy is to increase the solar cell efficiency. This can be achieved by moving to next generation solar cell concepts gradually. And indeed, the industry is more and more moving from optimised industrial full aluminum rear p-type solar cells to both-sided passivated solar cells (PERC for *p*assivated *e*mitter and *r*ear *c*ell). A slightly different approach is to switch the base substrate from p-type to n-type, which, in combination with boron emitter diffusion, can drastically enhance solar cell efficiency. One approach for this would be the ISC Konstanz' BiSoN (*B*ifacial *i*ndustrial *s*olar cell *o*n *n*-type substrate) process technology. Yet, several challenges have to be met if such a relatively new technology for the industry is to be transferred to industrial scale mass production. It needs to be noted here that in research groups working with silicon solar cells around the world these technologies have been around for up to several decades.

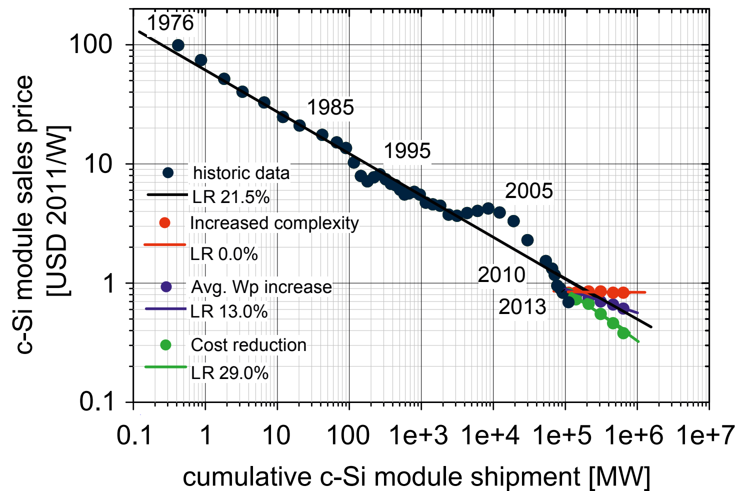

Fig. 1.1: Module sales prices plotted against module shipment, often referred to as the learning curve, including possible scenarios with increasing, constant and decreasing learning rates (LR) for the future development [1, 3, 4].

The prediction scenarios for the crystalline silicon solar cell industry in **Fig. 1.1** hint at several outcomes for the advance of the technology. The worst scenario is labelled as "Increasing complexity". It assumes that increasing W_{peak} (maximum module output power) of solar modules will be accompanied by an additional cost factor for complexity that almost

cancels out the benefits gained through cell efficiency. The scenario “Average W_p increase” relates to mere efficiency increase on cell level based on existing technology and accordingly decreases in cost. The scenario “Cost reduction” adds new and cheap metallisation technology, strongly decreasing the costs on top of the previous scenario [4]. In any of the cases, as efficiencies increase, processes get more and more sensitive to smaller variations and require more advanced process control. Furthermore, these processes are expected to require an improved contamination management, as recombination of charge carriers due to impurities will increasingly interfere with gains in efficiency. The purer the material, the more defined junctions and interfaces the more likely external contamination will become one of the limiting factors. This is a fact that has been very much neglected so far, but has to be considered as one of the main challenges of processing advanced solar cell concepts on large industrial scale.

This work is meant to give a first guidance to contamination management in crystalline solar cell processing. It covers the most important contaminants, studies and compares their impact on several process steps and works towards gaining sufficiently clean surface by industrially feasible cleaning techniques. Cheap and efficient cleaning technologies are crucial to avoid the scenario “Increasing complexity” from **Fig. 1.1**, as both the further optimisation of existing technology and the introduction of new process steps are likely to increase the sensitivity towards surface contamination. The topic of metal contamination management includes two main parts: To study the impact of surface contamination and to learn how to handle the (unavoidable) metal freight.

1.1 Motivation

It is a well-known fact that the main source for metallic contaminants in solar cell manufacturing is the surface of the as-cut wafer. The usually slurry-based sawing process leaves traces of the sawing wire itself on the surface. As the sawing wire usually is made from a brass or Cu coated steel wire, highest surface contamination values are measured for Cu and Fe. Extensive work on the impact of Fe and Cu contamination on silicon device manufacturing can be found in [5, 6]. However, the contamination level may differ from supplier to supplier, as different wires are on the market [7, 8]. The classical slurry-based sawing with silicon carbide particles is more and more replaced by fixed abrasive diamond wire sawing [9]. The diamond wire sawing process is reported to reduce surface contamination [8]. However, Cu, a fast diffusion impurity, is replaced by another slightly slower diffusing species: Ni, which is found to be especially harmful in near-surface regions [10]. Nonetheless, not many data have been published on the actual variation. Furthermore, not much information on the behavior of the impact of the first surface preparation steps, most commonly etching, is available.

Another source for metal contamination is inherent to the preparation of wafer surfaces as required for the production of solar cells: alkaline etching solutions (KOH/NaOH based). These solutions are employed for the etching of saw damage, for the texturing of the surface and for the removal of porous silicon after acidic, HF/HNO_3 based, etching. The solid bases that are diluted for making up alkaline etching solutions cannot be purified to the same grade (at competitive costs) by distillation as acids, hence, they contain comparatively high metal concentrations. In addition to that, the high pH value in the process reduces the solubility of these metal species and leads to increased wafer surface contamination [7]. The same has been observed for non-optimised cleaning bath setups that may reach critical metallic contamination loads in mass production [11].

Effective metal contamination management is required in particular before high-temperature steps, such as diffusion and thermal oxidation and surface passivation, as metals can easily penetrate the silicon due to their high solubility and diffusivity [12]. The detrimental effect of metallic impurities can be explained by their impact on the lifetime of photo-generated carriers as they cause defect levels which lead to “early” recombination of the separated charge carriers. In consequence, the charge carriers cannot be used for electrical power generation and accordingly the efficiency of the solar cell drops. Especially high diffusivity and solubility in silicon in combination with high recombination activity have been reported for Fe, Cu and Ni [12]. Furthermore, metal impurities can increase recombination at the surface [13, 14] by increasing the defect density of the interface. They may also give way to leakage currents [15] and may lead to junction breakdown [16]. A recent study on the impact of the most common contaminants on solar cell performance when added to the molten silicon for the wafer production was published by Coletti *et al.* [10].

With the introduction of new process steps the requirements for the wafer cleaning has to be re-evaluated. Several process steps employed in the production for “new” solar cell concepts are well-known to require very clean surfaces and also defined surface conditioning, e.g. thermal oxidation, passivation with aluminum oxide (Al_2O_3) [17] and deposition of doped

amorphous silicon for hetero junction solar cells [18]. While the phosphorus-diffusion with its ability of gettering metal impurities [19] is relatively robust against surface contamination [20], this may not be the same with boron emitter diffusion for n-type junction formation [15, 21]. However, good gettering efficiencies have recently been shown for boron emitter diffusion as well [22].

In general, as the efficiency of the solar cells increases, either by optimization of existing processes or the introduction of new process steps, the influence of single steps may become dominant; so-far minor losses are no longer covered up by factors such as material quality or badly optimised steps. A good explanation for this phenomenon is given by Glunz as he compares process optimization with fixing the “leaky bucket” [23]: once the main efficiency limiting step has been optimised (the biggest hole in the bucket), another step becomes predominant and thus requires attention. Hence, the optimization and further development of the whole process includes the optimization and/or exchange of cleaning steps.

1.2 Structure of the work

In the first chapter following this introduction (**Chap. 2**) information about **crystalline silicon solar cells** relevant for this work is given, starting from the physical properties of silicon crystal and the fabrication of wafers, moving via an electrochemical description of the Si crystal surface to the chemistry of etching and cleaning and preparation of said surface. Next, the *pn*-junction formation and properties of the junction are introduced and the back-end solar cell processes (contact formation) are briefly discussed. Last, this chapter lists common and not so common solar cell concepts and cell processes.

This part is followed by an introduction to the **physics of contamination in silicon devices** (**Chap. 3**). Defects, such as metal contaminants, in silicon and at the silicon surface cause photo-exited charge carriers to recombine. In order to study the effect of these defects on silicon, knowledge about the electric charge carrier recombination (and, inversely related to this, of the carrier lifetime) is required. First, the basic physics of recombination in the silicon bulk, in highly doped regions and at the surface are given. Second, the physical measurement techniques for the determination of lifetime of charge carrier pairs and of recombination properties of defects are introduced.

The "results and discussion" part of this work is composed of **Chap. 4** and **Chap. 5**. It is structured according to the following scheme, which is based on the idea of contamination management. It is split up in two parts. The first part studies the **impact of the metal surface contamination** on several solar cell devices and their production steps. It consists of the following points:

- Empirical determination of the most relevant contaminants
- Determination of critical process steps
- Fundamental study of the impact of surface metal contamination
- Experimental determination of threshold concentrations.

The second part deals with the topic of **cleaning of wafers for solar cell production** using means of process analytics and process optimization with the following key aspects:

- Description of the working system of initial contamination, subsequent processing and cleaning
- Quantification of contamination loads
- Study of the impact of the relevant surface treatment procedures on said contamination load (cleaning, etching)
- Test and comparison of standard cleaning procedures for high efficiency solar cell concepts
- Development, optimization and testing of industrially feasible cleaning procedures.

In more detail, **Chap. 4** presents results and discussions of intentional contamination studies. The main contamination species are identified and their impact on different relevant process steps, based on experimental results, are discussed. This section is split into passivation and diffusion processes for p-type cells and diffusions for n-type cells. It concludes with the simulation of the impact of the investigated contaminants on the wafer surface before diffusion processes on the final solar cell device. The purpose of this section is to compare the sensitivity of several important solar cell process steps and to take a closer look at the mechanisms behind the detrimental effects. Furthermore, the impact of variations of process parameters of two selected processes (namely phosphorus diffusion and fast firing) on the adverse effects of surface contamination is presented. Finally, in this chapter the influence of said contaminants present on the wafer surface before high temperature diffusion processes on several solar cell devices (p-type full aluminum back surface field cells and n-type high efficiency bifacial cells) is simulated. The goal of the simulations is to estimate the impact of surface contamination concentrations on final solar cell efficiencies, using the experimental findings on the simplified lifetime structures. The results of the simulations can be considered as a first step for the determination of threshold surface contamination concentrations before sensitive high temperature steps in the respective processes.

Chap. 5 deals with the wafer cleaning in solar cell processing. First, the investigated work system of cleaning and successive processing is introduced, including main input parameters, such as surface contamination of as-cut wafers, type of etching and chosen cleaning methods. Surface contamination data before and after processing are presented and the dynamics of the front end of line (FEOL) processes are revealed. Next, different cleaning sequences used for several solar cell processes are compared and the necessity for "advanced" cleaning in high efficiency solar cell processes is tested. As it proved that advanced cleaning is necessary, in the next section the development of an industrially feasible cleaning sequence is presented. Subsequently, the optimisation of the testing for high efficiency solar cell processes is elaborated. Finally, the impact of cleaning sequences on surface roughness—a "hot topic" in the processing of integrated circuits (IC)—is discussed and the impact on a state-of-the-art solar cell tested.

The penultimate chapter (**Chap. 6**) gives more details about **experimental procedures**. An overview of the experiment runs that were required for this thesis is given and detailed descriptions of the used analytical methods are provided. The last chapter (**Chap. 7**) is a collection of details of the used **simulation models**.

2 Crystalline silicon solar cells

In this chapter an introduction to the fabrication of a modern crystalline silicon solar cell is given. It is subdivided into five parts: First, the properties of crystalline silicon are briefly discussed (**Sec. 2.1**). The subsequent section (**Sec. 2.2**) deals with the silicon surface and its preparation. It covers such topics as etching, texturing, cleaning and surface passivation. In the following section of this chapter (**Sec. 2.3**) the function and formation of the *pn*-junction is explained, which is followed by a very short summary of the current industrial standards of contact formation (**Sec. 2.4**). Last, in **Sec. 2.5** an overview on possible c-Si solar cell structures is given. The structures that are relevant for this work are explained in more detail and the respective process sequences are introduced.

2.1 Properties of crystalline silicon and crystalline silicon wafers

In this section the basic solid state and physical properties of the silicon crystal are introduced briefly. Fundamental semiconductor principles are listed and the first equations such as the *Fermi-Dirac* statistic are discussed in the first **Sec. (2.1.1**) of this chapter. The second part (**Sec. 2.1.2**) deals with the different fabrication routes of the silicon wafer from metallurgical silicon and discusses the current silicon market shares of the differently obtained silicon wafers. It is shown that the silicon wafer, despite recently falling prices, still makes up a large part of the overall costs of a solar module.

2.1.1 Properties of crystalline silicon

Silicon is the second most abundant element of the Earth's crust making up about 26% of its weight and is used as most common semiconductor for both integrated circuits (ICs) and solar cells. As the Si−Si bond strength is relatively low ($226\,\mathrm{kJmol^{-1}}$) compared to bonds with other elements such as hydrogen ($328\,\mathrm{kJmol^{-1}}$) and oxygen ($362\,\mathrm{kJmol^{-1}}$), silicon is solely found as compound. SiO_2 is found in sand and quartz minerals and there exists an enormous amount of silicate-based minerals [24].

Once reduced (usually from quartz using coke and an electric arc) Si crystallises in diamond structure (face centered cubic, fcc). Si forms a network of sp^3 hybrids that are tetrahedrally connected to its neighbouring atoms. The covalent atomic radius of Si is 1.11 Å and the lattice constant 5.43 Å with a density of of $2.320\,\mathrm{gcm^{-3}}$ [25]. From the energy band diagram in **Fig. 2.1** (right hand side) it can be deduced that Si is an indirect semiconductor. The energy distribution of the different orbitals is plotted against the crystal vectors[1] from the Brillouin zone (drawing in the middle of **Fig. 2.1**). The Brillouin zone denotes the so-called inverse lattice of the crystal, which is derived from the two entangled actual fcc lattice cells on the left hand side (the gray atoms denote the atoms belonging to the second fcc cell). As it can be deduced from the energy diagram, the minimum of the conduction band (E_C) is not located directly above the valence band maximum (E_V), which is found along the axis from Γ to X [26]. Therefore, a change in crystal impulse is required for an electron to surpass the bandgap (the band gap energy is denoted with E_g) in either direction. Light itself does not have the necessary energy for that. Thermal vibration of the crystal (also referred to as phonon-assisted absorption events) is required for the electron transfer as indicated by the arrows in the graph [27].

The structure of valence (E_V) and conduction (E_C) band that is commonly used in semiconductor physics to describe the semiconducting properties of a material can be derived from the molecular orbitals in accordance to organic macromolecules (see **Fig. 2.2**) with the former being the equivalent of the HOMO and the latter denoting the LUMO [30, 31]. In the case of a semiconductor the bandgap is small enough for electrons near the valence band edge to reach into the conducting band for temperatures above 0 K. This distinguishes

[1]The vectors are derived from the solution of the Schrödinger's equation for the model of an almost free electron in a crystal.

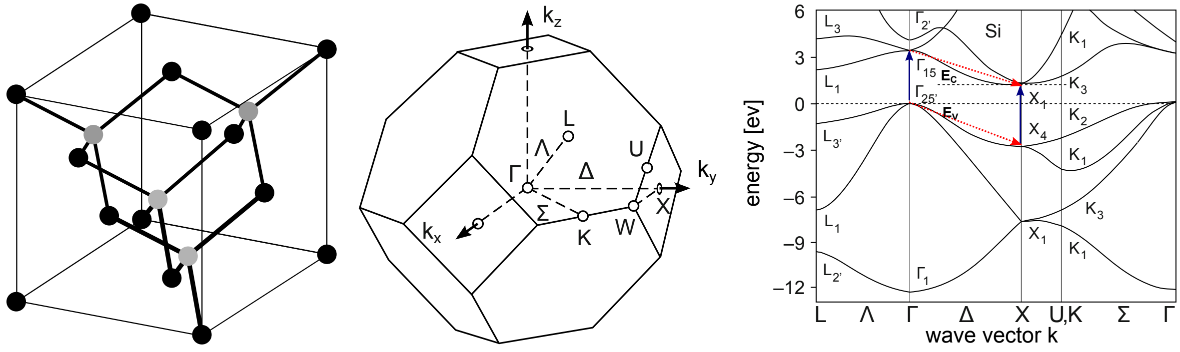

Fig. 2.1: Left: Diamond crystal lattice cell, gray atoms represent centers of a tetrahedron and belong the second entangled fcc lattice cell. Middle: Brillouin zone (inverse lattice) of a fcc lattice (adopted from [28]). Right: Energy band structure of Si (modified from [29]), the phonon assisted (dotted arrows) electron transfer is indicated.

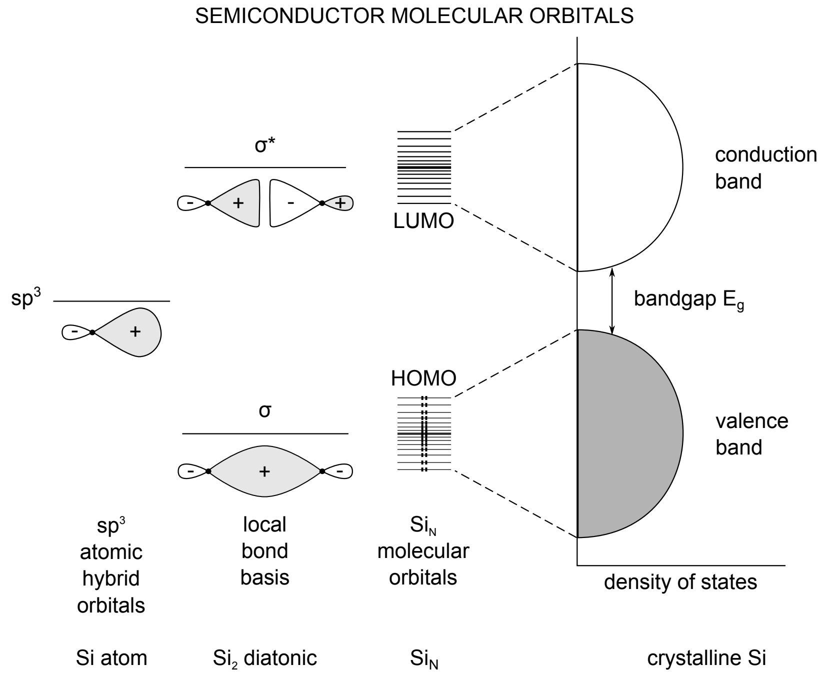

Fig. 2.2: Semiconductor band model derived from MO theory (adopted from [31]).

semiconductors from insulators.[2]

The population distribution P of the bonding and anti-bonding orbitals can be calculated using the *Fermi-Dirac* equation. This is a derivation of the classical *Boltzmann* equation taking the *Pauli* principle into account, which forbids two *Fermions* of the same spin (such as electrons and protons) to occupy the same energy level:

$$P(E,T) = \frac{1}{\exp\left(\frac{E-E_F}{k_B T}\right)+1} \tag{2.1}$$

with E_F being the *Fermi* energy for $P = \frac{1}{2}$ at the given absolute temperature T and k_B being the *Boltzmann* constant. The *Fermi* energy denotes the chemical potential at $T = 0\,\mathrm{K}$ [32]. Electrons found in the conduction band and therefore free for electrical transport are

[2] Semiconductors have a bandgap smaller than 4 eV, insulators greater than 4 eV.

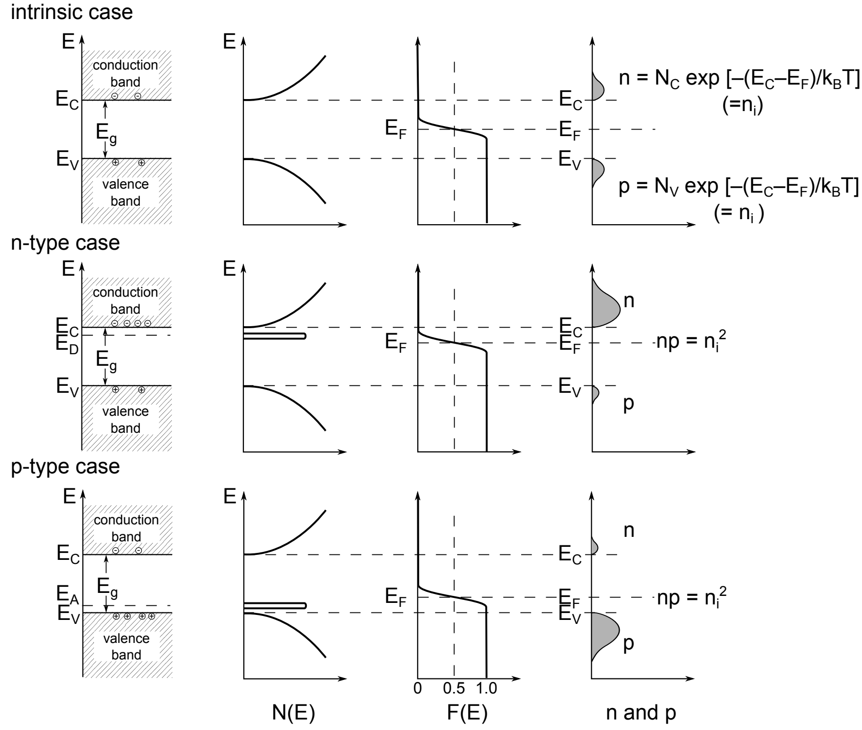

Fig. 2.3: Schematic band diagram, density of states, Fermi-Dirac distribution and the carrier concentrations for intrinsic, n doped and p doped silicon (adopted from [33]).

from now on referred to as carrier electrons (n, for "negative") and the sites that are left unoccupied in the valence band are from now on called the respective holes (p, for "positve"). Holes may as well be responsible for current transport, as the neighbouring atom's valence electron may take over the space and then the next and so forth; thus the hole begins to "move". As the electrons and holes movement refers to different forms of electron transport, to each of the two carrier types different effective masses and mobilities can be assigned. For an intrinsic, i.e. non-doped, semiconductor the number of electrons and holes with an energy near the conduction and valence band edge, respectively, can be calculated at a given temperature by

$$n = N_C \exp\left(-\frac{E_C - E_F}{k_B T}\right) \tag{2.2}$$

and

$$p = N_V \exp\left(-\frac{E_F - E_V}{k_B T}\right) \tag{2.3}$$

with N_C and N_V being the effective densities of states in the conduction and valence band.[1] In the intrinsic case p equals n and is usually referred to as intrinsic carrier density n_i [33]:

$$np = n_i^2 = N_C N_V \exp\left(\frac{-E_g}{k_B T}\right). \tag{2.4}$$

The conductivity of a semiconductor can be dramatically increased when it is doped with

[1]The two equations are obtained when solving the integrals $n = \int_{E_C}^{E_{top}} N(E)F(E)dE$ and $p = \int_{E_{bottom}}^{E_V} N(E)F(E)dE$ for the occupied conduction and valence band levels. For more details refer to [33].

foreign atoms. This is usually achieved by elements with one more or one less valence electron than the semiconductor itself. In the case of Si either group III (acceptors) or group V (donors) elements of the periodic table are added to the purified and molten silicon in order to obtain p- and n-doped material, respectively. When crystallising the silicon, the foreign atoms are built into the crystal lattice. In the first case “extra holes” are added as only three valence electrons can form covalent bonds with its neighbouring Si atoms. In the second case extra valence electrons—free electrons—are introduced. The outcome of the doping on the band diagram is an extra defect level near the bandgap from the extra peak within the forbidden band. As a result, the “step” of the Fermi-Dirac statistics is shifted towards the band edges as the numbers of either electrons or holes are increased by the foreign atoms. The total amount of carriers is not affected by the doping, accordingly the *Fermi* level shifts and therefore $np = n_i^2$ applies in all three cases—intrinsic, p- and n-type case—to maintain charge neutrality [33]. A summary of the introduced concept of doping is shown in **Fig. 2.3**.

2.1.2 Production of a silicon wafer

After reduction of silica and purification of obtained silicon (“poly silicon”) the substrate is doped and crystallised.

A typical crystalline silicon wafer for the fabrication of solar cells is made from a lightly doped silicon of either p- or n-type. Currently most of the poly silicon (80% market share) is purified using the classical *Siemens* process[1] obtaining semiconductor grade silicon (9N, which refers to 99.9999999% pure silicon, or even 12 N). An alternative way to obtain high purity silicon is to reduce it in a fluidised bed reactor (FBR). The FBR process is based on silane (SiH_4) that decomposes to Si at much lower temperatures than the $SiHCl_3$ used in the *Siemens* process. The FBR process is expected to gain a large share in the market due to its much lower energy consumption [34–36]. A relatively recent overview of the FBR technique and the other purification technologies in use can be found in [37]. Despite efforts to reduce feedstock costs by using less pure silicon, so-called solar grade silicon (5–6 N) [38], most of the current solar Si is of 8–9 N quality [4].

The most common dopant for industrial use is boron. Accordingly doped p-type silicon had a marked share of 95% in 2013 (cf. left hand side graph of **Fig. 2.4**). Phosphorus doped n-type silicon is, however, gaining its share, due to several advantages such as higher minority carrier diffusion lengths and the absence of light induced degradation [35] (cf. **Sec. 4.5**). This results in higher obtainable efficiencies as shown in the right hand side graph of **Fig. 2.4**.

Apart from the doping, the silicon used for solar cells can be subdivided according to the fabrication of the brick from which the wafers are sawn. Currently, most solar cells are made either from “normal” or high quality multi-crystalline silicon. Multi-crystalline silicon bricks are fabricated by cooling molten silicon that had either been poured into SiO_2 or Si_3N_4 coated crucibles or had directly been molten in such a crucible. Silicon bricks with mixed crystal orientation are thus obtained. The more advanced the cool-down process, the lower is the density of defects and accordingly the higher the obtainable efficiencies with the material [39]

[1] The metallurgical Si is molten and brought into reaction with HCl to form $SiHCl_3$ at 300°C that can be distilled and reduced back to Si by the use of H_2 at 1100°C.

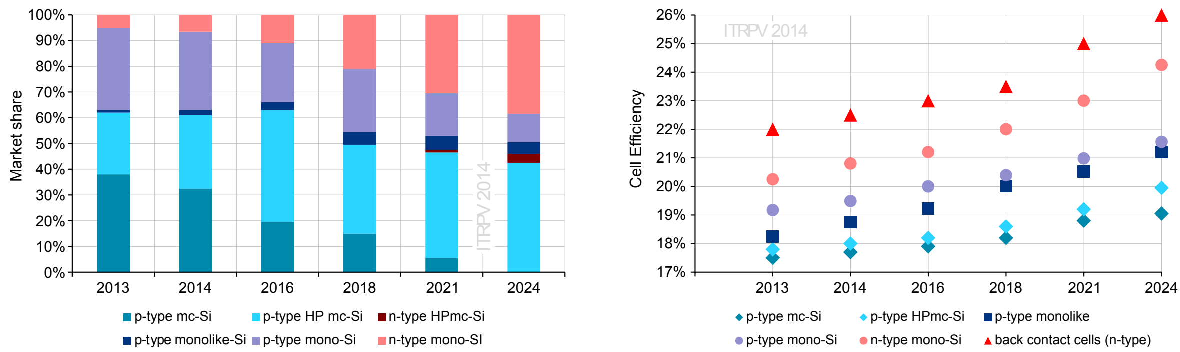

Fig. 2.4: Left hand side: Current and expected market share of different base material and ingot fabrication method. Right hand side: Current and predicted solar cell efficiencies for the different materials. The market analysis and predictions are taken from the SEMI International Technology Roadmap for Photovoltaic (ITRPV) 2014 [36].

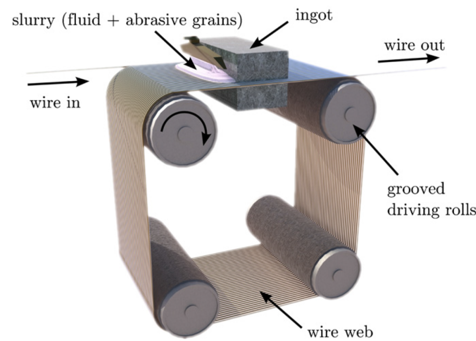

Fig. 2.5: Working principle of an endless-wire saw. Taken from [40].

are. The crucible sizes of the current generations 5 and 6 (5x5 and 6x6 ingots can be cut from the brick) have reached an area of about up to 100x100 cm^2 and a height of 26 cm resulting in a weight that can exceed half a ton [36]. The other commonly used solidifying technique with a market share of 40% is the *Czochralski* process from which single crystalline silicon (“mono-Si”) rods are obtained by dipping a seed crystal into molten Si attached to a pulling system. The seed crystal is slowly pulled up in a rotating manner, triggering the silicon to solidify in a rod-like structure. Usually an Ar atmosphere is used to avoid additional O_2 incorporation. The advantage of this process is the fact that the crystal orientation can be predetermined by choosing the seed crystal.

Industrial solar cells are produced from wafers with an initial thickness of 150 μm to 220 μm. Both the multicrystalline (mc) ingots and the Czochralski (Cz) grown rods are cut into wafers using multi-wire sawing processes. The blocks of silicon are glued to a holding plate and then up to four blocks can be cut at a time using endless-wire (multi wire) saws with organic slurry coolant (commonly polyethylene glycol, PEG) and loose SiC abrasive particles according to **Fig. 2.5** [9]. Apart from the so-called slurry sawing technique, more and more wafers (currently about 30% of the wafers on the market [36]) are sawn by the so-called diamond wire process, using wires with fixed abrasive diamond particles. Both techniques have a yield of just under 50% as wires have diameters of 120 μm and overall kerf loss of about 130 μm. Benefits of the diamond wire sawing process are a faster throughput and that

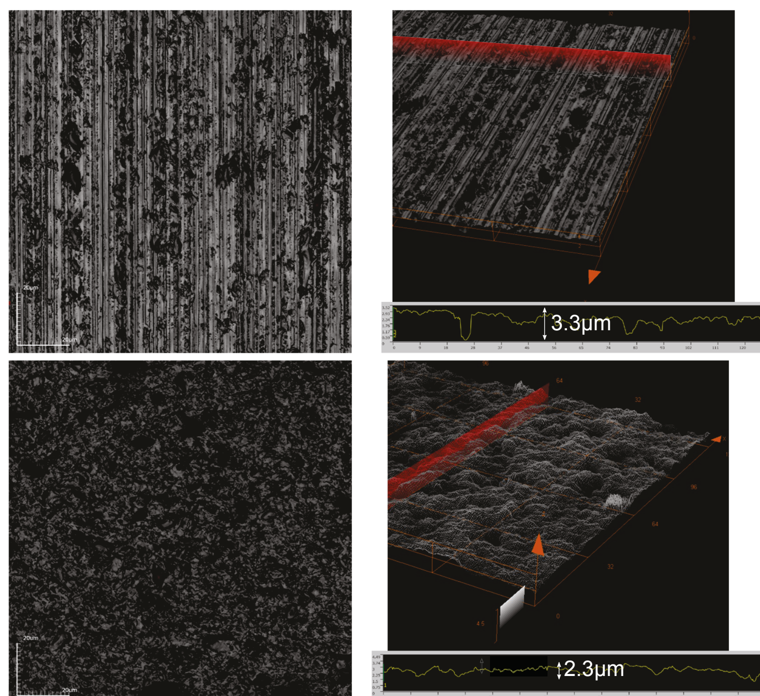

Fig. 2.6: Confocal microscope images of as-cut wafers. Top row: Diamond wire sawn surface; Bottom row: Slurry sawn surface. Left hand side: Top view. Right hand side: 3D image and line scan, the approximate depth of the visible saw damage is indicated.

no organic slurry needs to be used. The required cooling during sawing can be achieved by water or glycole instead of the greasy organic slurry full with SiC particles that is used in the conventional wire sawing. This simplifies subsequent wafer cleaning and the recycling of the kerf loss [9]. Furthermore, back-and-forth movement of the wire can be applied reducing the consumption of wire compared to the endless wire sawing process [35]. One drawback of the diamond wire sawing technique is the formation saw-marks that cannot be removed in acidic texturing (the main surface preparation technique for multi-crystalline wafers). The saw marks are clearly visible in the microscope images from **Fig. 2.6**. The depth of the visible saw damage is indicated. The depths of the crystal damage inflicted by the wire saw, however, tends to be deeper for the slurry sawn wafers. The crystal damage commonly ranges from roughly 15 μm in the slurry case to about 10 μm in the diamond-wire case as determined via Raman shift measurement reported by Radet *et al.* and published in [41].

Considering the whole module prices, which have drastically decreased in the last few years, still Si and wafer production costs make up for about one third of the overall costs following the module, which makes up almost half of the overall costs. The values for absolute and relative costs at the beginning of the years 2010, 2013 and 2014 are found in **Fig. 2.7**. The solar cell process remains at around one fifths to one quarter of the overall module costs. Reducing module costs further is difficult, as the main cost contribution is the material such as glass and frames. Wafering costs are also relatively difficult to decrease, as they are mostly driven by the loss in silicon due to the wire sawing process. Silicon costs will certainly further be reduced by scaling effects and the FBR process. The solar cell process costs are mostly driven by consumables which can be decreased by lean processing. The most elegant way of

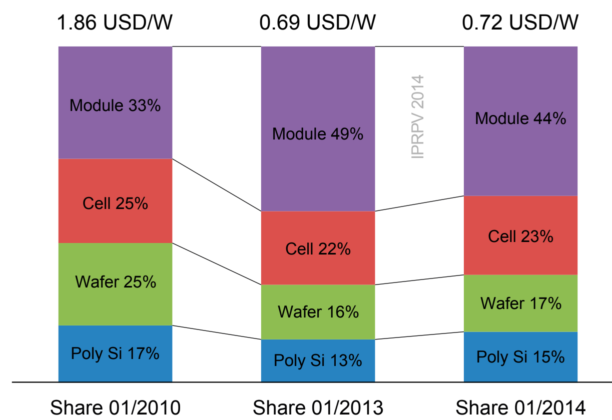

Fig. 2.7: Absolute module prices and relative shares of the contributing costs at the beginning of 2010, 2013 and 2014 [36].

reducing overall costs per watt further, however, would be to increase solar cell efficiencies by only slightly increasing production costs, which is the motivation of many companies and research institutes. Some of the possible alternatives that we suggest for next generation solar cells will be discussed at the end of this chapter.

2.2 Preparation of the silicon wafer surface

When discussing surface contamination and wafer cleaning, a closer look at the silicon surface is required. In the following, properties such as crystal orientation and reactivity of the (idealised) silicon surface are discussed (**Sec. 2.2.1**). The most relevant surface preparation techniques, which are chemical etching (**Sec. 2.2.2**) and cleaning of silicon surfaces, are discussed and put into the context of solar cell processing (**Sec. 2.2.3**).

2.2.1 Properties of the silicon surface

The silicon crystal structure has been introduced earlier. The diamond lattice with the cubic face centered crystal can be described by the Miller indices indicating the vectors in a lattice cell [42]. The three representative crystal vectors, [100], [110] and [111], and their resulting planes, (100), (110) and (111), are indicated in **Fig. 2.8**. Using the Cz-crystal pulling process, the crystal orientation can be predetermined by the choice of the seed crystal so that wafers of a defined crystal orientation are obtained.

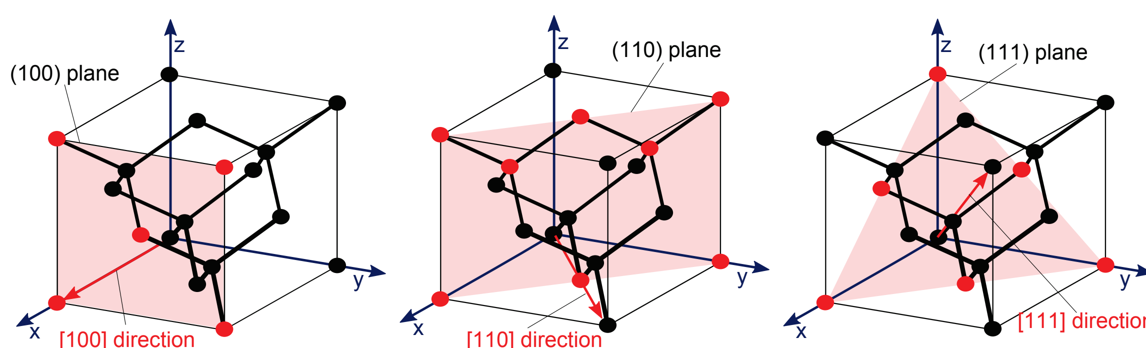

Fig. 2.8: Crystal planes and orientation of the diamond structure. The atoms located on each plane are indicated by the red colour.

When plotting the top row of atoms of the ideal surfaces of the three crystal orientations, it becomes obvious that two out of the three variations have a much more uneven surface. The "voids" in between the terminal silicon atoms are much larger for the (100) and (110) planes than for (111) plane which makes the two former much more reactive than the latter. For example, the oxidation of the silicon surface in water is faster for (100) and (110) surfaces which can be explained by the fact that oxygen/water can more easily penetrate the surface [43]. Furthermore, terminal atoms in (100) and (110) surfaces are only connected with the silicon bulk by two Si−Si bonds. The other two sp^3 hybrid orbitals form so-called "dangling" bonds, i.e. bonds without counterpart. In contrast to that, the terminal atoms of the (111) plane are much more tightly bond to the crystal lattice by three Si−Si bonds and form only one dangling bond.

In reality, however, the silicon surface will never be as perfect as assumed so far. Neighbouring terminal Si atoms (=Si:) tend to form dimers, or Si atoms may form bridges, so-called addatoms or restatoms, and the surface may have steps or contain other forms of strains [44].

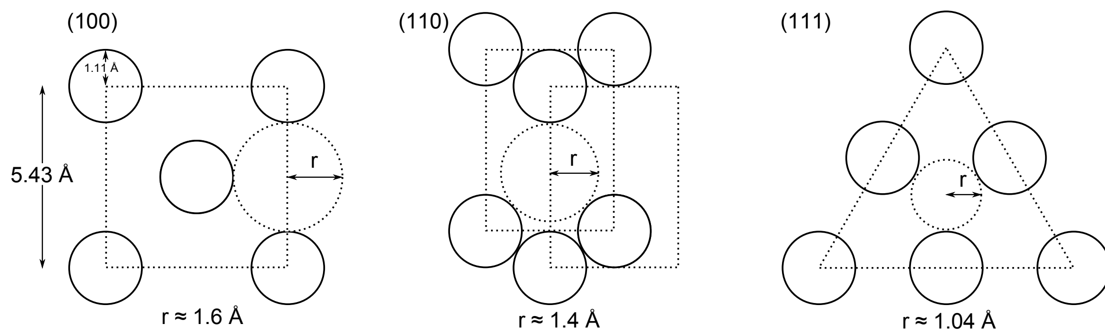

Fig. 2.9: Surface morphology of the three ideal crystal surfaces including the “voids” in-between. Data from [25].

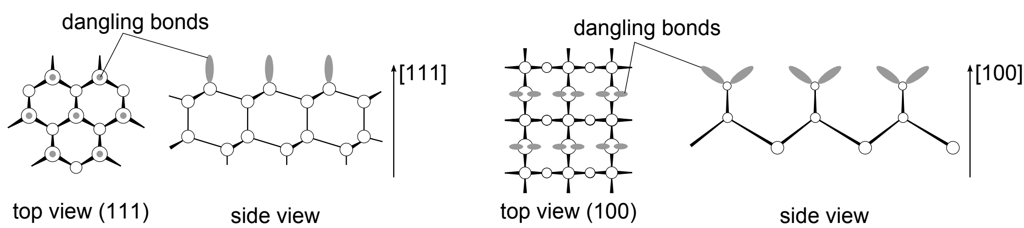

Fig. 2.10: Sticks and balls model of the (111) and (100) Si surface, top and side view. Based on [45].

Native and wet silicon oxides

Virgin Si surfaces easily adsorb water and get oxidised quickly. Dangling bonds split the H_2O molecule and form ≡Si−OH and ≡Si−H. Two dangling bonds in close vicinity are required for the reaction, which is the reason why H_2O has a much higher adhesion to (100) surfaces than to (111) surfaces [46]. On (111) surface the adsorption of water occurs first at surface faults. The −H and −OH groups have been shown to be mobile among dangling bonds once they have been formed. Soon after adsorption of water the oxidation of the surface starts [47].

A pattern for the reaction of Si surfaces with oxygen and water is suggested by Gräf *et al.* [48] (**Fig. 2.11**). In water a second reaction path, which is the dissolution of Si to “$Si(OH)_4$”, runs in parallel as demonstrated by an increasing silicon content in ultra pure water by Morita *et al.* [49]. They also show that the oxidation in air is significantly increased by moisture in air (6.7 Å in seven days with a humidity of 42% vs. 1.7 Å in O_2/N_2 and 1.9 Å in N_2 in both cases with an H_2O concentration below 0.1 ppm). In ultrapure water in turn, the oxide growth rate correlates with the O_2 that is dissolved in it, leading to the conclusion that room temperature oxidation of the Si surface requires both humidity/water and oxygen (also indicated in **Fig. 2.11**). A dependency on the doping type and concentration was also found: highly doped regions (n^+ on n-type) were shown to oxidise much more quickly but eventually to saturate at a thickness of 10 Å indicating a field assisted mechanism [49].

In case of a hydrogen terminated surface, the Si−H bonds have been shown to be more stable towards oxidation than the Si−Si backbone bonds, which get oxidised first [50]. The in air or water grown silicon oxide layer is of amorphous, irregular structure and the top layer

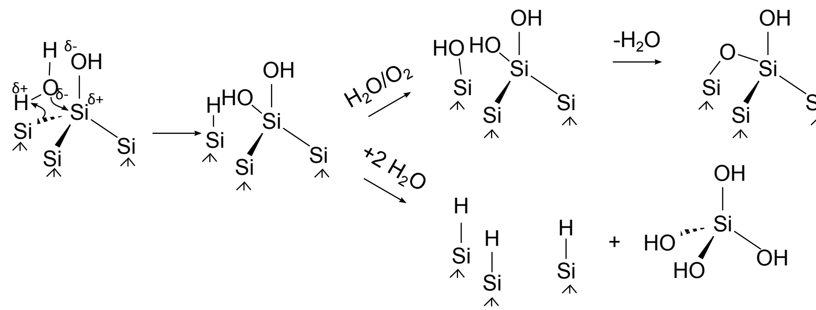

Fig. 2.11: The growth of native oxide as suggested in [48].

Tab. 2.1: Oxide thicknesses as measured by Angermann *et al.* and published in [51].

Oxidation process	Temperature [°C]	Time [min]	Thickness [Å]
DI H_2O	80	210	15.0
$NH_4OH+H_2O_2$ (SC1)	75	10	12.7
$HCl+H_2O_2$ (SC2)	75	10	10.7
$H_2SO_4+H_2O_2$	90	10	18.0
Thermal oxide (O_2/N_2)	500	10	17.5

is covered by −OH groups that are responsible for the hydrophilic properties of silicon oxide layers [49].

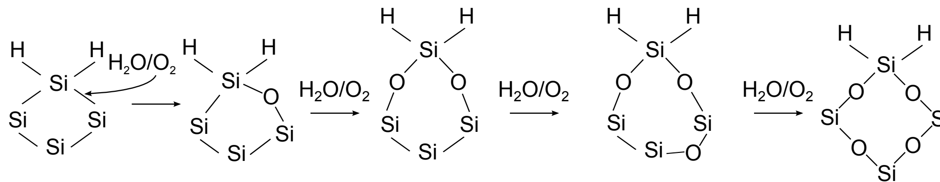

Fig. 2.12: Layer by layer growth of silicon oxide on hydrogen terminated silicon surfaces as suggested in [49].

An example for oxide thicknesses after treatment in different chemical surroundings commonly used for wet chemical cleaning on (111) surfaces as provided by Angermann *et al.* in [45] is given in **Tab. 2.1**. The table shows how the addition of oxidising reagents accelerates the oxide growth.

Depending on the pH, the termination of the oxide varies and shows amphoteric behaviour as depicted in the graph in **Fig. 2.13**. This behaviour strongly determines the surface properties such as chemisorption and physisorption of reactive species like fluorine containing solutions and the adsorption of contaminants such as metal ions and particles.

Hydrogen termination

Hydrophobic surfaces are quickly obtained when oxidised wafers are dipped into hydrofluoric acid containing solutions. The etch rate depends strongly on the structure of the silicon oxide. The more amorphous the character of the oxide, the faster it etches. Also, impurities

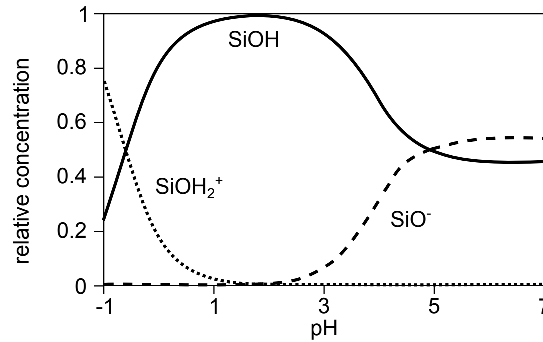

Fig. 2.13: Amphoteric behaviour of silicon oxide in water calculated by Knotter in [52] according to data from [53]. This corresponds very well with the isoelectric point of silica of pH≈2

such as phosphorus, as found in phosphorus silicate glass (P_2O_5/SiO_2 = PSG), increase the etch rate. Interestingly, this is not the case for boron silicate glass, which shows a slower etch rate that decreases until boron makes up 20 molar percent of the glass layer when it slowly starts to increase [54]. Thermal oxide and wet chemically grown oxides heated above 500°C tend to be most ordered in structure and to etch the slowest [55].

Hydrofluoric acid reacts with silicon dioxide forming hexafluorosilicic acid according to

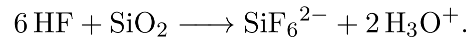

$$6\,HF + SiO_2 \longrightarrow {SiF_6}^{2-} + 2\,H_3O^+.$$

The reaction mechanism is slightly more complicated than this equation might suggest. One reason for this is the hydrofluoric acid that, as a relatively weak acid (with an acidity constant of 6.5e–4 at 25°C), is reacting in several different equilibrium reactions as reported by Verhaverbeke *et al.* in [56]:

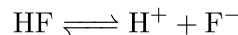

$$HF \rightleftharpoons H^+ + F^-$$

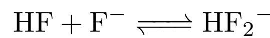

$$HF + F^- \rightleftharpoons {HF_2}^-$$

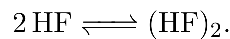

$$2\,HF \rightleftharpoons (HF)_2.$$

In addition to that, ${H_2F_3}^-$ and even higher conglomerates have been reported for moderate concentration of HF [57, 58]. The interconnected equilibria shift depending on pH and fluoride concentration. For a 7.5 $\mathrm{molL^{-1}}$ solution Verhaverbeke *et al.* report predominantly HF and $(HF)_2$ for pH values below 2. Between pH 3 and pH 5 the ${HF_2}^-$ modification gains in importance and at even higher pH values towards pH 7 F^- becomes the predominant species. For this work and in solar cell processing in general, the first condition is most relevant, as diluted HF with at least 2%wt. is used (1 $\mathrm{molL^{-1}}$ and pH 1.5). The pH of cleaning or process baths is often found at even lower values when HCl is added.

If oxidised wafer surfaces are dipped into HF containing solutions with low pH values, the silicon oxide is present as $Si{-}{OH_2}^+$ that can be easily removed by F^-. The strong electronegativity of the −F termination species allows for further fluoride containing species to attack nucleophilically so that finally SiF_4 is formed which in aqueous HF solutions reacts to ${SiF_6}^{2-}$, as depicted in **Fig. 2.14**. This nucleophilic attack has been determined to be

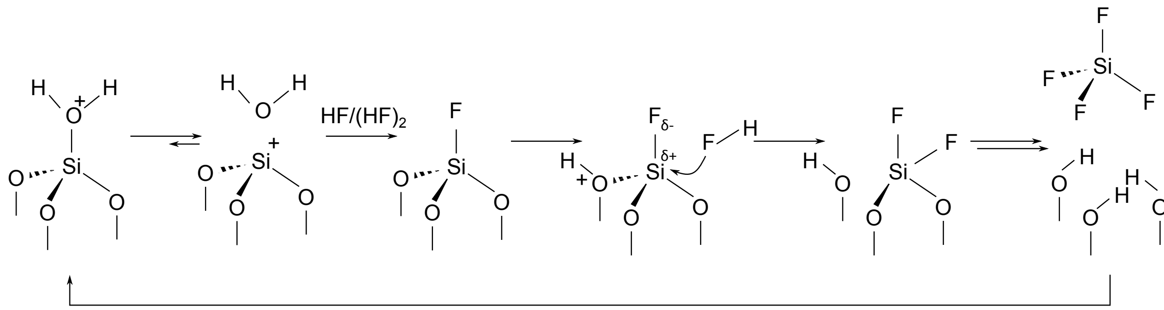

Fig. 2.14: Reaction mechanism of SiO_2-removal in HF [59].

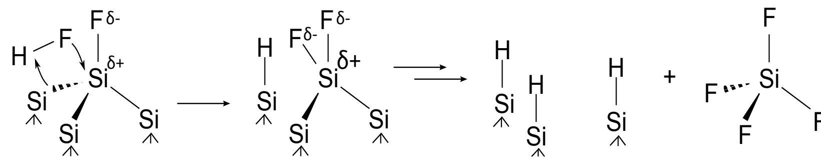

Fig. 2.15: Reaction mechanism for surface passivation.

much faster than the the replacement of the $-OH_2^+$ or $-OH$ groups by $-F$ which is mostly governed by the pH [52]. The last step, when all the oxide has been removed, leaves most of the surface hydrogen terminated [59], the mechanism behind that is sketched in **Fig. 2.14**. As soon as the hydrogen terminated surface is removed from the hydrofluoric acid the re-oxidation starts. A comprehensive overview about all equilibria involved in this process, including the equilibrium constants, can be found in [52].

2.2.2 Wet chemical etching

Wet chemical etching has several applications in solar cell processing. First of all, silicate glass layers are etched in HF-based solutions similar to oxides (cf. previous section). Second, caustic solutions are used to remove the highly defective and contaminated surface area of the as-cut wafer. Monocrystalline wafers are commonly etched in anisotropically etching KOH/NaOH-based solutions. Depending on the solution composition and the employment of additive, they can be used to produce flat or textured surfaces which are used to reduce the reflectance of the wafers. In the case of multi-crystalline wafers, isotropic acidic solutions are used, usually $HF+HNO_3$-based, sometimes also CH_3COOH containing [60–62], that apart from removing the saw damage also decrease the surface reflectance by texturing the surface. Furthermore, single side acidic etching solutions ($HF+HNO_3$-based often including H_2SO_4), are used to remove doped areas or to chemically polish the wafer surface [63, 64].

A significant boost of solar cell efficiency was the introduction of wet chemical texturing of monocrytalline (100) silicon surfaces in alkaline solutions first patented in the 1970s [65]. This patent claimed to increase the light coupling by random pyramid texturing. This texturing of the front surface is commonly either obtained in a combined etch step that removes the saw damage or is performed separately.

In standard solar cell fabrication texturing, is performed at the beginning of the process

sequence (front end of line, FEOL). However, for more recent high efficiency solar cell concepts the front surface is textured after pre-processing the backside of the wafer further at the back end of the line (BEOL). The following will deal with etching silicon in general by giving a very brief overview about the different possible etching techniques. It focuses on alkaline etching, as all the samples produced for this work were etched in such solutions.

There have been approaches to use other etching techniques than wet chemical etching for structuring the surface known from IC manufacturing, such as reactive ion etching (RIE), plasma etching, laser etching and reactive gas etching [66]. Also, electrochemical etching has been used. The oxidation of the Si is achieved by injection of carriers into the crystal either by light or electrical contact and subsequent dilution in the solvent (most commonly diluted HF) [67, 68]. Moreover, surface structuring by metal assisted etching has shown some promising results. Furthermore, partly covering the surface with etching masks in combination with reactive ion etching or wet etching have been explored [69–71]. But to my knowledge, none of these approaches has gained widespread use in industrial solar cell process chains. Instead acidic and alkaline etching are applied as they are cheap and well understood. Process improvement is mostly achieved by fine-tuning or the development of additives slightly changing the behaviour of existing processes.

General mechanism of silicon etching

Generally speaking, the etching of silicon is a two step process. Firstly, the terminal Si atoms need to be oxidised and secondly they need to be dissolved. The oxidising component of the etching solution oxidises first the Si−Si bond and subsequently the Si−H bond, allowing the nucleophilic attack of a nucleophile, such as OH^- and F^-, and thus dissolving the oxidised Si. A general scheme is sketched in **Fig. 2.16**.

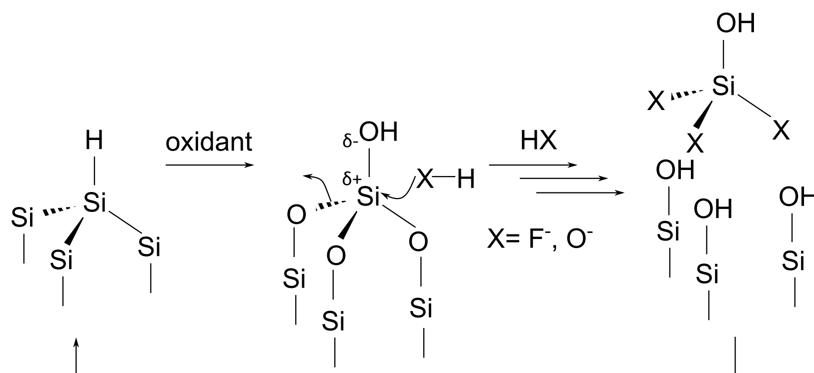

Fig. 2.16: Si etching mechanism [52].

Acidic etching

Strong oxidants together with HF can have a high etch rate for Si. The etch rate is calculated from the material loss, usually in μm per side, per unit of time. The most common system applied for fast texturing or polishing of silicon surfaces is the use a mixture of aqueous HF

and HNO_3. The reaction with silicon can be subdivided into the oxidation reaction and the dissolution reaction of Si with an overall reaction:

$$3\,Si + 4\,HNO_3 \longrightarrow SiO_2 + 4\,NO + 2\,H_2O$$

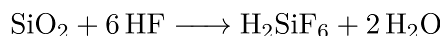

$$SiO_2 + 6\,HF \longrightarrow H_2SiF_6 + 2\,H_2O$$

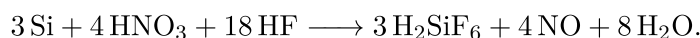

$$3\,Si + 4\,HNO_3 + 18\,HF \longrightarrow 3\,H_2SiF_6 + 4\,NO + 8\,H_2O.$$

The exact reaction mechanism is much more complex than these equations suggest and is discussed in much greater detail in [72]. Depending on the bath make-up, the resulting surface can be of textured or of polished morphology [73]. The etching takes place almost independently of the silicon crystal orientation (isotrop), which is why it is used as texturing solutions for multicrystalline Si surfaces. For single sided etching in inline etching tools, H_2SO_4 may be added to the mixture in order to increase the viscosity, further insight into this system is given in [74].

Alkaline etching

Etching of Si in alkaline solutions with bases such as KOH, NaOH, NH_4OH and tetramethyl ammonium hydroxide (TMAH) can be described by the following overall equation:

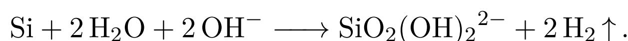

$$Si + 2\,H_2O + 2\,OH^- \longrightarrow SiO_2(OH)_2{}^{2-} + 2\,H_2\uparrow.$$

KOH and NaOH are the most widely used bases in PV manufacturing as they are comparably cheap. In IC technology, the relatively high metal content, as they cannot be purified via distillation, has been a severe issue. In contrast to this, in PV manufacturing this problem has not shown up much. Apart from transition metals, the contamination of the Si surfaces with Na or K is very much undesired. For that reason, IC manufacturing has to a large extend switched to organic bases such as TMAH for alkaline etching.

The etching velocity of alkaline solutions depends on the surface orientation, a phenomenon that is referred to as anisotropy. Etch rates and selectivity for etching different surface orientation depend on type of base, concentration, temperature, potential additives and on the doping of the silicon (highly B-doped layers may function as an etch stop) [75–77]. Generally, the relationship between the etch rates for the three different planes is (110) > (100) > (111), which does not quite follow the surface package density (cf. **Fig. 2.9**). The density increases in the following order: (100) < (110) < (111) (from 6.77e+14 to 9.59e+14 to 11.76e+14 cm^{-2}). The reason for the high etch rate for the (110) surface can be attributed to the "more corrugated structure" relative to the other surface planes as Fahlmann puts it in [78].

The strong selectivity between (100) and (111) surfaces (up to several hundreds to one) is explained by Seidel's electrochemical model for the alkaline etching reactions as published in [79]. It is traced in the following. The band diagrams before and after contact with the electrolyte are shown in **Fig. 2.17**. Relative energy levels to vacuum are indicated for the Si crystal and the $H_2O/OH^- + \frac{1}{2}H_2$ redox couple. For pH 14 the energy potential of the

$H_2O/OH^- + \frac{1}{2}H_2$ couple can be estimated to be –3.7 eV[1] . The energy levels of the Si–Si bonds to the crystal backbone (B) and the dangling bond states (A) are indicated. On contact, electrons flow from the electrolyte to match the Fermi-levels. The first reaction step is the "saturation" of the two dangling bonds by OH^- with the injection of two electrons into the conduction band. The terminal –OH bonds are weakened, indicated by the shift of the energy state to B'. Then $Si(OH)_2{}^{2+}$ is removed and reacts to silic acid. The excess electrons in the conduction band then reduce water to H_2.

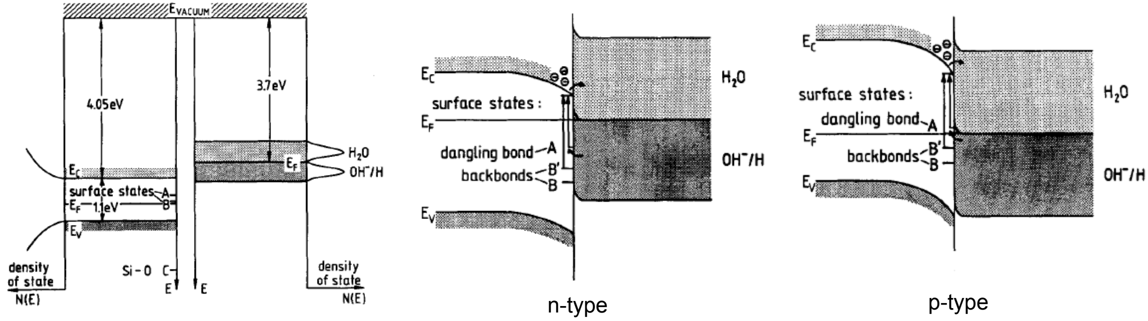

Fig. 2.17: Left hand side: Band model and density of states for Si and the electrolyte before contact (Si model neglects band bending at the surface). Middle and right hand side: Band structure after contact for n-and p-type Si. Backbonds are referred to bonds to the silicon backbone. From [79].

In contrast to the (100) oriented surface, which injects two electrons per Si into the conduction band, only one electron at a time can be generated in (111) orientation when saturating the dangling bond. Furthermore, the energy level B of the three backbone bonds is significantly lower than of the two in the (100) plane accounting for the difference in activation energy (E_a), as observed, and accordingly lower etch rates for the (111) surface.

The selectivity towards the (110) plane can be explained by the even higher energy level calculated for the bonds to the backbone and the easier penetrability for water molecules due to the "channel-like" structures; an advantage that is lost, when an isopropyl alcohol is added which mainly just covers the surface [80].

Saw damage etch

For the removal of the saw damage in the concentrated KOH or NaOH solution the anisotropy only plays a minor role. Here etch rate is of importance to minimise process times. The reaction rate (etch rate) for the relevant (100) surfaces (as [100] is the preferred crystal orientation for silicon wafers for solar cells) was found to be

$$R = k_0[H_2O]^4[KOH]^{\frac{1}{4}} \exp\left(\frac{-E_a}{k_B T}\right), \tag{2.5}$$

with $E_a = 0.595\,\text{eV}$ and $k_0 = 2480\ \mu\text{mh}^{-1}\cdot\text{mol}^{-4.25}\text{L}^{4.25}$ [79]. Highest etch rates well above $1\,\mu\text{min}^{-1}$ are found for temperatures exceeding 80°C in the range between 15 and 20 %wt. KOH. The etch rate was found to be independent for various alkali metal cations (Na^+,

[1] at pH 1 it equals the normal hydrogen electrode (NHE) with potential of –4.5 eV, for pH 14 this is shifted by 0.8 eV according to the *Nernst*-equation.

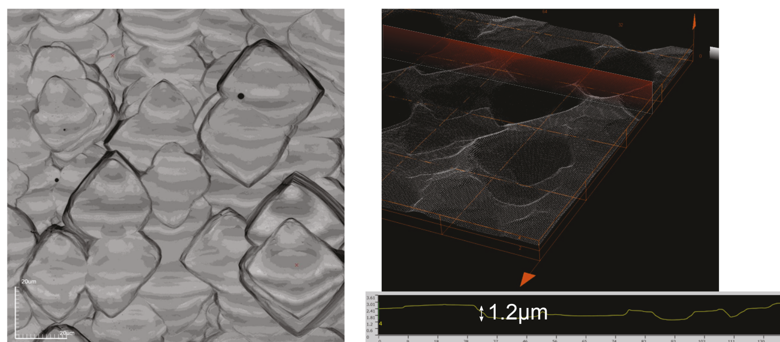

Fig. 2.18: Confocal microscope picture of a saw damage etched surface. Left hand side: Top-view. Right hand side: 3D image and line scan including the roughness Sq.

K^+, Li^+) [79]. The surface topography after KOH saw damage etch is shown in **Fig. 2.18**. The root of the mean squared height Sq^1 lies in the range of 1.2 μm. Diamond-like etching features are visible, indicating that the (111) plane at the walls of the structures has been uncovered resulting in the step like cross-section. Such a surface will be in the following referred to when speaking of "flat" surfaces.

Texture etch

The properties of anisotropically etching of silicon surfaces can be made use of to structure the surface in a number of very useful ways, for example in combination with etch mask and masking layer, in designing and fabricating micro-scale machines such as sensors and three dimensional microchip structures [81, 82]. In solar cell processing one special case is widely used for obtaining a surface texture for improved light coupling: the random pyramid texturing [83]. It is a long-known fact that relatively low concentrated KOH forms pyramid shaped structures on (100) wafer surfaces, an effect that was problematic in the beginning as it caused undesired roughening when flat surfaces were desired [84]. The mechanism behind the pyramid formation is that the (111) surface is etched much slower than the (100) surface. Once the first surface atoms are removed (surface defects or partly covered surface may favour the process of non-homogeneously removing (100) surface atoms), the etching further down the slope of pyramid-like structures is favoured as perpendicular facing (111) surfaces are "opened up" until a fully pyramid-covered surface develops.

In order to obtain good quality surface textures, the addition of an organic additive is required. One of the first published and optimised system, is the KOH+isopropyl alcohol (IPA) system [85–88]. The first texturing additive to be patented, however, was ethylene glycol in 1979 by Bailey *et al.* [65], already indicating that this effect of surface shaping not really limited to one class of chemical species. A whole range of chemical classes have has patented ever since: dioles, other alcoholes (almost of every kind), glycoles, alcoxyglycoles, sodiumcarbonate, but also all sorts of other surfactants and generally all sorts of organic molecules with functional −OH groups. This variety of different chemical classes indicates an

[1] The surface roughness can be expressed with several parameters. The Sq used here expresses the root mean squared of Z(x,y) in the measured area. More roughness definitions of common roughness parameters can be found here: http://www.olympus-ims.com/en/knowledge/metrology/roughness/3d_parameter/.

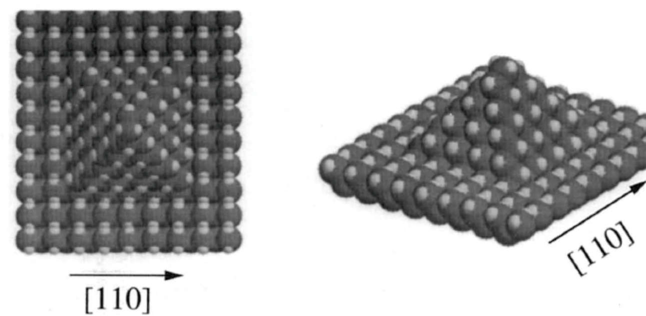

Fig. 2.19: Atomic model for a pyramid on (100) surface. All Si are hydrogen terminated. From [84].

only indirect impact on Si dissolution reaction, such as partly adhering to ≡Si−OH surface group and thus partly blocking the etch attack, "freeing" the (111) surface and adding to the anisotropy.

In this work surfaces were commonly (unless noted otherwise) textured using KOH and the commercially available additive RENA monoTEX^{TM} M/D purchased from RENA. A thereby obtained surface is displayed in **Fig. 2.20**. A homogeneously textured surface is obtained after etching between 4 and 5 μm per side (12 minutes of etching time at 80°C).

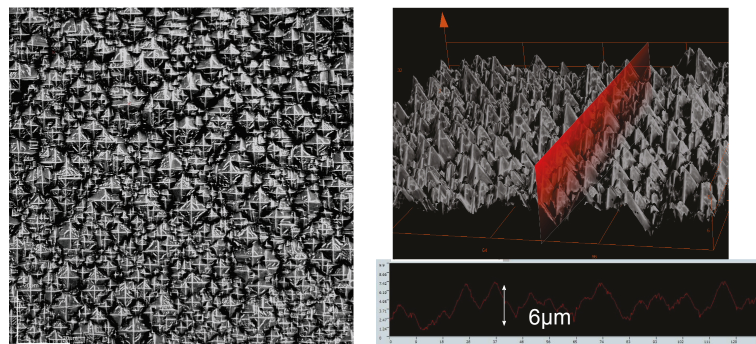

Fig. 2.20: Confocal microscope picture of a alkaline textured surface. Left hand side: Top-view. Right hand side: 3D image and line scan.

2.2.3 Wet chemical cleaning

Wafer cleaning technology has a long history in IC fabrication. There are several textbooks about the topic, for example [89, 90]. To obtain good yields in IC technology on ultra large integration scale (ULSI), cleanest surfaces are crucial. Up to several hundreds of process steps are required for the assembly of micro chips such as processors and RAM so that even smallest amounts of contamination on the wafer surface may lead to device failure and drastic yield reduction. Accordingly, long time process experience has been built up in this field.

One of the key concepts of Si surface cleaning is the employment of a sacrificial oxide layer. In a first step the strong oxidant oxidises not only the silicon surface but also organic contamination and metal contamination of metals nobler than Si, which may be present in the reduced state (such as Cu). In a second step this oxide and the oxidised metals are removed in a HF-containing solution.

A number of such cleanings sequences are part of the "IC toolbox" to obtain highest purity surfaces. At first glance, it seems to be a good idea to draw from this and use similar process sequences. In terms of wafer throughput numbers, however, the two industries differ by about two orders of magnitude: in solar cell fabrication up to several thousand wafers per hour are produced, a number that large semiconductor factories might not even reach in a week [91]. Consequently, process requirements differ to a large extend. Highly efficient cleaning sequences such as best know reference procedure developed by Kern *et al.* [92] at the Radio Corporation of America and hence called RCA cleaning sequence might be suitable for research and development application but not for solar cell mass production. The number of steps required for the RCA cleaning consisting of the SC1 and SC2 (standard clean 1 and 2) is high and the steps require high temperatures (80 to 90 °C) and long process times which massively drive the cost of ownership. SC1, also referred to as APM, includes of a solution of NH_4OH (29% wt.) and H_2O_2 (30% wt.) in water (1:1:5 to 1:2:7) and is dedicated to remove organic contamination and particles. After rinsing, the accordingly grown oxide is removed by a dip into diluted hydrofluoric acid. Then the SC 2 step follows. It contains a solution of HCl (32% wt.) and H_2O_2 in water (1:1:6 to 1:2:8). The SC2 step is dedicated to the removal of metallic contamination that might have been present on the surface before cleaning or may have been deposited from the SC1 step (as the alkaline condition favours the redeposition of metallic contamination on the wafer surface [93]).

A deviation of the SC1 is obtained when the volatile NH_4OH is replaced by KOH. The resulting mixture is still quite effective in the removal of organic contaminants. The most common organic contamination in solar cell processing are texturing additives that remain on the surface after the alkaline texturing. Accordingly, an adopted version of the SC1 is used in this thesis as reference clean after alkaline texturing: the mixture consists of 2% wt. KOH and 2% wt. H_2O_2, abbreviated in the following as "pSC 1" and is usually combined with a following diluted acid clean (cf. **Fig. 2.21**).

Most common wet chemical cleaning solutions in solar cell processing are made from diluted acids, such as hydrofluoric acid and hydrochloric acid. These also have been suggested and tested for IC wafers, however, prerequisites such as initial concentration and throughput were completely different [94, 95]. The principle behind acidic cleaning is the good solubility of metal contamination species in acidic solutions. Most common metal impurities and their compounds have a very good solubility—particularly in HCl—and are dissolved easily. One widely used diluted acid cleaning sequence is first to first dip the wafers into diluted HCl (usually around 1 to 5% wt.), followed by a rinsing step, mostly conducted in two cascaded overflow rinsing baths (alternatively by extended rinsing or dump-rinse). Subsequently, the wafer is dipped into diluted HF (1 to 2% wt.), a step that removes any grown silicon oxide and is, in addition to that, also quite effective in metal removal from the silicon surface. This sequence or variations of it have been shown to be effective when used in large throughput solar cell production lines after different process steps such as acidic and alkaline texturing or PSG removal [8]. As shown in **Fig. 2.21**, the sequence referred to as "HCl+HF" is used in order to mimic industrial production reality.

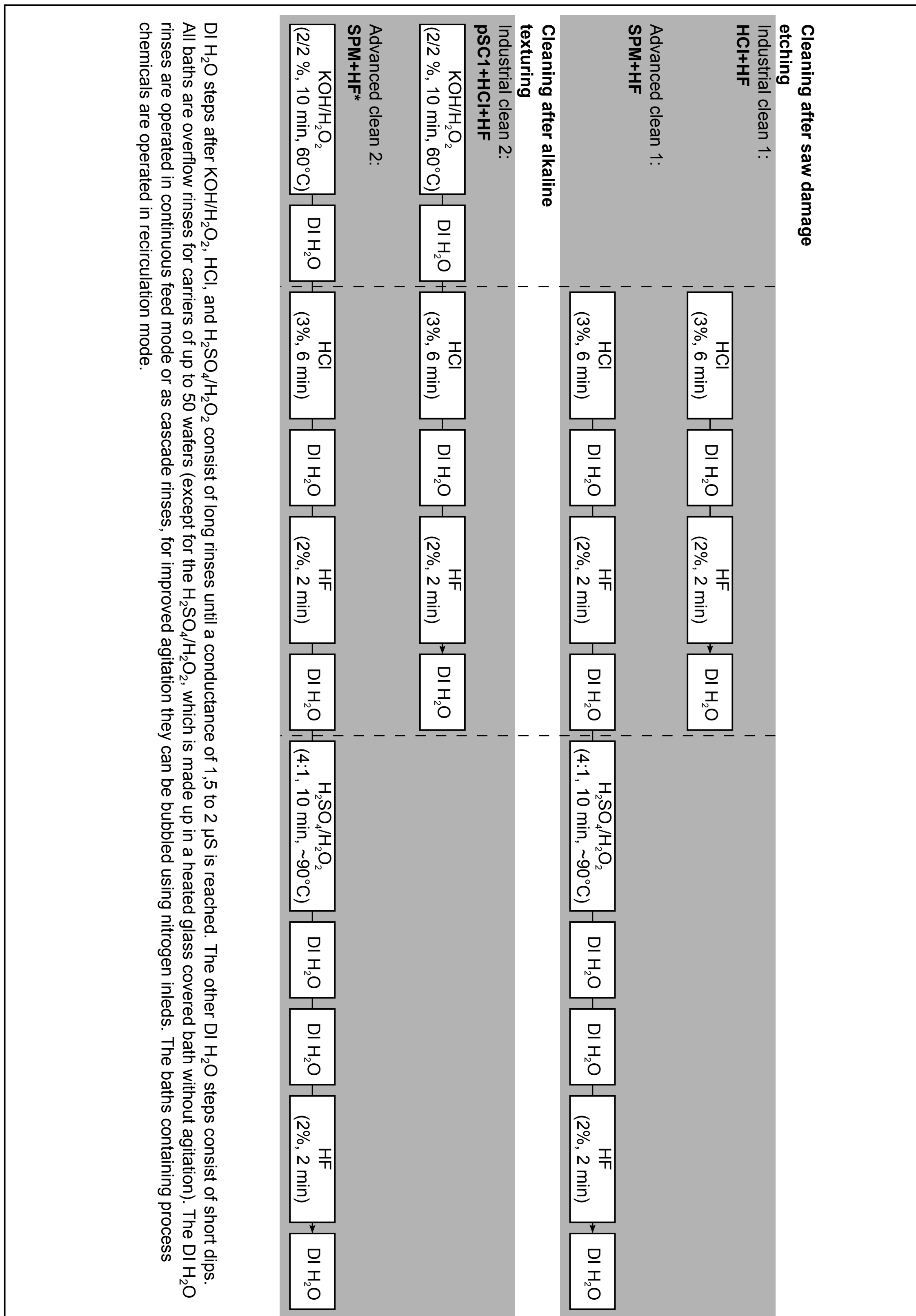

Fig. 2.21: Standard cleaning sequences at ISC Konstanz used throughout this work.

“Advanced” cleaning procedures

In order to remove organic contamination and noble elements, which are not so easily removed from the wafer surface, more “advanced” cleaning procedures are required. The most common noble metallic contaminant is Cu. As residue from wire sawing it is introduced to FEOL etching and may, if not successfully removed in the first cleaning step, impact following high temperature steps. Accordingly, cleaning baths with high oxidation potential are required. The conventional IC solutions for oxidative cleanings were mentioned above, but most of them are hardly feasible to be used in solar cell manufacturing, as they require high temperatures and a large amount of expensive chemicals (e.g. H_2O_2 is consumed in RCA cleaning procedures as metal contamination, especially Fe builds up acting as decomposition catalyst [96]).

Apart from the RCA cleaning sequence, another powerful oxidative clean that is used in IC manufacuring and in PV research labs, is the SPM-based (sulfuric acid hydrogen peroxide mixture) cleaning [97, 98]. It is used as reference high efficiency cleaning step and in the following referred to as “SPM+HF” as the oxide obtained by sulfuric acid hydrogen peroxide mixture is stripped in diluted hydrofluoric acid. At ISC Konstanz it is normally used as “add-on” to the industrial “HCl+HF” (standard cleaning sequence 1) or the “pSC1+HCl+HF” (standard cleaning sequence 2 after texturing) to obtain low metal surface contamination (advanced cleaning 1 and 2 as described in **2.21**). The “pre-cleaning” of wafers, before placing them in the SPM bath, allows for longer bath usage as only a relatively small amount of metal contamination is introduced to the bath. SPM, also known as “piranha” clean or “IMEC” clean, is known for serving as a strong oxidant due to the formation of peroximonosulfuric acid H_2SO_5, also known as Caro’s acid, according to the following reaction [99]:

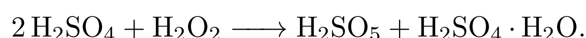

$$2\,H_2SO_4 + H_2O_2 \longrightarrow H_2SO_5 + H_2SO_4 \cdot H_2O.$$

The mixture is made up from 4:1 to 5:1 parts of concentrated sulfuric acid and 30% hydrogen peroxide and operated at 90 to 140°C. Wafers are immersed for ten minutes. The main purpose of SPM in IC manufacturing is the removal of photoresists and other organic layers which are oxidised by the Caro’s acid. Another benefit from the highly acidic and oxidising surrounding is the high removal efficiency of metal surface contamination. In addition to that, the combination with a diluted HF dip has proven to be efficient at particle removal. Therefore, it was suggested by scientist at the IMEC research center in Belgium, to completely replace the RCA sequence in IC processing by the SPM based cleaning procedure [97]. However, the SPM based sequence can hardly be introduced to solar cell mass processing as the solution enriches water so that the bath has to be replaced frequently [100]. Even in semiconductor manufacturing the need for simplification was recognised and also some approaches were published [101], for example the introduction of ozone-based cleaning solutions. This can be done by either replacing only the hydrogen peroxide in the SPM by ozone to prolong the bath usage in larger scale production [102] or changing the whole bath make-up to water based ozone mixtures as it will be discussed later in this work. What needs to be to stressed here is that, if IC technology processes are to be mimicked for solar cell

mass production, thorough testing on the suitability and cost effectiveness is required.

2.2.4 Passivation of silicon surfaces

The native surface of a semiconductor crystal is full of unsaturated bonds, so-called dangling bonds. These dangling bonds are very effective recombination centers for charge carrier pairs. In order to reduce surface recombination, these bonds need to be saturated for high charge carrier lifetimes. A simple method to saturate dangling bonds of silicon is a dip into diluted HF. The thus obtained hydrogen termination (cf. **Sec. 2.2.1**) is very effective in passivating the silicon crystal. However, as the hydrogen terminated surface is quickly prone to oxidation, this very effectively passivated surface starts to degrade within several minutes. A more effective way to obtain passivation, is to covalently saturate the silicon surface with the help of a dielectric layer.

Apart from this so-called chemical passivation mechanism, an electrical field may be induced by the dielectric, which can improve passivation quality by band-bending. The so-called field effect passivation due to "fixed charges" is the passivating film[1] . The most common dielectric films are silicon oxide [104, 105], aluminum oxide (negatively charged) [106–108] and amorphous silicon nitride (positively charged) [109, 110]. If the correct dielectric is chosen (negatively charged for p and p^+ surface, positively charged for n and n^+ surfaces), the minority carriers can be repelled by the electrical field adding to the passivation of surface as sketched in **Fig. 2.22** [111]. The dielectric films in solar cell processing are mostly deposited by chemical deposition techniques, such as chemical vapor deposition (CVD), most commonly plasma-enhanced (PECVD), or by atomic layer deposition (ALD).

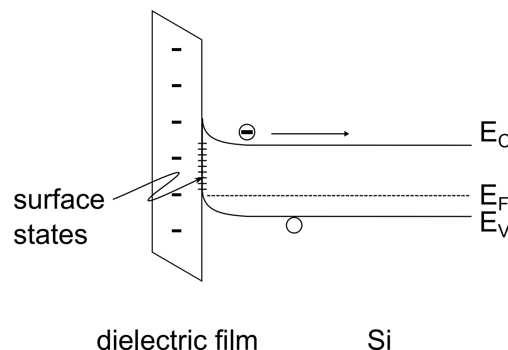

Fig. 2.22: Band diagram for passivation of a p-type sample with an dielectric layer containing negative fixed charges that drives the valence and the conduction bands into accumulation; adopted from [111].

A similar effect as field effect passivation, is obtained, when highly doped areas are applied at the surface of the crystal of the same type as the base to obtain n^+n or p^+p high-low junctions. These areas contribute to surface passivation due to a shift of conduction and valence band near the surface, functioning as repellant for minority carriers and are usually referred to as back-surface fields (BSF), as they are commonly applied on the back-side of

[1]The term of fixed charges was claimed in the PV-community for what is in IC-fabrication referred to K-centers: essentially defects in the passivation layer. In the case of SiN_x: Si bond to three N species that tend to lose the unpaired electron to form stable positive charges. A comprehensive summary on charge properties of SiN_x can be found here [103].

solar cell devices.

Front side passivation of solar cells has to serve yet another purpose: anti-reflective coating. By tuning the passivation film to the right thickness and refractive index, the light coupling of the solar cell can be optimised. Stacks of different films may be applied. These stacked additional layers may serve as protection, e.g. to prevent blistering during contact firing [112], as a top-up to reach the required film thickness required for minimum front side reflection or as double anti-reflective coating layer [113].

The most common industrially used passivation techniques are thermal oxide and silicon nitride. In this thesis, both are investigated in terms of susceptibility to metal contamination when used as passivation of *p*-doped silicon. Therefore, more details about the process steps and the resulting layers are given in the following.

Thermal oxide passivation

As seen above, native oxide growth starts quickly after hydrogen passivation. However, native oxide grown due to moisture in air or in cold water can hardly be used for effective surface passivation. The reason is the high defect density of these oxides caused by the uncontrolled growth.

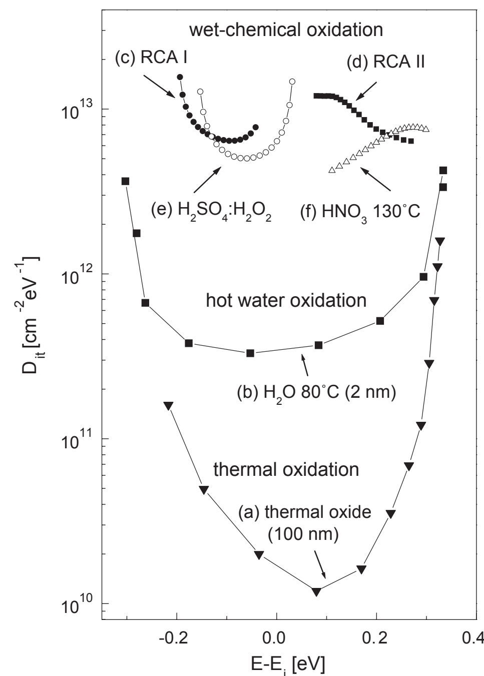

Fig. 2.23: Interface trap densities of differently grown oxides for solar cell surface passivation measured by surface photovoltage technique (SPV [114]). The thickness of the investigated layers (if not shown) was in the range of 1 – 1.5 nm. The number of interface defects is plotted against the position in the bandgap, resulting ideally in U-shaped curves. The higher the defects, the lower is the interface quality and thus the surface recombination, cf. **Sec. 3.2.4**.

Especially for the passivation of surfaces without additional field effects such as highly doped emitter or back-surface regions the interface quality is essential. In this case the thermal oxidation is preferred to the other oxide growth techniques. The amorphous thermal oxide is obtained by thermally oxidising the surface under high temperatures either in O_2 or

H_2O atmosphere in quartz glass tube furnaces. The first is usually referred to as dry and the latter as wet thermal oxidation. Oxide growth rates for (100) surfaces lie in the range of 1.5 nm/hr at 800°C and 38 nm/hr at 1000°C (dry) and 23 nm/hr at 800°C and 290 nm at 1000°C (wet)[1]. The accelerated oxidation rates in H_2O can be explained by the higher diffusivity of H_2O compared to O_2 in fused silicon oxide [115]. Although, batch sizes may contain up to 1000 wafers per diffusion tube, oxidation times may well exceed 1.5 hours and therefore become critical in length for mass production. Furthermore, processing at high temperatures requires high amounts of electrical power. To reduce process times, in addition to the thermal oxide often a silicon nitride capping layer is applied. In this work, thermal oxides were grown in a Centrotherm quartz glass tube oven.

In **Fig. 2.23** the passivation quality of several wet oxides is compared to thermally grown oxide. Sufficiently high passivation qualities for highly doped regions may be obtained by wet chemically grown oxides [114, 116] and the low costs of the wet oxide compared to thermal techniques may make up for the loss due to the relatively high defect density.

Silicon nitride

Deposition of amorphous silicon nitride (usually abbreviated by SiN_x) has long been the standard process for passivating and anti-reflective coating of solar cell front sides replacing TiO_2 which had been common until the early 2000s. The major deposition technique of SiN_x is PECVD, as it requires relatively low temperatures (400–500°C compared to above 800°C and more in common CVD reactors) and allows high film growth rates [117]. Several plasma deposition setups are used commercially: inline and batch systems with direct (just over the wafer surface) and indirect or remote (outside the deposition chamber) plasma generation [118]. There are several ways to excite the reactants to the plasma state: microwaves, oscillating electrical fields, hollow cathodes, arc jet, just to name a few. The pressure is usually reduced to below 1 torr. As silicon source serves silane SiH_4 or a mixture of SiH_4/N_2. The commonn nitrogen source is ammonia NH_3. The resulting film is a hydrogen rich amorphous silicon nitride layer, which is often referred to as a-SiN_x:H. The hydrogen plays an important role, as upon firing some of the relatively loosely bound hydrogen diffuses into the silicon bulk, where it is thought to passivate bulk defects, e.g. dangling bonds at grain boundaries [119–121]. The optical (refractive index) and passivation properties of SiN_x films depend on thickness, stoichiometry, density and subsequent processing temperatures. The stoichiometry of the film can be adjusted by the mass flows of the reagent gases and the deposition parameters, such as plasma power, temperature and pressure [122]. Film thickness usually scales with deposition time. The density of the film is strongly dependent on subsequent heat treatment [123].

When varying input gases, silicon oxides or silicon oxinitrides can be obtained. For oxygen rich layers either O_2 or N_2O can be used. Also different Si containing compounds may be used [109]. For this work a Centrotherm direct plasma reactor with parallel plate boats and

[1] An online calculation tool for oxide thickness from temperature, time and crystal orientation can be found under http://www.cleanroom.byu.edu/OxideThickCalc.phtml provided by the Brigham Young University based on [115]

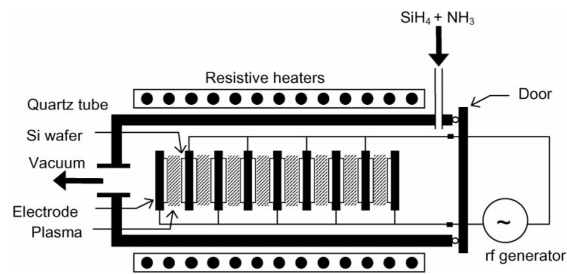

Fig. 2.24: Schemiatic setup of the PECVD reactor used for the SiN_x depositions in this thesis [117].

low frequency plasma excitation (40 kHz) was used at low pressure (0.5 torr) and elevated temperatures (450°C). As process gases N_2, SiH_4, NH_3 and N_2O were available. A scheme of the reactor can be found in **Fig. 2.24**.

2.3 The *pn*-junction

In the following the function of the *pn*-junction in diodes and under illumination in solar cells is described.

A solar cell in principle is nothing but a large area diode. For the function of a diode a *pn*-junction is required which is obtained when a highly doped region of opposite doping (n^+ for p-type base, p^+ for n-type) is diffused into the semiconductor from an external source. Where the two differently doped regions meet, an electrical field forms, the so-called space charge region. This is due to "diffusion" of electrons from donor atoms near the junction to acceptor atoms on the opposite side, leaving positively and negatively charged atoms behind. The resulting band diagrams of idealised (abrupt) junctions for the respective n-type and p-type base are plotted in **Fig. 2.25**.

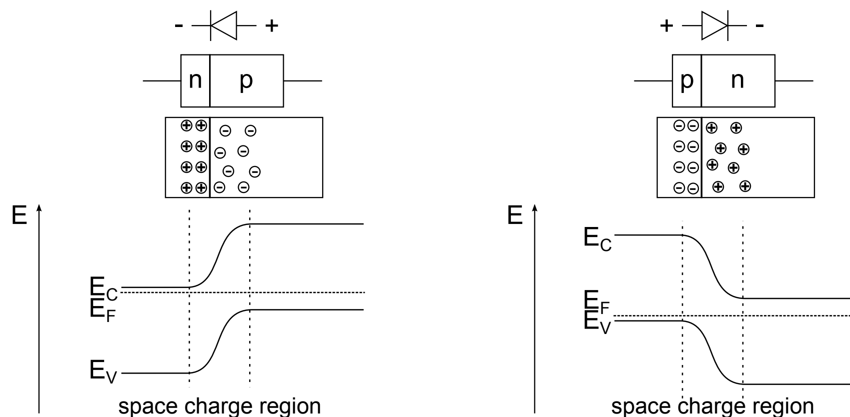

Fig. 2.25: Scheme of np-and pn-diodes and the respective band diagrams at thermal equilibrium.

In the following the processes for creating highly doped regions in silicon are summarised and the most common ones discussed in more detail. From the *pn*-junction and the diode properties the most commonly used solar cell properties are derived and explained.

2.3.1 Junction formation

As doping source commonly serves a silicate glass layer with a high dopant concentration (usually phosphorus or boron silicate glass, PSG/BSG). Such a glassy layer is usually obtained by placing the wafers in quartz glass tubes, which are flooded with dopant containing gas at high temperatures. The most common phosphorous source for phosphorus diffusion (in the following abbreviated as P-diffusion) is phosphoryl trichloride $POCl_3$ and for boron boron diffusion (in the following abbreviated as B-diffusion) the boron source is boron tribromide BBr_3. For the diffusion of the dopants into the silicon relatively high temperatures are required to reach a sufficient high amount of dopant concentration in the range of 1e+19 to 1e+21 cm^{-1} in surface near regions (temperatures above 850°C and diffusion times of 0.5 to 1 h or longer). Typical depths of highly doped regions lie in the range of 200 to 500 nm.

As an alternative phosphorus source phosphoric acid can be used and applied relatively simple by a spin-on or spray-on process and diffused into the silicon on an inline belt-furnace [124, 125]. Furthermore, all sorts of dopant containing films (mostly silicon oxide based

and containing either P_2O_5 or B_2O_3) can be used as precursors for dopant diffusion. As deposition techniques for the films have been reported: screen printing [126, 127], ink-jet printing [128] and PECVD [129]. Apart from indiffusion from deposited precursors, ion implantation, a technique common in semiconductor manufacturing, has been transferred to mass production of solar cell applications despite challenges such as high cost of tools and restrictions concerning throughput [130]. In the following, the two most common techniques which were used and investigated in the scope of this work, phosphorus and boron diffusion, are described.

Phosphorus diffusion

Phosphoryl trichloride ($POCl_3$), a liquid at room temperature, is pre-heated and transferred via an inert carrier gas, usually nitrogen, into the heated quartz tube of the diffusion furnace. The $POCl_3$ reacts with additionally provided oxygen to form phosphorus pentoxide according to the following equation:

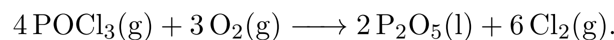

$$4\,\mathrm{POCl_3(g)} + 3\,\mathrm{O_2(g)} \longrightarrow 2\,\mathrm{P_2O_5(l)} + 6\,\mathrm{Cl_2(g)}.$$

The chlorine gas that is formed is useful in transferring possible remaining surface contaminants, such as metals, into the gaseous phase and removing them from the system. P_2O_5 is reduced at the silicon surface according to

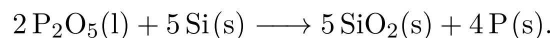

$$2\,\mathrm{P_2O_5(l)} + 5\,\mathrm{Si\,(s)} \longrightarrow 5\,\mathrm{SiO_2(s)} + 4\,\mathrm{P\,(s)}.$$

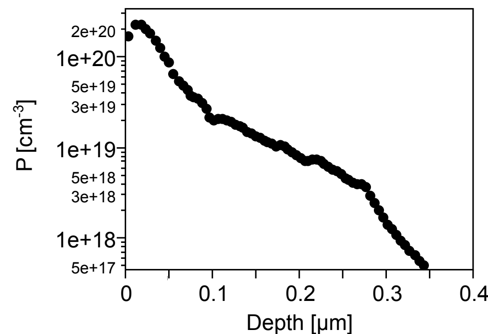

Fig. 2.26: Typical phosphorus diffusion profile, the typical kink and tail shape of the curve is the result of two different diffusion mechanisms of P in Si. The P-diffusion resulting in this profile is the "new" diffusion used for most of the p-type cells and test structures in this work.

The silicon dioxide forms a glassy layer containing phosphorus (phosphorus silicate glass, PSG). At elevated temperatures the phosphorus diffuses into the silicon. Temperatures above 800°C are desired for a sufficiently high amount of phosphorus diffusion into the Si bulk [131]. The properties of the glass layer and the amount of phosphorus indiffusing can be controlled by the amount of $POCl_3$, the gas flows, pressure and the applied temperatures. By varying these parameters the diffusion profile can be fine-tuned to reduce the thickness of the phosphorus rich layer (often referred to as dead layer), the surface concentration, the total dopant concentration and the depth of the emitter to reach low surface recombination

and good contactability. Modern diffusion tubes load up to 500 wafers in single load and up to 1000 in back-to-back (two wafer per slot), which adds another important factor for optimisation: uniformity of dopant across the wafer and across the boat.

A typical diffusion profile as measured by ECV[1], only displaying electrically active phosphorus, is shown in **Fig. 2.26**. The typical “kink and tail” shape of the curve is the result of two diffusion mechanisms: interstitial and subsitial diffusion with different diffusion constants.

Boron diffusion

The principle of the tube furnace B-diffusion is quite similar as the P-diffusion. Instead of $POCl_3$, boron tribromide BBr_3, also a liquid at room temperature, is used. Instead of chlorine, bromine gas is formed and the intermediate is boron oxygen species B_2O_3 instead of P_2O_5. However, the whole process is much more difficult to control as the formation of a boron rich layer (BRL) is likely to occur, introducing lifetime diminishing defects near the surface. The boron rich compounds, responsible for the defect formation, are thought to form in the boron silicate glass, BSG, a mixture of SiO_2 and B_2O_3, when a so-called “boron pile up” occurs. Elemental boron, formed by the reduction of B_2O_3 with Si, reacts when formed in excess with Si according to the following reaction [132]:

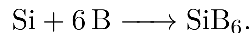

$$\mathrm{Si} + 6\,\mathrm{B} \longrightarrow \mathrm{SiB_6}.$$

A summary on the literature on this topic can be found in a paper by Kessler *et al.* [133]. They also provide a solution to the problem: oxidising excess B when working under oxygen atmosphere:

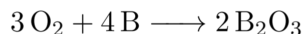

$$3\,\mathrm{O_2} + 4\,\mathrm{B} \longrightarrow 2\,\mathrm{B_2O_3}$$

or by reaction of SiB_6 with oxygen that may occur in situ or after the diffusion process according to the following reaction:

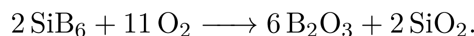

$$2\,\mathrm{SiB_6} + 11\,\mathrm{O_2} \longrightarrow 6\,\mathrm{B_2O_3} + 2\,\mathrm{SiO_2}.$$

As all these reactions at the interface may occur simultaneously [134], the B-diffusion process is quite difficult to control and the uniformity across the wafer and across whole full diffusion boats challenging to obtain. A typical B-diffusion profile is plotted in **Fig. 2.27**. In contrast to the P-diffusion profile, the dopant surface concentration is significantly lower than the peak, which is found in a depth of about 0.1 μm. This is due to the high solubility of boron in silicon oxide, causing some of it to segregate to the growing BSG when the diffusion source at the surface has depleted.

[1] ECV stands for Electrochemical Capacity Voltage and is an electrochemical measuring technique to determine the active dopant concentration by gradually dissolving the surface and measuring the electrical capacitance between substrate and solution.

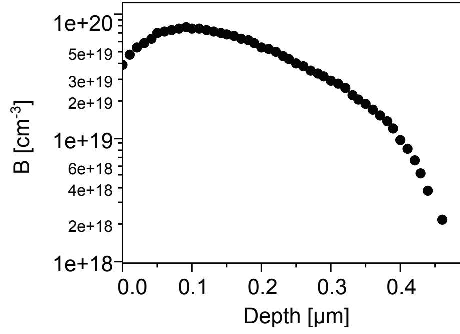

Fig. 2.27: ECV profile of the B-diffusion used for the n-type solar cells and test structures in this work.

2.3.2 Junction parameters in the dark and under illumination

When an external voltage is applied to a diode device, current flow is only possible in one of the two directions due to the internal electrical field. The direction of the current flow is indicated by the arrows in **Fig. 2.25**. Also, for relatively small applied bias voltages the diode does not allow current transport due to recombination mechanisms in the space charge region. Once a threshold value is reached, the current increases exponentially. To characterise the properties of a diode, the current-voltage (J-V) characteristics are recorded. In the case of an idealised diode the J-V curve can be described by the *Shockley* equation

$$J = J_0 \left(\exp\left(\frac{qV}{k_B T}\right) - 1 \right) \tag{2.6}$$

V corresponding to the shift in quasi-Fermi-levels of electrons and holes (Φ_n and Φ_p), which denotes the change in density of states in the conduction and valence band due to injection of minority carriers, and with J_0 corresponding to the "saturation" current which denotes current passing through the diode due to recombination and generation of carriers at defect states [135].

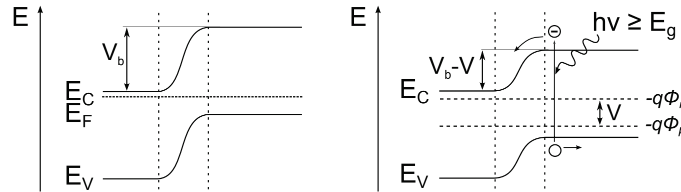

Fig. 2.28: Left: *np*-junction in equilibrium. Right: *np*-junction under illumination.

The current-voltage curve of a *np*-diode in the dark and under illumination (functioning as solar cell) is plotted in **Fig. 2.29**. Under illumination a photocurrent in the opposite direction of the bias is produced (as sketched in **Fig. 2.28**) modifying **Eq. 2.6** to

$$J = J_0 \left(\exp\left(\frac{qV}{k_B T}\right) - 1 \right) - J_{Ph}[136]. \tag{2.7}$$

The most important solar cell parameters can be derived by measuring the J-V-curve under standard testing conditions, STC of 25°C, 1000W/m^2, solar spectrum under 1.5 air

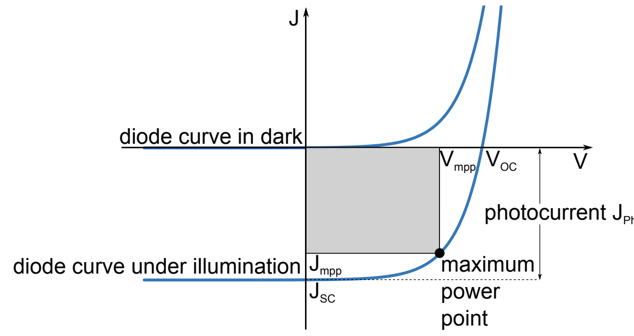

Fig. 2.29: Current-voltage (J-V) characteristics in the dark and under illumination. From the latter the solar cell characteristics are derived.

mass[1]. The current density produced without external voltage equals the photocurrent J_{Ph} and is also referred to as *short circuit current* J_{sc}. When the applied bias voltage completely cancels out the internal voltage of the cell and no current flows, the *open circuit voltage* V_{oc} is obtained. The product of the current and voltage equals the power that can be obtained under the respective conditions. From the shape of the J-V-curve the maximum power point (mpp), denoted by the product of J_{mpp} and V_{mpp}, can be obtained. If the resulting product is put into relation to the theoretical maximal obtainable power $V_{oc} \cdot J_{sc}$, the so-called *fill factor* (FF [%]) is obtained. The higher the fill factor, the more "ideal" is the measured solar cell. The *efficiency* η of a solar cell in percent is given by the relation of the maximum obtainable power divided by the power contained in the irradiated light (1 sun equates 100 mWcm^{-2}) and thus is written as

$$\eta = \frac{J_{mpp} \cdot V_{mpp}}{100\, mWcm^{-2}} \cdot 100\% \tag{2.8}$$

or when using the equation for the fill factor $FF = (J_{mpp} \cdot V_{mpp})/(J_{sc} \cdot V_{oc})$

$$\eta = \frac{FF \cdot J_{sc} \cdot V_{oc}}{100\, mWcm^{-2}} \cdot 100\%. \tag{2.9}$$

J-V-curves are usually measured quickly under a calibrated flash lamp. In solar cell production lines the cells are then sorted by efficiency classes to allow the fabrication of modules with cells of the same performance to ensure high module quality. Efficiency, FF, J_{sc} and V_{oc} provide valuable information about solar cell failure modes. Losses in FF often result from resistance losses within bulk, emitter or metallisation. J_{sc} losses often result from recombination losses or insufficient generation (e.g. due to non-optimised anti-reflective coating). V_{oc} losses are often caused by process or bulk contamination or insufficient passivation of surfaces. Apart from these parameters, the shape of the J-V-curve can reveal other solar cell parameters such as shunt- and series-resistance. Information about recombination within the measured solar cell may be read from the curve by skillfully fitting it [137].

[1] 1.5 air mass refers to sunlight penetrating the Earth's surface through the atmosphere at an angle of 48.2° at which the intensity of the sun reaching the ground equals 1000 W/m^2. The thus obtained spectrum can be downloaded from the homepage of the National Renewable Energy Laboratory, Golden (Colorado): http://rredc.nrel.gov/solar/spectra/am1.5/.

2.4 Contact formation

In order to extract the generated current from a solar cell, metal contacts are required. Whereas IC manufacturing provides a whole range of metal deposition techniques, such as sputtering and CVD or plating of all sorts of different material, the solar industry has long relied on mostly one single technique: screen printing of silver and/or aluminum containing pastes. Commonly, one side of the solar cell is printed, the paste is dryed in hot air (200 to 250°C) and then flipped around for printing the other side. In order to form the contacts, heating to high temperature is required, which is usually performed in an infrared heated conveyor belt fast firing furnace. As metals are opaque, only very thin fingers are printed on front sides to minimise shading, the current is collected in wider so-called busbars stretching perpendicular to the fingers from one end to the other of the front side of the cells [138].

Apart from the finely ground metal, printing pastes contain other substances, such as glass-frites, solvents, dopant and/or silicon particles. Glass frites are added to penetrate through passivation layers, such as SiN_x anti-reflective coating. Silver is used due to its low resistivity and its slow diffusion in silicon. Cu, which is much cheaper and more abundant, cannot be used as it easily diffuses into silicon, a fact that makes it an effective efficiency killing contaminant, as it will be discussed later. When Al containing pastes are used, the fast firing produces a SiAl alloy and some of the Al diffuses into the silicon forming a highly doped p^+ region that is commonly used as back-surface-field in p-type solar cells [139]. There have also been approaches to use such layers as emitters for n-type solar cells evaluated in [140]. The use of Al requires either a large amount due to the relatively low conductivity or the addition of silver to the paste. If full areas of Al paste are printed, silver pads are required, as Al cannot be soldered for module interconnection.

2.5 Solar cell structures and processes

An overview on different solar cell structures is given in **Fig. 2.30**. The colour of the bulk indicates the base material. While all of the p-type base solar cells, indicated by the blue bulk, are commercially available in large scale production, most of the n-type solar cell concepts have only recently started into production. Boron doped p-type historically has been the predominant wafer material for the last 60 years[1]. One of the reasons for the widespread use of boron doped p-type material is the more favourable segregation coefficient of boron over phosphorus in silicon leading to more homogeneously doped bricks after crystallisation.

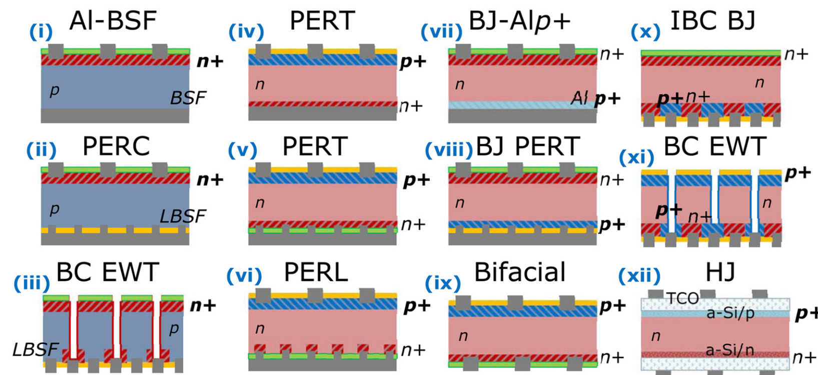

Fig. 2.30: A summary of (commercially) available solar cell structures: (i) Full Al-BSF; (ii) passivated emitter and rear (PERC) cell; (iii) backcontacted emitter wrap through (BC EWT) cell; (iv), (v) passivated emitter and rear totally diffused (PERT) cell; (vi) passivated emitter and rear locally diffused (PERL) cell; (vii) backjunction Al alloyed rear emitter ("BJ-Alp^+") cell; (viii) backjunction PERT cell; (ix) bifacial cell; (x) interdigitated backcontacted backjunction (IBC BJ) cell; (xi) backcontacted emitter wrap through (BC EWT) cell; (xii) heterojunction (HJ) cell [108].

The main benefit that is commonly attributed to n-type material is the comparably small sensitivity to common metallic contaminants. The reason for this is that, due to the capture cross sections (cf. **Sec. 3.1.1**), of many transition metals, electron capturing is more efficient than hole capturing. Example for such elements are Fe, Ni and Ti [15, 142, 143]. The absence of highly recombination active B−O defects that cause light induced degradation in p-type solar cells (cf. **Sec. 4.5.3**) also allows to achieve higher minority carrier diffusion lengths, ideally exceeding the wafer thickness (cf. **Sec. 3.1**). To find out if the lower sensitivity towards metal contamination holds true not only for the bulk material [144] but also the cell processes, is one of the goals of this work.

2.5.1 Full aluminum BSF solar cells

The full aluminum BSF solar cell has long been the standard cell type in industrial solar cell processing. The concept that is mostly still in use today was developed in the 1970s. The development of the "The black cell" (as it was named due to its black looking surface finish) was more or less finalised in 1984, when SiN_x coating was developed. Laboratory scale conversion efficiencies were not too far away from today's industrial scale efficiencies, as they

[1]Despite the fact that the first practical silicon-based photovoltaic cell, invented by *Chapin*, *Fuller* and *Pearson* of the *Bell Laboratories* and filed for patent in 1954 [141], was fabricated from n-type material.

were in the range of 17 and 18%. An overview on the history of silicon-based solar cells can be found in a paper by one of the pioneers Prof. M. A. Green [145]. A scheme of the cell structure is sketched in **Fig. 2.31** (left hand side). The full-Al BSF solar cell technology has been well suited for scale processing due to several reasons. First of all, screen printing is a relatively simple process for metallisation, plus, the printing of the full aluminum backside not only creates a contact but the AlSi alloy that forms under fast-firing conditions acts as back-surface field (hence the name). Second, the AlSi alloy and the P-diffusion are very effective in gettering impurities [22, 146–149]. Third, the use of SiN_x:H can passivate extended defects in low quality material, thus allowing for very low quality material to be processed with an outcome of decent solar cell efficiencies [150, 151]. A typical process sequence is listed in **Fig. 2.32**. With fine-tuning of all the process steps efficiencies exceeding 19% on Cz-material can be achieved [152] before being limited by the recombination on the backside [153].

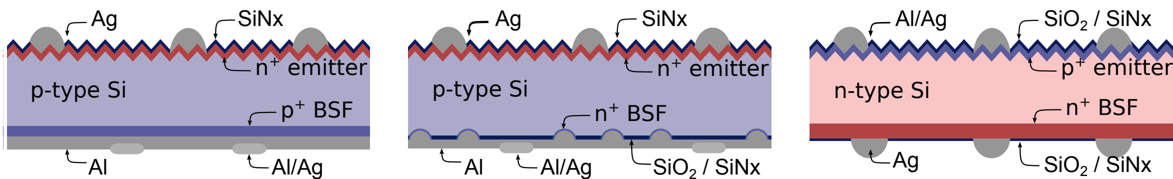

Fig. 2.31: Schemes of the solar cell structures discussed in the scope of this thesis. Left hand side: Typical Al-BSF industrial solar cell. Middle: Passivated emitter and rear solar cell (PERC). Right hand side: Bifacial solar cell on n-type substrate (BiSoN).

2.5.2 PERC solar cells

For higher efficiencies the back surface may be covered with a suited dielectric layer. In combination with a polished rear side this may also serve as mirror like structure increasing the potential for higher efficiencies. The resulting cell structure is commonly referred to as *p*assivated *e*mitter and *r*ear local *c*ontact solar cell (PERC). To contact the rear, openings in the dielectric layer are required. The most common way of opening dielectrics for industrial application is by laser ablation of lines or dots [154]. Not so common, but also possible, is the local opening by screen printing or sputtering of etching pastes [155]. A typical process sequence is displayed in **Fig. 2.32** (right hand side). As the backside passivation is applied early in the displayed process chain and can thus be referred to as FEOL-passivation, a layer stable against further high temperature and chemical processing is required (e.g. thermal SiO_2 capped with SiN_x). Another common approach, which is more suitable for less stable films (e.g. Al_2O_3), is applying the film later in the process (BEOL-passivation). To achieve this, additional chemical steps are required such as single side polishing and single side emitter removal. Solar cell efficiencies exceeding 21% have been reported [152]. PERC solar cells are currently gaining importance in industrial application and are often referred to as the next step for the solar cell mass production, e.g. by Centrotherm (Centaurus) [156], Solarworld [157] and Schott Solar [158].

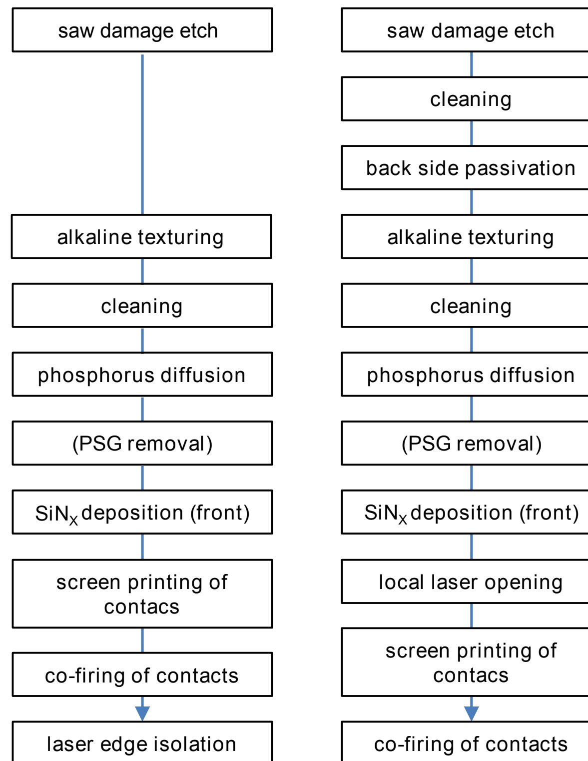

Fig. 2.32: Process sequence of p-type processes: full Al-BSF cell (left hand side) and PERC (right hand side).

2.5.3 PERT and bifacial solar cells

Another solar cell concept on the brink of large scale fabrication is the (n-type) PERT cell (*p*assivated *e*mitter, *r*ear *t*otally diffused cell). In addition to back-surface passivation, a back-surface field is diffused underneath. This allows direct fire-through contacts, similar to common front-side contact schemes [159]. Accordingly, finger grids with busbars are usually printed on front-and back-sides of the cells. Two thermal diffusions require highly stable material and an advanced fine tuning of emitter/BSF profiles. Also, if tube diffusion is applied, masks or local etching need to be applied. Despite these challenges, first commercial approaches have been reported on n-type material, which due to its inherently higher lifetime is well suited for high efficiency solar cells. Two examples are the Panda/Pasha cells developed by ECN (Energy research Centre of the Netherlands), commercialised with Yingli [160], and a similar cell, the BiSoN (bifacial industrial solar cell on n-type) developed by ISC Konstanz in cooperation with Bosch Solar [161] and currently commercialised with MegaCell in Italy [162]. One promising approach to surpass the challenge of co-diffusion would be the use of ion implantation of one or both sides of the cells [163]. Yet, the capital expenditure of high throughput ion implanters is relatively high. Of course, a similar cell structure can be used with p-type silicon as base material [164].

Apart from relatively high efficiencies exceeding 20%, when measured as normal solar cells and reported in the references in the previous paragraph, one key advantage of the PERT cell concept is that—as the front-side looks pretty much like the back-side—bifacial

installation is possible. When the module technology is adjusted, the back-side of the solar cell can contribute to light harvesting, which adds another interesting degree of freedom to the installation of the modules (compare **Fig. 2.33**). Furthermore, it helps to increase the effective efficiency and can reduce the levelised cost of energy (LCOE), which measures the cost per KWh (instead of commonly used cost per kWpeak) [165].

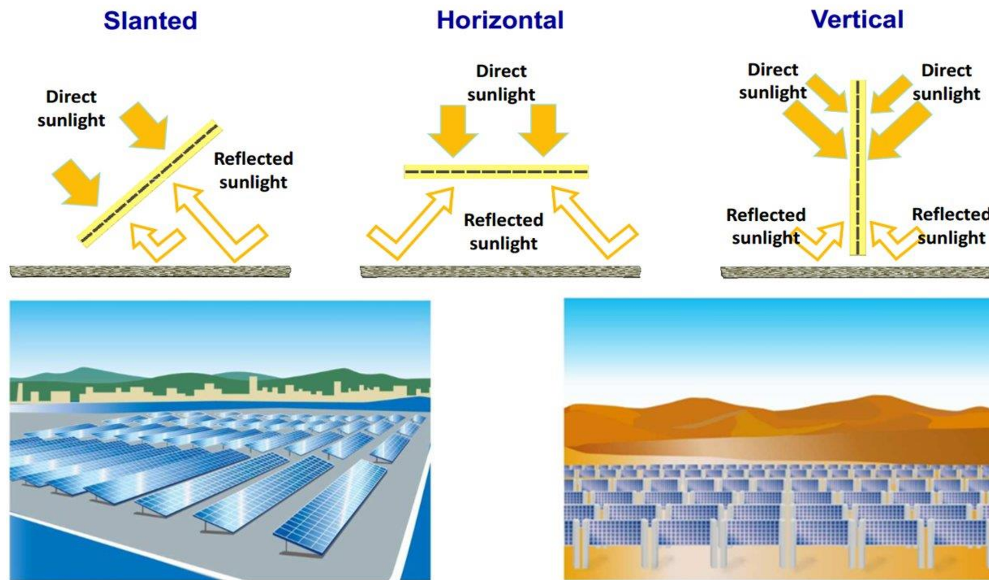

Fig. 2.33: Possible installations of bifacial modules [165].

3 Physics of contamination in silicon devices

The detrimental effect of metal impurities in the silicon crystal or at the interface is most easily accessible via the measurement of the lifetime of a generated electron hole pair. The following chapter first deals with the physics of said impurities and introduces the concepts of “lifetime” that help to understand the degradation mechanisms (**Sec. 3.1**). In the second section it introduces the physical characterisation methods later used for the interpretation of the impact of surface contamination at different steps of the solar cell process (**Sec. 3.2**).

3.1 Recombination mechanisms of charge carriers

The most common parameter for the quality of a semiconductor device is the recombination lifetime of charge carriers, a very sensitive measure for the detection of impurities and process failure. The numerical lifetime values obtained by the different measuring methods, however, can only be interpreted correctly when the different impact factors and contributions to the commonly measured “effective lifetime” are fully understood [111]. For this reason in the following section the different recombination mechanisms of and contributions to the effective recombination lifetime are summarised and the relevant equations are given.

Generally, the faster a (e.g. by a light pulse) separated carrier couple recombines, the higher the likelihood that it may not contribute to the output of a solar cell. Charge carrier recombination can be measured quite easily throughout the process from the silicon block to the finished solar cell, by several measuring methods, such as the photoconductance (decay), detected by a coil or microwave reflection and the laser induced photoluminesence. Some will be discussed below.

There are two contributions to the charge carrier recombination: bulk and surface recombination. The effective lifetime, τ_{eff} can accordingly be calculated via

$$\frac{1}{\tau_{eff}} = \frac{1}{\tau_{bulk}} + \frac{1}{\tau_{surface}}. \tag{3.1}$$

In order to determine one or the other, either large $\tau_{surface}$ values and accordingly very good surface passivation or high material quality with large values of τ_{bulk} are required

The lifetime is directly related to the minority carrier diffusion length L. The diffusion length can be simply calculated by

$$L_{eff} = \sqrt{D\tau_{eff}} \tag{3.2}$$

with the diffusivity of D [$\mathrm{cm^2s^{-1}}$]. The diffusivity of electrons is roughly three times higher than the diffusivity of holes and mostly depends on the doping density and on the fact whether the respective charge species is minority or majority carrier.[1]

For good solar cell performance sufficiently high L_{eff} values are required. The longer a minority carrier can diffuse, the more likely it can be collected for the generation of power. In order to collect minority carriers that are generated deep in the bulk of the solar carrier the carrier diffusion length for high efficiency solar cells should well exceed the thickness of the cell.

3.1.1 Bulk recombination lifetime

There are three different mechanisms described in the literature (see for example [166] and [167]) for charge carriers to recombine in the semiconductor bulk: trap assisted recombination

[1] Values for the diffusivity (and the respective mobility μ) can be calculated using PC1D, a popular open source 1D solar cell simulation software. For example for a base doping of 8.5e+15 $\mathrm{cm^{-3}}$ the D_e is calculated to be 30.81 $\mathrm{cm^2s^{-1}}$ and 29.23 $\mathrm{cm^2s^{-1}}$ and D_h to be 11.09 $\mathrm{cm^2s^{-1}}$ and 11.36 $\mathrm{cm^2s^{-1}}$ as majority and minority carrier respectively.

(known as Shockley-Read-Hall), radiative recombination (inverse effect of absorption) and Auger-mechanism (recombination by energy transfer to a second electron, accordingly referred to as three carrier process). The effective bulk lifetime can accordingly be calculated by

$$\frac{1}{\tau_{bulk}} = \frac{1}{\tau_{SRH}} + \frac{1}{\tau_{rad}} + \frac{1}{\tau_{Auger}}. \tag{3.3}$$

While the radiative and the Auger recombination mechanism are intrinsic effects, i.e. they are material inherent properties defined by the doping concentration and the injection level, the Shockley-Read-Hall (SRH) mechanism is extrinsic which means it is caused by defect levels within the band gap of the semiconductor.

Shockley-Read-Hall recombination

Especially effective for recombination are deep bandgap levels (with energy levels near the middle of the bandgap). Such levels are introduced by defects in silicon either from crystallographic defects such as non-saturated (dangling) bonds in the bulk or grain boundaries, or impurities, such as metallic and non-metallic contaminants from the silicon or solar cell production process. Due to the good solubility at elevated temperatures, especially metallic impurities may easily be introduced into the silicon bulk during device manufacturing [168]. The mechanism for the defect level induced recombination rate was suggested by *Shockley* and *Read* [169] and *Hall* [170] in 1952. It is schematically depicted in **Fig. 3.1**.

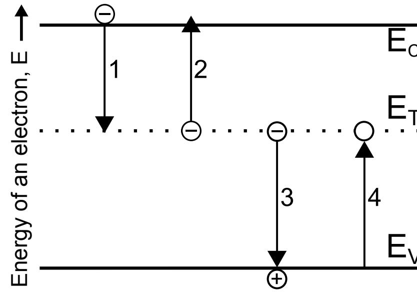

Fig. 3.1: The basic processes involved in defect level-induced recombination: 1–electron capture, 2–electron emission, 3–hole capture, 4–hole emission [169].

The recombination rate mostly depends on trap-inherent properties which are the impurity density, capture cross sections and energy level in the band gap of silicon. Furthermore, it depends on the injection level. The energy that is liberated by the recombination event is "lost" by lattice vibration [111].

The most general form to mathematically describe the SRH recombination event by the recombination rate, R_{SRH},

$$R_{SRH} = \frac{pn - n_i^2}{\tau_p\,(n + n_1) + \tau_n\,(p + p_1)} \tag{3.4}$$

from which the SRH recombination lifetime τ_{SRH} can be deduced with the relationship

between lifetime, injection level and recombination rate $R = \Delta n/\tau$, resulting in

$$\tau_{SRH} = \frac{\tau_{p0}\left(n_0 + n_1 + \Delta n\right) + \tau_{n0}\left(p_0 + p_1 + \Delta n\right)}{n_0 + p_0 + \Delta n} \ , \tag{3.5}$$

with n_0 and p_0 being the carrier concentration in thermal equilibrium, n_1 and p_1 being the statistically occupied trap levels and $\Delta p = \Delta n$, which is necessary for charge neutrality, being the excess carrier density (also referred to as the injection level) [166]. The said assumption is often referred to as "quasi-neutrality" and holds true as long as no electrical fields are present [171]. The effect of temporary trapping and re-injection of charge carriers at more shallow levels is excluded here. τ_{p0} and τ_{n0} are the capture time constants and can be calculated using the capture cross section for electrons σ_n and holes σ_p with $\tau_{p0} = 1/\left(N_T \sigma_p v_{th}\right)$ and respectively $\tau_{n0} = 1/\left(N_T \sigma_n v_{th}\right)$, where v_{th} is the thermal velocity of holes and electrons and N_T the impurity density of this specific point defect. The larger the capture cross section for the respective species, the more likely the recombination event becomes. The ratio between the capture cross section of holes to electrons $k = \sigma_n/\sigma_p$ determines, whether the respective impurity is a more effective "lifetime killer" in n- or p-type material. **Tab. 3.1** summarises the recombination properties, such as trap energy levels E_T, capture cross sections and k-values of several elements. Trap levels with k values above 1 are more likely to capture electrons and vice versa.

Tab. 3.1: Recombination properties of several transition metals in Si [142].

element	type	E_T $[eV]$	σ_n $\left[cm^2\right]$	σ_p $\left[cm^2\right]$	$k = \sigma_n/\sigma_p$
Ti	donor	$E_c - 0.27$	3.1e–14	1.4e–15	22
	double donor	$E_v + 0.26$	1.3e–14	2.8e–17	460
V	double donor	$E_v + 0.36$	5.0e–14	3.0e–18	17000
Cr	donor	$E_c - 0.22$	2.3e–13	1.1e–13	2
Mo	donor	$E_v + 0.28$	1.6e–14	6.0e–16	30
Fe	donor	$E_v + 0.38$	5.0e–14	7.0e–17	700
Au	acceptor	$E_c - 0.55$	1.4e–16	7.6e–15	0.02

The values for the number of occupied traps n_1 and p_1 can be calculated in the simplified case that the Fermi-level coincidences with the trap level according to

$$n_1 = n_i \exp\left(\frac{E_T - E_i}{K_B T}\right) \tag{3.6}$$

and

$$p_1 = n_i \exp\left(\frac{E_i - E_T}{K_B T}\right) \ , \tag{3.7}$$

with n_i being the intrinsic carrier concentration[1] It can be calculated E_T being the trap energy level within the band gap and E_i being the Fermi-level in the intrinsic case. This can be further simplified, for example for p-type silicon with $n_0 \approx 0$ and $p_0 = N_A$:

[1] As intrinsic carrier concentration n_i at 298.15 K 8.3e+9 cm^{-3} was used. According to Misiakos *et al.* it can be calculated for different temperature levels using the following equation: $n_i(T) = 5.29 \times 10^{19} \cdot (T/300)^{2.54} \cdot \exp(-6726/T)$ [172]. As measurements were performed at 298.15 K and parts of simulations at 300 K incorporating n_i^2, some error needs to be taken into account.

$$\tau_{SRH} = \frac{\frac{n_1+\Delta n}{N_T \sigma_p v_{th}} + \frac{N_A+p_1+\Delta n}{N_T \sigma_n v_{th}}}{N_A + \Delta n}. \tag{3.8}$$

Intrinsic recombination mechanisms

The two possible intrinsic recombination mechanisms as schematically described in **Fig. 3.2** are radiative and *Auger* recombination. *Radiative recombination* is a recombination event in which the energy is liberated in form of electromagnetic emission (cf. **Fig. 3.2**). This recombination event is inversely proportional to the carrier concentration times the radiative recombination coefficient B by **Eq. 3.9**. It plays a minor role in indirect semiconductors like silicon (cf. **Fig. 3.3**), as the necessary change in electron spin makes it relatively unlikely [111].

$$\tau_{Rad} = \frac{1}{B(p_0 + n_0 + \Delta n)}. \tag{3.9}$$

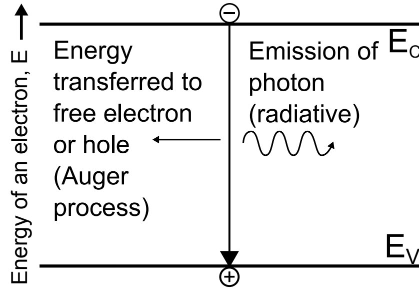

Fig. 3.2: Direct band-to-band recombination by Auger and radiative mechanism

Auger recombination, named after its discoverer *Pierre Victor Auger* [173], is of more importance. As it requires a third carrier for the energy to be absorbed, it is inversely proportional to the carrier density squared [111]. The equation for the *Auger* recombination lifetime is found in [174] using the *Auger* recombination coefficients C_p for holes and C_n for electrons:

$$\tau_{Auger} = \frac{1}{C_p(p_0^2 + 2p_0\Delta n + \Delta n_{av}^2) + C_n(n_0^2 + 2n_0\Delta n + \Delta n^2)}. \tag{3.10}$$

Eq. 3.10 can be simplified for the cases of n- and p-type silicon and different injection levels.

Contributions of bulk recombination

The contributions of the different bulk recombination lifetimes to the effective lifetime can be plotted using the introduced equations **Eqs. 3.3** to **3.10**. An example is given in **Fig. 3.3**. The parameters required for the calculation of the curves are summarized next to the graph and correspond to typical solar silicon parameters (with elevated Fe content). Fe is assumed to be the only impurity present.

The curve for τ_{SRH} is strongly excess carrier concentration dependent. Its strongest effect on the effective bulk lifetime can be found for low excess carrier densities (injection levels). The shape of the *SRH* curve depends on the capture cross sections σ_n and σ_p (probabilities for the recombination of electrons and holes) and on the energy level of the trap.

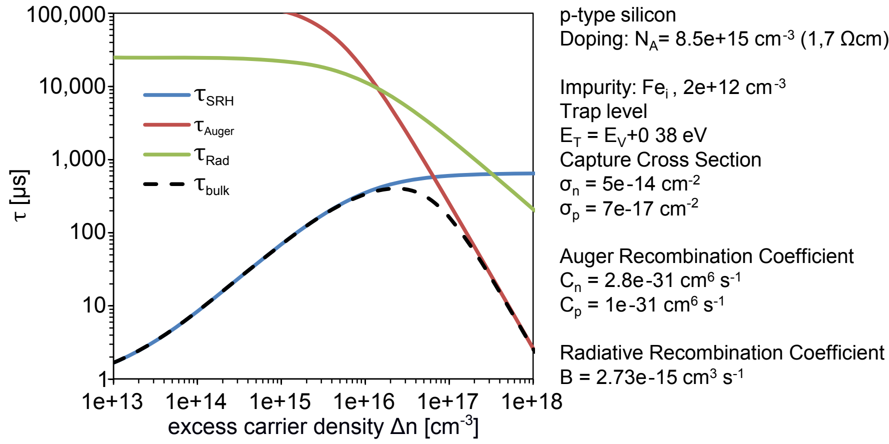

Fig. 3.3: Contribution of SRH, Auger and radiative recombination on the bulk lifetime in a typical semiconductor device. Parameters for Fe_i from [175] and for the other parameters from [174].

Another impact factor for the shape of the *SRH* curve is the dopant type and concentration. *Auger* recombination (τ_{Auger}) becomes bulk lifetime limiting in high injection (above about 3e+16 cm^{-3}). Only in purest material the radiative recombination ($\tau_{radiative}$) will become significant, a grade of purity that can hardly be obtained.

3.1.2 Emitter recombination

The description of recombination mechanisms in highly doped regions is highly complex: "The degeneracy of the semiconductor, bandgap narrowing and free-carrier absorption need to be included, along with intrinsic recombination processes and the normal *SRH* recombination processes related to defects, both within the emitter and at the emitter's surface", as *Kerr* summarises in his thesis [176]. The complexity can be reduced, however, when the fact of the high doping density in the emitter region is considered. According to that the minority carrier concentration in the emitter region remains comparatively low. Due to the strong impact of doping level on Auger recombination, this recombination mechanism is dominant. From this can be deduced that the recombination in the emitter region is constant with injection level, as done by *Kane* and *Swanson* [177]. Thus the recombination current that flows into the emitter region can be defined as

$$J_{rec} = J_{0E}\frac{np}{n_i^2} \tag{3.11}$$

where J_{0E} is commonly referred to as emitter saturation current density (emitter recombination current) and n and p refer to bulk properties. If the contribution of emitter recombination to the effective lifetime is considered, the emitter recombination rate R_E is to be calculated using the charge of an electron q and the thickness W of the device:

$$R_E = J_{0E}\frac{np}{qWn_i^2}. \tag{3.12}$$

As already defined above, the fact that $n = n_0 + \Delta n_{av}$ and $p = p_0 + \Delta n_{av}$ allows simplifications for different doping concentrations and injection levels. The assumption that the

minority carriers are distributed evenly across the semiconductor so that Δn_{av} can be used instead of much more difficult to obtain $\Delta n_{surface}$, also greatly helps simplifying the issue. The validity of this common simplification is confirmed and discussed in detail in [178].

For n^+pn^+ or p^+np^+ test structures, which are commonly used for the determination of J_{0E}, the effective recombination rate R_{eff} can be written as

$$R_{eff} = R_{bulk} + 2R_E. \tag{3.13}$$

The recombination rate is defined as $R = \Delta n_{av}/\tau$. Therefore follows

$$\frac{\Delta n_{av}}{\tau_{eff}} = \frac{\Delta n_{av}}{\tau_{bulk}} + 2 \cdot J_{0E} \frac{np}{qWn_i^2}, \tag{3.14}$$

which can be simplified for the p-type case of n^+pn^+ to

$$\frac{1}{\tau_{eff}} = \frac{1}{\tau_{bulk}} + 2\frac{J_{0E}}{qWn_i^2} \cdot (n_0 + \Delta n_{av}). \tag{3.15}$$

The recombination lifetime in the heavily doped region near the surface can be extracted in high injection conditions by the *Kane-Swanson* method [177]. It makes use of the fact that, as shown above at high injection conditions, the effective lifetime limiting recombination mechanism becomes surface near recombination and for high lifetime samples bulk *Auger* recombination. In such cases of high lifetime the contribution $1/\tau_{Auger}$ can be be calculated using **Eq. 3.10** for the base material (the doping and the injection level need to be known). After subtracting this correction factor from the inverse effective life time a linear slope is obtained when plotting $1/\tau_{eff}$ against Δn_{av}, from which the recombination current of the highly doped surface near region (including the surface) of a n^+pn^+ structure can be deduced. An analysis of validity of this method for several different material qualities and diffusions can be found in [178], more accurate modelling of emitter structures was performed in [179]. The contribution from emitter recombination is added to the graph of **Fig. 3.3** thus obtaining **Fig. 3.4** now plotting the *effective lifetime curve* (dashed line).

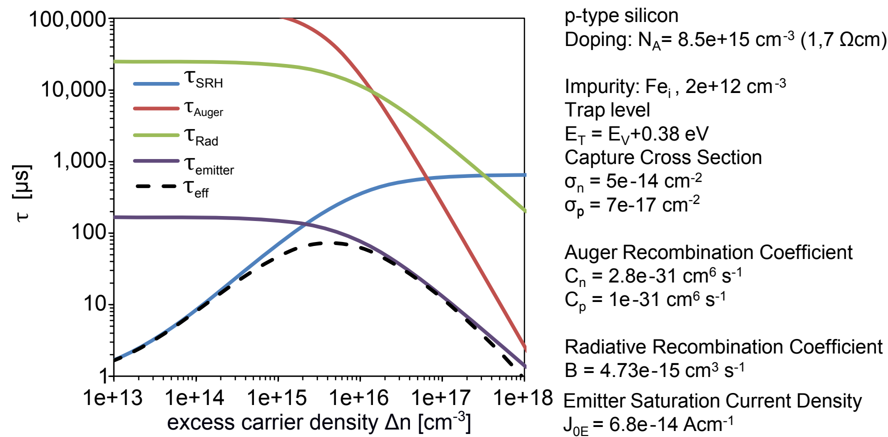

Fig. 3.4: The emitter recombination contribution of a typical phosphorus emitter is added to the device from **Fig. 3.3**.

How effective lifetime curves can be measured will be shown in the next section. From **Fig. 3.4** it can be deduced that such curves bear important information about recombination events in the measured semiconductor piece. Accordingly obtained fits of measured curves will be used later for in depth analysis of differently contaminated samples.

3.1.3 Surface recombination

The surface of a semiconductor can be seen as a huge crystallographic defect, with a band of defect levels (instead of a single defect level) quantified as density of interface deep level traps D_{it}. As the the surface recombination can be explained by a similar mechanism as the SRH lifetime, a similar term can be used for the calculation. Therefore bulk properties are replaced with surface properties and the number of defects is changed into the aforementioned density of interface states, D_{it} [$\mathrm{cm^{-2}eV^{-1}}$], which is the integrated term of the number of interface traps across the deep region of the band gap, $N_{it} \approx k_B T D_{it}$. Commonly, the term that is used for the description of surface properties, is the surface recombination velocity SRV, S_r [$\mathrm{cm\,s^{-1}}$]. From the SRV the term for the surface lifetime can be derived according to Schroder [180]

$$\frac{1}{\tau_{surface}} = \beta^2 D \tag{3.16}$$

with D being the minority diffusion constant and β found from the relationship

$$\tan\left(\frac{\beta W}{2}\right) = \frac{S_r}{\beta D}. \tag{3.17}$$

These term already indicates that surface recombination lifetime depends on factors such as diffusivity of carriers and the thickness of the sample W. In the simplest case of a both sided passivated semiconductor piece with two identical surfaces the term for the surface lifetime can be derived via the surface recombination by

$$\frac{1}{\tau_{eff}} = \frac{1}{\tau_{bulk}} + \frac{2S_r}{W}. \tag{3.18}$$

When considering more complicated cases such as heavily doped regions, the surface recombination is best addressed locally. The surface recombination rate, $R_{surface}$ can be similarly modelled as defect induced recombination by the SRH formalism [111]. Now all values denoting surface (instead of bulk) properties:

$$R_{surface} = \frac{p_s n_s - n_i^2}{\frac{p_s+p_1}{S_n} + \frac{n_s+n_1}{S_p}} \tag{3.19}$$

with $S_n = \sigma_{ns} v_{th} N_{it}$ and $S_p = \sigma_{ps} v_{th} N_{it}$ representing the surface recombination velocity for electrons and holes, using similar symbols for the capture cross sections as in the bulk case. N_{it} refers to the number of interface traps. The generated hole pairs n_s and p_s are similarly derived as in the bulk recombination case, as are the occupied number of surface defect states n_1 and p_1. From this term the surface recombination lifetime can be extracted

using the already introduced relationship between lifetime, generation rate and access carrier density $\tau_{surface} = \Delta n_s / R_{surface}$.

What further complicates the matter is the dependence of surface states on injection level. This might, for example, turn a depleted surface into accumulation at higher injection level, which in turn would strongly increase the measured lifetime [111]. Also, the recombination lifetime differs for different wavelengths as the charge carriers generated in different depths need to diffuse to the surface before they recombine. In general, surface recombination is a rather complex phenomenon that will not be further discussed here. If the question arises, whether a certain impurity decreases the bulk lifetime or increases the surface recombination velocity, then it will be tried to answer this question indirectly, for example by determination of the recombination current density J_{0E} or by measuring the D_{it}, which is integrated defect density across the bandgap (cf. **Sec. 3.2.4**).

3.2 Semiconductor characterisation methods

For quality inspection, process monitoring and optimisation of semiconductor devices the measurability of minority carrier lifetime is crucial. There are a number of different methods to determine effective minority carrier lifetimes. Most measure the decay in minority carriers after a very short light pulse (transient) by various methods such as photoconductance decay, microwave reflectance, capacitive coupling or the use of a conductive coil [181].

Apart from minority carrier lifetime, interface properties are of interest, if the behaviour of metal surface contamination is to be studied. Properties of surface-near regions such as highly doped emitters or back surface fields can be characterised by the recombination current density (J_0) and passivation layers by interface trap density (D_{it}) measurements. While the first can again be determined via lifetime measurements, the latter can be determined using corona charge measurement techniques.

Another application of lifetime measurements that is described in the following is the determination of interstitial Fe in p-type silicon making use of semi-stable properties of Fe−B pairs.

3.2.1 Quasi-steady state photoconductance

In contrast to transient methods, the quasi-steady state photoconductance (QSS-PC) method developed by *Sinton et al.* [181] uses a light pulse that "varies very slowly compared to the effective lifetime of the wafer". The light intensity of the slowly decaying flash intensity is simultaneously to the decay of the photoconductance of the sample recorded by a calibrated reference cell. From the light intensity and an optical factor that takes different surface properties, i.e. texture and/or anti-reflective coating, into account the generation current J_{ph} can be estimated. The common tool for this measurement technique is the *WCT-120* by *Sinton Consulting inc.* as used throughout this work.

Steady-state illumination can be assumed if τ_{eff} is smaller than the exponentially decaying light pulse of the *Sinton* measurement setup which is around 2 ms. The current generated by the illumination, J_{Ph}, then equals the recombination current J_{rec} to satisfy equilibrium conditions. The generation current can be calculated based on the generated excess carrier density across the wafer thickness, Δn, for a silicon piece of the thickness W:

$$J_{ph} = \frac{\Delta n \cdot q \cdot W}{\tau_{eff}}. \tag{3.20}$$

The increase in conductivity by illumination σ_L (as measured by a coil) from the excess (compared to the number of carriers present at thermal equilibrium in the dark) of the generated electron-hole pairs (excess carriers) is a result of the following [182]:

$$\sigma_L = q\left(\Delta n \mu_n + \Delta p \mu_p\right) W = q \Delta n \left(\mu_n + \mu_p\right) W \tag{3.21}$$

where μ_n and μ_p are the mobility of the electrons and holes, which can be taken from literature and q is the elemental charge of an electron. Using **Eq. 3.20** and **Eg. 3.21** the

effective lifetime can be determined from the measured photoconductance [182]:

$$\tau_{eff} = \frac{\sigma_L}{J_{ph}\left(\mu_n + \mu_p\right)}. \tag{3.22}$$

The relationship between the lifetime and excess carrier density (also referred to as injection level) Δn can be extracted from equation

$$\tau_{eff}(\Delta n) = \frac{\Delta n(t)}{G(t) - \frac{d\Delta n(t)}{dt}} \tag{3.23}$$

with G being the generation rate. The generation rate is derived from the photocurrent of a typical solar cell with a flat blue surface. The assumed solar cell produces a current of 0.038 mAcm^{-1} under standard testing conditions (25°C, 1 sun, 1.5 AM spectrum). From this value the generation rate is derived. The generation rate is obtained by dividing the photocurrent of the assumed solar cell by the elemental charge q. Depending on the surface of the examined silicon piece of the thickness W, it has to be corrected by an optical factor OF via $G = \frac{2.38\times10^{17}}{W} \cdot OF$ [cm^{-3}s^{-1}] [183]. The optical factor for textured blue samples is found to be 1.1 and for flat blue samples 0.8[1].

Under steady state conditions (the decay of the light flash is assumed to be slow enough to fulfill this condition at any point of time) **Eq. 3.23** is simplified to

$$\tau_{eff}(\Delta n) = \frac{\Delta n(t)}{G(t)}. \tag{3.24}$$

Injection dependent lifetime curves

From **Eq 3.23** curves plotting the lifetime against the excess minority carrier density can be obtained. The range of the injection level span can be extended when filters in front of the flash lamp are used and the thus obtained curves are overlaid. An example is provided in **Fig. 3.5**. These curves provide valuable information about recombination properties of the defects present in the investigated samples. They directly relate to the assumed curves in the previous section (**Fig. 3.3** and **3.4**). Injection dependent lifetime curves, if samples are chosen carefully, can be used to extract the contribution of different defects or to extract information on the recombination behaviour of single defects. An extensive study on the recombination activity of Cu defects using this technique can be found in **Sec. 4.5.1**.

Depending on the excess carrier density level different contributions to the effective lifetime can be (more or less) directly extracted from such curves. The most prominent example is the J_{0E} from a fit of the inverse of the high injection lifetime, corrected by a calculated Auger term following the Kane-Swanson method described earlier (**Sec. 3.1.2**).

[1] The optical factor can be determined by matching transient with quasi-steady-state data. When the flash duration is lowered to a short single pulse (1/64 of the original flash duration), the resulting lifetime can be extracted by analyzing the exponential decay of the photoconductance according to the equation $\tau_{eff}(\Delta n) = -\frac{\Delta n(t)}{d\Delta n(t)/dt}$, which can be derived from **Eq. 3.23** when the generation rate due to the short light flash becomes small. The transient method is a stand-alone method that does not require the simultaneous measurement of the generation rate [183].

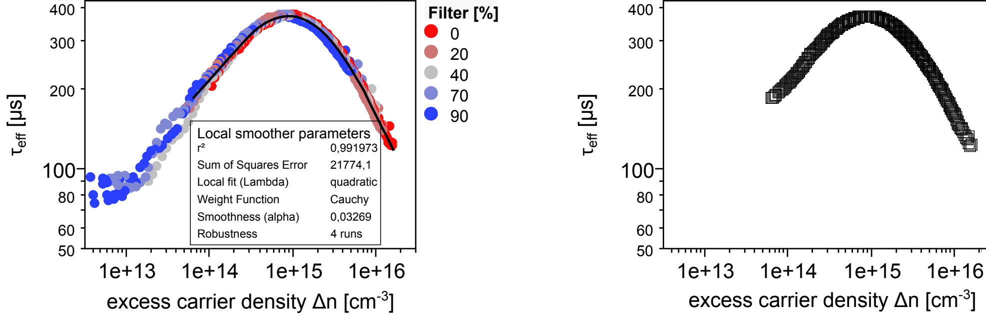

Fig. 3.5: Injection dependent lifetime curves. Left hand side: as measured; right hand side: as extracted from the fit using the the JMP10 smoothing fit, typical smoother parameters as used in the following are displayed.

The implied V$_{oc}$

The excess carriers generated by the light flash at a given illumination create an internal voltage which can be calculated by the separation of the quasi-Fermi-levels ϕ_n and ϕ_p (the quasi-Fermi levels denote the electron and hole concentration when the state of thermal equilibrium is left, e.g. by a light flash). In case of a full solar cell device this voltage describes the open circuit voltage V_{oc}. Using the equations for the carrier concentrations for n and p

$$n = n_0 + \Delta n(0) = n_i e^{-q\phi_n/k_B T} \tag{3.25}$$

$$p = p_0 + \Delta p(0) = n_i e^{q\phi_p/k_B T} \tag{3.26}$$

where n_0 and p_0 are the carrier densities at thermal equilibrium, $\Delta n(0)$ and $\Delta p(0)$ are the local excess carrier concentrations in case of a diode at the pn-junction [184] and n_i is the intrinsic carrier density, the *implied* V_{oc} can be expressed as

$$implied\ V_{oc} = -\left(\phi_n - \phi_p\right) = \frac{k_B T}{q} \ln\left(\frac{np}{n_i^2}\right) \tag{3.27}$$

[184] which can be rewritten as

$$implied\ V_{oc} = \frac{k_B T}{q} \ln\left[\frac{\left(n_0 + \Delta n(0)\right)\left(p_0 + \Delta p(0)\right)}{n_i^2}\right] [185]. \tag{3.28}$$

Sufficient accordance with simulated data could be obtained in the case of a diode with the assumption $\Delta n(0) = \Delta p(0) = \Delta n_{av}$ [185]. Depending on the base doping, either n_0 or p_0 is much smaller than the other and thus becomes negligible, which further simplifies the equation. Since for doped semiconductors N_A or $N_D \gg n_i$ applies, for p-type semiconductors $p_0 = N_A$ and for n-type $p_0 = N_D$, for the *implied* V_{oc} follows, when extracted under V_{oc} STC:

$$implied\ V_{oc} = \frac{k_B T}{q} \ln\left[\frac{\Delta n_{av}\left(N_A + \Delta n_{av}\right)}{n_i^2}\right]. \tag{3.29}$$

As this equation only refers to bulk and illumination properties of the silicon piece in question, it can be used to interpret lifetimes of diffused and passivated as well as only passivated

samples by indicating the highest possible obtainable V_{oc}. Any further processes, however, will reduce this value [184]. Strictly speaking, of course, no voltage is obtainable, if no *pn*-junction exists. However, especially when interpreting the lifetime data of symmetrically passivated samples, e.g. for comparison of the performance of intrinsic amorphous Si passivation layers or PERC backside passivation layers, the usefulness of *implied* V_{oc} for the prediction of the effect of single process steps on final solar performances has been demonstrated [186–188].

The *implied* V_{oc} is especially useful to study the impact of contaminants on process steps, as *differences* in lifetime expressed by the *implied* V_{oc} caused by the contamination can directly be used to estimate the differences later obtained in V_{oc} of the final device. In other words: The *implied* V_{oc} is used here as a more descriptive/demonstrative parameter than effective lifetime values.

In order to demonstrate the relationship between *implied* V_{oc} and lifetime, *implied* V_{oc} is plotted against lifetime under steady state conditions at 1 sun illumination for different values of base doping using **Eq. 3.29** with the injection level calculated from the lifetime at 1 sun illumination according to

$$\Delta n_{av} = G \cdot \frac{\tau_{eff}}{W}. \tag{3.30}$$

The thickness W of the silicon piece was chosen to be 165 μm (a typical thickness for solar wafers after texture etching). The optical factor (OF), which takes reflection and transmission losses as well as gains by anti-reflective coating and surface texture into account, was assumed to be 1.05, a typical value for textured samples with a not quite optimised SiN_x coating.

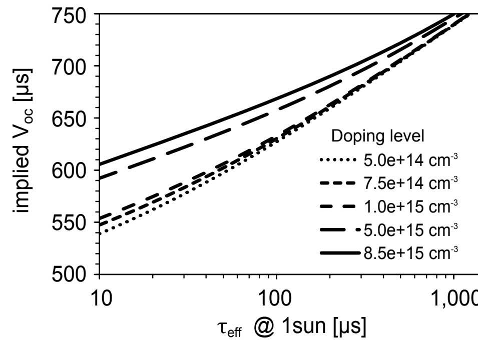

Fig. 3.6: Dependence of *implied* V_{oc} on lifetime at 1 sun illumination for different base doping densities.

One example for the usefulness of the *implied* V_{oc} is shown in **Fig. 3.7**, where *implied* V_{oc} data are plotted against measured lifetime at 1 sun illumination. Wafers from different ingot positions were used and accordingly the base resistivity varied. The lines in the graph are calculated in accordance to **Fig. 3.6**. If the *lifetime* was used for the analysis and fitting of the experimental data, an offset for on cell level similarly performing samples would have been detected due to the difference in doping density (6.6e+15 vs. 8e+15 cm^{-3}). In contrast to the effective lifetime the *implied* V_{oc} includes the information of the impact of doping density on the final cell device.

To sum this up, the QSSPC measurement is a powerful technique which not only can determine the intensity and injection level dependent minority carrier across a wide range, but also provides a handy factor: the *implied* V_{oc}. In a comprehensive study Cuevas *et al.* [185] have

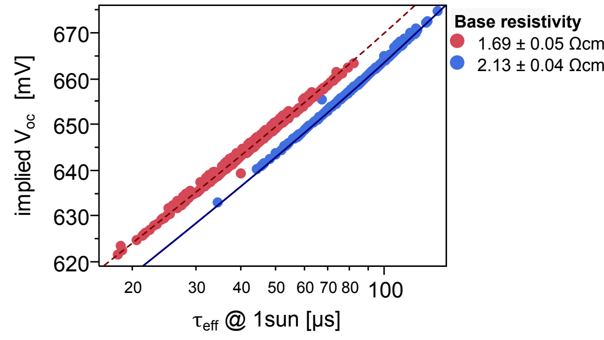

Fig. 3.7: 1 sun lifetime and calculated *implied* V_{oc} for two different materials in one experiment (detailed analysis is found in **Fig. 5.25** of in **Sec. 5.6.2**), with different cleaning conditions after thermal oxidation and SiN_x deposition.

shown that the *implied* V_{oc} directly relates to how, in the case of test structures *pn*-junction, linking it directly to the final solar cell device properties. Due to the fast data acquisition, multitude of output data (also the recombination current density) and the comprehensiveness of this technique, it will be used as main measurement technique in the following. From the obtained injection dependent lifetime curves an insight into recombination mechanism can quickly be gained. The other techniques explained in the following sections were used in addition and/or for special purposes.

3.2.2 Quasi-steady state microwave-detected photoconductance decay

Another method to detect and measure the change of photoconductance is measuring the change in microwave reflection, triggered by a laser pulse and detected by a microwave antenna above the laser spot [189]. In conventional microwave-detected photoconductuance decay (μPCD) lifetime testers the lifetime is extracted from the decay of the photoconductance σ_L after a single laser pulse by determining the decay constant of the exponential decay according to:

$$\Delta\sigma_L \propto e^{-t/\tau_{eff}}. \tag{3.31}$$

The measurement setup is depicted in **Fig. 3.8**. While the setup on the upper half of measuring chuck correspondents to conventional QSS-μPCD setups, the lower half is the improved setup that was used in this work. It features tunable illumination from the bottom of the test sample that allows to measure across a whole range of illumination and accordingly injection levels of bias illumination. For each level of bias illumination a small laser pulse ("small perturbation") is given and the minority carrier lifetime measured. This measurement principle is sketched in **Fig. 3.9**. For each measurement the quality of the exponential decay (QDC) is determined by checking if the same decay parameters apply to the whole decay curve to ensure a correct determination of the differential small perturbation ($\tau_{eff.d}$) lifetime [190].

The so obtained steady state lifetimes for several intensities in the high injection range can be used for the determination of saturation currents J_0 according to the *Kane-Swanson* method described in **Sec. 3.1.2**. According to Wilson *et al.* [191] the thus obtained data

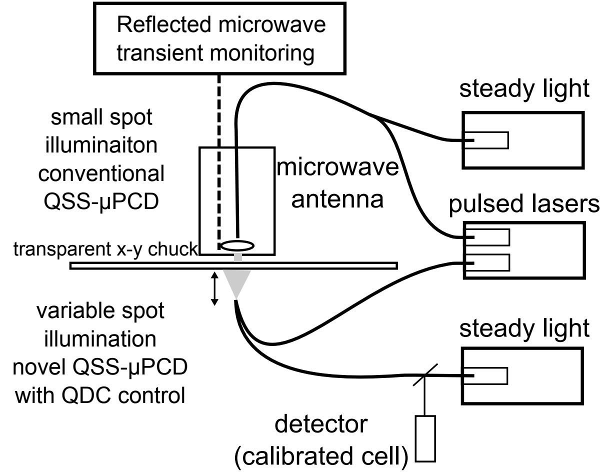

Fig. 3.8: QSS-μPCD setup featuring a variable back-light illumination and quality of decay control (QDC) [191].

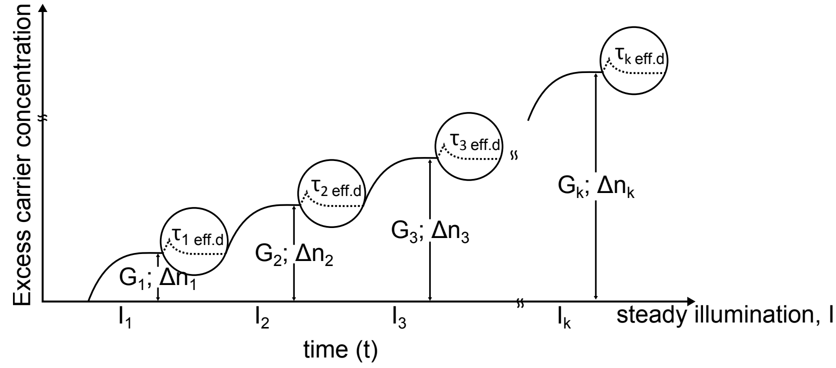

Fig. 3.9: Illustration of small perturbation QSS-μPCD at different injection levels [191].

nicely correlate with *Sinton WCT-120* measurements. The same is reported for the *Basore-Hansen* method [192] that allows direct determination of J_0 from small perturbation lifetime measurement. It allows the determination of the J_0 according to the equation for J_0 under steady state conditions

$$\frac{1}{\tau_{eff}} = \frac{1}{\tau_{bulk}} + 2\frac{J_0}{qn_i^2 W}(N_A + \Delta n_{av}), \tag{3.32}$$

which has to be modified in the case of small perturbation laser pulse which creates additional minority carriers to the bias light induced injection level $\Delta n'$ as depicted in **Fig. 3.9** into

$$\frac{1}{\tau_{eff.d}} = \left(\frac{1}{\tau_{bulk}} + 2\frac{J_0}{qn_i^2 W} \cdot N_A\right) + 4\frac{J_0}{qn_i^2 W} \cdot \Delta n'. \tag{3.33}$$

As the total recombination rate equals the generation rate ($\Delta n' = G \cdot \ \tau_{eff.d}/W$) this can be rewritten

$$\frac{1}{\tau_{eff.d}^2} = \left(\frac{1}{\tau_{bulk}} + 2\frac{J_0}{qn_i^2 W} \cdot N_A\right)^2 + \left(8\frac{J_0}{qn_i^2 W^2}\right) \cdot G \tag{3.34}$$

[192] and a linear relationship between $1/\tau_{eff}^2$ and the photogeneration rate due to light bias is obtained. If measured at several illumination intensities, the slope of the obtained line can

be used to calculate J_0 independently of the base doping N_A. The device allows illumination intensities between 0 and 22 suns. The intensities used for the linear fit were predetermined to be between 2 and 16 suns, sufficiently high to reach high injection conditions to fulfill the assumption of J_0 limitation.

The Quasi-steady state microwave-detected photoconductance decay lifetime measurement technique as implemented in the *PV2000* setup by *SemiLab/SDI* can be used to measure the effective lifetime in a similar injection range as with the QSS-PC measurement tool. The advantage of the *SemiLab/SDI* tool is that it is equipped with automated wafer handling and a whole range of additional features such as several hotplates and an high intensity flash light that can be used (among other purposes) for Fe−B pair dissociation and repairing. Furthermore, it is able to record maps of the measured lifetimes.

3.2.3 Measurement of iron concentrations in p-type silicon

In terms of recombination activity there are two significantly differently behaving modifications of Fe in boron doped p-type silicon, which can be quickly interchanged into each other using heat and high intensity light flashes. The following reaction is suggested for this phenomenon:

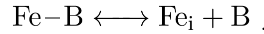

$$\mathrm{Fe{-}B} \longleftrightarrow \mathrm{Fe_i} + \mathrm{B} \ .$$

High intensity light flashes dissociate the Fe−B pairs and release interstitial iron ($\mathrm{Fe_i}$). Moderate heating (70°C) for a couple of minutes reverses this effect. The different recombination behaviours of the two modifications can be used for the determination of the bulk Fe concentration by measuring the minority carrier lifetime before and after Fe−B dissociation using the following equation [193, 194]:

$$[\mathrm{Fe_i}] = C\left[\frac{1}{\tau_{eff(\mathrm{Fe_i})}} - \frac{1}{\tau_{eff(\mathrm{Fe-B})}}\right]. \tag{3.35}$$

The term to calculate the $\mathrm{Fe_i}$ concentration is simply derived from subtracting the effective lifetime before and after Fe−B pair dissociation, assuming that no other defects change their recombination behaviour during the procedure. The factor C can be determined empirically or calculated using the *SRH* equation for the recombination at point defects, namely **Eq. 3.8**, as was shown by Macdonald *et al.* [175]. In the following equation the τ_{SRH} terms have to be solved for the N_T value using the *SRH* parameters listed in **Tab. 3.2**. The value for N_T can assumed to be the same for Fe−B and $\mathrm{Fe_i}$ as a nearly 100% transformation is assumed to be reached by the high intensity light flashes [195]:

$$\frac{1}{\tau_{eff(\mathrm{Fe_i})}} - \frac{1}{\tau_{eff(\mathrm{Fe-B})}} = \frac{1}{\tau_{SHR(\mathrm{Fe_i})}} - \frac{1}{\tau_{SHR(\mathrm{Fe-B})}}. \tag{3.36}$$

As the recombination behaviour of both Fe-species, but especially of $\mathrm{Fe_i}$, is highly injection level dependent, the C-factor is as well. The injection dependency of 1/C is plotted in

Tab. 3.2: Recombination properties of Fe_i and Fe−B point defects as used by Macdonald *et al.* in [175].

species	E_T $[eV]$	σ_n $[cm^{-2}]$	σ_p $[cm^{-2}]$
Fe_i	$E_V + 0.38$	5e–14	7e–17
Fe−B	$E_C - 0.23$	3e–14	2e–15

Fig. 3.10, as taken from Macdonald *et al.* [175].[1]

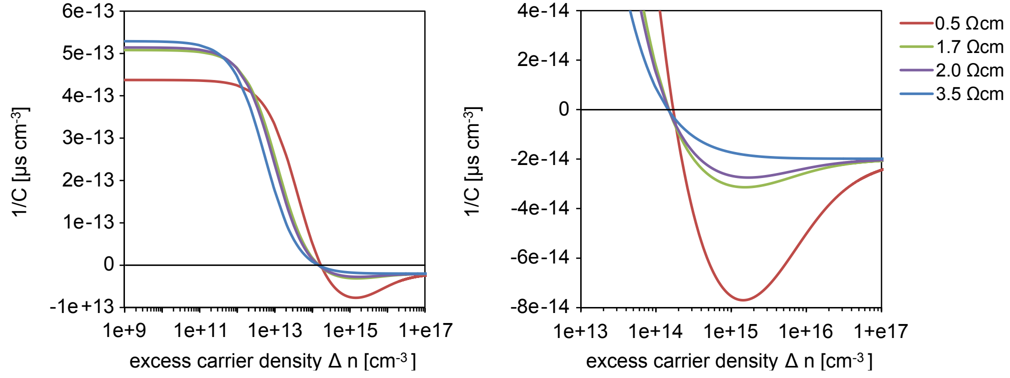

Fig. 3.10: 1/C for different doping levels (typical for solar cell production) plotted against the injection level; right hand side graph: Zoom-in for the relevant injection level range of the QSS-PC and QSS-μPCD methods.

3.2.4 Corona-charge

Properties of passivation layers can be determined using a combination of a so called "corona gun" with the measurement of surface contact potential difference in the dark and under intense illumination using a vibrating Kelvin probe, an adaption of a common IC dielectric characterisation method [196, 197]. The measuring setup is depicted in **Fig. 3.11**.

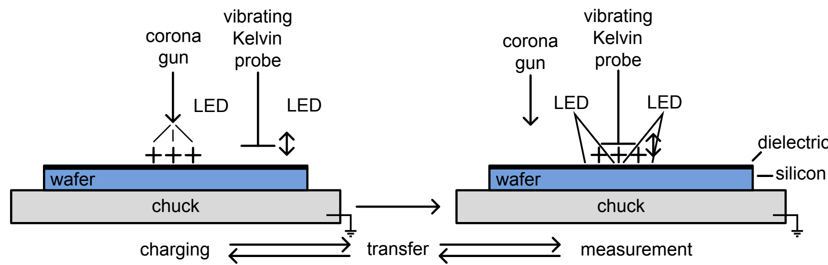

Fig. 3.11: Passivation layer properties measurement setup [198].

A passivated Si wafer is placed on a X-Y chuck and defined surface charges from ionised air (negative or positive) are applied by a high voltage corona gun according to **Fig. 3.11**. The corona gun can be calibrated using an IC wafer passivated by a high quality thermal oxide with known passivation layer properties. Positive ions from air predominately consist of $(H_2O)_nH^+$ and negatively charged ions of $CO_3{}^-$. After the application of a defined amount of charge, the charged spot is moved to the high frequency vibrating Kelvin probe (1100 Hz)

[1] The value for the thermal velocity v_{th} of electron and holes this and the following calculations are based on is 1.1e+7 cms^{-1} as it was used in the publication by Macdonald *et al.* in [175].

where the surface contact potential difference V_{CPD} is measured. The V_{CPD} contains several information about the interface as expressed in the following equation:

$$V_{CPD} = \phi_{ms} + V_{SB} + V_D, \tag{3.37}$$

with ϕ_{ms} being the work function difference between the metal of the Kelvin probe and the semiconductor, V_{SB} being the surface barrier between semiconductor and dielectric layer (also referred to as band bending) and V_D being the dielectric voltage of the passivating layer as sketched in **Fig. 3.12**. V_{SB} can be extracted by measuring the difference in V_{CPD} in the dark and under intense illumination. The effect of the illumination is the injection of a large amount of minority carriers, filling up the bent band edges and driving the surface potential V_{SB} from either depletion or accumulation to flatband conditions (V_{FB}). As the work function and the dielectric voltage are not affected by the illumination, the surface barrier can be extracted by

$$V_{CPD}^{dark} - V_{CPD}^{illuminated} = V_{SB}[196]. \tag{3.38}$$

[196] The valence and conducting band of semiconductor that are depending on the kind of the so-called "fixed charges" in the dielectric at the semiconductor interface are either bent up- or downwards by the surface barrier V_{SB} in the initial state.

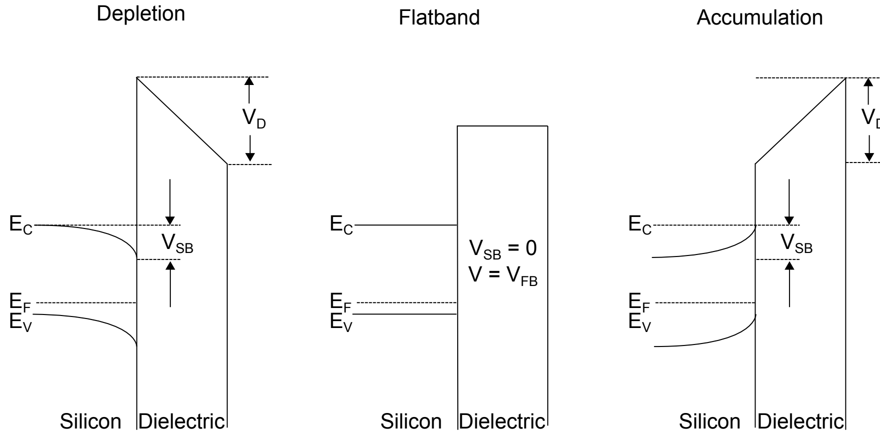

Fig. 3.12: Band diagrams of the silicon interface in case of p-type silicon. The dielectric can be modified using the corona-charge.

Depending on the direction of scanning, a large amount of negative or positive charge, is applied. Either the V_{SB} of the interface is overcompensated into inversion or further depleted/accumulated. By stepwise charging the dielectric now of the opposite kind and measuring the change in surface barrier ΔV_{SB} important information about the passivation layer and the interface can be extracted. Stepwise the interface trap states are filled. The smaller the increase in V_{SB} relative to the applied charge, the higher is the defect density. The obtained output data are shown in **Fig. 3.13**. From the left hand side graph the total amount of fixed charges in dielectric Q_{tot} as the difference between flatband conditions and the initial state can be read. Flatband conditions cause the two curves ($V_{CPD}^{illuminated}$ in blue and V_{CPD}^{dark} in red) to meet, as no difference can be recorded, when the applied charge completely cancels

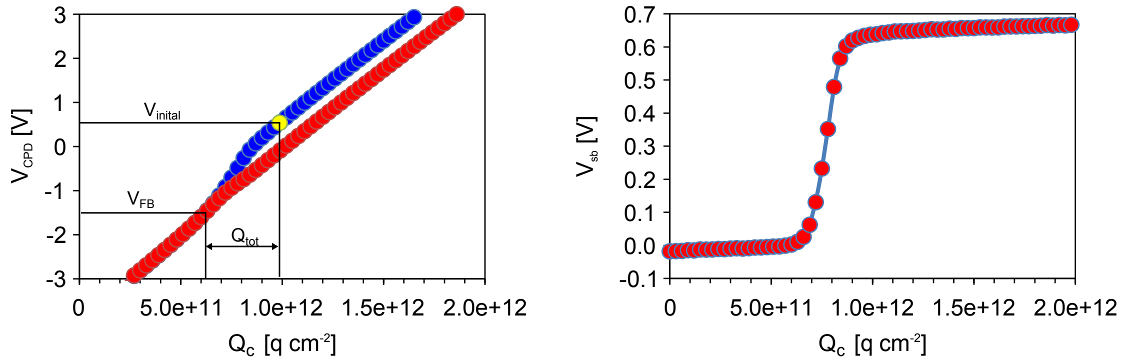

Fig. 3.13: Measured data V_{CPD} and V_{SB} plotted against the surface charge applied (ΔQ_C).

out the band bending.

From the V_{SB} the surface space charge Q_{sc} can be calculated using the standard space charge function F_s, which can be found in [199] (the doping densities $N_{A/D}$ and the bulk Fermi potential are required for this calculation, for more details please refer to [200]). The difference in charge ΔQ_{sc} represents the impact of the applied charge ΔQ_c on V_{SB}. In the case of no present traps, the change in space charge should equal the applied external charge. The observed difference then corresponds to the charge that is "absorbed" by filling the interface trap levels according to the following relationship:

$$|\Delta Q_{sc}| = |\Delta Q_c| + |\Delta Q_{it}|[196]. \tag{3.39}$$

This only holds true when no leakage currents flow through the interface. When relating the thus obtained $|\Delta Q_{it}|$ with the change in ΔV_{SB}, the density of the interface traps can be obtained

$$D_{it} = \frac{|\Delta Q_{it}|}{\Delta V_{SB}}. \tag{3.40}$$

[196]

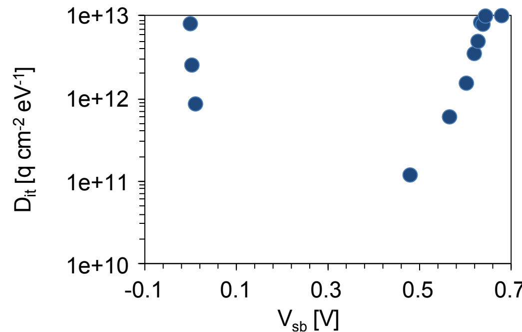

Fig. 3.14: Defect density D_{it} plotted against V_{sb}.

The trap density at the interface against the change V_{SB} is plotted in **Fig. 3.14**. The data shown above were acquired, starting the corona charge from flat band conditions of a p-type wafer with SiO_2/SiN_x. Thus the E_V can be located around 0.1 V and E_C around 0.7 V. The highest D_{it} values are found for the band edges, while the lowest are found towards mid gap.

The lowest measured value is often referred to as the the value for the density of interface traps D_{it}. The highest recombination potential is expected for traps near the center of the band gap. For low density of traps across the band gap this typical U-shaped curves are found (it represents similar information as the data shown in **Fig. 2.23**). When impurities or other defects are introduced, this shape will change towards higher values. The resolution is determined by the chosen dose of charge that can be applied. For low densities of defects the smallest possible dose may be too large resulting in non-continuous curves in regions with small defect densities. The accordingly obtained plot is quite useful to compare different levels of contamination in terms of impact on the passivation layer.

4 The impact of metal surface contamination on solar cell devices

As highest possible lifetimes (and *implied* V_{oc} values) for highest efficiencies are desired, “cleaninest” surfaces are required [201]. Yet, to keep production costs as lean as possible, a compromise between cleanliness and costs may be necessary. In order to shed light on process specifications, the first step of metal contamination management is to identify the most relevant metal elements, study their effect and establish a relationship between surface contamination and impact on the final device in order to obtain reliable threshold values.

For this purpose in the following chapter, first of all, an introduction into metal surface contamination is given (**Sec. 4.1**) and the most relevant elements are identified. In order to study the effect of surface contamination, a method for controlled contamination was developed that was designed to be as close to production conditions of solar cell processing as possible. It is presented in **Sec. 4.2**. The contamination method was applied to processes required in p- and n-type solar cell processing in order to correlate surface contamination and lifetime and compare the different processes in terms of sensitivity. The results are presented in **Sec. 4.3** (p-type processing) and **Sec. 4.4** (n-type processing). The mechanisms of the observed lifetime degradation are discussed at the end of each section.

Last, the impact of surface contamination on solar cell efficiency was simulated based on the experimental data acquired in this chapter (**Sec. 4.5**). For this purpose, first of all, it was necessary to gather data of the recombination behaviour of Cu in p-and n-type silicon by injection dependent lifetime analysis, as data in the literature are rare. Then, the collected data from test structures were used to simulate the impact of surface contamination present before high temperature diffusion processes by a numerical simulation software.

4.1 Surface contamination

4.1.1 Measurement of surface contamination

In order to investigate the impact of metal surface contamination, a suitable measurement technique for the determination of the surface concentration is required. There are several methods to extract the metal surface contamination of silicon wafers in the literature. As the expected contamination is very small, it can hardly be directly measured (or only by using extensive methods such as synchrotron radiation scattering [202]). Usually, either the surface contamination is collected, pre-concentrated and then measured directly on the surface by total x-ray fluorescence (TXRF) or it is collected and then subjected to quantitative elemental analysis (such as atomic absorption spectroscopy, AAS, or inductively coupled plasma mass spectroscopy, ICP-MS).

The most common method for extraction and/or pre-concentration is the vapor phase decomposition method (VPD) [203–206]. A wafer is placed on a cooled chuck into a closed chamber, which is flooded with HF vapor. HF vapor dissolves the native oxide on the wafer surface and is subsequently collected by a single droplet. This method works nicely on flat IC wafers but can hardly be used on textured or very reactive surfaces such as highly doped regions. An alternative way to extract the surface contamination of structured wafers is the pack extraction method suggested by Shimizu *et al.* in [207], in which the wafer is placed in a clean plastic bag that is filled with HF/HNO_3 mixtures to etch the surface. This method, however, requires a lot of preparative skills to avoid unwanted contamination from the plastic bag. Also, it requires a relatively large amount of etching solution, which in turn lowers the limit of detection.

A much more elegant method to extract the surface contamination of two sister wafers (wafers of the same kind on neighbouring positions within the respective process) is the sandwich etch (SE) method suggested and evaluated in [7, 208]. It is loosely based on a work by Shabani *et al.* [209]. A schematic description of the sampling method can be found in **Fig. 4.1**. A droplet of 700 μg or 1000 μg of 5% wt. HF in 30% wt. H_2O_2 is placed on flat or textured surfaces, respectively (1). Highly pure chemicals are required to enable a sufficiently low detection limit[1]. A sister wafer is placed on top (2), the wafers are rubbed against each other (3) and the solution is left to soak for ten minutes (4). Then the top wafer is removed (5), the solution is collected (6) and shipped for ICP-MS analysis for multi-element mass spectrum analysis of a predefined selection of elements. Apart from metals, silicon is routinely measured in order to estimate the etch depths of the sampling solution. Usually between 0.6 and 6 μm are etched.

The surface concentration can then be calculated from the measured concentration by the following equation:

$$c_{SF} = \frac{m_{Me}/1\text{g} \cdot m_{solution} \cdot N_A}{2A_{wafer} \cdot M_{Me}} \left[\text{cm}^{-2}\right], \tag{4.1}$$

in which $m_{Me}/1\text{g}$ is the measured concentration of the metal (Me) in ppb [1e–9 g of metal in 1 g sampling solution] in the amount of employed sampling solution, $m_{solution}$ in g (which

[1] 1 ppb in sampling solution roughly corresponds to 1e+10 atoms cm^{-2}.

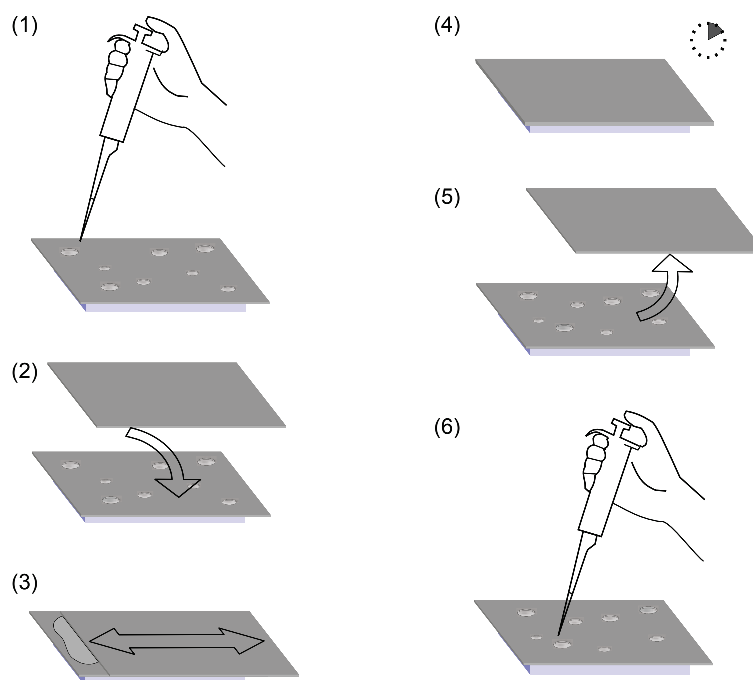

Fig. 4.1: Scheme of the droplet etch sampling method used for the extraction of surface contamination within this work [208].

was measured beforehand), N_A is Avogadro's number (mol^{-1}), A_{wafer} is the surface area of the wafer in cm^2 and M_{Me} is the molar mass of the respective metal in g mol^{-1}. More details about the method can be found in the experimental section (**Sec. 6.2.1**).

4.1.2 Choice of elements used for further contamination studies

Highest surface concentrations of metals are found on as-cut wafers and the initial surface contamination is hardly reduced by the first alkaline etching step. An example for the contamination load of diamond wire sawn Cz wafers after alkaline etching is given in **Fig. 4.2**. The high Fe and Cu concentrations on the surface are stemming from the etching bath itself (high Fe concentration according to specifications of NaOH and KOH; Honeywell Puranal specifications: 1000 to 3000 ppb) and the as-cut wafers (the cutting wire is most commonly made up from stainless steel with Cu or brass coating [210]).

Apart from as-cut wafers and process chemicals as contamination source, Fe and Cu are the most common contaminants in a process surrounding. Especially Fe, as main component of steel, can easily be transferred to the wafer surface, either by metal particles contained in dust—solar cell fabrication often does not employ cleanroom environment—or in direct contact with metal surfaces (measurement chucks, conveyor belts) or by contaminated water or etch/cleaning baths.

Naturally, other elements will find their ways on the wafer surface. However, insufficient cleaning on the one hand will most of the times result in increased Cu contamination, as Cu, due to its noble nature, is easily reduced to the elemental state on the wafer surface. Environmental contamination on the other hand will in most of the times be accompanied by Fe. Consequently, these two elements may be used as markers for the detection and mon-

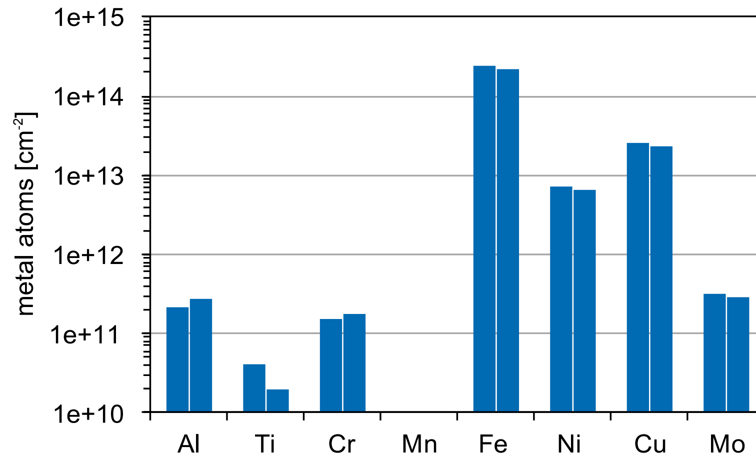

Fig. 4.2: Example for surface contamination of diamond-wire sawn Cz-wafers after saw damage etch in NaOH (22%), as measured by sandwich etch ICP-MS, two neighbouring sets of wafers were analysed.

itoring of metal contamination. Deeper knowledge and understanding about the behaviour of these two species will help to identify harmful contamination during processing and allow to distinguish process failure due to contamination from other failure causes.

Tab. 4.1: Diffusivity and solubility at 875°C [12] of several metals in Si. The flux is calculated by multiplying diffusivity with solubility.

	$D_{875°C}$ [cm^2s^{-1}]	$S_{875°C}$ [cm^{-3}]	$(D{\cdot}S)_{875°C}$ [$cm^{-1}s^{-1}$]
Ti	1.4e–10	1.81e+11	2.6e+01
Cr	4.9e–07	3.96e+12	1.9e+06
Mn	1.2e–06	3.98e+13	5.0e+07
Fe	1.4e–06	2.91e+13	4.2e+07
Co	2.1e–05	4.81e+13	1.0e+09
Ni	1.8e–04	5.98e+16	1.1e+13
Cu	9.0e–05	1.80e+17	1.6e+13
Zn	5.7e–09	1.03e+15	5.9e+06

Another reason for using Fe and Cu for further studies is the fact that both are relatively fast diffusing and highly mobile in silicon and can therefore easily penetrate critical parts of the solar cell device. The mobility (flux) of several elements is calculated by the product of diffusivity and solubility [211]. The thermodynamic information for the calculation of diffusivity and solubility is taken from Graff [12]. The higher the flux is, the more mobile the species is within the Si crystal at the given temperature. The metals can be divided into three groups: slow diffusing elements (Ti, but also Al), medium fast diffusing elements (Mn, Fe, Co and Zn) and fast diffusing elements (Ni and Cu). In accordance with their mobility in the crystal, elements with a similar flux have similar properties: the fast diffusing elements will almost always reach the thermodynamically favourable location in the bulk (grain boundaries or the surface), where they tend to form precipitation clusters, while slower diffusing elements can be quenched in the Si lattice, when the cooling ramp of a high temperature process is too steep, where they are more likely to form small highly recombination active point defects [150, 211–214]. Very slow diffusing elements will hardly penetrate the silicon even during

long high temperature steps but may still be harmful at the interface. Within the respective groups not only the chemical properties but also the electrical recombination properties are similar [12]. Fe can be chosen as typical representative of the medium fast diffusion metals and Cu of the fast diffusion ones.

4.2 Intentional contamination of silicon surfaces

Numerous data and information about intentional contamination exist in the literature from IC research. Many authors use single sided contamination applied by spin-on techniques [215–218], or by drying a droplet on the wafer surface [219]. When contamination from dipping into spiked solution is considered, the most common and well understood system is the standard clean 1 (SC1), made up from DI water, NH_4OH (30% from NH_3) and H_2O_2 (30%) (5:1:1), which shows a strong tendency to metal precipitation on wafer surfaces [220–222]. A comparison of the spin-on and the SC1 dipping method is given in [222].

For a most realistic contamination scenario for solar cell fabrication a setup was chosen that mimics a dipping sequence, which is most common at the end of wet chemical processing equipment: before drying, the wafers are rendered hydrophobic in diluted hydrofluoric acid, which is removed in a rinsing cascade. If contaminated, these last steps of a cleaning sequence are most likely to have a detrimental effect on the the subsequent (high temperature) process steps.

For the study of intentional contamination clean wafers had to be processed first. Cz-wafers of both n- and p-type were saw damage etched in 22 %wt. NaOH at 80°C for 5 minutes and subsequently cleaned in SPM. Flat wafers were chosen to reduce the influence of surface morphology properties such as roughness and pyramidal structure of random pyramid texture. The oxide produced by the SPM step was left on the wafers.

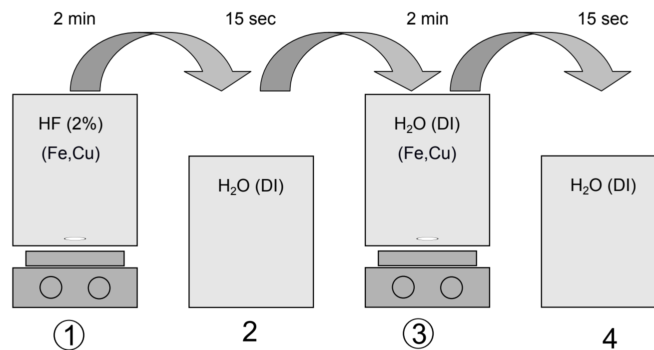

Fig. 4.3: Dipping sequence for controlled contamination.

In order to contaminate a batch of wafers at a time, a carrier for up to 25 wafers was used. A scheme of the contamination sequence, including the dipping times and HF concentration, is found in **Fig. 4.3**. For each contamination level fresh baths were made up (except the HF bath, which was, if not contaminated, reused). Stirring was applied in bath 1 and 3 to ensure the even dissolution of the contaminant. A first set of wafers was obtained by spiking the HF, a second by spiking the second DI water bath with 25 to 420 ppb Cu and Fe solution made up from $Cu(NO_3)_2 \cdot 3\,H_2O$ and $Fe(NO_3)_3 \cdot 9\,H_2O$. The short dip in a DI water bath after the HF bath was required to avoid an uncontrolled drop in pH for the contaminated bath by carry-over from the HF; and the dip after the contaminated rinse (bath 3) was meant to get rid of droplets containing the metal.

4.2.1 Contamination from diluted HF

First of all, the sensitivity of diluted HF (2%) was tested. For this purpose p-type wafers were immersed into differently contaminated HF and the surface contamination was measured. This was performed within the experiment run 1274[1]. The results are found in **Fig. 4.4**.

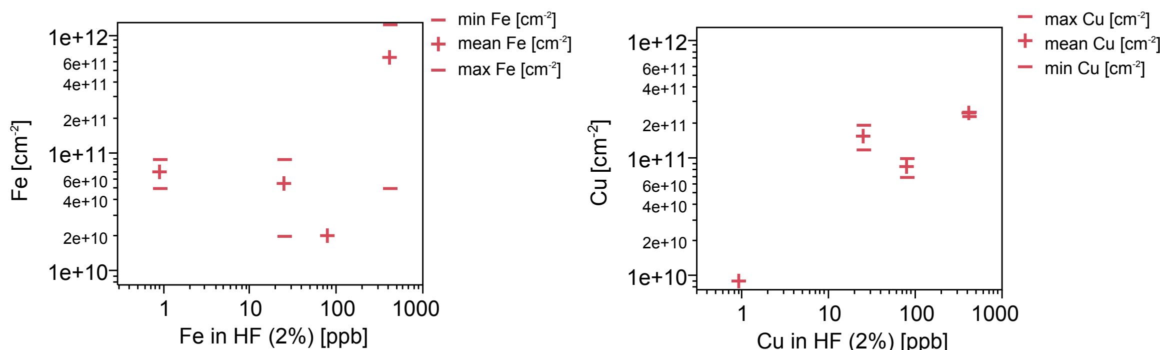

Fig. 4.4: Measured surface contamination from run 1274 plotted against the Fe and Cu concentration in 2% HF . Two values were measured for each concentration level.

No clear trend for the contamination from HF for both species was extracted. Fe shows a strong variation for the highest contamination level, which also was attributed to an erroneous measurement. Although the Cu surface concentration increased significantly with increasing concentration in solution, no clear trend was observed. From the literature much higher Cu concentrations in the range of 1.2e+12 [223] to 1e+13 cm^{-2} [224] were expected. Norga found that Cu precipitation from diluted HF on silicon surfaces also depends on doping type, concentration and illumination level [223], which makes this method rather unsuitable for controlled intentional contamination studies.

4.2.2 Contamination from DI water

The data obtained for dipping of hydrophobic wafers into contaminated DI water collected in several experiments (run 1274, 1288, 1333) are summarised in **Fig. 4.5**. In general, an increasing trend for surface concentration with increasing concentration in solution is observed. The Fe and Cu concentrations of the made-up solutions were measured using spectrophotometric measuring technique developed together with METROHM and implemented into a ProcessLab® system. Samples were taken right after the contamination step; acid (50%HF or 32%HCl) was added to the Fe containing solution to avoid precipitation (the resulting 2% diluted acid was then measured). It became apparent that Fe concentrations differed significantly from target concentrations (25, 80, 420 ppb). This can be explained by the instability of the predominant Fe species (Fe^{2+}) according to the three dimensional Pourbaix [225] diagram, in which the predominant species of Fe in solution are plotted against concentration, electrochemical potential of the solution and pH [226]. From the red circle in **Fig. 4.6** it can be concluded that the experimental conditions that were chosen (indicated by the red

[1]The "run" numbers correspond to an overall list of experiments at ISC Konstanz to enable scientists and operators to track and trace their wafers during processing. An overview (including the most important parameters) of the experiments performed within the scope of this thesis can be found in the appendix.

lines) coincide with the point where Fe^{2+} tends to be oxidised and the predominant species becomes FeO(OH) (s) (indicated by the red line), which would cause precipitation.

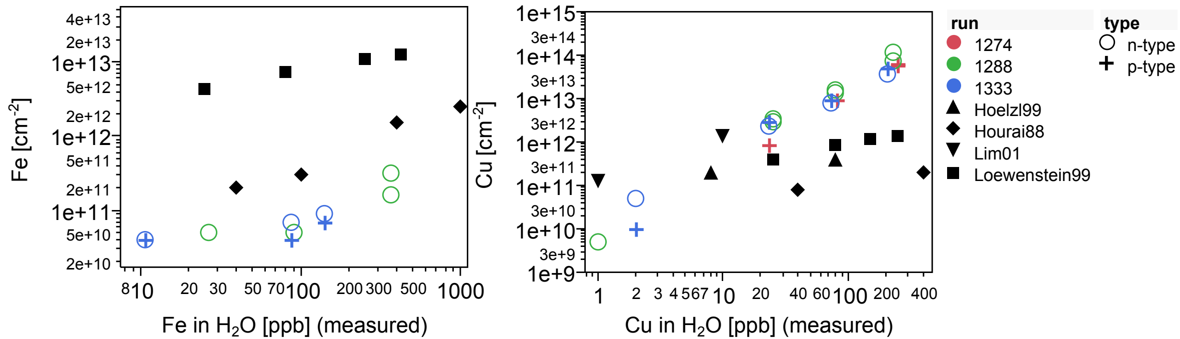

Fig. 4.5: Surface concentration plotted against the concentration in DI water. Literature values are taken from Hoelzl [222], Hourai [215], Lim [227] and Loewenstein [217].

The variation of the literature values for Fe is quite strong. The data for the contamination from H_2O originate from Hourai (1988), Hoelzl (1999), Lim (2001) and Loewenstein (1999). Loewenstein *et al.* published a statistical model for the relationship between setup properties (concentration, pH and time) by fitting experimental data using thermodynamic assumptions such as the ionic exchange equilibrium assumption of Si−OH and cationic metal species[1] [216, 217]. Similar to Hourai, Loewenstein *et al.* used a single side contamination method, in which a puddle (several milliliters) of contaminated solution is placed on the wafer surface, which is removed by spin drying after a certain time. However, the deviation between both their results is quite large [217, 222]. Lim *et al.* also found a dependency on the wafer resistivity and doping type for Cu precipitation, both relatively small. The crystal orientation turned out to have a stronger impact: (111)-surfaces exhibit a much smaller coverage than (100)-surfaces [227].

The main reason for the large discrepancy between the Fe surface contamination produced by Hourai and Loewenstein is most likely the difference in surface termination—hydrophilic, oxide terminated surface obtained by an SC1 dip and HCl/O_3 dip were used, respectively—while in the series of experiments presented here the surfaces was hydrophobic, thus hydrogen terminated. Costine *et al.* [229] have shown by XPS studies that oxidised surfaces are much more prone to Fe adhesion, especially at higher pH values, as, due to the amphoteric behaviour (cf. **Fig. 2.13**) of the Si−OH, terminated surface becomes much for favourable to be covered by cations. Furthermore, they noted that not only the surface termination but also the oxidation state of Fe and its ligands in solution play an important role. The generally small Fe surface coverage at the given conditions (low Fe concentration in solution and near-neutral pH) can be further explained by the complex structure of the Fe cation in solution, as Miyashita *et al.* have calculated using *ab initio* MO calculations [230]. With increasing pH more hydroxides are coordinated by the Fe central atom causing the energy of the HOMO shift to higher values closer to the LUMO of the Si−OH surface increasing the rate of the frontier orbital controlled adsorption.

[1] The data points from Loewenstein *et al.* [216, 217] the conditions used in the experiment (pH 7 and two minutes immersion time) were obtained by refitting his model using the statistical software JMP10 .

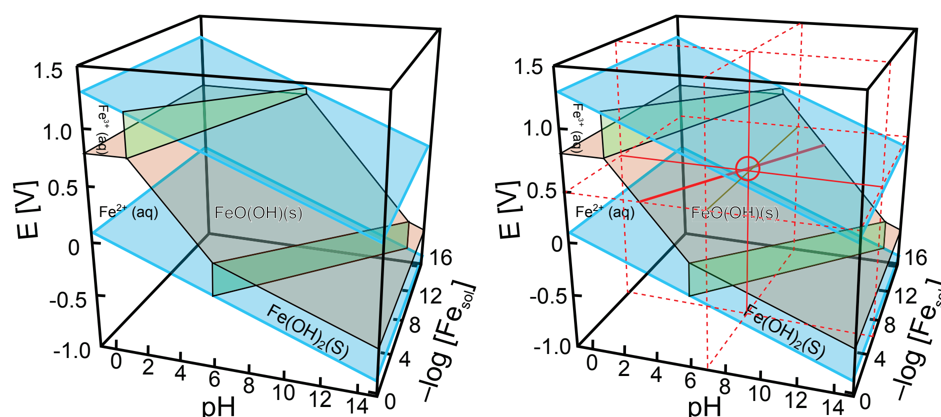

Fig. 4.6: Three dimensional E-pH diagram of Fe in aqueous solution on the left hand side. The diagram was constructed according to [226]. The parameters relevant for this experiment are added to the diagram (dashed red lines) on the right; the pH was measured to be between 6 and 7 during the experiment, the used Fe concentrations differ in the range of 0.44 to 7.4e–5 $\mathrm{mol L^{-1}}$, the electrochemical potential of the DI-water was assumed to be 0.5 (as Kim *et al.* did in [228]). The red circle indicates that under the working conditions the red plane between Fe^{2+} and FeO(OH)(s) (indicated by the thick red line) is met.

In the following for each set of data (run) blanks were measured on cleaned surfaces dipped into the same bath sequence without the addition of Fe or Cu. The blank value was found to be in the range of 4 to 5e+10 $\mathrm{cm^{-2}}$ for Fe and in the range of below 1 to 4e+10 $\mathrm{cm^{-2}}$ for Cu. This, as shown in **Fig. 4.7**, proved to be problematic in certain cases, as, for example, in run 1288 only the highest Fe contamination level in the solution produced data above the blank value. Accordingly, if possible, data from several experiments were combined to increase the validity of the experimental data[1]. Blank samples or data points below the blank value are denoted with gray or lighter coloured symbols in the following.

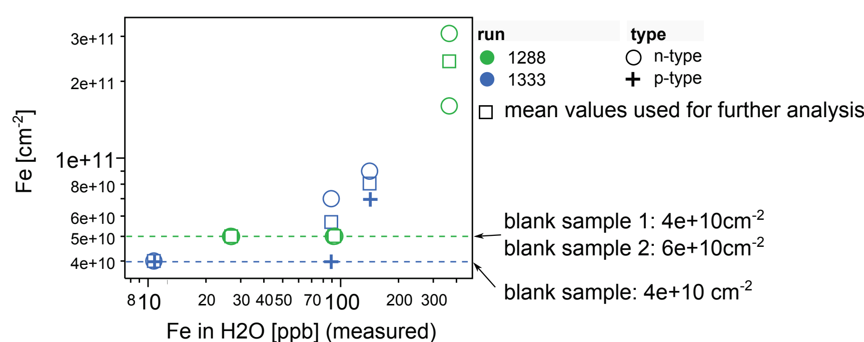

Fig. 4.7: Zoom in of the graph for Fe in **Fig. 4.5**. The dashed lines show the blank values of the two experiments.

Cu contamination from H_2O proved to produce higher surface contamination than most of the data found in the literature, showing an inverse effect as seen in the case of Fe. The presented data from the three different experiments and the data provided by Lim *et al.* [227], who also used hydrogen terminated wafers, show much higher surface coverage as the data by the other authors, who applied contamination to oxide terminated surfaces. This indicates a different mechanism for surface-metal interaction more like the one reported for

[1] As the ICP-MS analysis was quite costly, also data points with one measurement just above the blank value and one below were included in the analysis. In this case a mean value was calculated using both.

Cu contamination in HF in [223].

Conclusion

Concluding, it can be stated that the system of Fe and Cu in H_2O proved to be more suitable for intentional contamination studies than the system of Fe and Cu in HF. In H_2O metal concentrations in the range between 10 and 420 ppb produce increasing surface contamination of the respective metal with the concentration in solution. The relationships, linear in the case of Fe and quadratic in the case of Cu, are plotted in **Fig. 4.8**. As the measurement of the contamination in solution requires less analytical costs and effort, it may replace the surface analysis in the presented system in the future. The large discrepancy between literature and experimental data may be explained by different experimental setups and shows the need for thorough calibration of each chosen contamination system.

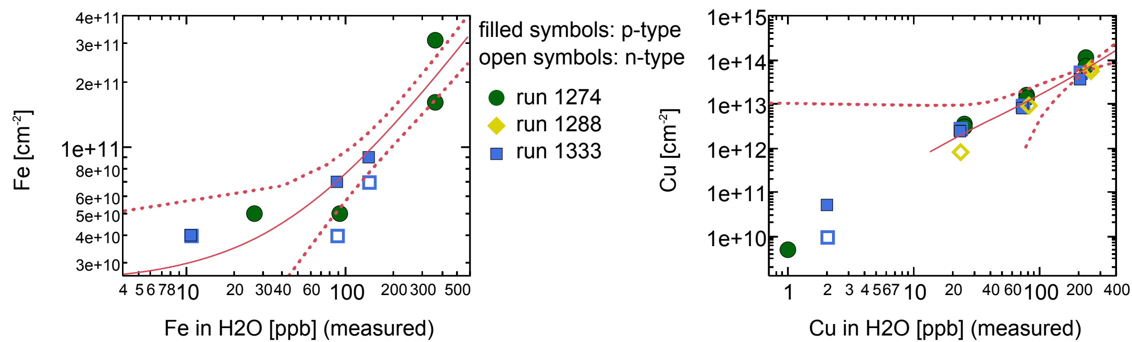

Fig. 4.8: Linear fits of the experimental data for intentional contamination studies. The respective equations may be used for further studies using the same setup: Fe [cm^{-2}] = 2.37e+10 + 5.39e+8.00·[Fe in H_2O [ppb] (measured)] with r^2=0.79; Cu [cm^{-2}] = –7.47e+12 + 2.45e+11·[Cu in H2O [ppb] (measured)] + 8.52e+8·[Cu in H2O [ppb] (measured)–90.5]^2 with r^2=0.83. Dashed lines show the 95% confidence belt. As published in [231].

4.3 Processing of p-type substrates

The relevant process steps in p-type solar cell technology, in which metal contamination is expected to play a role, are back-side passivation steps, as used in PERC cell technology, and phosphorus diffusion for p-n-junction formation. The following section therefore investigates the impact of Fe and Cu on two different passivation stacks (**Sec. 4.3.1**) and the current ISC Konstanz standard P-diffusion (**Sec. 4.3.2**). In two excursuses the potential impact of fast firing and the impact of variation of cleaning and phosphorus diffusion parameters are discussed.

4.3.1 Back-side passivation

The polished back sides of passivated emitter and rear side solar cells (PERC) [232] are quite challenging to be passivated. In addition to chemical passivation the suitable field effect passivation is required [109] to avoid so-called parasitic shunting effects [233]. In p-type structures this is obtained by negative fixed charges in the passivation layer, which are created by silicon oxide growth [234] or aluminum oxide deposition [235], creating a repelling field for minority carriers. Apart from this, the passivation layer needs to withstand the process sequence: when applied at the very beginning of the sequence, it has to undergo wet chemical etching and cleaning, thermal treatment (diffusion), screen printing and co-firing of contacts. The process induced stress is reduced when the passivation is applied further at the back end of line (BEOL). Nevertheless, especially for aluminum oxide, phenomena such as blistering during contact firing have been challenging [236]. To overcome these challenges the initial passivation is commonly capped by a silicon nitride protection layer, deposited by PECVD [112].

At ISC Konstanz, PERC solar cells are commonly fabricated using either a thermal oxide/silicon nitride stack or an all-PECVD stack, also referred to as “magic” silicon nitride ($MSiN_x$). Both ways of fabrication can be integrated into the process sequence as FEOL or BEOL step. Solar cell efficiencies close to 20% were reported using these layers [237, 238].

In the following, both all-SiN_x and thermal oxidation passivation layers will be tested in terms of sensitivity towards surface contamination. The mechanisms of degradation of minority carrier lifetime due to metal surface contamination of lifetime samples made up from flat 1.7 to 2 Ωcm Cz wafers are investigated. The thermal oxidation was performed at 885°C for 60 min, resulting in a thermal oxide with a thickness of about 25 nm. The silicon oxide is subsequently capped by a silicon nitride layer (about 150 nm). The all-PECVD stack was tuned to a similar thickness (by adjusting the deposition time) resulting in a passivation layer of the same yellow colour and accordingly similar optical properties. The thicknesses were measured by ellipsometry. The samples were fired after processing with the standard firing recipe with the peak temperature 860°C.

Experimental results

The sensitivity of both back side passivation processes (all-SiN_x and thermal oxidation) against Fe and Cu surface contamination is shown in **Fig. 4.9**. The different orders of mag-

nitude for critical surface contamination values for the different species are apparent. While Fe starts degrading the effective lifetime and hence the *implied* V_{oc} at a level of 5e+10 cm^{-2}, Cu does not start to degrade the lifetime until a level above 1e+12 cm^{-2} for the thermal oxidation process and above 1e+13 cm^{-2} for the all PECVD-based process. Virtually no difference can be found for the two passivation layers in terms of Fe contamination. Note that these measurements were performed after firing. The data were fitted using the non-linear fit function in JMP10 applying sigmoid functions, such as Gompertz functions[1]. These are especially suitable for a strong impact, when the test structure is "killed" beyond a certain point and accordingly reaches a lower limit, or exponential decay functions[2] suitable for comparatively small impacts (when the lower limit is not reached within the investigated range). The function fitting the collected data best was chosen by comparison of the fit quality using the coefficient of determination (r^2). The fits used in **Fig. 4.9** are Gompertz curves.

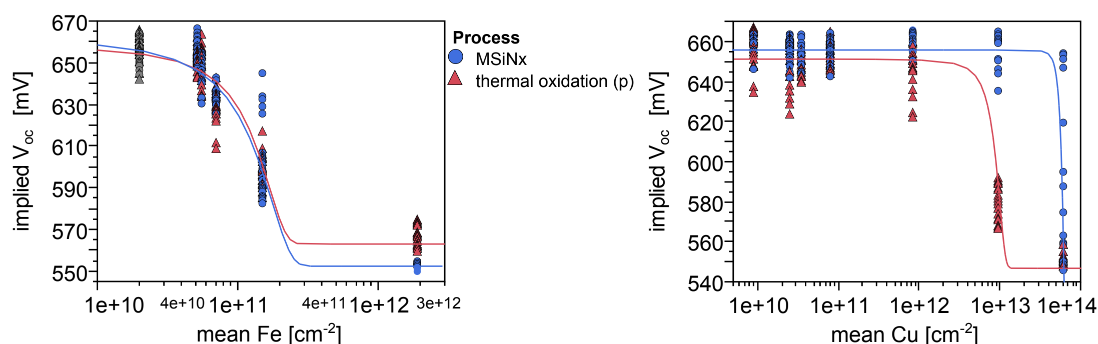

Fig. 4.9: Comparison of the sensitivity of the two passivation stacks against Fe and Cu contamination. The data summarise samples contaminated from H_2O and diluted HF from run 1274 (i.e. surface concentrations are measured concentrations).

Note further that the *implied* V_{oc} values are relatively low, representing maximum lifetime values of 100 μs at an injection level of 1e+15 cm^{-3}, most likely due to poor material quality. In a second experiment (run 1333—the first experiment was run 1273) higher quality material with a similar base doping (1.7 to 2 Ωcm) was used reaching up to 550 μs with the same passivation layers (corresponding an *implied* V_{oc} of up to 715 mV), proving the excellent passivation quality. To check whether the elevated bulk recombination by material inherent defects affects the drop in *implied* V_{oc}, the two experiments were combined in the following graphs of **Fig. 4.10** using the differences in *implied* V_{oc} between the contaminated samples and the reference instead of absolute values.

From **Fig. 4.10** it can be deduced that both experiments show a similar trend concerning the drop in *implied* V_{oc} independently of the material quality. Fe contamination has a strong effect on both passivation layers even for very small contamination levels, being close to the limit of quantification for the measurement technique in use, which explains the relatively strong variation below 1e+11 cm^{-2}. For Cu the deviation from the fits is relatively small, independently of the material, indicating good reproducibility of the used contamination and

[1]Gompertz4P: $f(x) = a + (b - a) \cdot \exp(-\exp(-c \cdot (x - d)))$ with a=lower asymptote; b=upper asymptote; c=growths/decay rate; d=turning point.

[2]Exponential3P $f(x) = a + b \cdot \exp(c \cdot x)$ with a=asymptote; b=scale; c=growth/decay rate.

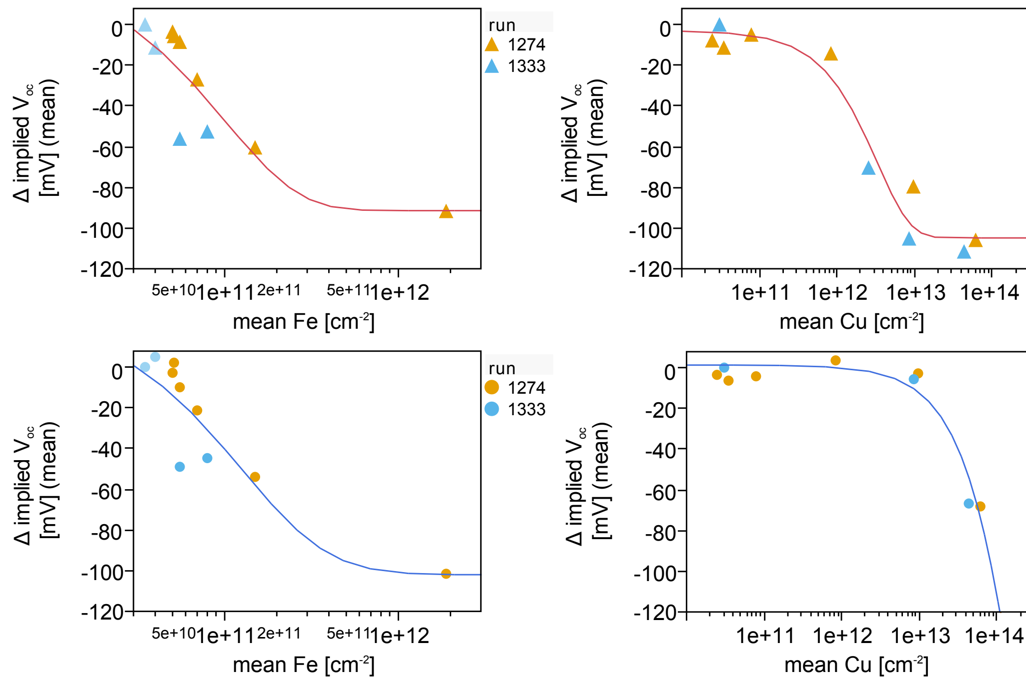

Fig. 4.10: Summary of two experiments, loss in *implied* V_{oc} due to Fe and Cu surface contamination; top row: thermal oxidation, bottom row: $MSiN_x$.

measurement setup. The second experiment confirms that the thermal oxidation is more sensitive to Cu surface contamination than the $MSiN_x$ deposition, with threshold values in the range of 1e+11 to 1e+12 cm^{-2} and 5e+12 to 1e+13 cm^{-2}, respectively.

Excursus I: Firing of solar cells

Firing of solar cells metallised by screen printing of metal pastes is required for formation of the contacts. For the standard p-type solar cell process this means: the silver front paste, containing glass frits, fires through the nitride to contact the emitter and the aluminum back side paste alloys with silicon to form a contact and the p+ doped region. In some cases firing is also required to activate the passivation layer. This is the case, for example, for the $MSiN_x$ and the boron silicate glass (BSG)/silicon nitride stack (cf. **Sec. 4.4.1**) as shown in **Fig. 4.11**. Various effects are attributed to this, such as in-diffusion of hydrogen for improved bulk and surface passivation [121, 239]. The results in **Fig. 4.11** were obtained by imitating typical fast firing profiles using a rapid thermal process (RTP) furnace, which allowed quick and easy single wafer processing. The peak temperature was varied across a range of 430 to 950°C. The graphs from **Fig. 4.11** show that both passivation stacks require temperatures above 700°C to reach full passivation capabilities. If the temperature is increased further, a degradation of passivation is observed. The stability range can be estimated to be around 100 K from the point of reaching maximum passivation quality. Three of the used profiles (790, 830 and 870°C) were recorded and plotted in **Fig. 4.12**. Not all of the investigated passivation stacks require firing (neither thermal oxide nor the PSG-SiN_x stack do), however, as firing is a crucial part in most solar cell process sequences, all of the following lifetime samples were fired.

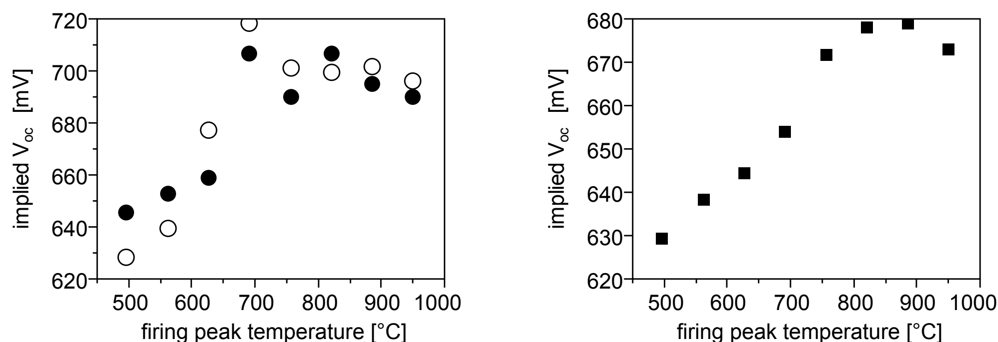

Fig. 4.11: Impact of the peak firing temperature of two passivation layers ($MSiN_x$, B-diffusion with BSG/SiN_x stack). Wafers were cut into 9 pieces.

A closer look was taken at the firing process, because, apart from activating the passivation layer, heating wafers to such high temperatures, even for a short time, may have serious consequences on metal contamination present in the investigated structure. Gettered metal species may be re-injected into the bulk, affecting especially the medium fast and fast diffusing metals, such as Fe and Cu. Considering the high cooling rates especially Fe may be easily trapped during this step in the bulk silicon, where it is expected to massively decrease the minority carrier lifetime. As Cu is still quite mobile at lower temperatures, as can be deduced from **Tab. 4.1**, it is expected to re-reach the gettering sinks. In order to estimate the extend

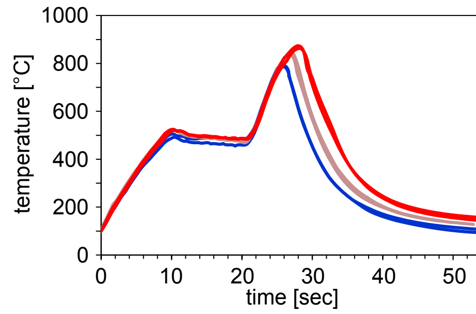

Fig. 4.12: Fast firing profiles as recorded during the RTP processing; two curves for each peak temperature are plotted (790, 830 and 870°C) indicating good reproducibility.

of this effect, a diffusion model, based on the solution of Fick's diffusion equation[1], with the constraint of a finite initial Fe amount of 5e+10 cm^{-2}, a finite maximal diffusion depth of $w = 80\mu$m (mittle of the wafer) and a solubility constraint (maximal solubility at the given temperature) was developed[2]. To simplify matters, only diffusion at the peak temperature was assumed for a very short amount of time (0.5 sec). The resulting profiles are plotted in **Fig. 4.13** and the resulting bulk concentration was calculated and displayed. Of course, these concentrations will be exceeded in reality as diffusion occurs before reaching the peak temperatures.

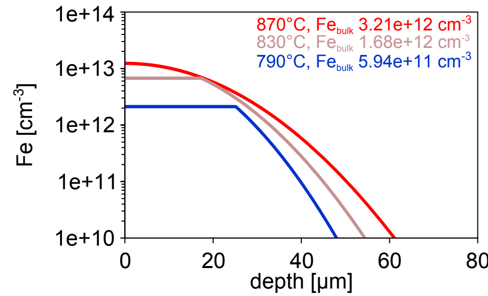

Fig. 4.13: Three diffusion profiles for Fe at 790, 830 and 870°C at a surface contamination of 5e+10 cm^{-3}. The resulting bulk concentrations were determined by integrating each diffusion profile across $\frac{W}{2}$ which was taken to be 80 μm.

From this relatively simple diffusion simulation, in which the thermal budget of the firing profile is disregarded, it can be learned, that the firing process can liberate large amounts of surface-near contamination into the bulk, strongly increasing bulk contamination levels. For this reason special attention was paid to the firing process in the following.

[1]The equation for diffusion from a finite source $c\,(x,t) = \frac{c_{SF}}{2\sqrt{\pi D t}} \cdot exp\left(-\frac{x^2}{4Dt}\right)$ (1) was modified by the "if" argument $(if\ \ c\,(x,t) > c_{max}\,(x,t)\ \ then\ \ c\,(x,t) = c_{max}\,(x,t))$ with $c_{max}\,(x,t) = S(T)$ in order to not exceed the solubility and adding the integral of (1) $c\,(x,t) = \int_w^\infty \frac{c_{SF}}{2\sqrt{\pi D t}} \cdot exp\left(-\frac{x^2}{4Dt}\right) dx$ divided by $\frac{w}{2}$, to compensate for diffusion that would exceed the middle of the wafer (in the considered case of symmetrical samples).

[2]The diffusion coefficient and the solubility were calculated using D_0=1.3e–3 cm^{2}s^{-1}, H_M=0.68 eV and S_S=8.2, H_S=2.94 eV [240] using the equations: $D(T) = D_0 \cdot exp\left(-\frac{H_M}{k_B T}\right)$ and $S(T) = 5 \cdot 10^{22} \cdot exp\left(\frac{S_s \cdot T - H_S}{k_B T}\right)$.

Mechanisms of lifetime degradation

In order to gain insight into the degrading mechanisms of Fe surface contamination on thermal oxidation/PECVD and all-PECVD passivation stacks, the *bulk* Fe concentration of differently contaminated wafers was measured using the QSS-μPCD technique as described in **Sec. 3.2.3**. 225 spots per wafer were measured after firing (with a peak of 830°C) and the median of the measurements was used for the analysis, eliminating exceptionally high values (outliers) or values below the limit of detection. Undefined measurements (when negative values were obtained due to $\frac{1}{C}$ changing its sign in low injection regions, compare **Fig. 3.10**) were excluded from the calculations of the median; this was in particular the case with high Fe values and accordingly low lifetimes. Therefore, with increasing Fe concentration the inaccuracy of the measurement strongly increases. **Fig. 4.14** (left hand side) depicts the relation between bulk and surface Fe concentrations indicating that small changes in Fe surface concentration have a huge impact on the magnitude of the measured bulk Fe (in terms of magnitude matching the prediction for bulk Fe after fast firing in **Fig. 4.13**). Similar Fe bulk concentrations were found for the two passivation stacks. The measurements of the reference groups of the two runs 1274 and 1333 reveal the reason for the difference in material quality. The material used in run 1333 shows minimum bulk concentration values of 1e+9 to 5e+9 cm^{-3}, whereas the material used in run 1274 shows minimum bulk Fe concentrations, almost one order of magnitude higher in the range of 2 to 3e+10 cm^{-3}.

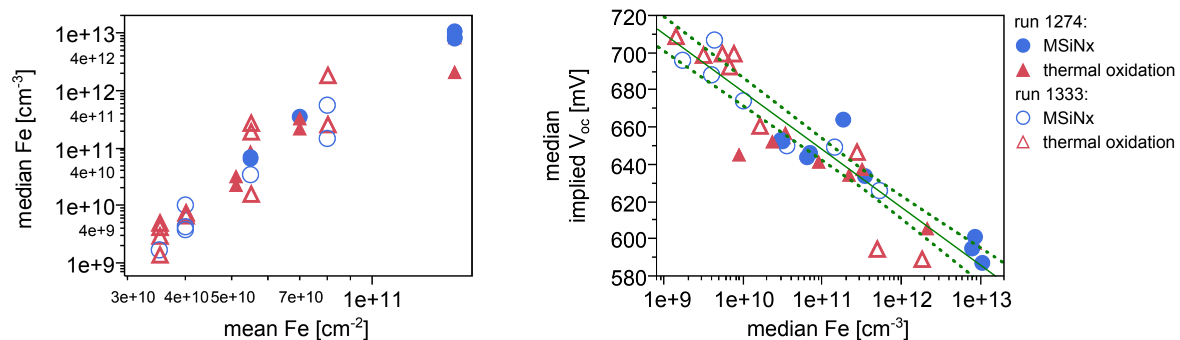

Fig. 4.14: Left hand side: Comparison of the Fe bulk contamination of the two different passivation stacks plotted against the measured surface contamination. Right hand side: Impact of the bulk Fe on the *implied* V_{oc}, the material from run 1274 shows much higher initial bulk Fe values and thus higher overall lifetime values.

Obviously, the *implied* V_{oc} of the samples is linked to the bulk Fe following the log-linear relationship as plotted in the right hand side of **Fig. 4.14**. The question, whether only the bulk Fe or, in addition to this, Fe remaining at the interface is responsible for this relation is discussed below. As introduced in Sec. **3.2.3**, the state of Fe plays a significant role on its influence on recombination behaviour. The bulk Fe concentration was obtained by the Fe measurement (before and after Fe−B separation) one 1 sun operation conditions. Under these measurement conditions, the Fe_i samples show higher lifetimes, as the 1 sun illumination produces excess carrier densities mostly above of 2e+14 cm^{-3}—the range in which C is negative (cf. **Fig. 3.10** in **Sec. 3.2.3**). The data collected by Istratov in [241]

show the opposite: the lifetime of the Fe_i case is significantly lower than in the Fe−B case. This apparent contradiction can be resolved when assuming that the published data originate from measurement at much lower injection levels. This is the reason, why solar cell efficiencies are expected to decrease after Fe_i activation.

The data presented so far indicate that, despite the large difference in process temperature between the thermal oxidation and the all-PECVD processes, similar amounts of Fe can penetrate the bulk. This would be a surprising fact unless the co-firing step at the end of the process sequence was to be taken into account. The temperature of 450°C during the plasma deposition would not nearly be hot enough for Fe to penetrate the bulk to such an extend. However, as shown in the **Fig. 4.11** in the excursus about firing of the solar cells, the $MSiN_x$ passivation layer requires high sintering temperatures (above 700°C), at which Fe is to be expected to produce significant bulk concentrations even during short treatment times.

In order to investigate the impact of the two contaminants on the passivation properties, D_{it} curves (cf. **Sec. 3.2.4**) were recorded of wafers with different surface contamination levels. One spot per wafer for each group was measured with the corona charge technique. Additionally, the effective minority carrier lifetime of that very spot was measured using QSS-PC. The results, including the *implied* V_{oc} values, are plotted in **Fig. 4.15**. Values for defect densities below 1e+10 cm^{-2} eV could not be resolved due to the minimal step width of the corona gun. The higher the D_{it} values, especially close to the middle of the bandgap which is located at around $V_{sb} = 0.3$ V, the more affected is the interface—an effect that was clearly visible for Cu contaminated wafers. Both passivation stacks strongly responded to increasing Cu contamination, with the thermal oxide/SiN_x being more sensitive than the all-PECVD SiN_x. The shapes of the curves nicely correspond to the *implied* V_{oc} values. The higher the surface coverage of Cu, the narrower the U-shape of the curve becomes. This indicates that Cu contamination is to a high degree found at the interface degrading its properties. The exact nature of the Cu states is not known. It was either dissolved in the silicon oxide or precipitated at the silicon/silicon oxide interface.

Zhong *et al.* [14] have used SIMS measurements in similar experiments showing that the interface between passivation layer and bulk (reaching up to 500 nm into the bulk in case of very high surface concentrations) serves as a gettering sink [14] which goes in line with the findings (cf. **Fig. 4.16**). The fact that the $MSiN_x$ is less affected by Cu contamination may be explained either by the higher amount of fixed charges and hence a higher field strength (7.6e+11 cm^{-2} measured for $MSiN_x$ versus 2.3e+11 cm^{-2} measured for the thermal oxide) or by a change in Cu configuration or distribution due to the high temperatures and long processing time of the thermal oxidation or a mixture of both.

In the case of the Fe contaminated wafers the effect of interface degradation was hardly visible for the thermally oxidised wafers. It can be deduced that Fe was distributed across the wafer bulk, hardly affecting the interface. In addition to this, Zhong *et al.* observed high Fe concentrations in the silicon oxide and a sharp decrease towards the bulk indicating that the interface does not play a role as gettering sink. The Fe in the silicon oxide was shown not to contribute to loss in effective lifetime, thus the amount of the Fe transferred into the bulk being responsible for the drop in lifetime [14]. The impact of bulk contamination for Fe, Cu

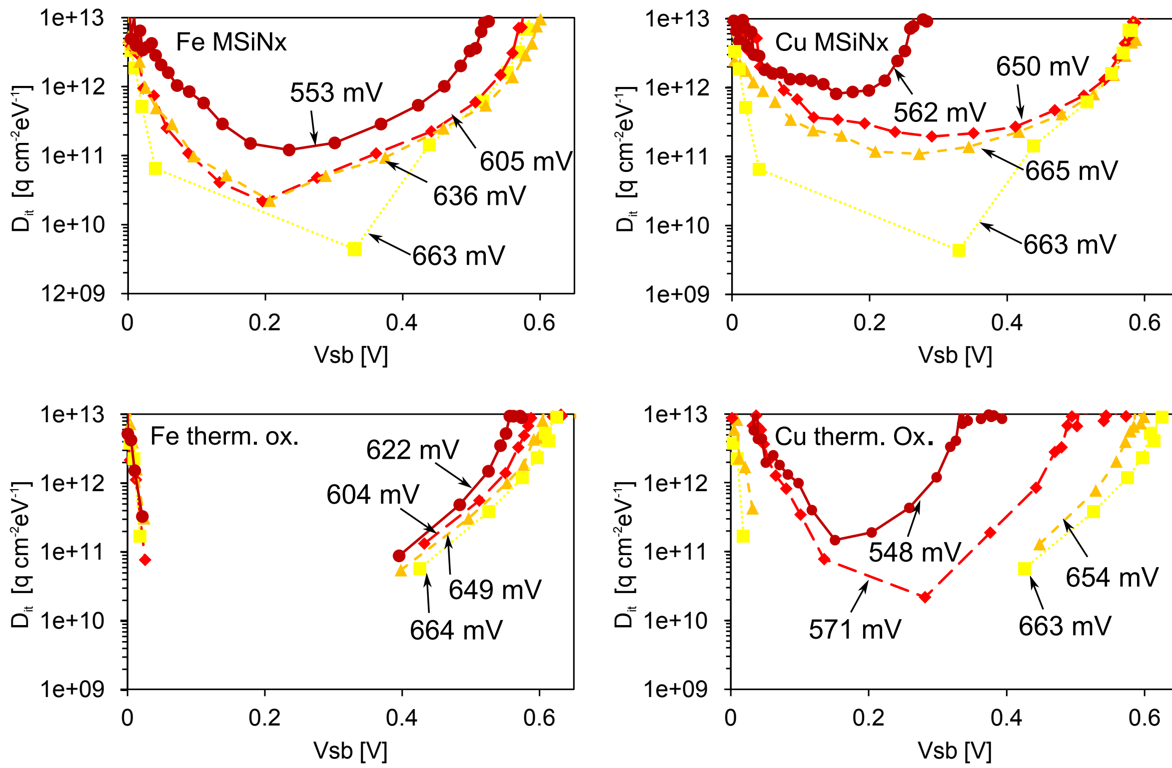

Fig. 4.15: Interface trap density D_{it} for passivated wafers with different contamination levels (squares: reference, triangles of the respective concentration groups: "25 ppb in H_2O", diamonds: "80 ppb in H_2O", dots: "420 ppb Fe" and "250 ppb Cu in H_2O", absolute concentrations numbers differed, due to the above mentioned factors). The respective surface concentrations values can be deduced from **Fig. 4.10** (run 1333). The *implied* V_{oc} for the same measuring spot is displayed in the graphs.

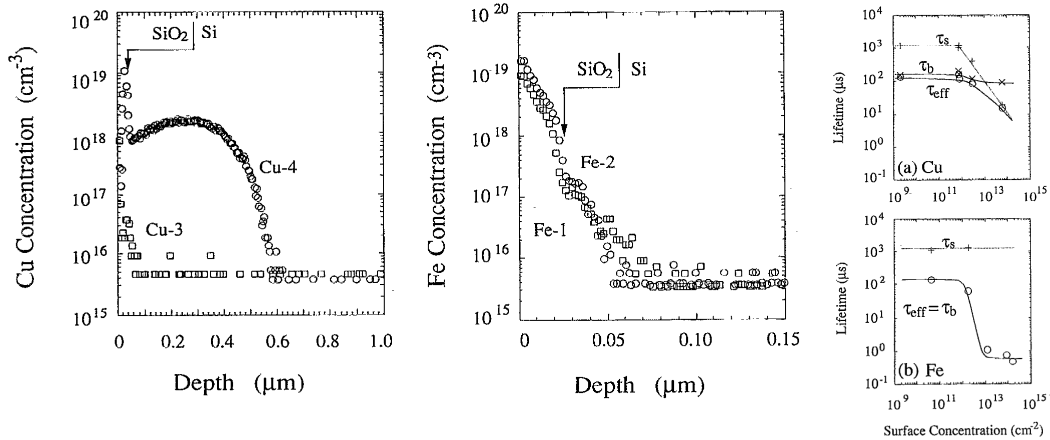

Fig. 4.16: SIMS measurements on contaminated and thermally oxidised wafers, measurements for different metal surface concentrations. Right hand side: Effective, bulk and surface lifetime as function of surface concentration. Taken from [14].

and Ni on carrier lifetime in p-type silicon was summarised by Istratov *et al.* in [151]. The results confirm the high sensitivity of the silicon bulk towards Fe.

In contrast to this, the interface of the $MSiN_x$ with the low temperature budget (except for the firing) showed signs of degradation for the highest Fe surface contamination, most likely caused by remaining Fe near the interface. As predicted by the diffusion simulation in

Fig. 4.13, not all of the Fe is injected into the bulk. Further thermal treatment—when the passivation step is used as FEOL passivation—is then expected to further distribute the Fe throughout the bulk. Depending on the gettering efficiency and the thermal budget that this steps introduces, further processing might also be able to remove it from the bulk.

The Cu from the interface, with an even higher mobility in silicon, may also be gettered in an n^+emitter region, if the solubility at the given temperatures further towards the end of the process sequence is higher at the front side of the PERC solar cell. A different behaviour of the effective lifetime would then have to be expected (as will be discussed in the next section). For the investigated processes no conclusive answer can be given if Cu, apart from affecting the interface quality and hence the surface recombination velocity, also decreases the bulk lifetime. Following Zhong *et al.* [14] (right hand side of **Fig. 4.16**), only a relatively small decrease in lifetime of the p-type samples was attributed to the bulk recombination. It can thus be assumed to be the case here as well.

Conclusion

The investigated passivation stacks (thermal oxide/silicon nitride and all-PECVD silicon nitride) both are highly sensitive towards metal contamination. A strong loss in lifetime was recorded for Fe concentrations well below 1e+11 cm^{-2}. The much higher temperature budget of the thermal oxidation has proven to play a minor role in the case of Fe contamination. This can be explained by the fast firing process that is required for good passivation quality but is also responsible for "driving-in" Fe surface contamination. As the measurements show that the Fe surface contamination is to a large extend transferred into the bulk, it may well be gettered if BEOL diffusions are applied.

In absolute numbers, Cu proved to be less harmful than Fe. Bulk Cu concentrations were found to be independent of the initial surface concentration by Zhong *et al.* [14]. The accumulation of the Cu near the surface was shown to have a severe impact on the interface trap density. The "low-temperature" passivation stack showed to be less sensitive with a strong drop in lifetime not seen until a contamination level of 1e+13 cm^{-2}, while the thermal oxidation showed substantial losses in the concentration range above 1e+12 cm^{-2}. The D_{it} measurements revealed a strong impact of Cu contamination on the interface in both cases. When combining these passivation layers with BEOL diffusions, Cu may also be gettered in the highly doped region at the front of the solar cell, due to its high mobility even at relatively low temperatures. Yet, due to this high mobility, Cu is expected always to reach or re-reach the most effective "gettering sink", the region in the solar cell with the highest solubility, which might well be the back-surface in the end.

4.3.2 Phosphorus diffusion

Doping via high temperature diffusion processes is well-known to create a solubility sink for metal contamination by creating a defect rich region near the surface [242]. Especially Cu is known to be effectively gettered by highly doped n^+ regions [241]. Similar finding exist for Fe [5].

The gettering efficiency of surface contamination of diffusion processes is studied by comparison of contaminated wafers that were thermally oxidised with the same oxide that was used in the previous section (at 885°C for 60 min, resulting in a thermal oxide of about 25 nm) with contaminated and then P-diffused wafers. Commonly, after P-diffusion, the phosphorus rich silicate glass layer (PSG) is removed in diluted HF before passivation. However, diffusion parameters can be tuned so that the PSG layer depletes almost completely of phosphorus. The main goal to achieve good passivation quality is to reduce the phosphorus dose to a minimum so that the PSG after processing resembles more to a thermal oxide than an amorphous phosphorus silicate glass.

The "oxide" after phosphorus diffusion was measured to be around 15 to 20 nm. Both kinds of samples were capped with the same silicon nitride layer, allowing for a direct comparison of the impact of Fe and Cu surface contamination on diffused and non-diffused samples. Again, at first, threshold values were determined for symmetrical n^+pn^+ lifetime samples (in comparison of p lifetime samples) and secondly, further investigations on the mechanisms of lifetime reduction were performed.

Impact of fast firing

First, in order to study the effect of the fast firing step on P-diffused samples, the *implied* V_{oc} of wafers was measured, after they had been intentionally contaminated and subjected to the P-diffusion (run 1333) process. The *implied* V_{oc} was measured before and after firing in the RTP furnace at different peak firing temperatures (731, 830 and 879°C).

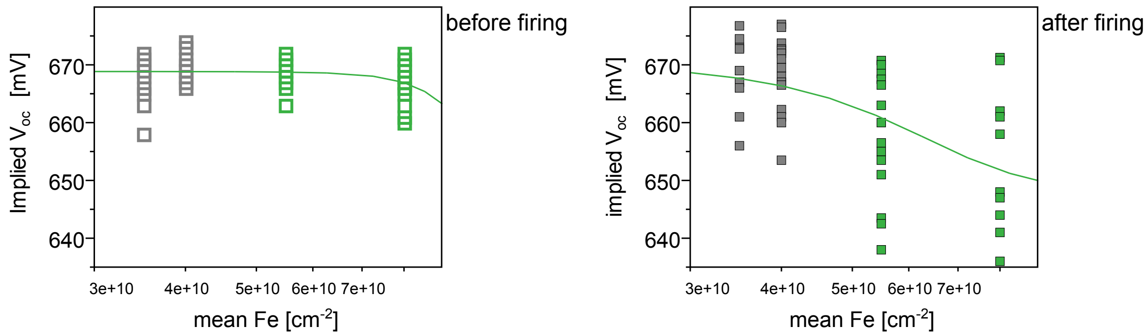

Fig. 4.17: Impact of fast firing on the *implied* V_{oc} vs. Fe surface contamination. Gray symbols signify values close to/below the limit of quantification.

No impact of fast firing on the Cu contaminated samples was detected. In case of Fe the critical surface concentration value before firing was measured to be 8e+10 cm^{-2} or above (see left hand side graph of **Fig. 4.17**). After firing the drop in *implied* V_{oc} became visible much earlier at concentrations in the range of 4 and 5e+10 cm^{-2} (right hand side of **Fig. 4.17**). As expected from the results shown before (cf. **Sec. 4.3.1**), this is due to the detrimental effect of Fe migrating from surface near regions (or the oxide-like PSG) to the bulk of the Si wafer during fast firing. After the fast firing step the bulk Fe concentration was significantly higher than before, as shown on the left hand side of **Fig. 4.18**. The right hand side graph from **Fig. 4.18** resolves the drop after firing in the graph of **Fig. 4.17** for the used peak firing

temperatures. A clear influence of Fe bulk concentration on the peak firing temperature could not be detected due to the small amount of samples (cf. left hand side graph of **Fig. 4.18**).

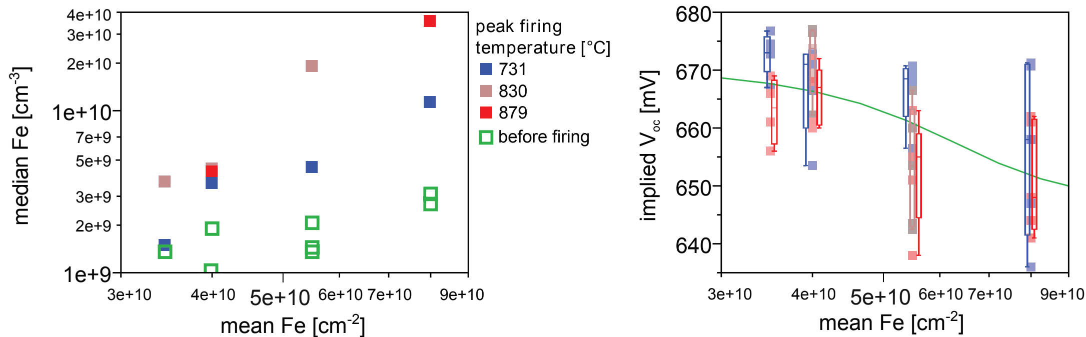

Fig. 4.18: Left-hand side graph: Bulk Fe before and after firing; right-hand side graph: Impact of peak firing temperature, same data as in 4.17 after firing, resolved for the peak firing temperature.

Results after firing

The results for run 1333 after fast firing are shown in **Fig. 4.19**. The increased recombination in the highly doped region of the P-diffused samples reduced the *implied* V_{oc} of the reference group. However, the vast differences between clean and contaminated samples, as observed for both elements if present before the thermal oxidation, were strongly reduced by the phosphorus diffusion. While Fe still produced a considerable impact (–20 mV) in the tested range (below 1e+11 cm^{-2}), Cu—even in concentrations above 1e+13 cm^{-2}—hardly affected the *implied* V_{oc}.

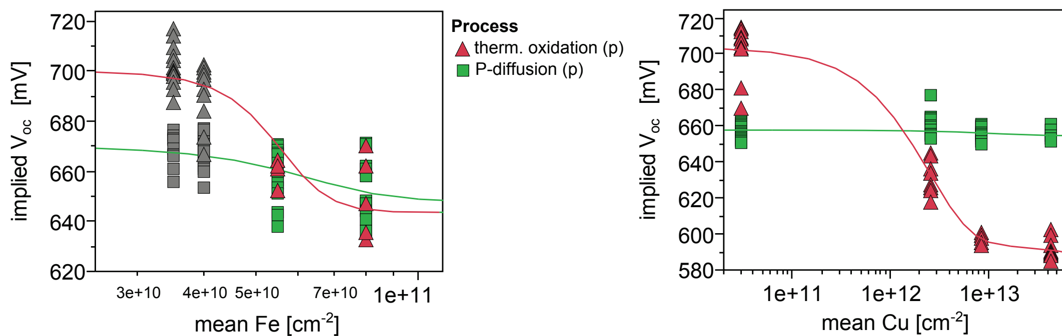

Fig. 4.19: Impact of surface contamination on p-diffusion compared to the thermal oxidation (run 1333). Results after fast firing.

Since the Fe surface contamination values measured in run 1333 were found to be just above the blank value (gray symbols), the data of run 1333 are combined with data from run 1288, the first experiment in which the impact of Fe and Cu on the P-diffusion was tested. However, there the low quality silicon wafers from run 1274 were used (cf. **Fig. 4.14**). The summary of the two experiments, based on the difference in *implied* V_{oc} from the control group, is found in **Fig. 4.20**. The combination of values from the two experiments for Fe proves to be consistent independently of the material quality. A decrease for several mV was measurable already for relatively small Fe quantities of around 3 to 5e+10 cm^{-2}, indicating

the devastating effect of Fe contamination in p-type solar cell processing.

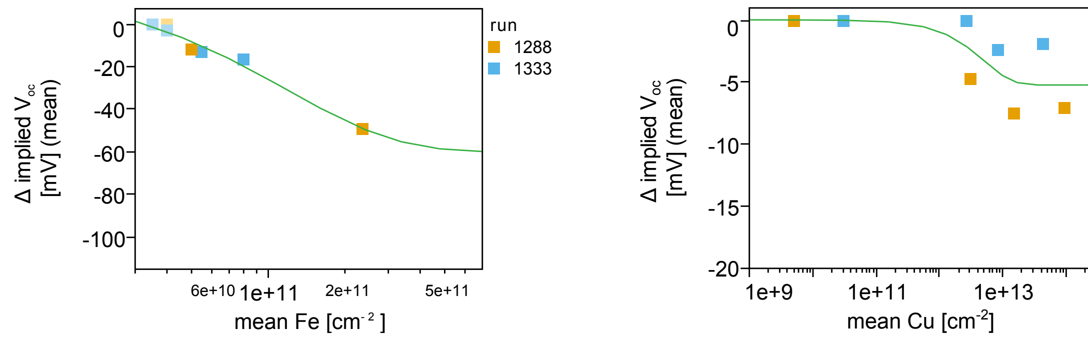

Fig. 4.20: *implied* V_{oc} plotted against various Fe and Cu surface contamination levels, in run 1288 the low quality silicon from run 1274 was used.

In contrast to Fe, the Cu contamination appears have a stronger effect on the lower quality material (run 1288). This can be explained by the fact that Cu tends to decorate already existing defects (in low quality material) with highly recombination active precipitates [6]. Even in case of the low quality material, however, the maximum loss in *implied* V_{oc} is only 5 mV even for surface contamination levels above 1e+14 cm^{-2}. A similar trend was observed by testing different cleaning procedures before the "old" P-diffusion (after the removal of PSG) and published in [20].

Mechanisms of lifetime degradation

A closer look at the recombination mechanisms is taken by studying the effect of Fe and Cu surface contamination on the saturation current J_{0E}. The J_{0E} was measured by QSS-μPCD using the Basore fit function (cf. **Sec. 3.2.2**), as it allowed the most reproducible measurement of J_{0E}. Using the effective lifetime values, which were measured at 1 sun illumination, and the J_{0E} values the impact of Fe and Cu on the bulk lifetime can be calculated. This was done using **Eq. 3.14** (**Eq. 3.15**) from **Sec. 3.1.2**. The results of the analysis can be found in **Fig. 4.21**. In the case of Fe, a strong drop in bulk lifetime from about 170 μs to below 50 μs was observed, while the J_{0E} only slightly increased from 56 to about 70 $fAcm^{-2}$, confirming the detrimental effect of Fe on bulk lifetime.

In contrast to Fe, Cu had hardly any effect on the bulk lifetime. The measured lifetime decreased only slightly with increasing Cu surface concentration before the diffusion. On the other hand a clearly increasing trend was found for the emitter saturation current J_{0E}, which almost doubles in value. Thus, similar to the passivation samples, a significant effect on the surface/emitter recombination for Cu was shown. The relative loss, however, turned out to be much lower, indicating an efficient Cu gettering sink in the emitter region with a high potential of inactivating the Cu contamination.

Best fits for J_{0E} and τ_{bulk} were obtained by using linear-log fits as performed in **Fig. 4.21** (the fitting parameters are summarised in **Tab. 4.2**). The thus obtained relationships were used to simulate the impact of surface contamination before the P-diffusion on solar cell parameters in **Sec. 4.5**.

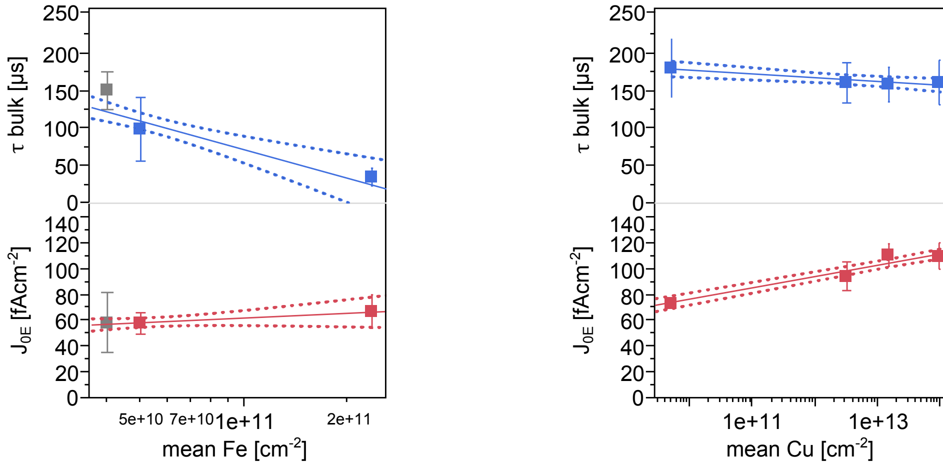

Fig. 4.21: Saturation current and estimated bulk lifetime (run 1288) plotted against the surface contamination before diffusion.

Tab. 4.2: Formulas of fits from **Fig. 4.21**.

	Fe	Cu
P-diffusion	Tau bulk [μs] = 1450 − 54.13 ∗ ln(mean Fe [cm^{-2}])	Tau bulk [μs] = 222.8 − 1.902 ∗ ln(mean Cu [cm^{-2}]
	J_{0E} [fAcm^{-2}] = −71.27 + 5.268 ∗ ln(mean Fe [cm^{-2}])	J_{0E} [fAcm^{-2}] = −10.25 + 3.787 ∗ ln(mean Cu [cm^{-2}])

Conclusion

It was shown that the ISC Konstanz' standard phosphorus diffusion is less sensitive towards Fe and Cu contamination than the thermal oxidation or MSiN$_x$ surface passivation steps. Especially remarkable is the threshold for Cu contamination: depending on material quality, only a small loss in *implied* V_{oc} of approximately 5 mV was recorded for concentrations above 2e+12 cm^{-2}. Material of higher quality proved to appear less affected by Cu contamination. Cu mostly contributes to increasing J_{0E} values.

Fe surface contamination is gettered effectively before firing. The fast firing process, however, releases Fe from surface near gettering sinks and injects it into the bulk. In consequence, Fe surface concentrations below 1e+11 cm^{-2} showed to have a considerable negative impact on the lifetime, mostly driven by a strong decrease in bulk lifetime: the *implied* V_{oc} drops by approximately 20 mV. Removing the phosphorus silicate glass is expected to lower the sensitivity towards Fe, as a segregation towards the PSG during P-diffusion is expected. A small study dedicated to shed light on the mobility of surface contamination during P-diffusion is presented in the second part of the following excursus.

Excursus II: Variation of diffusion parameters and segregation of metals at the PSG/n$^+$ interface

Variation of diffusion parameters

The gettering efficiency of diffusion processes is generally assumed to depend mostly on two parameters: diffusion time and temperature [147, 150, 211, 242]. These are directly related to the time the wafers are exposed to the plateau temperature and the cool-down rates. The higher the plateau temperatures and the longer the exposure to such high temperatures, the more likely impurities will penetrate the bulk from the surface. The faster the cool-down, the more likely impurities will be trapped within the bulk and will not make it to the gettering sinks, which are mostly expected to be found at the surface. In order to study the impact of diffusion parameters on surface contamination present before the diffusion, parameters were varied according to **Tab. 4.3** and applied to wafers with and without cleaning. The wafers were kept in a $POCl_3$ stream for the *deposition time*. Afterwards the $POCl_3$ flow was switched off for the *drive-in time*. The parameters that were varied in run 700 are summarised in **Tab. 4.3**, including the resulting *sheet-resistance* as measured by four-point-probe. As the cool down times were kept similar (which was possible as the cool down was achieved by removing the wafers from the diffusion furnace), the cool down rate directly correlated with the *plateau temperature*: the higher the peak temperature, the higher the cool-down rate.

Tab. 4.3: Variation of diffusion conditions from run 700.

Plateau-temperature [°C]	deposition time [min]	drive-in time [min]	sheet resistance [Ω/sq]	sheet resistance after etch back [Ω/sq]
802	15	10	120.1 ± 4.4	129.5 ± 4.1
812	15	10	78.3 ± 0.9	83.2 ± 1.5
845	20	5	56.1 ± 0.7	58.4 ± 0.8
860	20	5	43.0 ± 0.8	45.0 ± 0.4

Four different diffusions were applied to cleaned and non-cleaned wafers (0.55 Ωcm, p-type material) after alkaline texturing with KOH/IPA. It was used, as no interference with texturing additives with metal surface contamination was thus to be expected. The surface contamination of the cleaned and the non-cleaned wafers[1] was measured and is shown in **Fig. 4.22**. After the different diffusions, the PSG was removed in diluted HF. One half of the wafers was then HCl+HF cleaned, the other half was cleaned using SPM+HF. This has, due to the high oxidising potential of the Caro's acid, an etch back effect on the emitter, removing some of the "dead" layer of high defect density and potentially gettered metals. As proof for the etch-back effect the *sheet resistance after etch back* in SPM+HF was measured and is also displayed in **Tab. 4.3**. In accordance with previous lifetime samples, wafers were then passivated on both sides using SiN_x and fired in the fast firing furnace.

[1] "No cleaning" refers to wafers that were rinsed for about 15 minutes to remove most of the water soluble elements with a potential detrimental impact such as potassium and sodium.

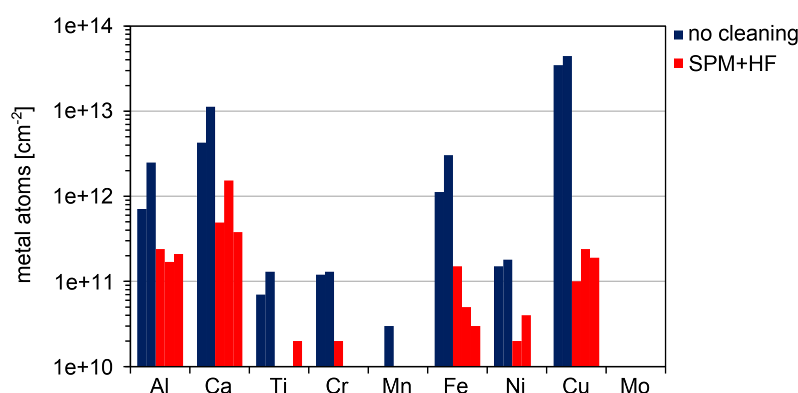

Fig. 4.22: Surface contamination of cleaned and non-cleaned wafers before the different P-diffusions. Lifetime samples were produced from both.

The particularly high Cu concentrations of the non-cleaned samples were found in the range of 3.5 to 4.5e+13 cm^{-2} (**Fig. 4.22**) and are expected to have a small, but detectable, effect on the measured lifetime. Especially, when assuming that most of the Cu is gettered in the surface near region—as expected from the so far presented results—one could expect that the effect of the post-PSG removal cleaning is stronger for the contaminated samples. The other metals were found in relatively low concentrations (Ti, Cr and Ni in the range of 7e+10 to 2e+11 cm^{-2}) in the non-cleaned case. The concentration of Fe without cleaning was in a range above 1e+12 cm^{-2} in which a vast drop in efficiency would be expected from the data presented so far. However, in contrast to the so far considered samples, in this experiment the PSG was removed before SiN_x deposition. As the PSG is known to act as gettering sink, the removal of it is expected change the impact of surface contamination present before diffusion on the lifetime of samples. In consequence a comparison of the data may not hold valid. A

When analyzing the data, initially mainly a strong dependency of the *implied* V_{oc} on the sheet resistance—which varies according to the chosen diffusion parameters—was found. Also, cleaning did have a small, but measurable, effect. A stronger effect was attributed to etch back by the SPM+HF clean. To get a clearer picture, the measured *implied* V_{oc} data were fitted using the multivariate regression function of the statistical software JMP10. As main input variables were chosen:

- cleaning: “no cleaning” vs. “SPM+HF”
- cleaning after PSG etching: “HCl+HF” vs. “SPM+HF”
- measured sheet resistance

The variables were crossed, using the response surface makro (A*A, B*B, C*C, A*B, A*C, B*C) and checked as model effects. The parameter estimates obtained for the crossed variables, however, did not significantly differ from zero so that no quadratic effect and no interrelation between the parameters was detected. Hence, the obtained statistical model (as summarised in **Fig. 4.23**) only contains the steps of the respective cleaning methods and the sheet resistance as linear factor. The top graph shows observed *implied* V_{oc} values plotted against the predicted values and the thus obtained fit parameters (the likelihood P,

the coefficient of determination r^2 and the root-mean-square error RMSE). In the table below the estimates (the impact) of the model, parameters are provided with their respective the estimate, error, t-value and likelihood.

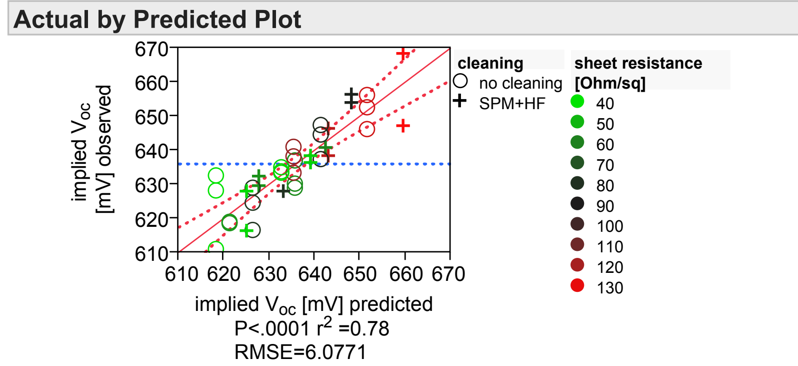

Estimates of parameter

Term	Estimate	Std Error	t Ratio	likelyhood>|t|
Intercept	618.80	2.67	231.51	<.0001*
cleaning[no cleaning]	-3.07	1.03	-2.97	0.0055*
Cleaning after PSG etching[HCl+HF]	-6.98	1.00	-6.96	<.0001*
sheet resistance [Ohm/sq]	0.23	0.03	7.22	<.0001*

Prediction Expression

618,802774369799

+ Match(cleaning) ["no cleaning" ⇒ -3.0660035868699 ; "SPM+HF" ⇒ 3.06600358686987 ; else ⇒ .]

+ Match(Cleaning after PSG etching) ["HCl+HF" ⇒ -6.9822677336 ; "SPM+HF" ⇒ 6.98226773360002 ; else ⇒ .]

+ 0.22795199222906 * sheet resistance [Ohm/sq]

Fig. 4.23: Fit of the obtained *implied* V_{oc} values. No interrelations between the factors were detected. The prediction equation for the model as fitted by JMP10 is shown.

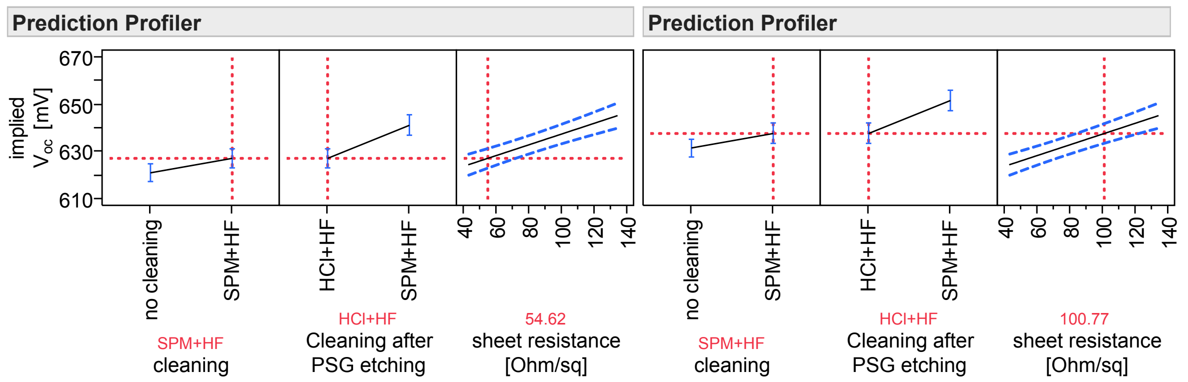

Fig. 4.24: Prediction profiler for the model presented in **Fig. 4.23** for two different sheet resistances. As predicted by the model, the impact of the two cleaning steps in the process sequence is identical in terms of differences in *implied* V_{oc} independently of the sheet resistance.

In **Fig. 4.24** prediction diagrams of the model are plotted. They allow the JMP10 user

to experience the impact of the parameters on the command variable by moving the vertical dashed red lines.

According to the model, the loss in *implied* V_{oc} due to the surface contamination is identical for all the different diffusion processes. The same applies for the gain by the etch-back. Apparently, the non-cleaned samples are limited by the surface contamination, independently of the diffusion strength and employed temperatures, which indicates a very similar gettering mechanism. With those offsets the *implied* V_{oc} depends linearly on the sheet resistance.

Analysis of PSG-layers

The relatively small loss of the non-cleaned samples in *implied* V_{oc} (of 3 mV) despite the high Fe concentration can most likely be explained by the removal of the PSG before fast firing. PSG, due to its oxide-like character, has been reported to serve as gettering sink for Fe [243]. In order to investigate this phenomenon further, a small study was performed making use of the capability of the sandwich etch method (cf. **Sec. 4.1.1**) to extract surface contamination from many different surfaces. As the gettering efficiency and the impact of the surface contamination appear similar for the different diffusions (see above), the sheet resistance was disregarded for this analysis (which was necessary as not enough samples of the same diffusion were kept for further analysis).

First, the gettering in PSG was investigated by dissolving the PSG in diluted HF (5%) and subsequently analyzing the samples by ICP-MS. Second, the surface-near region below the PSG was extracted and analysed using the same FPM (flouric acid peroxide mixture) as was used for the extraction of surface contamination (5% HF in 30% H_2O_2) throughout this work. The reaction time was lowered to one minute (instead of ten) as the reaction, especially of the contaminated samples, was quite vigorous. The sampling plan is sketched in **Fig. 4.25**. It includes measurements of the emitter surface after regular PSG removal to detect potential incomplete removal of PSG contamination by the analysis extraction. The cleaned sample was used as reference.

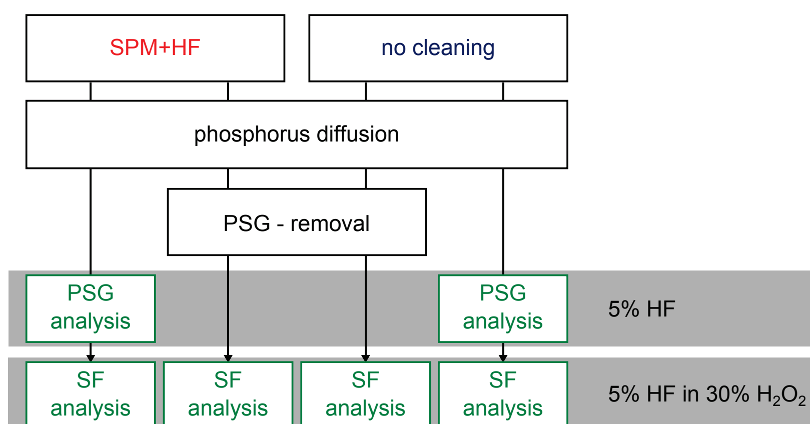

Fig. 4.25: Experiment plan to study the segregation at the PSG-emitter-interface. The concentration of the sampling solutions used for the PSG and the surface below are displayed.

The results of the extraction and analysis are found in **Tab. 4.4**. The etch depth of the

Tab. 4.4: Results of PSG and surface extraction. Since the thickness of the layers that have been etched can only be estimated (from the Si concentration in the sampling solution), "projected" concentration values (surface concentrations in atoms/cm^{-2}) are used. The estimated etching depths can still be used to relatively compare the obtained values.

	sheet resistance [Ω/sq]	pre-diffusion cleaning	[1e+10 cm^{-2}]									etch depth
			Al	Ca	Ti	Cr	Mn	Fe	Ni	Cu	Mo	[nm]
before diffusion		SPM+HF	17.5	153	1.5	0.3	0.3	5.5	4	24	<DL	1.0
			21.1	38.4	2.3	<DL	<DL	3.5	0.6	18.8	<DL	1.2
PSG analysis	45 & 43		140	1540	12.2	10.9	1.9	82.3	17.9	<DL	0.8	
→ SF analysis			10.6	51.4	<DL	<DL	0.1	7.0	0.9	<DL	<DL	2.9
SF analysis after PSG etch	43 & 43		46.2	371	3.80	<DL	0.6	22.4	2.1	0.3	<DL	5.5
before diffusion		no cleaning	71.4	426	6.9	11.7	1.4	112	15.2	3470	0.3	1.7
			249	1126	13.5	13	2.9	305	18.3	4430	<DL	1.9
PSG analysis	56 & 120		498	3930	40.9	12.1	6,8	740	6.3	<DL	1.1	
→ SF analysis			77.1	440	2.9	2.2	1.2	204	5.2	348	0.4	4.8
SF analysis after PSG etch	43 & 43		77.1	1450	6.7	<DL	0.6	24.9	11.1	1290	<DL	15

surface extraction was calculated from the dissolved silicon in the sampling matrix, which was also determined by the ICP-MS. Due to the vigorous reaction, the etch depth of the surface analysis on the contaminated surfaces varied between 4.8 and 15 nm and between 2.9 and 5.5 nm in the case of the cleaned samples. The highly doped n^+ region etches much faster than comparable p/n-surfaces, where only between 0.6 and 1.2 nm are reached in ten minutes with the same solution. The reason for this is the high density of lattice defects caused by very high dopant concentrations, partly in interstitial lattice positions. This causes a large amount of stress on the crystal structure promoting the etching reaction. The difference between the contaminated and the clean surfaces can be attributed to the catalytic effect of transition metals (especially Cu) [244]. Since the phosphorus silicate glass composition is not known in detail, this layer thickness is not estimated. PSG and surface concentration are assumed to be "true" surface concentrations disregarding the layer thickness for reasons of comparability.

The results of the PSG extraction indicate that Fe indeed is almost completely gettered in the PSG layer. When looking at the cleaned wafers, it appears that even some bulk Fe was gettered in the PSG as the Fe value in PSG is higher than the initial surface contamination. This segregation was expected according to the literature [243]. The same applies to most of the elements, namely Al, Ti, Cr and Mo and also the lighter elements Al and Ca. The latter was also found in the layers below the PSG of the non-cleaned wafers.

In the case of the non-cleaned wafers, much more Fe was detected in the PSG than before, which is unlikely to originate from the bulk as the value was much higher than in the SPM+HF cleaned case. This thus may be considered as outlier, which, however, could not be confirmed due to the small sample size.

Fe detected on the surface after PSG etch is likely to originate from the etching bath, as

for both types of wafers the concentration was almost identical. The Fe still detected on the surface after PSG extraction might have not been dissolved in the first place and would have to be added to the initial Fe concentration.

Cu, on the other hand, is not detected in the PSG. It most likely had not been dissolved in the first place due to the low collection efficiency of Cu in HF [204]. In the case of the non-cleaned samples an etch depth of about 5 nm dissolved almost exactly one third of the amount that was dissolved in the case of 15 nm. This strongly indicates Cu contamination to be accumulating in the defect rich surface near region.

Having a closer look at the Ni contamination, it can be concluded that Ni behaved somewhat in between Cu and Fe. Some of it was measured in the PSG and some remained in surface-near regions.

In order to shed more light on the observed phenomena and to verify the conclusions made from the first experiment, a second experiment was designed (run 824). The KOH/IPA textured wafers were split into three groups according to their pre-diffusion treatment: SPM+HF, HCl+HF and no cleaning. The surface contamination was measured before the diffusion and is displayed in **Tab. 4.5**. Afterwards, the PSG of all three groups was dissolved in 5% HF and the metal contamination analysed by ICP-MS. For the second step, in order to avoid uncontrolled etching as observed in the first experiment, two different concentrations of HF in H_2O_2 were used. A solutions of 0.06% HF in H_2O_2 was made up for very shallow etching and a solution of 10% HF in H_2O_2 for deeper etching. The two solutions produced quite reproducibly etching depths of ≈0.5 and ≈2 nm (as determined from the silicon measured in sampling solution by ICP-MS) in the ten minutes of etching time. After PSG extraction, the wafers were rinsed with ultrapure water. At first the low concentrated HF was used. For the high HF concentrations a second set of sister wafers was treated similarly. The small concentration was not used in the case of the HF/HCl-cleaned wafers. A scheme of the experiment is plotted in **Fig. 4.26**.

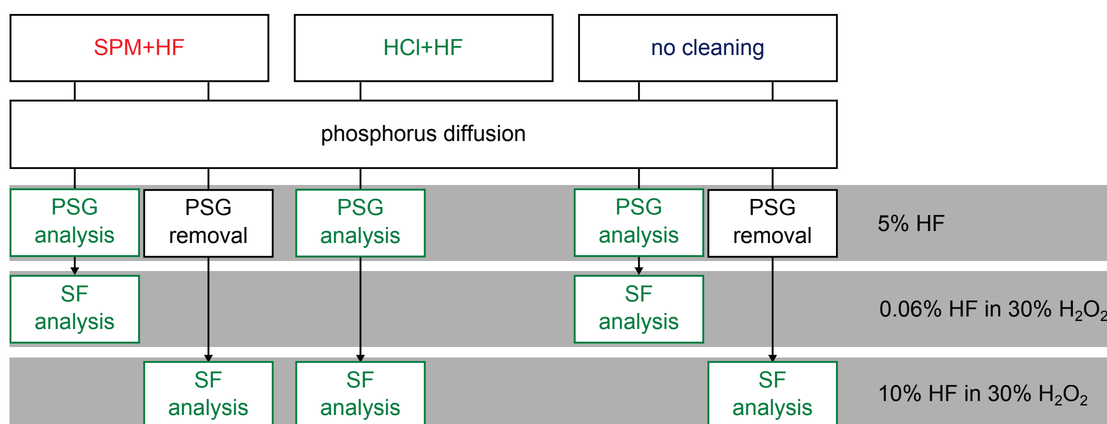

Fig. 4.26: Scheme of the second experiment on the distribution of metal contamination during P-diffusion. Two different HF/H_2O_2 mixtures were used to obtain different etching depths.

From the data can be deduced that Fe is dissolved in the PSG, but is also found in the surface near regions. Elevated concentrations, roughly scaling with etching depth, are found for the highly contaminated non-cleaned sample, but also in the case of the SPM+HF cleaned

Tab. 4.5: Second experiment for the analysis of PSG and the layers below (run 824). Again "projected" surface concentrations were used instead of volume concentrations.

	pre-diffusion cleaning	Ti	Cr	Fe	Ni	Cu	etching depth [nm]
		[1e+10 cm^{-2}]					
before diffusion	SPM+HF	<DL	4	20	3	4	
		<DL	<DL	<DL	1	3	
PSG analysis		8	<DL	6	1	2	
→SF analysis		1	<DL	3	5	1	0.6
SF analysis		<DL	1	75	7	3	2.0
before diffusion	HCl+HF	6	2	2	6	347	
		2	3	16	7	428	
PSG analysis		10	4	13	1	1	
→SF analysis		2	2	3	7	18	1.8
before diffusion	no cleaning	16	7	338	20	22823	
		17	10	565	50	22384	
PSG analysis		20	6	75	2	2	
→SF analysis		3	1	22	10	1603	0.5
SF analysis		9	4	60	10	2057	1.9

group. Only very low Cu concentrations were detected in the PSG (as expected from the low solubility). In the cases of non-cleaned and the HCl+HF cleaned samples Cu was detected and quantified in the surface-near regions. In both cases, the amounts that were measured in up to 2 nm depths did not come close to the amount that was present before diffusion indicating that it is distributed to deeper lying regions. Furthermore, from experience, cross-contamination in the high temperature diffusion processes is an issue (clean samples placed behind contaminated samples in the direction of the gas flow suffer from decreased lifetime), so that it is not quite clear, how much of the initial contamination was removed by the gas phase. However, from the first experiment, it can be well assumed that large amounts of the initial Fe and Cu are buried deeper below the surface.

Again, it was shown that Ti from the surface (and from the wafer) is nearly quantitatively gettered in the PSG. In the non-cleaned case Ti is still found in deeper lying areas. Cr concentrations are low, but also indicate a trend of segregation towards the PSG. Ni, in all cases, remains below the PSG right at the interface.

Summarizing, it can be stated that most of the measured elements, if present as surface contamination before diffusion, segregate towards the PSG layer during the diffusion process and will be removed if the PSG is removed. Accordingly, very clean surfaces are required when the PSG is not removed but has to serve as oxide-like passivation layer. However, if concentrations on the surface are large, especially Fe is also found in deeper lying areas. The only element that does not appear to accumulate in the PSG but in the surface near region is Cu. However, it seems to be mostly inactivated there, as the etch back of the emitter after diffusion in highly oxidising SPM solution does not improve the solar cells made from highly contaminated wafers more than the ones made from clean wafers, as shown with the model in **Fig. 4.23**.

4.4 Processing of n-type substrates

The following section deals with the impact of Fe and Cu surface contamination on process steps required for the fabrication of n-type solar cells. First the impact of Fe and Cu on the *implied* V_{oc} of the test structures for boron emitter and phosphorous BSF diffusion as well as thermal oxide passivation of n-type samples is studied. Subsequently, the phenomenon of temporary gettering, as observed during the experiments, is described. Last, the mechanisms of lifetime degradation as caused by Fe and Cu surface contamination are discussed.

4.4.1 Phosphorus and boron diffusion

In contrast to p-type processes, thermal oxidation is not used in ISC Konstanz' current standard n-type process sequences (at least not to passivate n-doped substrates). The symmetrical thermal oxide/nitride stack samples are, however, a useful means to determine the impact of the impurities on material quality. Most of ISC Konstanz' n-type solar cell structures feature all-diffused surfaces. The p^+ emitter is formed by boron diffusion and the BSF n^+ by phosphorus diffusion. Both silicate glass layers are used for passivation purposes (similar as in the p-type case). The schemes of the test structures are depicted in **Fig. 4.27**.

The BSF structures were obtained by depositing a phosphorus seed layer in quartz tube diffusion furnace at relatively low temperatures for a comparatively short time, which was then capped by SiNx, serving as diffusion barrier and driven-in by the B-diffusion step. The symmetry of the samples was achieved by both-sided SiN_x deposition. As the thermal budget of the second B-diffusion is much larger than the deposition of the seed layer, one can assume that both diffusions experience a similar thermal budget. Most importantly, the last cooling ramp from almost 1000°C is the same for both processes, as gettering is thought to be closely related to the speed of cooling [150]. The cooling speed is often considered decisive for the the gettering efficiencies, as it determines, which parts of the wafers can be reached by the differently fast diffusing elements, as the solubility and diffusivity decreases with decreasing temperature.

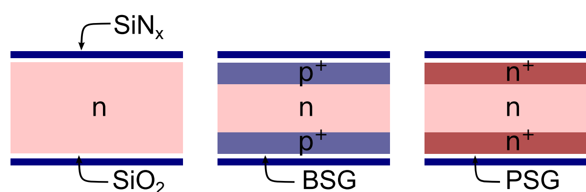

Fig. 4.27: Test structures for n-type processes: Thermal oxidation on the left, boron emitter passivated by BSG in the middle, phosphorus "back-surface-field" passivated by PSG on the right. All of them were capped by SiN_x.

Experimental results

In run 1333, in addition to the already discussed p-type samples, also n-type samples were prepared. In order to avoid cross contamination, Fe and Cu contaminated wafers were oxidised and diffused separately. 8 Ωcm n-type wafers were used. The impact of Fe and Cu

contamination is plotted for the different diffusions and compared to the thermal oxidation in **Fig. 4.28**.

As expected from the capture cross section of interstitial Fe for minority carriers in n-type material [142], a much smaller impact of Fe surface contamination on oxidised samples was measured compared to the same process performed on p-type material (cf. **Sec. 4.3.1**) in low to median injection levels. Cu, however, is responsible for a similar drop in *implied* V_{oc} in the n-type as in the p-type case. If this is due to increased bulk or also due to interface degradation, is closer investigated in the section about the mechanisms of lifetime degradation.

The different levels of *implied* V_{oc} of the two diffusions can be attributed to the fact that the P-diffusion is heavier (i.e. has a lower sheet resistance and higher surface concentration as required for the contact formation) than the B-diffusion. Both diffusion processes proved to be very effective in deactivating Fe and Cu surface concentration. In fact, only very small differences between the different surface contamination levels can be deduced from **Fig. 4.28**. However, the scaling of the graph to extract these is not ideal.

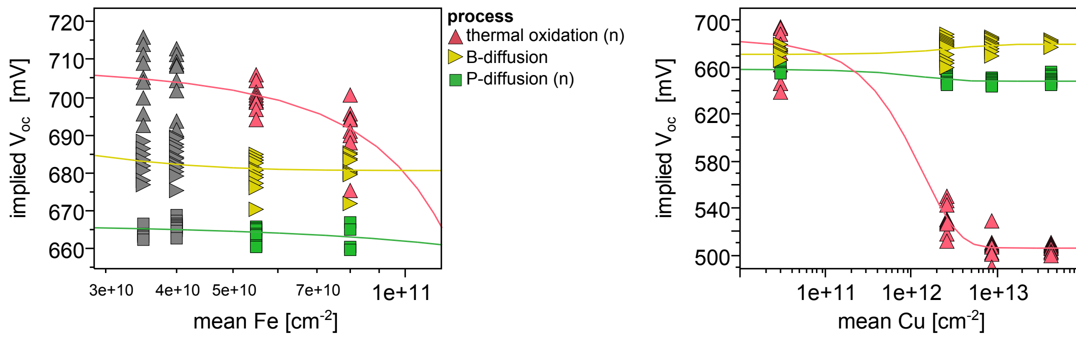

Fig. 4.28: *Implied* V_{oc} against Fe and Cu surface contamination for thermal oxidation, P-and B-diffusion. Note the different scaling of the graphs. Gray symbols refer to surface contamination values that were below or close to the limit of quantification.

A clearer picture was obtained, when correlating the *implied* V_{oc} differences between reference and increasing Fe and Cu concentrations of several experiments. The thus obtained losses in *implied* V_{oc} are plotted in **Fig. 4.29**. The data summarise measurements directly after firing of three experiments (run 1214, 1288 and 1333). The data from run 1214 were obtained without intentional contamination but by insufficient cleaning. The agitation (by a circulation pump) of an oxidising cleaning bath was unintentionally left out so that insufficient mixing of the reagents occurred. In consequence, the high initial Cu contamination of the wafer was hardly removed (it was measured to be in the range of 1e+12 to 1e+13 cm^{-2}, unfortunately only Cu and Fe surface contamination was measured in this experiment). As the *implied* V_{oc} recorded in this experiment fits nicely the data that were obtained by intentional contamination, it can be assumed that the other elements had been mostly removed by the non-agitated cleaning bath and/or the subsequent 2% HF/HCl step involved in the cleaning sequence.

The data from the three runs reveal two clear trends. First, the P-diffusion is far more sensitive towards surface contamination than the B-diffusion. While in the case of the B-diffusion a loss in *implied* V_{oc} of about 5 mV was recorded for the highest tested Fe contamination level,

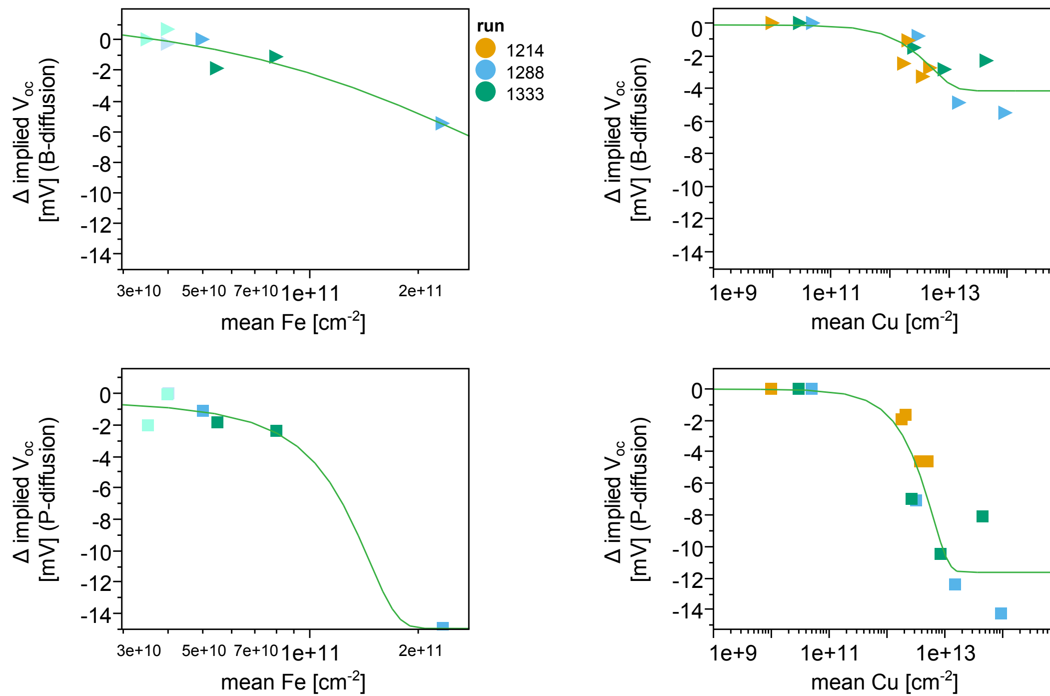

Fig. 4.29: Comparison of sensitivity of B-and P-diffusion to Fe and Cu surface contamination. Summary of several experiments. The lightly coloured values refer to concentration values below or close to the limit of quantification.

the P-diffusion already lost about 15 mV. A similar behaviour was observed for the highest investigated Cu contamination levels. Second, in terms of absolute numbers Fe is a much more efficient "lifetime killer" than Cu—similar as observed for the investigated p-type process steps. A measurable decrease in lifetime was found for concentrations just below 1e+11 cm^{-2}, while critical Cu concentrations were found to be about one order of magnitude higher in the range just below 1e+12 cm^{-2}. A fact that was quite surprising, as Cu is known to be much more recombination active in the n-type bulk than in the p-type bulk [245].

Temporary gettering

An interesting observation was made, when the lifetime samples from run 1333 were remeasured two months later. No change in lifetime was measured in the case of Fe contaminated samples, both for P- and B-diffusion. The same was true fore Cu contaminated B-diffused samples. The Cu contaminated P-diffused samples, however, showed a much stronger impact of the Cu surface contamination on the *implied* V_{oc} as when measured right after co-firing. As plotted in the two graphs of **Fig. 4.30** the Cu contaminated samples showed a significantly stronger decrease in *implied* V_{oc} after the storage period in a closed box, indicating that deactivated, gettered Cu had been released and become recombination active.

Similar, as performed by Macdonald *et al.* in [15] (and as above), J_0 and τ_{bulk} were estimated and plotted for the Cu contaminated and P-diffused samples from run 1333 in **Fig. 4.31**. As discussed before, Cu has the tendency to precipitate in surface near regions, where it would be expected to mainly increase the J_0 as observed in the first measurement. The initially small impact on bulk lifetime increased strongly with storage time. It appears

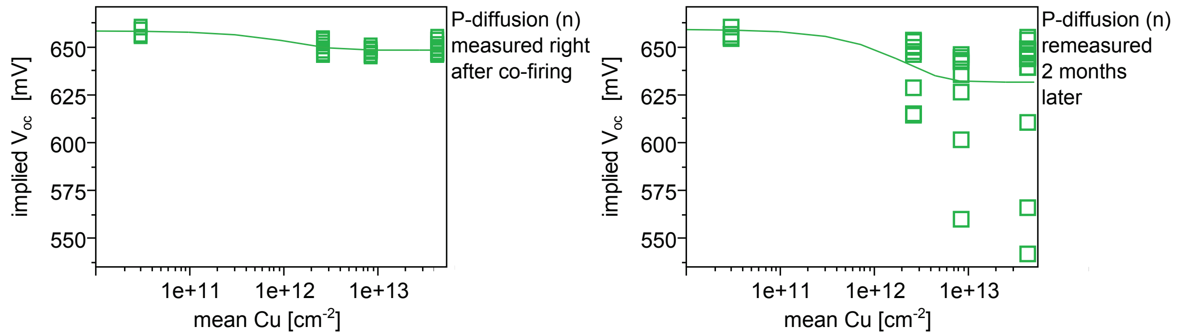

Fig. 4.30: *Implied* V_{oc} plotted against Cu surface concentration on P-diffused BSF test structures before and after storage in a box at room temperature (from run 1333).

that Cu had been liberated from the highly doped gettering sinks and penetrated into the bulk where it strongly decreased the lifetime as estimated by QSS-PC. As not all of the measuring points show this drastic increase in recombination, the injection into the bulk was either a local phenomenon, i.e. precipitation to unstable clusters at certain precipitation sites. Alternatively it may be considered to be an ongoing process, kinetically hindered at certain sites, and had not been completed, yet. The measured relationship between surface contamination and J_{0E} did not appear to have changed over time.

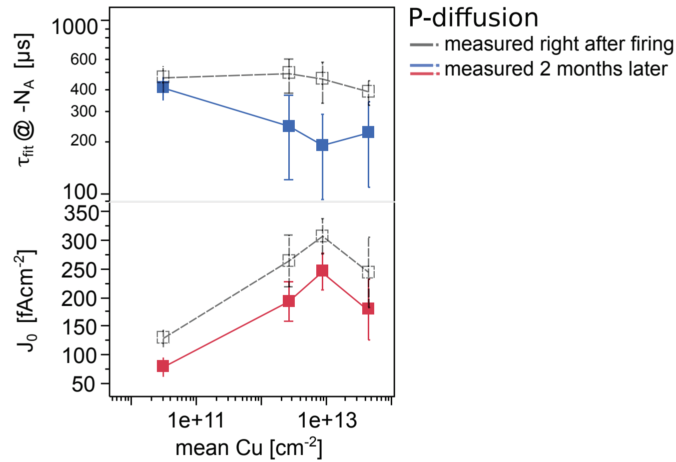

Fig. 4.31: Saturation current density J_0 for the highly doped region and estimated bulk lifetime (run 1333) plotted against the Cu surface contamination before P-diffusion. The gray curves are plotted to show the shape of the curves before storage. Absolute values need to be disregarded, as a tilt in the QSS-PC flash lamp produced incorrect readings for the flash intensity, when measuring the second time, resulting in incorrect lifetime and J_0 values.

Interestingly, in the other experiment (run 1288) the P-diffused samples did not show any further degradation as shown in the top row of graphs in **Fig. 4.32**. One possible reason is additional contamination by Fe, as in run 1288 a similar cross contamination phenomenon occurred as discussed at the end of **Sec. 4.3.2**. One indication for this is the fact that the mean values of *implied* V_{oc} of the reference groups of the two P-diffusions in run 1288 and run 1333 differed by about 10 mV (645 mV in run 1288 vs. 655 mV in run 1333). While just after firing in the case of the diffusion with additional Fe, the different Cu contamination levels showed a much stronger effect on the *implied* V_{oc} values, no further drop after storage was

found. As reason for this tendency of Cu to decorate already existing defects was considered. Obviously, these precipitates are highly electronically active and hence cause the stronger initial drop, but they are very effective in “keeping” the already precipitated Cu. If no additional contamination is present (obtained by the two separate diffusions in run 1333), the Cu is temporarily trapped in surface near areas, from where it will be released to the bulk to become strongly recombination active: The drop after storage at room temperature is impressive, in some spots hardly any lifetime was measured.

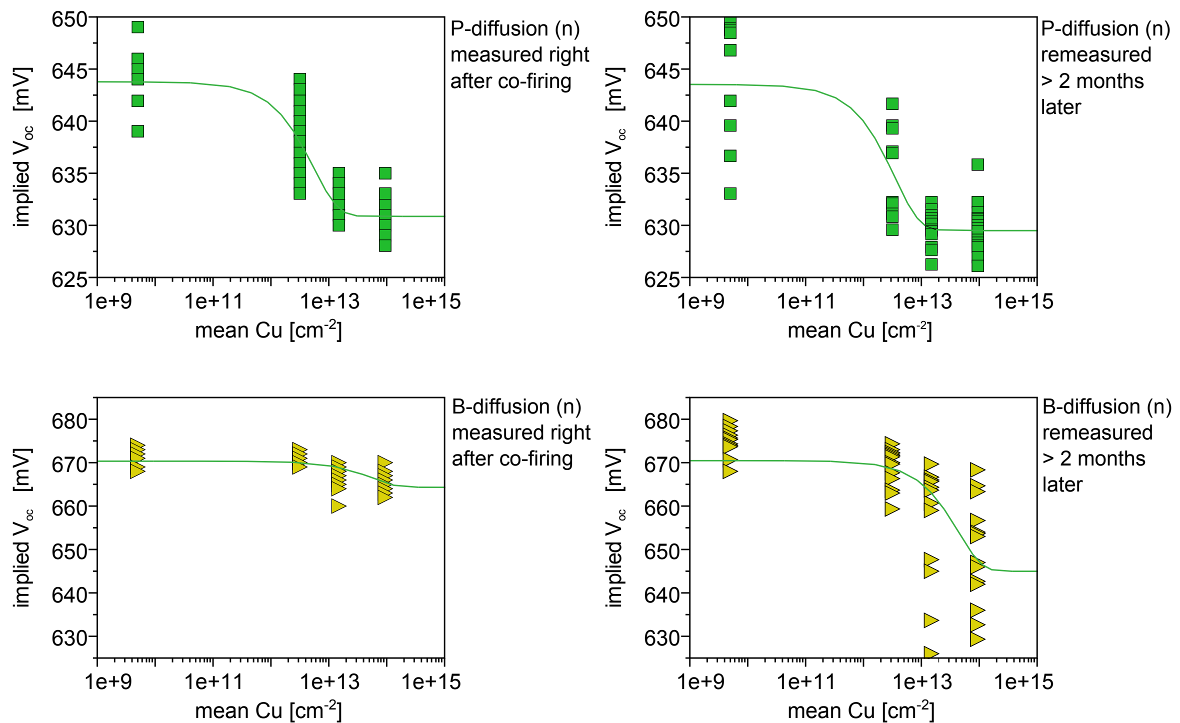

Fig. 4.32: N-type samples from run 1288; measured directly after co-firing and after extended storage in a box at room temperature.

The two graphs on the bottom of **Fig. 4.32** indicate that the phenomenon of degradation over time can also occur in the case of B-diffused, Cu contaminated samples. Evidently, a similar behaviour as in the case above can be observed, the loss is not quite as pronounced, but still up to 40 mV in certain spots.

The phenomenon of Cu migration at low temperature itself is not so surprising, as several authors have noted that Cu can diffuse quite far within a silicon wafer even at room temperature [6, 241]. The fact, however, that gettering takes place in the first place—at least in B-diffused samples—contradicts modelling results from Istratov *et al.* [241]. They show that no enhanced gettering is to be expected from heavily doped p^+ regions, despite the fact of increased solubility of Cu in such regions and the tendency of Cu_i^+ formation. From their modellings Cu is likely to be redistributed into the n-doped bulk where the formation of Cu-precipitates is favourable due to Fermi-level effects: the high Fermi level, above E_C – 0.2 eV, causes already precipitated Cu clusters to change their polarity from positive to neutral or negative, enabling further Cu to precipitate and thus enhancing the recombination

activity. Istratov *et al.* conclude that a n-type (and n^+) layer would be more efficient for Cu gettering [241]. The exact phenomenon of the temporary gettering of Cu contamination certainly needs further investigation to shed light on questions concerning activation barrier, energy levels and mechanism.

Mechanisms of lifetime degradation

Analogous to the p-type wafers, one group of wafers from run 1333 was thermally oxidised. The impact of the different surface contamination values on the *implied* V_{oc} is shown in **Fig. 4.28**. Like in case of the p-type samples, the interface trap density was measured as well using the corona charge measuring technique. The results including the respective *implied* V_{oc} can be found in **Fig. 4.33**. The small impact of Fe contamination, as observed by the *implied* V_{oc} measurements, is mirrored by the shape of the curves on the left. The same applies to the huge impact of the Cu contamination. The U-shape of the curves is strongly narrowed in the right graph. In terms of the function of V_{sb} Cu shows a very similar behaviour in the p-type case. The fact that the drop in lifetime, respectively *implied* V_{oc}, for Cu is so vast—the first step brings the lifetime down close to the limit of detection—is indicating that Cu not only increases the surface recombination velocity but also adds to bulk recombination. From these findings it can be concluded that Fe appears to be of less concern, as it appears to not increase surface recombination and only slightly increases the bulk recombination, when no highly diffused region is present (as expected from the much lower capture cross section for holes than for electrons as minority carriers).

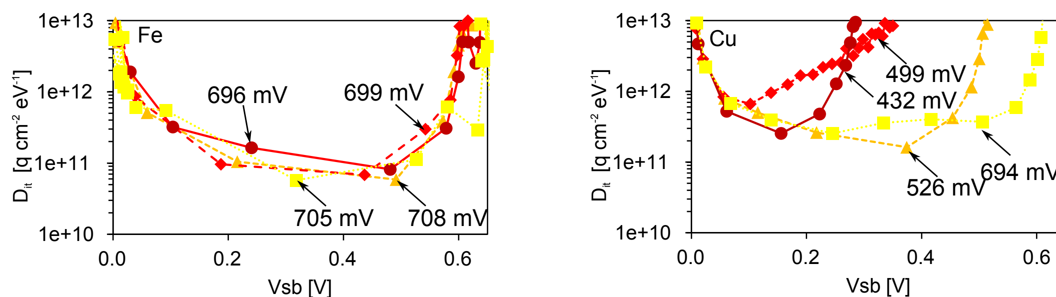

Fig. 4.33: Interface trap density D_{it} of thermally oxidised n-type wafers. The surface concentrations of the four groups can be deduced from **Fig. 4.28**. Of each contamination group one wafer was measured.

In contrast to findings by Macdonald *et al.* [21, 246, 247] no improved gettering capacities for P-diffusion in n-type processing but rather the opposite was observed: the investigated P-diffusion showed a stronger sensitivity towards Fe surface contamination than the B-diffusion; at least in one of the two series of experiments. Phang *et al.* have shown that Fe gettering efficiency for both diffusion types can be optimised by changing process parameters [22], e.g. lower cooling rates or extended plateaus below the actual diffusion temperatures of the dopand.

In order to determine the impact of Fe and Cu on surface and bulk recombination properties, the J_0 and the bulk lifetime τ_{bulk} of the wafers from run 1288 and run 1333 were measured by QSS-μPCD using the Basore-fit function as it was done in the p-type case. The obtained data were plotted and fitted by linear-log plots in **Fig. 4.34**. The measurements

were performed after the prolonged storage period so that the drop in lifetime due to the temporary gettering phenomenon was taken into account.

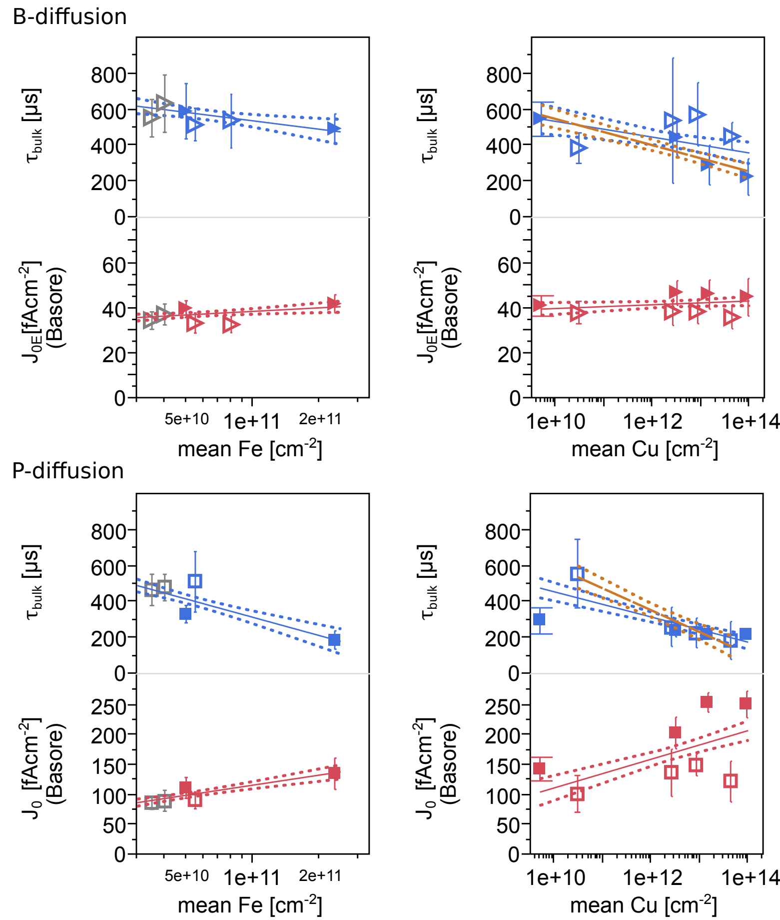

Fig. 4.34: J_0 and bulk lifetime at 1 sun illumination plotted against the Fe and Cu surface contamination before the diffusion step (top B-diffusion, bottom P-diffusion). Filled symbols are data from run 1288 and hollow symbols from run 1333. The fits are logarithmic and will be used in the following section (the equations can be found in **Tab. 4.6**).

The results confirm the comparatively small impact of Fe and Cu on the B-diffusion. Good gettering capacities of B-diffusion for Fe contamination have been shown on p-type material by Joge *et al.* [248] and modelled by Haarahiltunen *et al.* [249]. Despite findings by Weber *et al.* [250], who observed a strong increase in J_0 with increasing Fe contamination, only slightly increased J_0 values was observed for the chosen concentration range. All of the three cited references work with Fe bulk contamination, which in turn means that for sufficient gettering during the high temperature process the bulk impurities need to reach the surface. In the case investigated here the elements are introduced at the surface, so that diffusion time and the temperature ramps are expected to play a less important role. This holds true in the case of Fe: the impact on the bulk lifetime is found to be negligible within the examined surface concentration range.

In contrast to this, Cu does affect the bulk lifetime, it drops from about 600 μs to below 200 μs. The brown, dashed fit in top right graph from **Fig. 4.34** is used for further analysis, as it takes the only temporary gettering phenomenon into account (only data from run 1288 are

fitted). The equation in italics in **Tab. 4.6** belongs to the brown, dashed fit. The reason for using only the strong observed decrease in lifetime after temporary gettering is the assumption that Cu tends to be released eventually due to its high diffusivity even at room temperature.

The impact of the Fe contamination on the P-diffusion is much stronger than on the B-diffusion. Within the small investigated surface contamination range of 5e+10 cm^{-2} to 2.5e+11 cm^{-2} the bulk lifetime at 1 sun illumination drops from 600 μs to about 200 μs. It causes an increase in both: recombination in the highly doped region and the bulk. The impact of Cu on the bulk lifetime is measured to be smaller, when related to absolute numbers of surface contamination. Lifetimes in the range of 200 μs are only reached between 1e+12 and 1e+13 cm^{-2}. Interestingly, temporary gettering is observed again, but only in run 1333. Again, for further analysis only the data from the degraded samples are used (brown, dashed fit).

The relatively strong impact of Fe is also observed in the Cu contaminated samples from run 1288 (filled symbols). Apparently some of the Fe had migrated to the Cu group, which was placed behind the Fe contaminated group (in direction of the gas flow), increasing the J_0 and the bulk lifetime of the reference. The impact on J_0 appears to affect all samples, as a similar trend is observed but on a higher level. A similar phenomenon (to a much lower extend) is observed in the B-diffusion of run 1288. To make up for this cross contamination phenomenon linear correction factors for J_0 were used for further analysis, denoted in the equations in **Tab. 4.6** by the values in italics.

Tab. 4.6: Formulas of fits from **Fig. 4.34**. Fits of bulk lifetime values in italics: equation taking temporary gettering into account; linear correction factors of J_0 values: Correction factors for cross contamination in the diffusion tube.

	Fe	Cu
B-diffusion	Tau bulk [μs] = 2253 – 67.71 * ln(mean Fe [cm^{-2}])	Tau bulk [μs] = 974.6 – 19.09 * ln(mean Cu [cm^{-2}]); *Tau bulk [μs] = 1279 – 31.75 * ln(mean Cu [cm^{-2}])*
	J_{0E} [fAcm^{-2}] (Basore) = –19.07 + 2.284 * ln(mean Fe [cm^{-2}])	J_{0E} [fAcm^{-2}] (Basore) = 31.80 + 0.3596 * ln(mean Cu [cm^{-2}]) *– 6 fAcm^{-2}*
P-diffusion	Tau bulk [μs] = 4036 – 146.9 * ln(mean Fe [cm^{-2}])	Tau bulk [μs] = 1157 – 30.42 * ln(mean Cu [cm^{-2}]); *Tau bulk [μs] = 1813 – 52.79 * ln(mean Cu [cm^{-2}])*
	J_0 [fAcm^{-2}] (Basore) = –498.5 + 24.272 * ln(mean Fe [cm-2])	J_0 [fAcm^{-2}] (Basore) = – 127.1 + 10.38 * ln(mean Cu [cm^{-2}]) *– 40 fAcm^{-2}*

Conclusion

Quite surprisingly, the B-diffusion turned out to be less sensitive towards metal contamination than the P-diffusion. Direct comparison was assumed to be possible as, due to the co-diffusion process, similar thermal budgets were applied. Most importantly, this way of processing

allowed for the final cooling ramp to be identical.

In the case of Fe, the decrease in *implied* V_{oc} for both diffusions appears to be similar for low Fe surface concentrations (below 1e+11 cm^{-2}). However, for the highest investigated contamination level (2.5e+11 cm^{-2}) the losses of up to 7 mV were recorded for the B-diffusion, the P-diffused samples had already degraded by 14 mV, stressing the higher sensitivity of P-diffusion. Fe contamination of the B-diffused samples caused a small decrease in the bulk lifetime and a small decrease in J_{0E} in the investigated concentration range of up to 1e+14 cm^{-2}. Both was observed in the P-diffused case to a much larger extend.

Cu surface contamination turned out to be more complicated to deal with. Initial studies indicated that critical surface concentrations were found in the range of 1e+12 cm^{-2}. Once again, the effect of the impact on P-diffusion was more pronounced than on the B-diffusion. What was found, however, was that after prolonged storage times of P- and B-diffused samples, the lifetime of the Cu contaminated samples had dropped to a large extend. A phenomenon that was referred to as “temporary gettering”. No clear reason for the fact that it did not occur in all cases was given. One effect was found to inhibit the temporary gettering effect: Fe defects tend to interfere with Cu contamination, increasing initial recombination activity but inhibiting the “release” of defects after storage. However, this effect was only observed in P-diffused samples. Cu contamination before B-diffusion caused the bulk lifetime to drop strongly, only after prolonged storage time, while the J_0 stayed almost constant. In P-diffused samples both parameters deteriorated. The J_{0E} was found do have almost doubled for Cu concentrations of approximately 1e+13 cm^{-2}. In both cases, when the gettering of the Cu contamination was only temporary, the bulk lifetime dropped dramatically (without affecting the J_0) indicating the release of Cu atoms into the bulk. For further studies it is assumed that parts of the gettered Cu after processing are very much likely to be released eventually. However, factors of this release remain unclear and require further studies.

4.5 Simulation of solar cells

Especially for Fe, many simulations of solar cells with different bulk Fe concentrations have been published based on more or less experimental data [251–254]. Hofstetter *et al.* combined diffusion and gettering simulation to a impurity-to-efficiency simulator based on [253] that can be accessed free of charge online (http://pv-i2e.mit.edu/i2e/applet.html). It allows to study the effect of heat treatments, such as diffusions, on the bulk lifetime of a silicon wafer. A more general approach towards metal contamination impact simulation, also including Cu, can be found in [255] and [256].

The novel approach of this work is to simulate the impact of Fe and Cu contamination present on the wafer surface before high temperature diffusion steps on different cell concepts, based on the experimental (lifetime) data presented so far. Full Al back-surface field solar cells and bifacial n-type solar cells were chosen for the comparison of the impact on the current industrial standard and a modern high efficiency solar cell concept. The advantage of using a simulation tool over experimentally producing solar cells from intentionally contaminated wafers is the possibility to easily vary solar parameters such as base doping or backside passivation. Also, processing of a larger amount of contaminated cells is expected to contaminate the diffusion furnaces.

A central point of solar cell simulation, when considering the effect of defects on solar cell devices, is the recombination behaviour of defects under varying excess carrier densities. So far, the lifetime analysis was restricted to the effective and bulk lifetime at 1 sun, i.e. at one single level of excess carrier density (injection level). As discussed in **Sec. 3.1**, the recombination behaviour of most defects changes with the injection level. Therefore, when trying to estimate the impact of a certain bulk lifetime τ_{bulk} on the final solar cell device, the exact recombination properties of the respective contaminating and thus lifetime limiting species need to be known. The reason for this is that the J-V-curve sweeps along a whole range of injection levels (from low-injection under short circuit current conditions to relatively high injection conditions under open voltage conditions). The *SRH* recombination theory has proven to be suitable for the prediction of such behaviour. However, not for all elements SRH-data are easily available, either due to the fact that they are difficult to obtain or simply not so commonly used. Cu, for example, as a fast diffusing element with a whole range of possible defect states is one of these elements. Therefore, **Sec. 4.5.1** is dedicated to the recombination behaviour of Cu.

Another issue that will be addressed briefly is variability of certain defects under (prolonged) illumination, such as Fe and “B−O” in p-type silicon that will alter the bulk properties. The recombination behaviour of Fe has been most intensively studied in the PV and IC communities. As in this work so-far, only the “deactivated” case, observed directly after processing, has been considered, the change of recombination behaviour after illumination will be addressed in **Sec. 4.5.2**.

The phenomenon of “B−O” formation, commonly referred to as light-induced degradation (LID), will also be discussed in this section. The presence of additional *SRH* recombination centers apart from the added metal contamination complicates matters when trying to predict

the impact of said contamination. Therefore, a short introduction of the LID phenomenon is given and the LID behaviour of the material used in this work, as experimentally determined, will be presented in the last section (**Sec. 4.5.3**).

In **Sec. 4.5.4** the used simulation software is introduced. Furthermore, a detailed step-by-step overview of the simulation process is given. It is described how the experimental data on the effect of surface contamination present before high temperature diffusion processes (from **Sec. 4.3.2** and **Sec. 4.4.1**) were used to generate input-variables for the simulation of p-type full Al-BSF and n-type bifacial cells. In the last two sections (**Sec. 4.5.5** and **Sec. 4.5.6**) the results of the simulations are presented.

4.5.1 Injection dependent recombination behaviour of Cu

While Fe recombination properties are well-known and the trap levels and capture cross sections are summarised in **Tab. 3.2** in **Sec. 3.2.3**, the properties of Cu contamination are not so commonly used. This is mainly due to two reasons: On the one hand Cu is very mobile in silicon. As described above, it may diffuse even at room temperature to different locations in the wafer and therefore change its impact on minority carrier lifetime [257, 258]. On the other hand it is likely to be present in several different states. Precipitates of different size and chemical consistency with different deep energy levels have been observed by deep level transient spectroscopy (DLTS) by several groups. A summary can be found in an overview article by Istratov *et al.* in [6]. Both effects complicate the analysis of the impact on minority carrier lifetime [241, 259]. It has been shown that Cu tends to form recombination active precipitates, particularly in n-type Si, introducing a whole band of deep and shallow levels within the bandgap in the range of $E_C - 0.2$ and $E_C - 0.5\,\text{eV}$ [6, 241]. Macdonald *et al.*, however, showed in 2002 [260] that the description of the recombination behaviour of Cu contamination in silicon is relatively straight forward. They used the measurement of injection dependent lifetime (cf. **Sec. 3.1** and **Sec. 3.2.1**) on intentionally contaminated p- and n-type wafers. They were able to demonstrate that a good fit of the injection dependent lifetime curves of Cu contaminated wafers was obtained, when using the *SRH* formalism with a deep and a shallow defect level at the edges of the defect band ($E_C - 0.2$ and $E_C - 0.5\,\text{eV}$).

Tab. 4.7: *SRH* parameters of Cu in p-and n-type silicon extracted from the data by Macdonald *et al.* [260].

	defect level [eV]	σ_n [cm^2]	σ_p [cm^2]
p-type	$E_C - 0.2$	2.0e–16	5.0e–15
p-type	$E_C - 0.5$	2.5e–16	1.5e–17
n-type	$E_C - 0.2$	2.0e–16	5.0e–15
n-type	$E_C - 0.5$	2.0e–17	3.0e–16

While the shallow level was found to be the same for both types of base doping, Macdonald *et al.* reported different recombination behaviours of the deep bandgap level depending on the doping of the material [260]. The capture cross sections were found to diverge for the different doping types, which was explained by the impact of the respective Fermi level on the charge of the Cu precipitates. As Macdonald *et al.* did not determine the exact number of active

Cu precipitates in their study, they simply assumed the respective trap densities N_T in order to obtain good fits of experimental data using **Eq. 3.4** and **3.8** [260]. As open parameters for variations, the values for the hole and electron capture lifetimes $\tau_{p0} = 1/\left(N_T\sigma_p v_{th}\right)$ and $\tau_{n0} = 1/\left(N_T\sigma_n v_{th}\right)$ were used. As N_T and $\sigma_{p/n}$ could not be extracted separately, "effective" parameters $N_T \cdot \sigma_p$ and $N_T \cdot \sigma_n$ were assigned. The relative relationship between these parameters determined the shape of the curve and an assumed value for N_T within the range of solubility was varied to match the absolute level of the measured injection dependent lifetime curve.

Cu in p-type Si

A similar technique was used in the scope of this work to experimentally determine the recombination behaviour of Cu in the used p-and n-type silicon. Macdonald *et al.* prepared their samples by driving the Cu into the bulk, etching the surface and subsequently passivating them by PECVD obtaining very low surface recombination velocities [260]. In contrast to this, the samples used in this work were diffused, featuring highly doped surfaces limiting the effective lifetime. Therfore, as shown in **Fig. 4.21**, the Cu contamination did not only have an impact on bulk recombination but also on recombination in surface-near parts of the silicon wafer.

In order to extract injection dependent "defect lifetime curves", the other factors determining the effective injection dependent lifetime, such as Auger recombination in the highly doped region and recombination due to the material quality in general, which were inherent for all samples, needed to be cancelled out. This was achieved by recording lifetime curves of "clean", non-contaminated reference samples and contaminated samples with the highest Cu surface concentration from run 1333. The thus obtained curves were overlayed and fitted for the clean and the contaminated samples using JMP10 and are plotted in the left hand graph of **Fig. 4.35**. The effective defect lifetime curve was extracted from the two curves by

$$\tau_{eff.\ defect} = \left(\frac{1}{\tau_{contaminated}} - \frac{1}{\tau_{reference}}\right)^{-1}. \tag{4.2}$$

By doing so, all the other components adding up to the effective lifetime were cancelled out. The accordingly obtained curve was then fitted (cf. right hand graph **Fig. 4.35**) using the *SRH* parameters from **Tab. 4.7**. In order to get a good fit of the effective defect lifetime curve in addition to the *SRH* recombination, the increase in emitter recombination needed to be taken into account. The contribution of recombination in the highly doped region was introduced using the equation for J_0 (**Eq. 3.15**). The difference in J_{0E} between the two samples was used to plot the curve that is displayed for the increase in J_0 in the right hand side of **Fig. 4.35**. The impact of the increase in emitter recombination is modelled by introducing a term that is calculating the difference in $\tau_{Emitter}$ by using **Eq. 3.15**:

$$\Delta\tau_{Emitter} = \frac{qn_i^2 W}{2\Delta J_{0E} \cdot \left(N_A + \Delta n_{av}\right)}. \tag{4.3}$$

The Cu defect concentration required for the deep level curve as displayed in **Fig. 4.35**

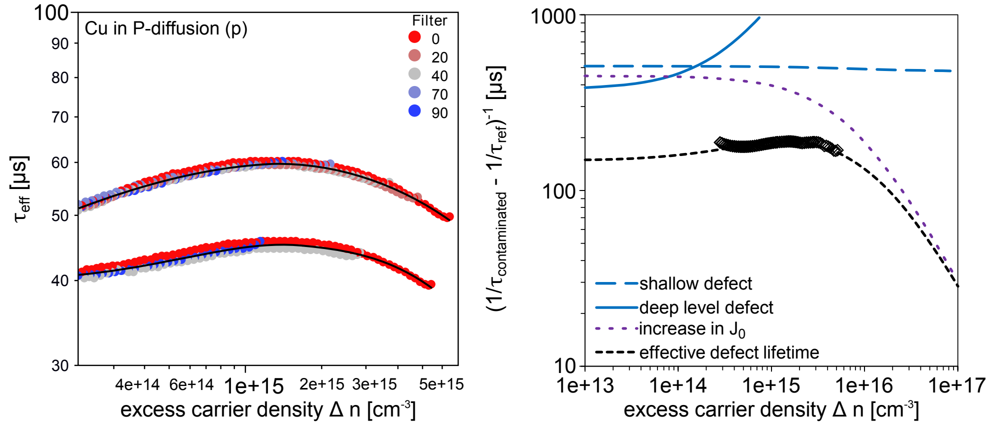

Fig. 4.35: Left hand side: Injection dependent lifetime of a wafer with (lower curve) and without Cu (upper curve) contamination. Right hand side: The contributions of the Cu contamination is extracted (effective defect lifetimes, black diamonds) and fitted using *SRH* formalism and the calculated increase in J_{0E}.

was calculated to be 1.0e+12 cm^{-3}. The ΔJ_0 that accounted for the purple, dotted curve, which was required to accurately fit the defect lifetime curve in addition to the deep level, was 27 fAcm^{-2}. This value was only slightly lower than the difference in J_{0E} that was measured by QSS-PC (40 fAcm^{-2}). This may be explained by the effect that the respective values of J_{0E} were extracted at an excess carrier density of 3e+15 cm^{-3} (by the QSS-PC method), in which a combination of the two recombination lifetimes—the increase in surface-near recombination and the shallow defect level—take effect.

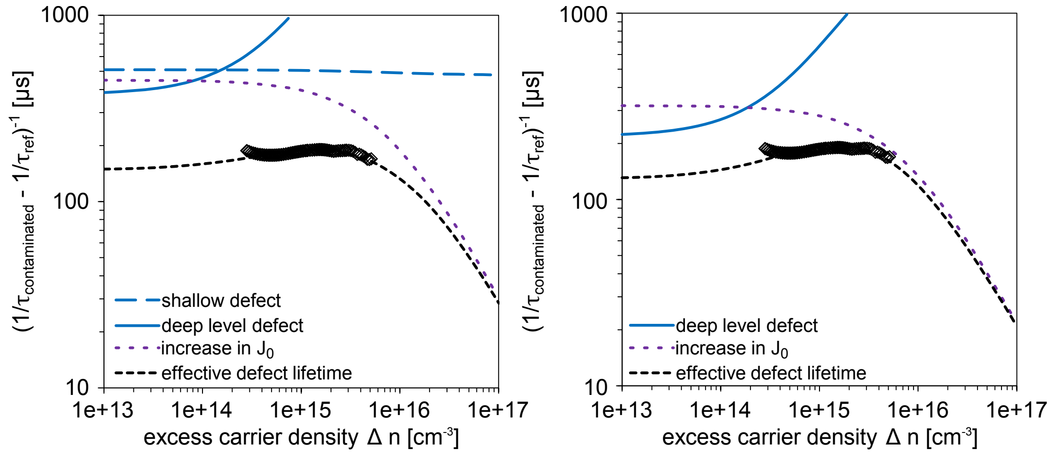

Fig. 4.36: Fits of the measured defect lifetime (black diamonds). Left hand side: Using both deep and shallow defect levels (from **Fig. 4.35**). Right hand side: Alternative fit disregarding the shallow level, assuming a higher decrease in J_{0E}. The resulting effective defect lifetime curves are in close agreement.

The conclusion from these measurements is that the recombination behaviour of Cu in p-type silicon as published by Macdonald *et al.* for the bulk defect lifetime was confirmed [260]. In order to obtain the best fit of the experimental data, both the deep and the shallow defect level with the identical number of defects, had to be used. In addition to that the impact of the emitter-near region had to be taken into account, which was possible by using a simple ΔJ_0 term.

As indicated on the right hand side of **Fig. 4.36**, a decent fit of the experimental data was

also obtained, if only the deep level fit was implemented. The contribution of the increase in J_{0E} had to be slightly modified. It proved to be a valid approach, as the shallow level effect contribution to the effective defect lifetime is the most pronounced under high injection conditions (>3e+15 cm^{-3}) and was included in the J_0 measurement anyhow (now ΔJ_0 matched the experimental value). As the investigated samples represent the group with the highest investigated Cu surface concentration and only a small error due to the simplified fitting approach is introduced, this approach was chosen for the simulation of the p-type cells in **Sec. 4.5.4**.

Cu in n-type Si

A similar study was performed using Cu contaminated P- and B-diffused n-type samples. First, the measured curves of P-diffused n-type samples of the two experiments run 1288 and 1333 from the group with the highest initial Cu surface contamination were plotted in **Fig. 4.37**.

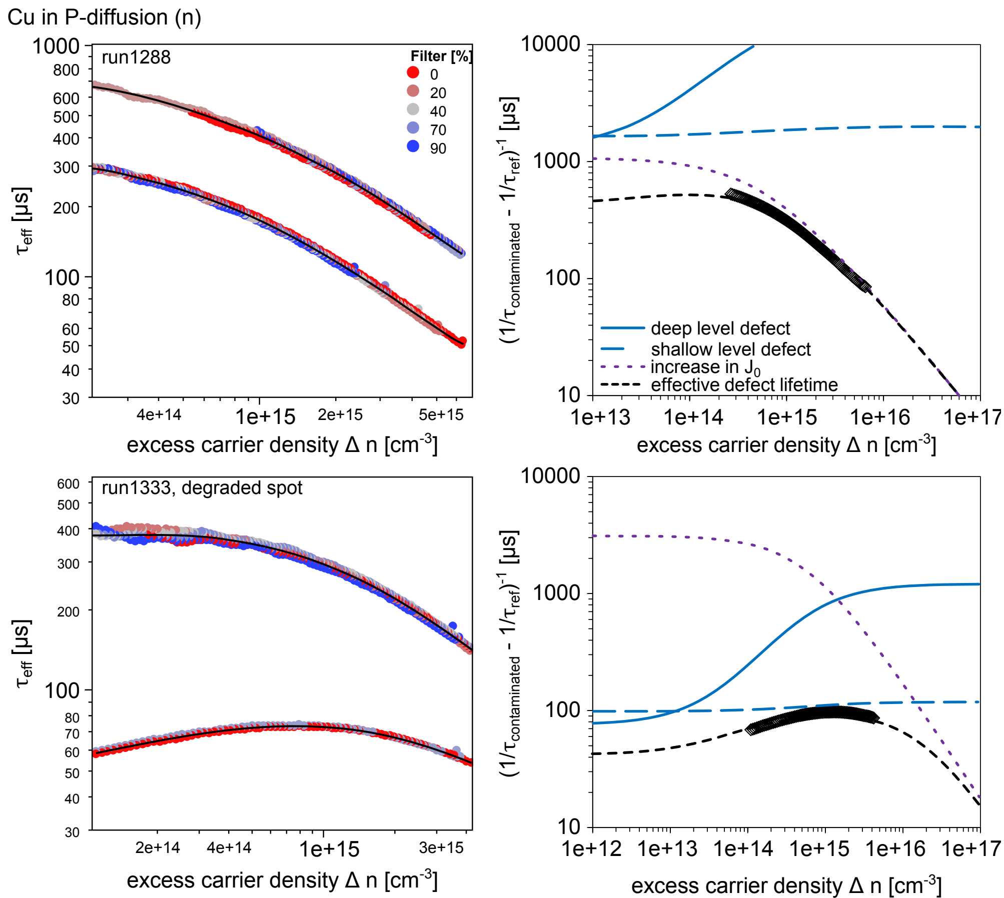

Fig. 4.37: Left hand side: Injection dependent lifetime curves of clean and Cu contaminated wafers after P-diffusion from run 1288 (top) and run 1333 (bottom). Right hand side: Fits of the extracted effective defect lifetime (diamonds), using data from Macdonald *et al.* [260] and the increase in J_0.

Again, as fit parameters for the deep and shallow level the values provide by Macdonald *et al.* were used. In addition to that, ΔJ_0 curves were required to obtain a good fit [260]. Macdonald's assumption that the shallow and the deep defect level are related to one and

the same defect was followed (therefore only one value for the density of traps N_T was used) [260].

The wafer from run 1288 is one that showed no further decrease in lifetime over time (cf. **Sec. 4.4.1**). The N_T values of Cu were quite low in the range of 9.0e+11 cm^{-3}, whereas the increase of J_0 was strong. It increased from 80 to 220 $fAcm^{-2}$ by 140 $fAcm^{-2}$. A loss in *implied* V_{oc} of 24 mV (from 658 mV on the reference wafer to 634 mV) was the consequence.

The spot measured on a wafer from run 1333 had degraded over time and lost 35 mV (from 651 mV on the reference wafer to 616 mV). This was mostly due to a massive increase in bulk recombination. About one and a half times more Cu defects, namely 4.0e+12 cm^{-3}, were required to accurately fit the data. Yet, the increase in ΔJ_0 was much smaller, only 48 $fAcm^{-2}$ were required to get a good fit. The measured difference between the two saturation current densities, however, was found to be 60 $fAcm^{-2}$, indicating that the J_0 determination was interfered with by the shallow level.

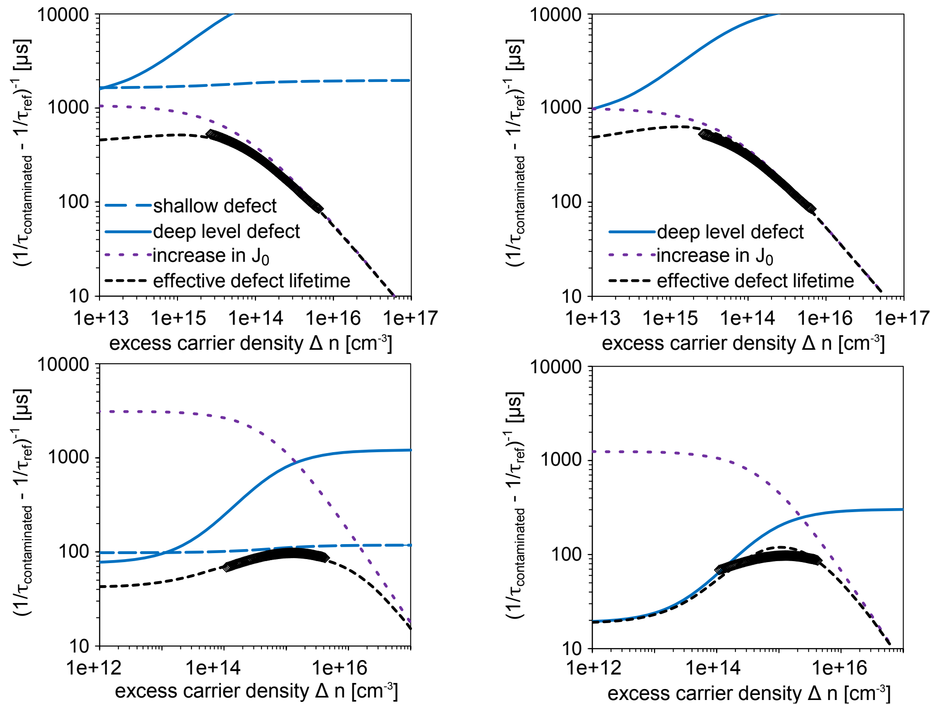

Fig. 4.38: Fits of the effective defect lifetime (diamonds) of Cu contaminated samples after P-diffusion. Left hand side: Fits using both deep and shallow defect levels (from **Fig. 4.37**). Right hand side: Simplified fits omitting the shallow defect level.

In order to describe the effective defect lifetime mathematically—similarly to the p-type case—a simplified model was used and compared to the exhaustive model. The curves calculated by the simplified model are plotted on right hand side of **Fig. 4.38**. Good agreements with the experimental data was found when only small amounts of Cu were present (< 1e+12 cm^{-3}). For high bulk Cu contamination levels and correspondingly low bulk lifetimes, however, the model became less accurate. The number of Cu defects N_T was overestimated and the low injection bulk lifetime was underestimated, which would cause especially J_{sc} values to be underestimated, when simulating solar cells (as the J_{sc} is extracted under low injection level conditions). The error which it introduces under high injection conditions

was expected to be relatively small, as, at least partly, some of the increased recombination had already been included in the measured ΔJ_0 values.

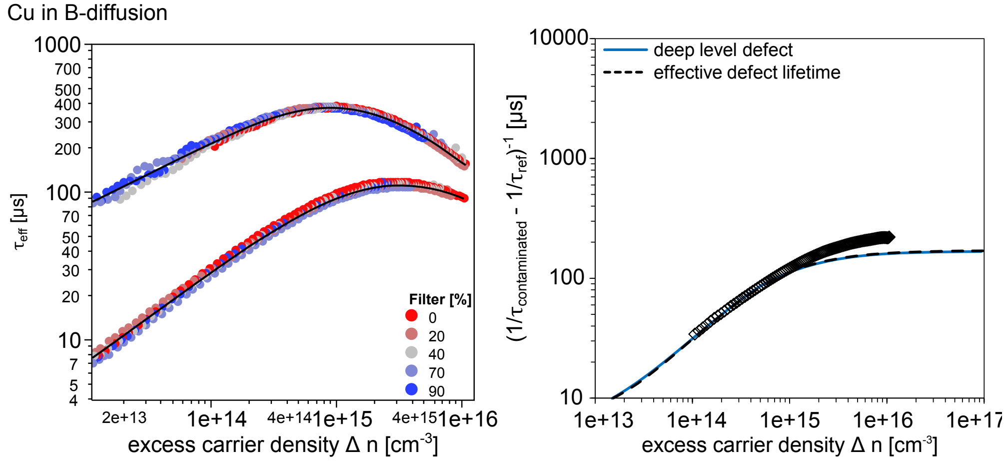

Fig. 4.39: Left hand side: Injection dependent lifetime curves of clean and Cu contaminated wafers after B-diffusion from run 1288. Right hand side: Fits of the extracted effective defect lifetime (diamonds), using only the deep level.

An interesting observation was made, when one of the degraded spots in the B-diffused samples (run 1288, degraded) was investigated. The measured injection dependent lifetime curve of a reference wafer and contaminated samples and the extracted defect lifetime curve are plotted in **Fig. 4.39**. The defect lifetime curve showed no sign of a shallow defect level. A relatively good fit was obtained, only using the deep defect level. A fact that certainly needs a more thorough investigation. The number of deep level traps N_T to fit the data was found to be 2.8e+13 cm^{-3} and therefore even higher than in the case of the degraded P-diffused sample. The *implied* V_{oc} decreases by 44 mV (from 668 mV on the reference wafer to 624 mV). As expected from the J_{0E}-behaviour in **Fig. 4.34** (no increase with Cu concentration was observed), the Cu gettered in the highly doped p^+ region did not increase surface-near recombination.

Conclusion

It was shown that *SRH* fitting of Cu defects in p-and n-type silicon is possible. The presented results mostly confirmed the data provided by Macdonald *et al.* [260], the only data found in the literature concerning this problem. For extracted effective defect lifetime curves of P-diffused samples good fits were obtained and thus the parameters of defect level and “effective” capture cross sections can be used for the simulation of Cu contaminated samples. Interestingly, the B-diffused Cu contaminated samples did not show any effect of the shallow level ($E_C - 0.2$ eV) that was observed in the other n-type samples—a fact that needs further investigation. A simplified model disregarding the shallow defect level was introduced and is used in the following. This is an approach that is expected to work sufficiently well for relatively small Cu contamination levels ($<$ 1e+12 cm^{-3}). With higher resulting bulk Cu concentrations it is thought to rather underestimate the impact, especially under low injection conditions.

4.5.2 Injection dependent recombination behaviour of Fe

In contrast to Cu, the *SRH* properties of Fe are well-known. What complicates matters in terms of Fe, is the fact that in p-type silicon—as shown before (cf. **Sec. 3.2.3**)—Fe can be transformed by illumination from the "Fe−B state" to Fe_i. This transformation completely changes the recombination behaviour. An example for the different shapes of the injection dependent lifetime curves of the two Fe modifications at different concentration levels is plotted in **Fig. 4.40**. The calculations are based on the *SRH* parameters from **Tab. 3.2** in **Sec. 3.2.3**.

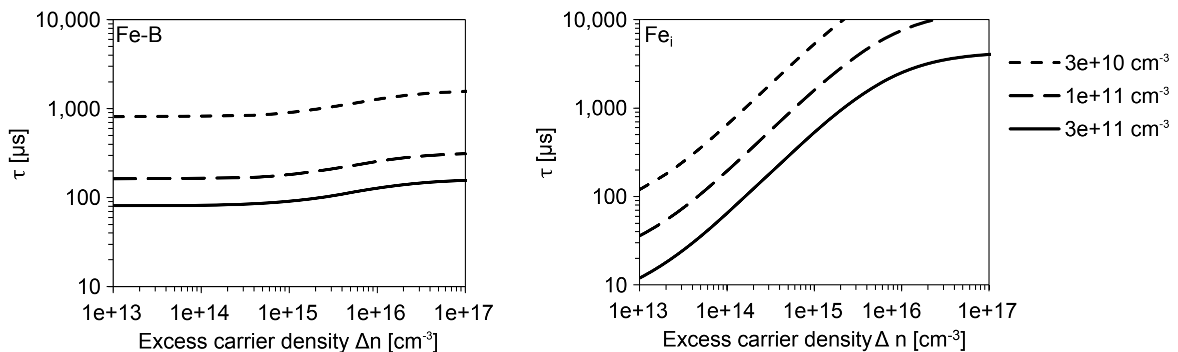

Fig. 4.40: Lifetime curves for different Fe−B concentrations and the respective Fe_i curves in 2 Ωcm p-type material.

As a consequence, p-type solar cells contaminated with Fe will perform even worse, when the "Fe−B" are split up and Fe_i is liberated. The reason for this is the strong decrease in lifetime in the low- to mid-level injection (1e+13 – 1e+14 cm^{-3}), which is exactly the injection range under which typical p-type solar cells operate. As plotted in **Fig. 4.40**, at high injection conditions the lifetime might actually increase—which can be misleading when interpreting lifetime measurements at high excess carrier densities only. In the following simulation section this fact will be taken into consideration. In contrast to this, Fe can only occur as Fe_i in n-type solar cells (as no boron is present), which decreases the complexity of the simulations.

4.5.3 Light induced degradation

There is another factor that complicates matters when discussing the bulk recombination properties of p-type solar cells: Due to the formation of meta-stable defects that tend to transform during illumination, the "background" recombination of the solar cell increases drastically. The state of the bulk as-processed is significantly different to the state after a prolonged illumination. This so-called "light-induced degradation" is an inherent feature of p-type Cz-material due to relatively high oxygen concentration in the bulk.

This effect is attributed to the formation of defect consisting of substitutional boron with oxygen (B_s−O_y). The oxygen originates from the walls of the crucible used to melt the silicon. The mechanism of defect formation is often assumed to be the incorporation of an interstitial oxygen O_{2i} dimer by substitial boron that is highly recombination active. The defect formation is triggered by light soaking of the crystal causing solar cell efficiencies to

drop under working conditions [261–265]. The exact mechanism behind this degradation is still quite controversial and will not be further discussed here, for further information on recent contributions to the topic refer to [266–268].

The impact of light induced degradation due to B_s-O_y pairing in the material used for the experiments in this thesis was determined by measuring effective lifetime curves of a non-contaminated, p-diffused wafer before and after high intensity light soaking at elevated temperatures (1000 s at 120°C). This procedure allows for almost complete degradation within a short time and is thus called light induced degradation conditions, ALID [195]. To ensure that no further degradation takes place, the procedure was repeated three times. Similar to Schmidt and Cuevas [262] effective defect lifetime curves were extracted by measuring QSS-PC before and after activation. For the extraction of the defective lifetime curve a similar method as in the case of injection dependent lifetime analysis of Cu (in **Sec. 4.5.1**) was used:

$$\tau_{B_s-O_y} = \left(\frac{1}{\tau_{degraded}} - \frac{1}{\tau_{initial}} \right)^{-1}. \tag{4.4}$$

Schmidt and Cuevas were able to identify a deep and a shallow defect level present in most samples and roughly determine the SRH parameters [262]. The deep levels were found to be located between $E_V + 0.35$ and $E_C - 0.45$ eV and the shallow levels were detected in the range of $E_C - 0.15$ eV and $E_V + 0.15$ eV. The ratio between the electron and hole lifetimes τ_{n0}/τ_{p0} derived from the respective capture cross sections was found to be 0.2. A typical defect lifetime curve derived from these parameters is plotted in **Fig. 4.41**.

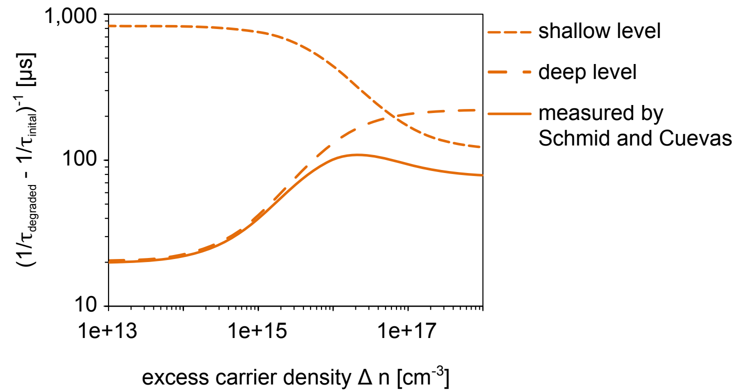

Fig. 4.41: Bulk lifetime as extracted by Schmidt and Cuevas [262].

A wafer from run 1288 was used to experimentally determine the B_s-O_x defect lifetime curve after light induced degradation. The measured injection dependent lifetime curves can be found in the left hand side graph of **Fig. 4.42**. The best fit was obtained using only the deep level with an energy level of $E_C - 0.65$ eV, matching the results by Schmidt and Cuevas, who reported that the shallow level could not always be detected [262]. The ratio τ_{n0}/τ_{p0} required for a good fit, however, was found to be 0.03 and thus smaller. The accordingly derived “effective parameters” N_T (2.9e+10 cm^{-3}), σ_n (2.7e–14 cm^2) and σ_p (2.5e–15 cm^2) will be used in the simulations of the set of degraded p-type solar cells in the following section.

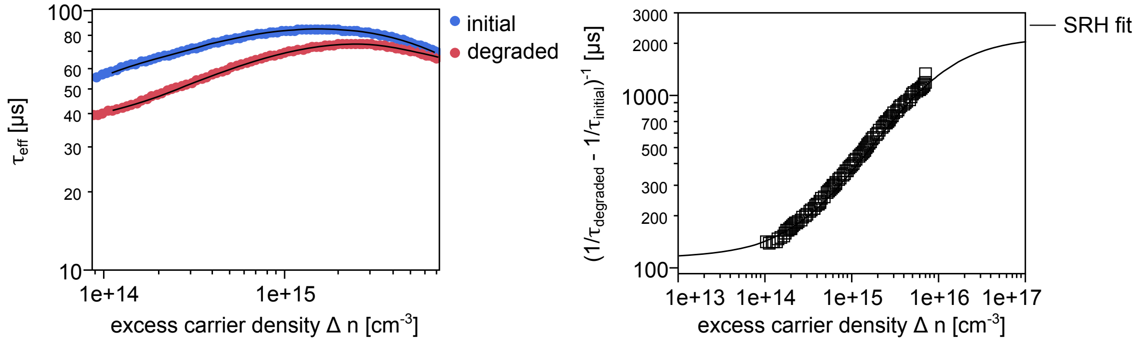

Fig. 4.42: Left hand left: Injection dependent lifetime curves as recorded before (blue) and after degradation (red). Right hand side: B_s-O_x defect curve as extracted according to **Eq. 4.4** and fitted using *SHR* formalism.

4.5.4 Simulation parameters

The simulation tool used for the analysis is SILVACO ATLAS that allows for simulation of solar cells using multiple bulk defects. This is a function that was made use of when simulating contaminated p-type solar cells in the presence of boron oxygen defects.

The applied solar cell simulation is largely based on commonly used models as summarised and compared in [269, 270] and the set of models has been published by Koduvelikulathu *et al.* in [271]. A detailed list of the used models and the respective references is given in **Chap. 7**.

The varied input parameters were **number of defects in the bulk** (N_T) derived from *SRH* fits of the measured bulk lifetimes and the **effective surface recombination velocity** (SRV) derived from the J_0 measurements. The way how these variables were extracted, is schematically shown in **Fig. 4.43**. The single steps, indicated by the numbers in the figure, are further elucidated in the following list.

Extraction of N_T

1. From the **symmetrical lifetime samples** from **Sec. 4.3.2** and **Sec. 4.4.1** a linear-log function was extracted for τ_{eff}, τ_{bulk} (both at 1 sun illumination) and J_0 against Fe and Cu surface concentration. Several correction factors were already introduced, the equations can be found in **Tab. 4.2**, **Tab. 4.6**, **Fig. 7.3** and **Fig. 7.4**. Several points of these functions (several contamination levels) were chosen (a “sweep” function could not be introduced, yet).

2. The **“defect lifetime”** was calculated by $\frac{1}{\tau_{defect}(x)} = \frac{1}{\tau_{bulk,cont.}(x)} - \frac{1}{\tau_{bulk,ref.}}$, with x being the respective metal surface concentration. As **reference bulk lifetime** $\tau_{bulk,ref.}$ the lifetime at a surface contamination level was taken at 1e+10 cm^{-2} in the case of Fe and 4e+9 cm^{-2} in the case of Cu, leaving the reference bulk lifetime at about 200 μs for the p-type cells and between 600 and 700 μs in the n-type case. This “dynamic” approach was used to compensate for different “blank” values of the non-contaminated samples in the experiments.

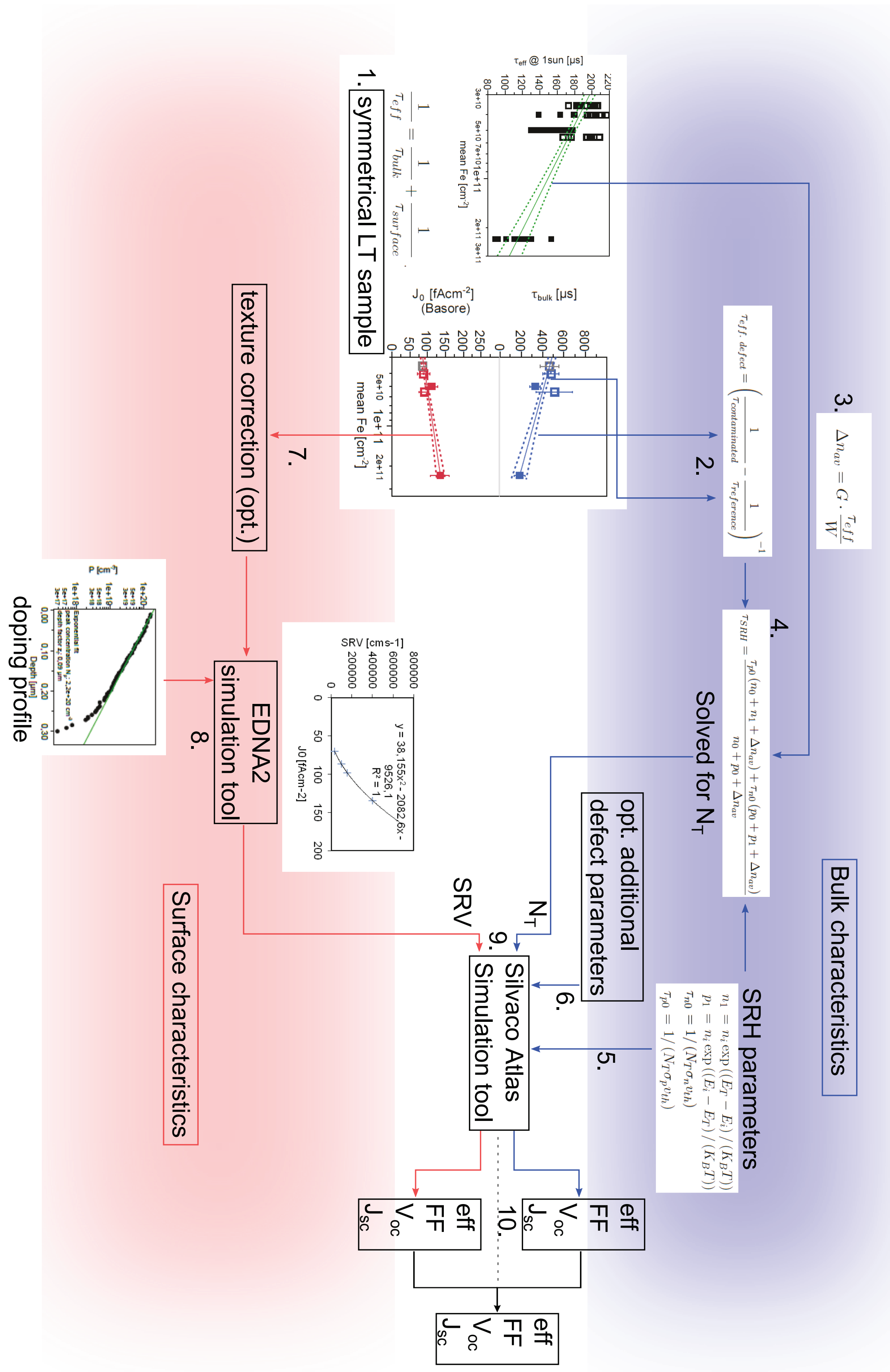

Fig. 4.43: Scheme of the extraction of simulation paramters from the data presented so far. The numbers refer to the numbers in the text.

3. In order to solve the *SRH* formalism correctly, the excess carrier density for the respective bulk lifetime values was required. The **injection level** Δn_{av} at 1 sun illumination in relation to the surface contamination was thus extracted from the linear-log fits of the effective lifetime τ_{eff} plotted against surface contamination using **Eq. 3.30** (cf. **Sec. 3.2.1**).

4. Using Δn_{av} the **trap density** N_T of the different elements present in the material after high temperature diffusion and fast-firing was calculated for several contamination levels. As $\tau_{defect} = \tau_{SRH}$ at the respective injection level, the N_T values were calculated using the *SRH* lifetime calculations[1]. The capture cross sections and defect energy levels, necessary for this operation, were in the case of Cu the deep levels from **Tab. 4.7**, ignoring the shallow level as discussed before, and in the case of Fe the well-known parameters from **Tab. 3.2**.

5. The complete set of *SRH* parameters (N_T, σ_n, σ_p, E_T) was fed into simulation for each contamination level data point.

6. In the case of the degraded p-type samples an additional defect state was introduced (cf. **Sec. 4.5.3**).

Extraction of *effective SRV*

7. As flat wafers were used for the contamination studies, the J_0 values were underestimated. The reason for this is the higher surface recombination due to the enlarged surface area due to random pyramid texturing. To **compensate for the surface texture** a correction factor of 1.5 was introduced that is based on the experimental data shown in **Fig. 4.44**.

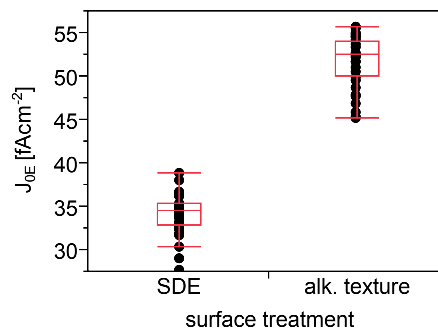

Fig. 4.44: J_{0E} values of textured and flat samples in the same B-diffusion. The medians of the two groups differ by almost exactly a factor of 1.5. A fact that can be attributed to an increase in surface recombination due to the enlarged surface area.

[1] For the fits the *SRH* equation as introduced in **Sec. 3.1.1** was used, which is, as common in the literature, based on Boltzmann statistics for the occupation of the trap levels. How the *SRH* has to be modified to match Fermi-Dirac statistics is demonstrated by Cotter *et al.* in [144].

8. As it is difficult to describe the exact recombination mechanisms related to the highly doped region, as it may interact with the impurities, it was assumed that the impurities only increase the surface recombination. In order to simplify matters, the lifetime contributions of surface-near regions was split into the emitter recombination and surface recombination. The *effective surface recombination velocity*, $S_{r,eff}$, was derived from the J_0 using the web-based emitter modelling software EDNA2 provided by the Australian company, PV Lighthouse Pty. Ltd. and developed by researchers from the Australian National University, Canberra, available online (http://www.pvlighthouse.com.au/calculators/EDNA 2/ EDNA 2.aspx). Details about the freeware 1D emitter simulation software can be found in the articles by McIntosh *et al.* [272, 273]. A set of models was chosen which is consistent with the models the ATLAS simulation software. The overview of the chosen models and input parameters can be found in the model section (**Chap. 7**) including the fits of the emitter and BSF profiles. The *effective SRV* was varied to match the measured J_0 values. The thus obtained *effective SRV* values were fed into the ATLAS simulation tool. A detailed discussion of the effective SRV is found in [274].

Extraction of data

9. The n-type samples were simulated in two different sets. The SRV and N_T were increased separately. For "realistic" solar cells the **relative losses were added up** (this assumption was checked against samples with both recombination sources present at the same time for two data points and found in close agreement).

10. The solar cells were simulated **without recombination underneath the contacts**. Edler *et al.* have shown that the contact resistance is the main limiting factor for V_{oc} levels in screen-printed solar cells and scales linear with the effective lifetime [275]. Accordingly, the V_{oc} data were used as **"normalising factor"** for slightly different starting values due to differences in initial lifetime. The maximum achievable V_{oc} was taken to be 650 mV in both cases. Accordingly, the linear correction factors for contact recombination were chosen slightly differently. In the n-type case this matched long time processing experience. In the p-type case this was slightly overestimating the experimental data.

General points

Several additional assumptions were made. The main points are summarised in the list below.

- It is assumed that the **bulk defects are evenly distributed across the wafer**, which, especially in the case of Fe, might not be the case. Experimental and simulation data indicate that Fe may penetrate the bulk only to a certain degree during fast-firing (cf. **Sec. 4.3.2**).

- The chosen approach is quite rough. Especially the **impact of the contamination on the emitter is simplified**, as electronic effects of the defects on the space charge

region and the recombination in the space charge region are neglected in this approach. In combination with the previous item, it can be concluded that absolute values can hardly be extracted from the results. It is nevertheless useful for the relative comparison between the processes, states of the material and contaminants.

4.5.5 P-type solar cell simulation results

The simulation of the impact of Fe contamination on solar cell efficiencies from lifetime measurements is not as straight forward as it is in the case of Cu. First of all, as made use of in the section about Fe measurements (cf. **Sec. 3.2.3**), Fe contamination is generally assumed to be present in either of two modifications [276, 277]. A fact that has been disregarded in the previously presented *implied* V_{oc}/lifetime data. All the measurements were performed straight out of the box after processing or long storage periods. It, therefore, can be assumed that the predominant Fe modification that has been discussed as "Fe" actually has been Fe−B [193]. Yet, under illumination the Fe−B pair is split and interstitial Fe is injected into the bulk with different recombination properties [278]. Especially at low injection levels (at which p-type standard solar cells tend to operate) a much stronger reduction of lifetime is observed (cf. **Sec. 4.5.2**).

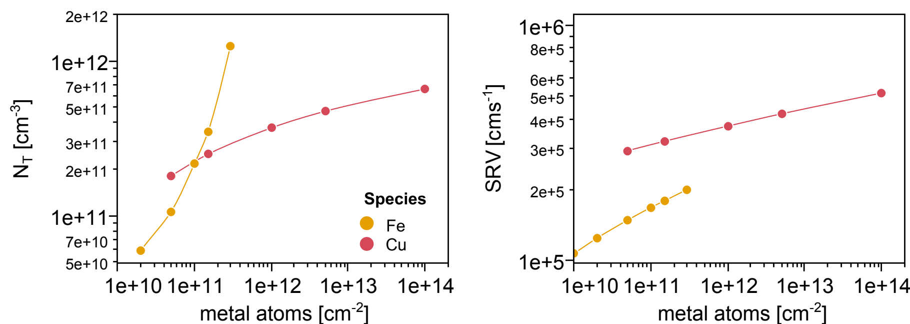

Fig. 4.45: Trap densities N_T and surface recombination velocities SRV used to feed the ATLAS simulation software. Lines are guides to the eye.

In order to investigate the impact of the two species of Fe, Cu and the light induced degradation due to "B−O" pairing on P-type Al-BSF solar cells, the experimental data as plotted in **Fig. 4.21** and **Fig. 4.42** were used to simulate cells on 2 Ωcm material. The N_T values and effective surface recombination values used to obtain the respective simulation data points are plotted in **Fig. 4.45**. The good gettering efficiency of the P-emitter for Cu is mirrored by the small increase in number of traps over a wide range of surface contamination levels. In contrast to this, the Fe bulk concentrations increase to a much more pronounced extend, while the surface recombination only slightly increases.

The simulation results based on the extracted SRV and N_T data can be found in **Fig. 4.46**. In order to estimate the impact of the split of the Fe−B pairs, it was assumed that complete split takes place (which is a common assumption). Thus, the same values for N_T were used in both cases. As a result of this split the bulk lifetime becomes strongly injection dependent. While under low injection conditions (J_{sc} conditions, as carrier constantly leave the solar cell and recombine) the lifetime is drastically reduced, it increases under high

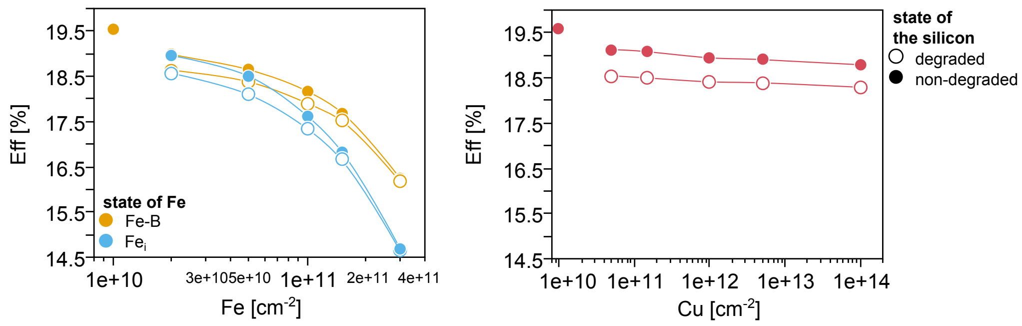

Fig. 4.46: Simulation results for the impact of Fe (left hand side) and Cu (right hand side) surface contamination on non-degraded (solid symbols) and degraded (hollow symbols) p-type solar cells. The different Fe modifications, Fe–B and Fe_i are taken into account. In the non-degraded reference cell (printed at 1e+10 cm^{-2} Fe and Cu) no bulk defects have been assumed (infinite bulk lifetime). Lines are guides to the eye.

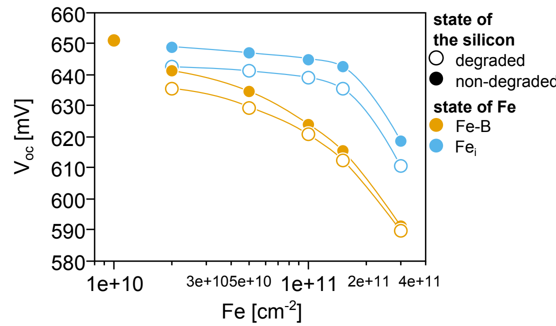

Fig. 4.47: Open circuit voltages for Fe present as Fe–B and as released and present as Fe_i. In the non-degraded reference cell (assumed contamination level: 1e+10 cm^{-2} Fe) no bulk defects have been assumed (infinite bulk lifetime). Lines are guides to the eye.

injection conditions (V_{oc} conditions, carriers are generated and recombine only by internal recombination mechanisms). Thus, as plotted in **Fig. 4.47**, an increase in V_{oc} occurs as soon as the Fe is released as Fe_i. The absolute efficiency, however, decreases—the higher the Fe content, the larger is the gap (cf. **Fig. 4.46**).

Material degradation due to the formation of "B–O" species in uncontaminated samples was also taken into account. It reduces the efficiency of the solar cells by about 0.4 to 0.5% absolute (open symbols in **Fig. 4.46**). With increasing bulk contamination, especially in the Fe case, this gap reduces, as the overall lifetime becomes dominated by the Fe impurity. The efficiency of the non-degraded reference cell (1e+10 cm^{-2} Fe/Cu surface contamination) represents the solar cells with infinite bulk lifetime and reference J_0-values and is thus dominated by other recombination mechanisms, namely surface recombination at the BSF and recombination in the non-contaminated emitter. The mechanisms behind this are surface recombination and Auger recombination. In consequence, the efficiency of the "reference" could only be obtained with purest material (i.e. float zone wafers).

The graphs confirm what has been observed by the *implied* V_{oc} samples: The impact of Fe contamination is much more pronounced than the impact of Cu surface contamination in terms of atoms per unit on the wafer surface, which has two reasons: First, the much higher gettering efficiency of the P-diffusion (the N_T values for large surface contamination values remain small) and second, the much lower impact on the bulk lifetime of Cu defects

due to the relatively small capture cross sections for electrons (being the minority carriers in p-type silicon). In fact, the relatively strong plunge of efficiency due to very small Cu surface concentrations is mostly caused by unrealistic assumptions for J_0 and bulk lifetimes. For higher Cu surface concentration values, only a small decrease in efficiency of only 0.17% absolute in efficiency (less than 1% relative) for the strongest contaminated group is simulated (1e+14 cm^{-2}). The increase in surface recombination caused Fe contamination is much smaller (cf. **Fig.4.45**). Yet, the efficiency degrades strongly (1% absolute in efficiency for as little as 1e+11 cm^{-2} Fe), emphasising the huge impact of Fe surface contamination.

The impact of the Fe contamination observed in the lifetime studies is even stronger when Fe−B paring takes place, which should happen quickly on a sunny day. Accordingly, if solar cells are processed using the investigated diffusion process, considerable care needs to be taken to remove even the smallest remains of Fe from the surface to achieve decent solar cell efficiencies. However, as the response to Cu contamination is much smaller, the cleaning is hardly expected to be improved by changing to oxidative cleaning solutions.

4.5.6 N-type solar cell simulation results

The input parameters for the simulation of the dependence of bifacial n-type solar cells (BiSoN) fabricated from 8 Ωcm material on surface contamination levels as present before the two high temperature diffusion steps are plotted in **Fig. 4.48**. The B-diffused emitter of the solar cells is found on the front side, the P-diffused side on the back side.

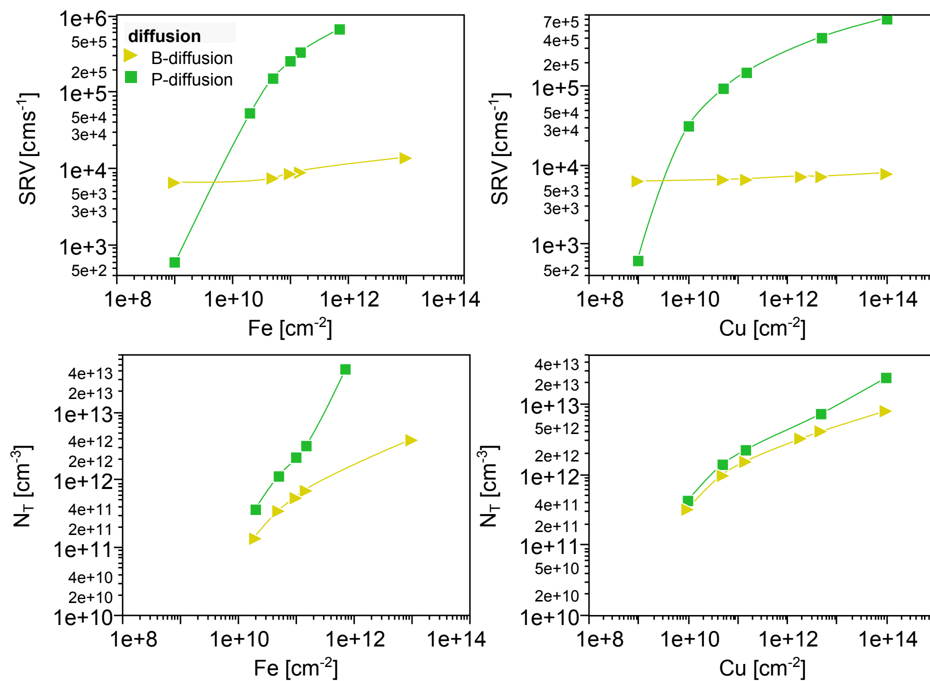

Fig. 4.48: Surface recombination velocities and trap densities extracted from the lifetime samples. Lines are guides to the eye.

The data from **Fig. 4.48** reveal the strong impact of both Fe and Cu on recombination in emitter near regions of P-diffused samples, in the graph denoted as *SRV*. In contrast to this, the *SRV* of B-diffused samples hardly increases.

The number of traps N_T increases much more pronounced, if the Fe contamination is present before the P-diffusion. For Cu these values increase to a similar extend for both diffusions.

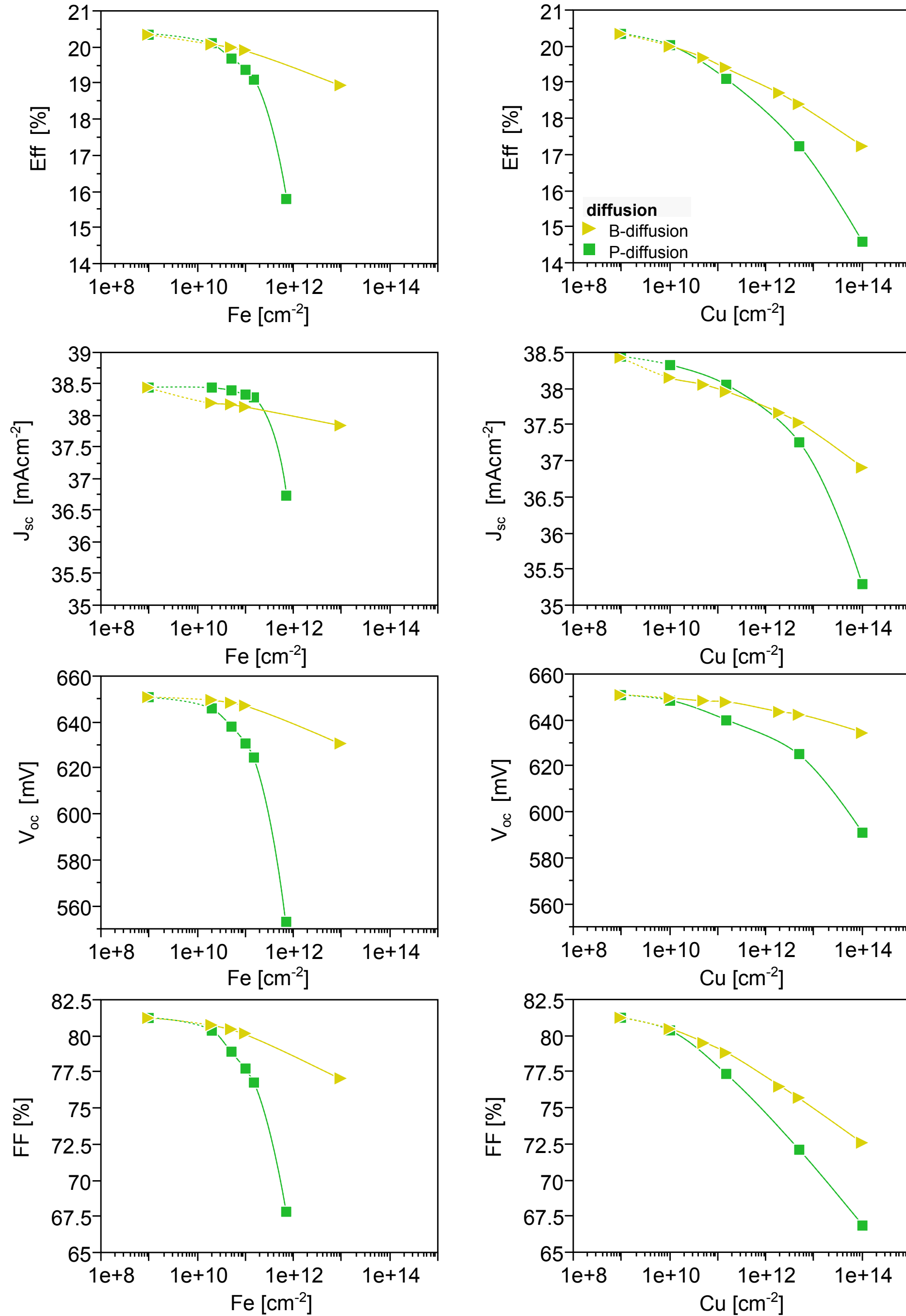

Fig. 4.49: Results of simulation of the impact of Fe and Cu present before B- and P-diffusion on the solar cell parameters. The reference cells (assumed contamination level: 1e+9 cm^{-2} Fe and Cu) are simulated as solar cells without bulk defects (infinite bulk lifetime). Lines are guides to the eye.

The impact of N_T and SRV combined on the solar cell parameters is plotted in **Fig. 4.49**. Similar to the p-type case the reference cells (at 1e+9 cm^{-2} Fe and Cu) represent cells with N_T and SRV values too small to affect bulk and surface recombination properties. Therefore, the reached efficiency with almost 20.4% is thought to be overestimated (only obtainable in

extremely low defect density material, such as float zone wafers).

The top left graph in **Fig. 4.49** shows that high efficiency solar cells above 20% are expected to require Fe contamination levels before P-diffusion below 2e+10 cm^{-2}. The decrease in efficiency below a 1% relative threshold[1] for the B-diffusion does not take place until surface concentrations above 1e+11 cm^{-2} (≈2e+11 cm^{-2}) are reached. On the other hand, the drop in efficiency in the case of the P-diffusion is expected to be much sharper: Concentrations of 5e+10 cm^{-2} are calculated to surpass the 1% threshold. The decrease in efficiency in the case of the emitter diffusion (B-diffusion) is mostly triggered by a loss in short circuit current, while the open circuit voltage remains relatively stable, indicating the high sensitivity of the emitter towards the effective *SRV*. In the case of the BSF diffusion (P-diffusion), the strong increase in both, the *SRV* and N_T, causes the efficiency to drastically decrease for the smallest Fe surface contamination values, mainly driven by the sharp loss in V_{oc}. The back side recombination (even if strongly increased) hardly affects the current generation under short circuit conditions. This can be explained by the effect that the generation rate of electron-hole pairs at back-side is small compared to the front side and the bulk of the solar cell.

Also in the case of Cu, the P-diffusion is simulated to be more sensitive towards Fe and Cu surface contamination. The surface concentration values, for which a significant loss in efficiency (below 1% relative) is expected, is approximately 3e+10 cm^{-2} and for the B-diffusion approximately 4.5e+10 cm^{-2}. These values are much lower than in the standard p-type solar cell case (by several orders of magnitude), indicating that highly efficient cleaning for Cu residues on the surface is required.

4.5.7 Conclusion

The impact of surface contamination as present before high temperature diffusions was simulated based on the experimental data presented so far and injection dependent lifetime measurements. The V_{oc} versus Fe/Cu surface concentration curves closely resemble the *implied* V_{oc} curves in shape. This indicates good agreement of the V_{oc} values simulated from J_0 and τ_{bulk} measurements (by QSS-μPCD) with the direct measurement of the *implied* V_{oc} (by QSS-PC). From experience, differences in *implied* V_{oc} of lifetime samples are a valuable measure to study the impact of process variations on the final solar cell device, and thus high validity of this approach may be assumed.

Of course, the experimental confirmation of the simulation results is still missing. One reason, why the impact of the metal surface contamination could have been mismatched by the chosen approach is, that apart from the effect of fast firing on gettered Fe in the P-diffusion, other interrelations between diffusion and other process steps have been neglected. Two interrelations to name would be the co-diffusion in the n-type case and the gettering due to Al-Si alloy formation at the back-side in the case of the Al-BSF solar cells. The co-diffusion might cause both investigated elements to redistribute in the wafer and potentially

[1] Output efficiency of a solar cell line is always subject to cost calculations. Lower efficiencies due to surface contamination may be acceptable, if more thorough cleaning increases the price per cell to an extend that is not covered by the overall performance gain. 1% is assumed to be the acceptable loss in this case.

reach the opposite side of the wafer during cooling, depending on which side proves to be the thermodynamically favoured gettering sink. This is a process that might also be influenced by the slope of the cooling ramp. The Al-Si alloy has been shown to be a highly effective gettering sink for transition metals, if they are able to reach the backside of the cell. Cu could easily be gettered, without changing much of the outcome due to the low sensitivity of the p-type P-diffusion. Fe, however, is not expected to traverse the wafer to a large extend (as the Fe source is the surface near regions). Furthermore, as the Al-BSF solar cell structure is more and more replaced by PERC structures with a much more limited gettering capacity at the backside due to only local contacting, the relevance of this gettering mechanism is expected to cease.

4.6 Summary and outlook

The main focus of this section was the impact of Fe and Cu surface contamination on several solar cell processing steps. Fe and Cu were chosen as they were assumed to be the most relevant contaminants in a solar cell processing line. In order to study the mentioned impact, a tailored intentional contamination setup was developed. Wafers were contaminated in a sequence that mimics common solar cell batch process tools. The contaminating species was added to DI water rinsing baths. Linear (Fe) and quadratic (Cu) relationships between measured concentrations in the rinsing bath and the wafer surface were found. The investigated DI rinsing bath concentrations of Fe and Cu between 25 and 420 ppb produced surface concentrations in the range of 1e+10 to 3e+11 cm^{-2} in the case of Fe and 1e+10 to 1e+14 cm^{-2} in the case of Cu. Special care needed to be taken when adding metal salts to near neutral DI water: The measurement bath concentrations (after acidifying) showed much lower values than expected. This was explained by the instability of Fe under the chosen conditions. Only measured values were used for fitting of the data.

Accordingly contaminated n- and p-type wafers were then processed in order to study the impact of the varying surface contamination levels on common solar cell surface passivation and high temperature diffusion processes by processing symmetrical lifetime samples. In order to simplify the comparison of the impact of surface contamination on lifetime samples (and simulated solar cells), a threshold value was defined: 1% loss of *implied* V_{oc} (and efficiency), corresponding to 6.5 to 7.1 mV (0.16 to 0.2% absolute in efficiency). The surface concentrations, as deduced from the data collected in this chapter, are summarised in **Tab. 4.8**. From the equations of **Fig. 4.8** in **Sec. 4.2.2** Fe and Cu concentrations in DI water at near neutral concentrations were calculated (as measured by spectrophotometric determination in acidified solution).

Examining different surface passivation steps for p-type PERC back side passivation (thermal oxide/silicon nitride and all-PECVD passivation stacks), it was found that Cu drastically increased the surface interface trap density, D_{it}, while Fe was driven to a large extend into the silicon bulk. Generally speaking, the passivation steps turned out to be most sensitive to surface contamination, when comparing them to emitter/BSF diffusion processes. This is due to their lack of gettering sinks where the contamination could (at least partially) be deactivated in terms of recombination activity. It was found that especially Fe has an highly detrimental impact on the *implied* V_{oc} at surface concentration values as small as 4 to 5e+10 cm^{-2}, concentrations just above the limit of quantification of the used sandwich-etch ICP-MS method. Cu increased the surface interface traps for concentrations below 1e+11 cm^{-2}, but only drastically reduced the measured *implied* V_{oc} above concentrations of 1e+11 cm^{-2}. The low temperature PECVD passivation $MSiN_x$ turned out to be less sensitive towards Cu (but not towards Fe) contamination compared to the thermal oxide based passivation stack.

The investigated P-diffusion (without the removal of the PSG) for p-type processing was less affected by the surface contamination compared to the surface passivation steps. The *implied* V_{oc} differences were smaller and especially Cu hardly affected the diffusion at all. However, the impact of relatively small Fe contamination values was still large. A drop

Tab. 4.8: Summary of critical Fe and Cu surface concentrations for different sample structures. "Critical" applies to a loss of 1% in *implied* V_{oc} (≈7 mV). Ranges are given when extrapolation was used. >/< signs indicate relatively high uncertainty. Values close to the limit of quantification for Fe (4e+10 cm^{-2}) have to be treated with care, as deviation of the experimental data was relatively high. The concentrations in water are calculated from the surface concentrations based on the equations from **Fig. 4.8** in **Sec. 4.2.2**. Rough magnitudes are shown and exact values are given in parenthesis.

			Fe critical concentrations		**Cu** critical concentrations		
type	sample structure	**Fig.**	on surface [cm^{-2}]	in DI water [ppb]	on surface [cm^{-2}]	in DI water [ppb]	remarks
p	therm. oxide / SiN_x	**4.9**	4e+10 – 5e+10	≈40 (30 – 49)	1e+11 – 1e+12	≈10 (6 – 14)	Fe reduces τ_{bulk}, Cu increases D_{it} drastically.
p	$MSiN_x$	**4.9**	5e+10	≈50 (49)	1e+13 – 3e+13	≈100 (68 – 141)	Fe reduces τ_{bulk} Cu increases D_{it}, but to a smaller extend.
p	P-diffusion / SiN_x	**4.19** **4.20**	5e+10	≈60 (58)	3e+12 – 5e+13	≈100 (29 – 194)	Fe is re-emitted into the bulk by fast firing, very insensitive towards Cu.
n	therm. oxide / SiN_x	**4.28**	5e+10	≈50 (49)	<1e+11	≈5 (<6)	Fe reduces the τ_{bulk}, Cu most likely reduces τ_{bulk} and increases D_{it}.
n	P-diffusion / SiN_x	**4.29** **4.30**	9e+10 – 1e+11	≈100 (123 – 142)	<1e+12	≈5 (<14)	Cu and Fe increase J_0 and τ_{bulk}, Cu is gettered temporarily.
n	B-diffusion / SiN_x	**4.29** **4.32**	2.5e+11	≈400 (420)	<2e+12	≈10 (<22)	Cu is drastically reducing τ_{bulk} after temporary gettering.

in *implied* V_{oc} of more than 20 mV was recorded for 6e+10 cm^{-2}. The mechanism for this eminent drop was found to be the re-emitting of gettered Fe from surface near regions into the bulk during fast firing, stressing the fact that the whole temperature budget of the process sequence needs to be taken into account when investigating the impact of metal contamination. From J_{0E} and effective lifetime measurements the contributions of emitter and bulk regions to the reduction of the *implied* V_{oc} was investigated. As expected, Fe mostly affected the bulk lifetime, whereas Cu increased the surface and/or the emitter recombination.

In addition to that, the effect of diffusion parameters on the impact of surface contamination was studied by diffusing cleaned and non-cleaned samples, using different diffusion temperatures and times. The variation of diffusion parameters produced wafers with different sheet resistances and thus different *implied* V_{oc}. The non-cleaned samples performed worse than the cleaned ones. When analyzing the data closely, no impact of the different diffusion conditions on *implied* V_{oc} of cleaned and non-cleaned samples was found other than on the sheet resistance (no matter if etched back or not, indicating that, within the investigated parameter space, the gettering of surface contamination is not affected by the diffusion conditions). In the same context the sandwich-etch ICP-MS method was used to study the migration of surface contamination during P-diffusion. It was found, that Fe (also Cr and Al)

if present on the surface before diffusion, dissolves mostly in the PSG, whereas Cu is found predominantly in surface near regions at least within the first 15 nm of the emitter structure, where it is mostly deactivated.

Cu showed to be much more critical for thermal processes applied to n-type material than to p-type material (at least partly a consequence of the capture cross sections). This was shown by applying the thermal oxidation passivation to n-type wafers. The drop in *implied* V_{oc} was even more pronounced than in the p-type case. The effect on the D_{it} of the interface was found to a similar extend. The effect of Fe on the thermal oxidation step, on the other hand, was much smaller than in the p-type wafer case due to the capture cross sections favouring n-type material.

The investigated n-type solar cell diffusion process steps (B- and P-diffusion) were found to be relatively efficient in gettering and inactivating surface contamination (of both Fe and and Cu) at first glance. Fe surface contamination was found to be less critical on the lifetime of n-type samples and efficiency of solar cells as in the p-type case. Cu, however, was observed to be gettered only temporarily. This means that it was emitted back into the bulk after it had been found inactivated directly after processing (most likely near the wafer surface). In consequence, the bulk lifetime was drastically reduced. Why the phenomenon of temporary gettering was not observed in all of the processed samples remains unclear. The P-diffusion was shown to be more sensitive towards both Fe and Cu contamination than the B-diffusion.

The J_0 and τ_{bulk} values plotted against the surface contamination present before P-diffusion (for p-type Al-BSF cells) and before P- and B-diffusion (for n-type BiSoN cells) were used to estimate the impact on final solar cell devices by device simulation. For the input of the bulk lifetime SRH-parameters, literature values were used in the case of Fe, as they have been widely accepted. About the SRH recombination behaviour of Cu only little information was found. Therefore, injection dependent lifetime was used to verify literature values. Based on the experimental data, solar cells were simulated using only the deep level defect state (at $E_C - 0.5$). In the case of the p-type samples, the light induced behaviour of "B−O" and "Fe−B" species was taken into account. The results of the simulations are presented in a similar manner as the results of the lifetime samples in **Tab. 4.9**.

From the results it turns out that generally good agreement between simulated solar cells and the lifetime samples was obtained. Critical concentrations were found to be in slightly lower regions, which can be explained by the fact that increased recombination not only reduces the V_{oc} (as predicted by the *implied* V_{oc}) but also the J_{sc} and FF.

The simulations of the p-type cells stress the high sensitivity of the investigated P-diffusion towards Fe contamination, whereas the cell efficiency is hardly affected by Cu contamination. In contrast, the n-type diffusion processes are much more sensitive towards Cu surface contamination indicating the need of highly efficient oxidative cleaning solutions employed as pre-diffusion clean.

The next step in this context would be the manufacturing of solar cells to review the conclusions obtained from the lifetime samples and simulation results. In such a study one key question would be, whether asymmetric samples with both highly doped regions behave as expected or if the diffusion processes interact, e.g. if Fe diffuses to B-side where it is less

Tab. 4.9: Summary of critical Fe and Cu surface concentrations present before high temperature diffusion (Al-BSF and BiSoN), as extracted from the simulation results. "Critical" applies to a loss of 1% relative in efficiency (≈0.2% abs.). Values close to the limit of quantification for Fe ($4e+10\,cm^{-2}$) have to be treated with care, as deviation of the experimental data was relatively high. The concentrations in water are calculated from the surface concentrations based on the equations from **Fig. 4.8** in **Sec. 4.2.2**.

			Fe critical concentrations		**Cu** critical concentrations	
type	sample structure	**Fig.**	on surface [cm^{-2}]	in DI water [ppb]	on surface [cm^{-2}]	in DI water [ppb]
p	P-diffusion (Al-BSF cell)	**4.46**	4e+10	30	>1+14	>290
n	P-diffusion (BiSoN cell)	**4.49**	4.5e+10	40	3e+10	5
n	B-diffusion (BiSoN cell)	**4.49**	2e+11	330	5e+10	5.5

harmful, or not.

Further experimental work is also required to study the effect of BSG/PSG removal. The question that remains here is whether the re-emitting of gettered contaminants into the bulk was prevented, when PSG were to be removed. Of course, other elements, such as Ni, Cr, Ti, etc. would be of interest for similar studies on the sensitivity of the process steps.

Based on such experimental data, the simulations should be refined. The first aspect to be implemented is the shallow Cu level. Also, the presence of other gettering sinks, such as metal contacts, e.g. in the Al-BSF case, have been neglected in the simulation of the solar cells and may be implemented. For better simulations work on the recombination behaviour of the different elements in the highly doped regions would be of interest. Furthermore, the simulations should be used to study the effect of variations such as base resistivity and sheet resistance.

5 Cleaning in solar cell processing

After studying the impact of metal contamination on a number of solar cell process steps in the previous section, this section focuses on the cleaning of wafer surfaces in the context of solar cell processing.

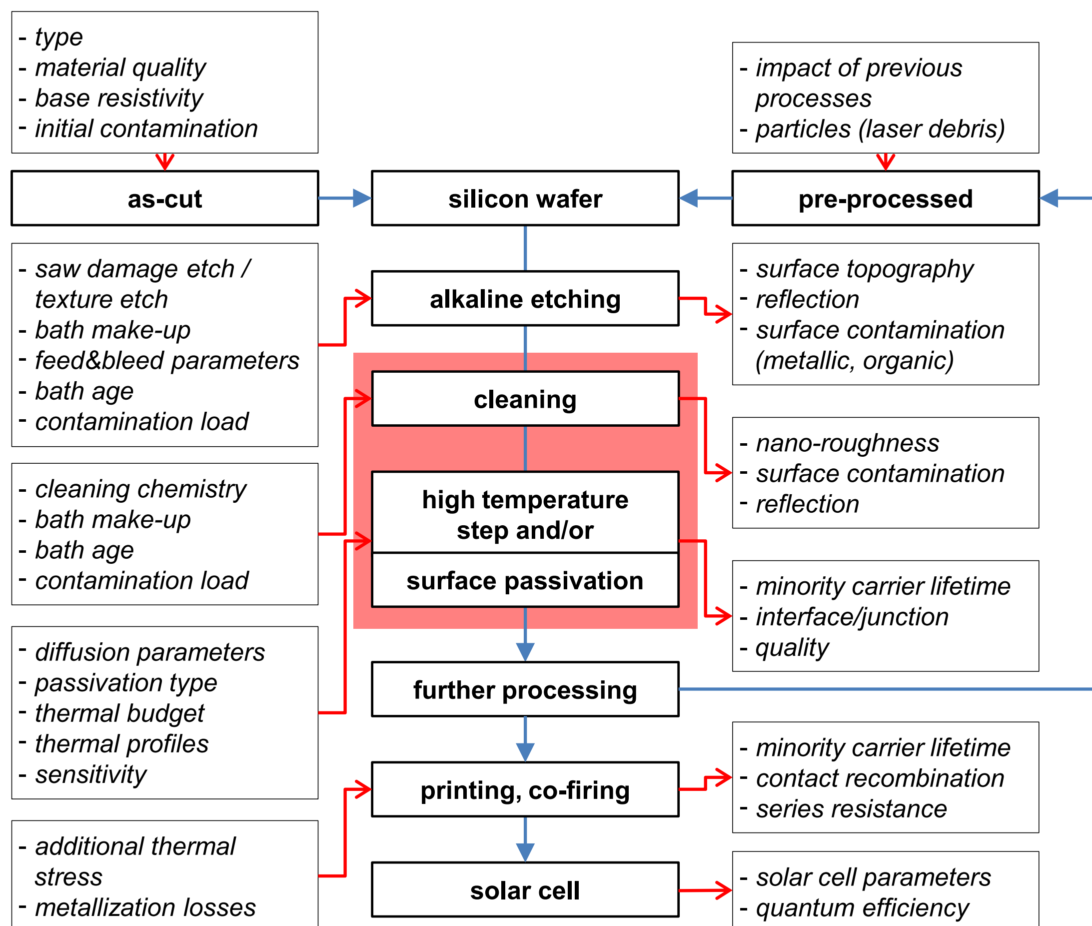

Fig. 5.1: Summary of the relevant process steps, indicating the central system of cleaning before high temperature processing. Including an (incomplete) list of process parameters.

Fig. 5.1 summarises the relevant process steps, including a list of input and output factors (indicated by the red arrows) of the ISC Konstanz high efficiency solar cell process toolbox. The shown sequence can be followed through from as-cut wafer to final cell, when following the blue arrows, independently of the high efficiency solar cell type. In the scheme it is assumed that cleaning is only necessary after alkaline etching, which is true for the aforementioned

ISC Konstanz' high efficiency solar cell process sequences (BiSoN, PERC, etc.). There are, however, plenty of other variations that may require wafer cleaning after other process steps, such as acidic single sided polishing, phosphorus/boron silicate glass removal, etc. However, the requirements for these cleaning steps are—most of the times—far less demanding than cleaning after alkaline etching.

This chapter is split into three main parts: First, the main source of metal contamination is investigated: the as-cut wafer. Different sawing processes are compared and the interaction with FEOL alkaline etching is discussed (**Sec. 5.1**).

The second part is dedicated to the comparison of different cleaning techniques used in standard (**Sec. 5.2**) and high efficiency solar cell processes (**Sec. 5.3**). A process sequence for the comparison, benchmarking and process optimisation of cleaning processes is suggested (**Sec. 5.4**). This sequence is then used to develop, optimise and test a straight forward cleaning sequence for high efficiency solar cells based on dissolved ozone (**Sec. 5.5** and **5.6**).

In the third part of this chapter, the effect of surface roughening/smoothing of cleaning solutions is studied and the effect on solar cells investigated (**5.8**).

5.1 The as-cut wafer and FEOL etching

It has been shown that slurry sawn as-cut wafers are the main source for metal contamination introduction in the solar cell process [7]. In the following the impact of the sawing technique on the initial surface contamination is investigated in more detail. In **Sec. 5.1.1** the loose abrasive slurry sawing technique is compared to the fixed diamond particle abrasive wire sawing technique. Furthermore, the homogeneity of surface metal contamination within an ingot is checked in order to get an idea of process variations, when treating as-cut wafers. In the next section (**Sec. 5.1.2**) the interdependency between the wafer surface contamination and the two most common alkaline etching techniques, namely saw-damage and texture etch, is studied.

5.1.1 Analysis of sawing residues

The residues of the sawing process on as-cut wafers sawn by the different sawing techniques was compared. For this purpose one column of each, n-type and p-type, 156 x$\dot{1}$56 mm^2 pseudosquare Cz-silicon wafers was cut in half. One half was sliced into wafers by diamond wire sawing, the other half was sliced conventionally by the slurry sawing technique. The p-type wafers were used for the surface contamination studies. The homogeneity of the surface contamination across the column was investigated by analyzing wafers from both ends of the column. The distribution and the respective IDs (all wafers were laser coded for further processing) of the analysed wafers can be found in **Fig. 5.2**.

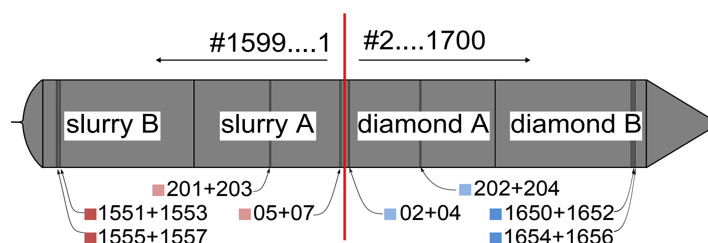

Fig. 5.2: Column prepared for the analysis of the impact of the sawing process. The colours and wafer ID numbers correspond to surface contamination measurement results from **Fig. 5.3**. About 700 to 800 wafers were cut from each half of the brick.

The surface concentration of the wafers, indicated in **Fig. 5.2**, was measured using the sandwich-etch ICP-MS technique introduced in **Sec. 4.1.1**. An array of elements was analysed that was chosen according to the subjected harmfulness as discussed in [208]. The surface concentration of the chosen elements of the two different sawing techniques are plotted in **Fig. 5.3**. Mo is detected using neither of the sawing techniques, which is good, as according to one of the first and most extensive studies about metal impurities by Davis *et al.* from 1980 [279], Mo was found to be the most effective solar cell “efficiency killer”.

Of the other transition elements the highest concentrations were measured for Fe and Cu (up to 2e+13 and 2e+14 cm^{-2}). Cu concentrations are highest on slurry sawn wafers, which was to be expected, as the steel wires used for the slurry sawing process are usually Cu coated. Interestingly, the Cu concentration of the diamond wires is still relatively high

(>2e+13 cm^{-2}). The base material of both types of wires appears to be steel, as Fe shows up in comparably high concentrations on both kinds of wafers. Ni and Cr are found to a similar extend as Fe on the diamond wire sawn wafers. On the slurry wire sawn wafers the Ni and Cr concentration is about one order of magnitude lower. From the high Ni concentrations on the diamond wires it may be concluded that the wires were Ni coated (which is a common coating of diamond wires). Mn and Ti follow in terms of magnitude and are, just like Cr, most likely part of the steel alloy making up the core of the wire.

Of the lighter elements highest concentrations of Al were measured. However, the variation between values is relatively high (a phenomenon observed throughout this work). Similar amounts for both sawing techniques are found of Na, K and Ca. Over origin of these high concentrations of alkali and earth alkali elements and Al can only be speculated. As the concentrations look similar, the post sawing treatment would be most likely the cause instead of sawing process related contamination sources, such as the slurry.

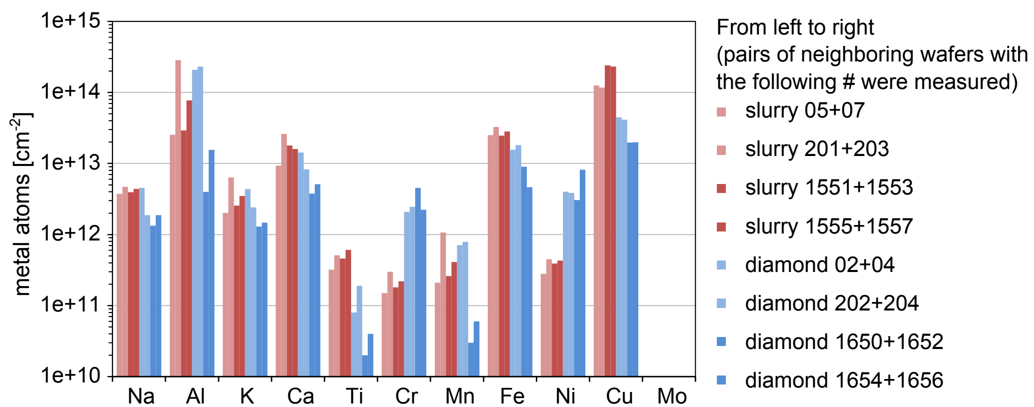

Fig. 5.3: Surface contamination of as-cut wafers. The numbers of the sampled wafers refer to **Fig. 5.2**.

Significant differences between one end of the brick and the other are detected for Cu for both sawing techniques and, in the case of the diamond wire sawn wafers, also for Al, Fe, Mn and Ti. The only difference that can be explained plausibly is the difference of Cu concentrations in the case of the slurry sawn wafers (by a factor of two). The Cu coating of the wire is "sawn off". The differences between ends that were measured in the diamond wire case point are due to the fact that a similar mechanism of progressive wire abrasion occurs when using a diamond wire saw.

Conclusion

It can be stated that every wire sawing technique leaves its "fingerprint" on the wafer surface. The surface concentrations of elements can differ by up to one order of magnitude or more between different sawing techniques. The largest differences between the sawing techniques were measured for Ni, Ti and Cr. The main contaminants (of the transition metal group) with the highest concentrations, however, are the same: Fe and Cu. Between wafers from the same brick, sawn with the same method, this difference is much smaller (a factor of two between inlet and outlet of the sawing wire was observed).

5.1.2 Alkaline etching

Most high efficiency solar cell processes start with alkaline etching (cf. **Sec. 2.5**) in order to remove the saw damage of the as-cut wafer. High surface contaminations have been measured after alkaline etching (saw damage etch and alkaline texturing) [20, 201], due to the high metal content of common bases and the low solubility of metal species at high pH values [280]. However, a conclusive relation between initial as-cut surface contamination, alkaline etching bath and surface contamination after etching has not been given. The development of new cleaning recipes and the supervision of cleaning baths in mass production require knowledge about the underlying dynamics. In the following, the impact of the saw damage etch and the texture etch on surface contamination is investigated with a special interest on the dynamics of surface contamination over the lifetime of alkaline etching baths. Last, the difference between alkaline etching at different points of the solar cell process sequence is addressed.

Saw damage etch

The saw damage of Cz-wafers at ISC Konstanz is removed in a hand wetbench. Carriers of up to 50 wafers are dipped into a 40 L etching bath of 22%wt. NaOH that is heated to 80°C. The bath is recirculated and constantly kept at that temperature (by cooling and/or heating). For the following experiment the bath was freshly made up from NaOH pellets for each of the series of experiments. The concentration was not adjusted over time, the slowing of the etch rate was compensated by adjusting the etching time, due to practical reasons. This is in contrast to industrial applications, where the etch rate is kept constant by adding fresh chemicals (feed) and removing some of the old etching bath (bleed). Apart from this, the etching bath that was used is basically a shrunken version of a typical industrial bath with a similar ratio between carrier size and bath volume. The etching time was adjusted to reach 9 to 10 μm etch depth per side. The wafers were processed in batches of four wafers and then 50 wafers and surface contamination was measured after extensive rinsing after varying amounts of processed wafers.

Fig. 5.4 shows the elements for which a trend across the investigated numbers of etched wafers was extracted. The same array of elements as in the as-cut wafer analysis section before was investigated. The data were fitted using exponential fits (3P). For the lighter elements no trend was found. Two different types of species can be extracted according to the main origin of the contaminants: the etching bath or the as-cut wafers. They can be discriminated by the fact that the surface concentration of the element is higher before or after etching.

A great deal of Fe, Ni and Mo stem from the etching bath. When no feed-and-bleed is applied, wafers will “clean” the bath from these species relatively quickly. As soon as the bath is “clean” the surface contamination on the etched wafer is expected to equal the initial value before etching. From the fits it can be concluded that the initial as-cut surface concentration of Ni is reached after 350 wafers. Fe and Mo are expected to reach the point of equilibrium roughly after a thousand to a couple of thousand wafers. Beyond this point the

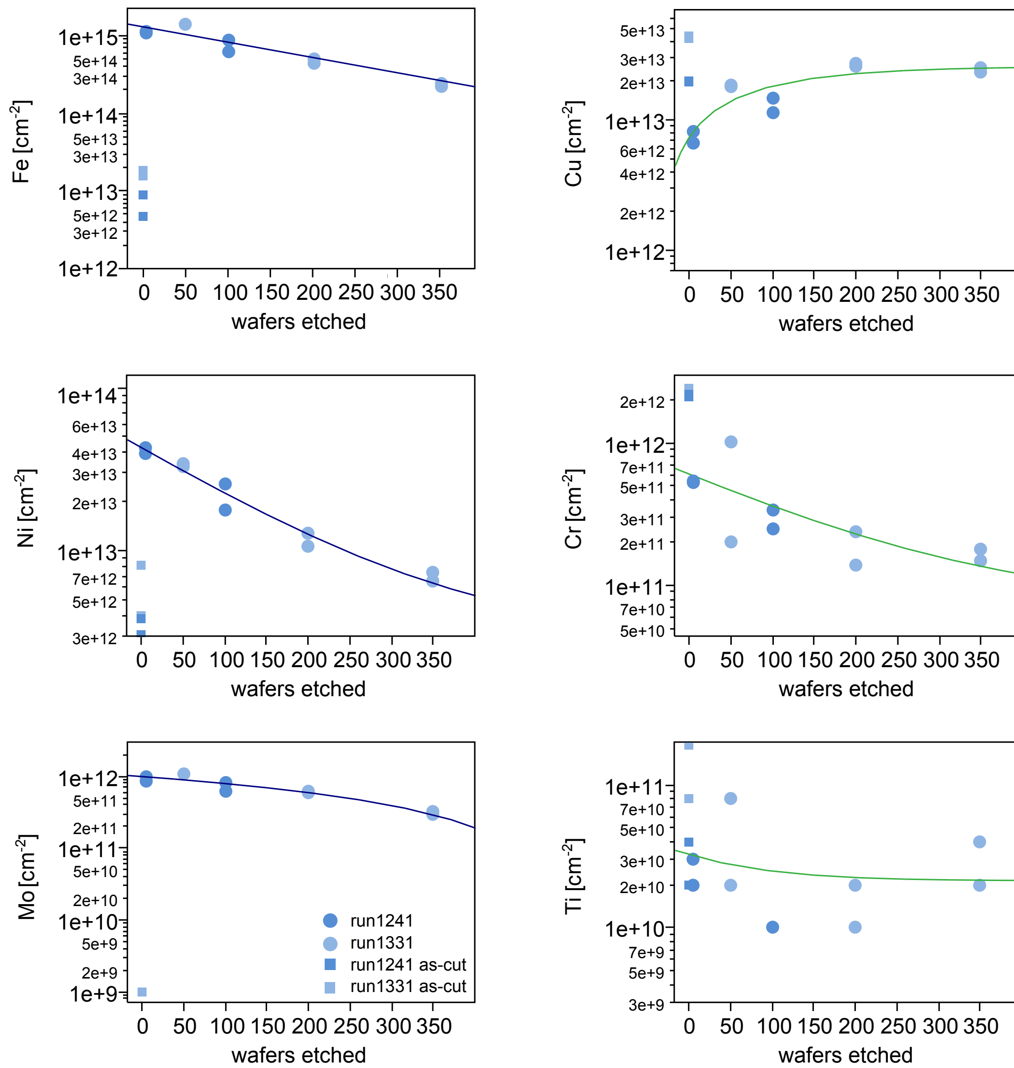

Fig. 5.4: Surface contamination before and after etching. Left hand side: elements stemming from the etching bath; right hand side: elements stemming from the as-cut wafers. The diamond wire sawn p-type wafers from the previous section were used in two experiments (in the first experiment wafers with small digit IDs, in the second with high digit IDs were used, cf. **Fig. 5.2**). The initial surface contamination (before SDE) can be found in **Fig. 5.3**

intake (by wafers) will equal the outtake, following the assumptions of a chemical equilibrium between contamination species in solution and on the surface. This is the case, when no fresh chemicals are added. In mass production, however, "fresh" contaminants are added under feed-and-bleed conditions. Consequently, the equilibrium will shift towards higher surface contamination and become mostly driven by the quality of the etching bath and the feed-and-bleed amount.

The main source for Cu, Ti and Cr, on the other hand, is the as-cut wafers. Without feed-and-bleed the wafer surface contamination is firstly expected to be removed from the wafer surface and thus to be enriched in the bath. Eventually, the surface contamination after etching will saturate in the range of the initial surface contamination. When operating in feed-and-bleed mode, the expected equilibrium concentration will remain below the intake contamination concentration. The etching bath is expected to have a cleaning effect. The

extend of this cleaning effect depends on the feed-and-bleed conditions. The more of fresh etching bath is added, the "cleaner" the wafers are after leaving the bath. The two so-far discussed scenarios, including the effect of feed-and-bleed, processing are sketched in **Fig. 5.5**.

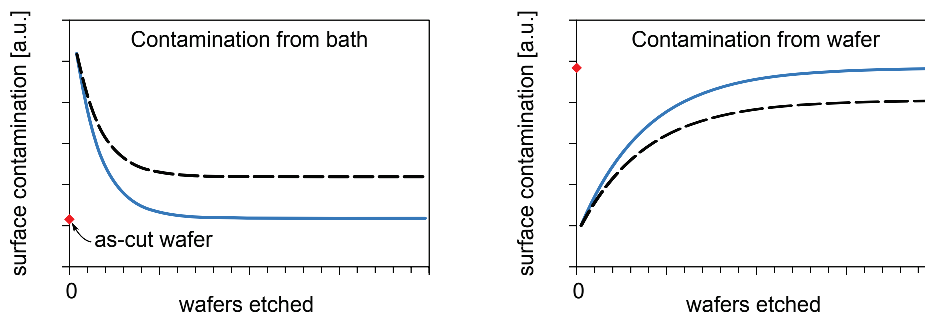

Fig. 5.5: Two different scenarios. Blue lines refer to without feed-and-bleed, dashed lines with feed-and-bleed.

Indicating that the dynamics between surface contamination, bath age and the respective etching bath concentrations in certain cases may be more complicated can be deduced from the behaviour of Ti and Cr. Both elements seem to be removed increasingly effectively for the first roughly 200 wafers. Then the surface contamination appears to be stabilising (Cr) or the element starts enriching again (Ti). Ti is expected to enrich in the bath until "the intake equals outtake" point is reached. Cr might behave accordingly or stabilise as sketched in **Fig. 5.6**. More likely, the Cr surface contamination after etching will eventually start to increase, as Cr is enriched in the etching bath. One can only speculate about the initial increase in removal efficiency of both elements. One of the reasons may be changes in the etching bath, such as the consumption of NaOH or the increase in Si concentration and thus connected an initial increase in solubility.

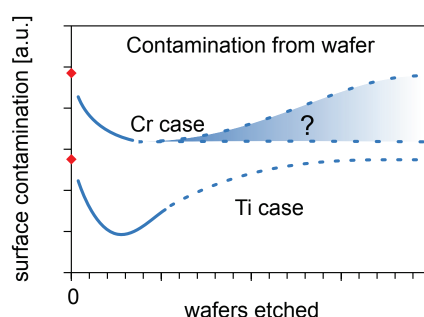

Fig. 5.6: Third observed case of relation between surface contamination and bath age.

Alkaline texturing

A similar study was conducted on the alkaline texturing. Random pyramids on the wafer surface were obtained by etching in 2% KOH with RENA monoTEX® as additive. A similar behaviour of contaminants, as in scenarios extracted in the last section, was expected. Thus, the number of analysed groups was decreased to two data points, one from the first wafers

in a fresh bath and one after a couple of carriers. The results for a number of elements can be found in **Fig. 5.7**. The fits are similar exponential fits (Exponential 3P) as used for the saw damage etching. A third set of data for the exponential fitting are the mean values of the initial as-cut wafer surface contamination, which are expected to be reached after a large, "infinite" number of wafers thus providing the asymptote for the fit. This assumption is made under the pretext of the saw damage etch results. They indicate that under equilibrium condition without feed-and-bleed dosage at some point the bath is saturated and thus intake will equal outtake. The role of the input surface concentration level was investigated by using slurry and diamond wire sawn wafers.

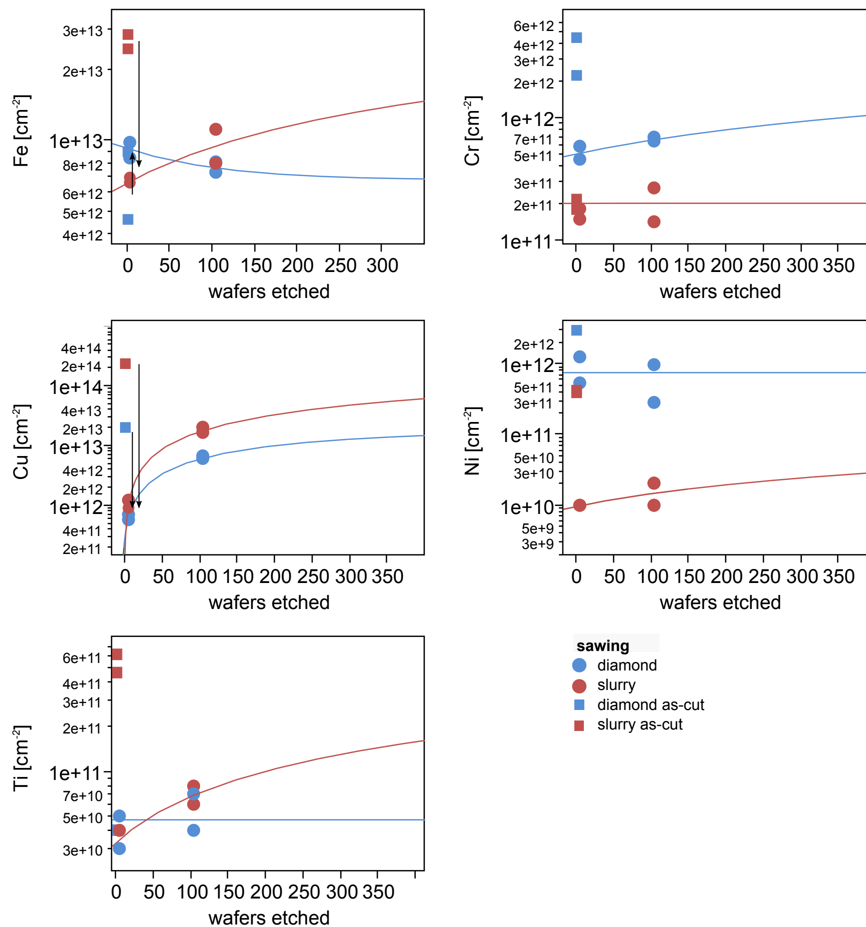

Fig. 5.7: Surface contamination before and after alkaline random pyramid texturing for two different sawing types (run 1331). The arrows indicate the minimum contamination levels stemming from the fresh etching bath.

From the graphs in **Fig. 5.7** several observations can be made. First of all, in most of the investigated cases the metal contamination of the first few wafers is strongly reduced and increases more or less pronounced over the following carriers, i.e. contamination is mainly determined by as-cut wafer contamination (cf. **Fig. 5.5**, right hand side). Cu enriches the fastest, not surprisingly since the initial concentration is the highest. The initial concentration on the surface is expected to be reached within a couple of hundreds or thousands of wafers. Fe, Ni and Cr are enriching much slower indicating a good solubility of these elements.

Taking a closer look at the impact of the difference in initial as-cut wafer surface con-

centration in **Fig. 5.7** (squares) reveals that in four out of five cases (Fe, Cu, Cr and Ti) the wafer surface concentrations after etching of the first wafers in each bath is lowered (or raised) to very similar level, indicating the amount of metal ions stemming from the "fresh" texturing bath. These concentration ranges are thus to be expected, if pre-cleaned wafers are immersed into the bath. The etching bath driven concentrations that can be extracted by the lower "limit" of the surface contamination observed in **Fig. 5.7** are for Fe 7e+12 cm^{-2}, for Cu 1e+12 cm^{-2}, for Ti below 4e+10 cm^{-2} and for Cr 2 to 5e+11 cm^{-2}. If the solubility of the respective contaminant in the bath is very poor, also lower concentrations are to be expected to stem from the bath, e.g. in the case of Cu were very rapid enrichment is observed.

Another striking observation is made in case of Ni on the diamond wire sawn wafers. In contrast to the slurry sawn wafers (which do not have much lower surface contamination values), hardly any "cleaning" by etching is observed, indicating that Ni is differently attached to the silicon surface. Ni, as introduced by the diamond sawing process, can hardly be removed, but remains on the respective level, indicating that either the particle size of Ni (clusters?) is different and/or the particles are deeper "cut" into the silicon surface.

FEOL versus BEOL etching

As shown before, alkaline texturing may be applied later in the solar cell process (cf. **Sec. 2.5.2**). The wafers that are immersed into alkaline texturing solution have been subject to extensive pre-processing and thus the surfaces before texturing are much cleaner. The effect of such clean surfaces before texturing was examined by comparing surface contamination after texturing of as-cut wafers and pre-processed wafers. Each was immersed into freshly made up texturing baths. The data of the first four textured as-cut wafers from **Fig. 5.7** in the previous section were compared to textured clean wafers in **Fig. 5.8**. It was assumed that the measured surface contamination of the first four wafers roughly corresponds to the contribution of the etching bath—lower values may be expected, if the solubility of the surface contamination species in the etching bath is very poor.

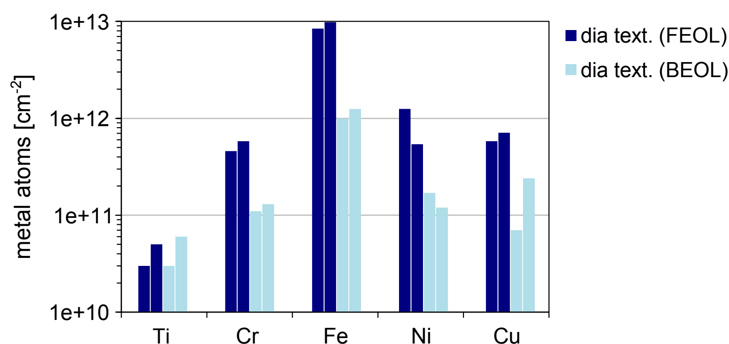

Fig. 5.8: Surface contamination after alkaline texturing: at the beginning of the process (FEOL), data taken from **Fig. 5.7** and during the process (BEOL), texturing performed after SDE, cleaning, diffusion, SiNx capping and HF-dip.

The data from **Fig. 5.8** reveal that this assumption actually holds true. The Ti concentration is measured to a similar extend when comparing FEOL and BEOL. However, the values are quite close to the LOQ and therefore might differ after all. The other investigated

elements show slightly higher concentrations in the case of the texturing of as-cut wafers, indicating that the concentrations measured above are already influenced by the high initial wafer contamination load.

As the surface contamination in the BEOL case is determined by the etching bath, the values after etching on the wafer are expected to be decreasing over time, depending on the feed-and-bleed conditions. Especially when fresh baths are used in the BEOL case, relatively high concentrations (1e+11 to 1e+14 cm^{-2}) are detected, stemming from the alkaline texturing solution. These values are backed by findings on HF/HNO_3 textured wafers, in which similar concentrations were found to be emitted by the diluted KOH (2% wt.) rinsing step, which is necessary for the removal of porous Si [7]. As the values are dominated by the etching bath, the surface concentrations after etching are expected to differ with the kind and grade of the used chemicals. If KOH, for example, is replaced by high quality TMAH, a common alkaline etchant in the IC industry the subsequent cleaning may be strongly simplified. This, however, is hardly feasible due to the high costs of the chemicals.

Conclusion

From the presented results it can be concluded that the chosen method to measure surface contamination before and after etching is well suited to reveal the interaction between contamination intake, etching bath and contamination output.

It can furthermore be concluded that surfaces after alkaline etching require thorough cleaning, especially when as-cut wafers are to be etched (FEOL). In industrial scale production contamination levels after etching are expected to be in the range of initial as-cut wafer contamination levels. In consequence the input of metal contamination into the process sequence strongly dependents on sawing or cutting processes. Saw damage etching of cz-wafers is commonly performed in highly concentrated KOH, which turns out to be the main contamination source at the beginning of a bath life. However, the etching bath gets “cleaned” over time until the surface contamination becomes wafer-dominated—intake will equal outtake, if none of the cleaning bath solution is replaced for feed-and-bleed purpose. When lower concentrations of KOH are used, as in the case of FEOL alkaline texturing, the initial solubility of contaminants is high so that the bath enriches over time until an equilibrium is reached.

When operating in feed-and-bleed mode equilibrium conditions directly relate to the amount of replaced etching bath. If 5% of the etching bath are replaced per batch, depending on whether the etching process is determined by wafer or bath contamination, the equilibrium is expected to settle 5% above or below the assumed case without feed-and-bleed.

When etching “clean” pre-processed wafers (BEOL etching), the surface contamination of the texturing process is typically etching bath governed. As a consequence significant amount of Fe, Cr, Ti and Cu, originating from the etching bath, are found on the wafer surfaces. These values still reach up to 1e+12 cm^{-2}, stressing the need for thorough cleaning after BEOL texturing.

5.2 Cleaning in Al-BSF processing

In order to investigate the necessity of cleaning in standard industrial solar cell processing, cleaning before P-diffusion and SiN_X deposition were varied according to **Fig. 5.9** (run 824). The surface contamination after alkaline KOH/IPA texturing before P-diffusion ("old" emitter, 65 Ω/sq, requires PSG removal) was measured. The resulting surface contamination values are found in **Fig. 5.10**. The applied cleaning sequences are: the standard industrial cleaning (HCl+HF) and the high efficiency cleaning (SPM+HF). One group was diffused without cleaning (no cleaning). In order to avoid potential cross contamination in the diffusion furnace, each group was diffused separately. Solar cells were fabricated according to the scheme displayed in **Fig. 5.9**. Assuming that most of the surface contamination remains near the surface, one half of the wafers was SPM+HF cleaned after PSG removal before SiN_x deposition, while the other half was only HCl+HF dipped. The SPM+HF step, due to the high oxidative potential of the SPM solution, was expected to remove the surface near contamination by removing several top layers of the surface and thus slightly etching back the emitter.

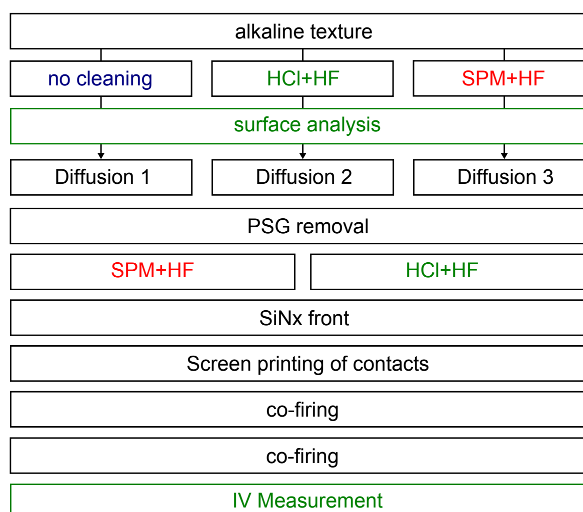

Fig. 5.9: Experiment flow for the determination of the impact of different cleaning sequences and no cleaning on Al-BSF standard solar cells.

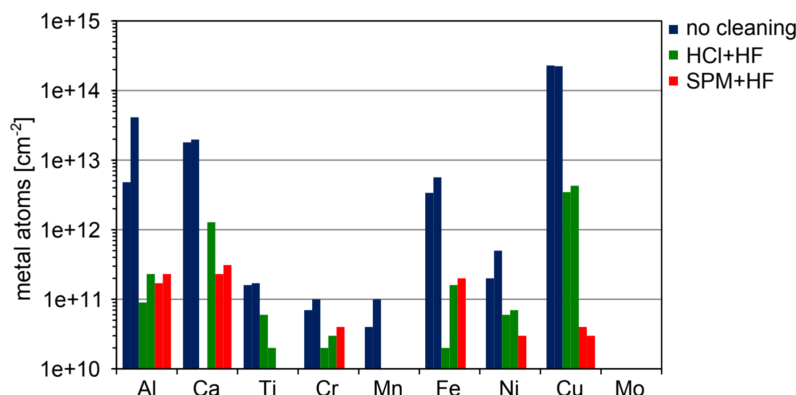

Fig. 5.10: Surface contamination of as-textured, HCl+HF and SPM cleaned wafers.

The surface analysis data reveal especially high concentrations for Cu for the non-cleaned wafers of 2.3e+14 cm^{-2}. The HCl+HF cleaning reduced the contamination by almost two orders of magnitude to about 4e+12 cm^{-2}. The high efficiency cleaning then lowered it down to the level of 5e+10 cm^{-2}. For the other elements the differences between the two cleaning procedures are relatively small. The most pronounced differences are found for Ni and Ti. The deviation in the case of Fe is too large for a definite comparison of the two cleaning methods. Apart from solar cells, lifetime samples were fabricated using the sequence described above to the point of SiNx deposition. Then, instead of being screen printed, the backside of the wafers was passivated in a second SiN_x-PECVD deposition. The lifetime samples were fired using the same firing profile as for the solar cells. The results of these symmetric *implied* V_{oc} samples were compared with the open circuit voltage of the solar cells. The values can be found in **Fig. 5.11**. They show that the *implied* V_{oc} samples nicely predict the differences in V_{oc} found between the groups. No differences between the HCl+HF and the SPM+HF cleaning before diffusion are observed. A statistically significant gain in *implied* V_{oc} and in V_{oc} of about 2 mV is found for the advanced cleaning after the PSG removal. This is independent of the cleaning before the diffusion indicating that the gain does not result from the removal of contaminants of the top layer of the emitter. It rather implies that the emitter is “etched-back” by the relatively aggressive SPM cleaning solution, resulting in a reduced “dead layer”. This is the top region of the emitter in which interstitial phosphorus strongly increases the surface recombination [281].

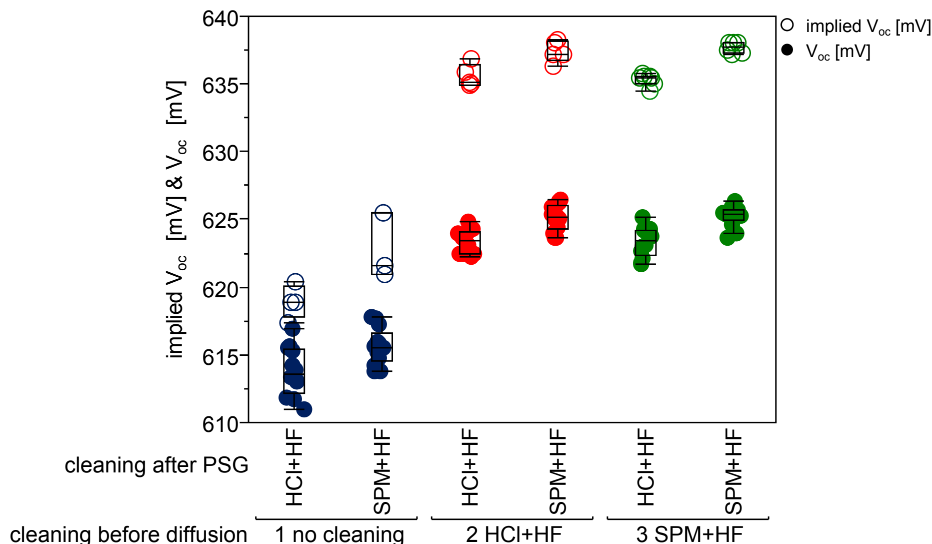

Fig. 5.11: V_{oc} and *implied* V_{oc} of the differently cleaned groups.

When analyzing the solar cell parameters of the different groups in **Fig. 5.12**, it can be observed that, apart from the open circuit voltage, the short circuit current is strongly affected by the different cleaning procedures. The contribution of the surface contamination on the fill factor is small. The efficiency, however, as a function of both short circuit current and open circuit voltage, is strongly reduced by not cleaning before the P-diffusion. The loss is in the range of 0.5% absolute. No difference between the HCl+HF and SPM+HF cleaning

sequence before diffusion was found.

The solar cell current does not only vary between cleaned and non-cleaned samples, but also between the ones with and without the etch back. This difference decreases from the wafers that have not been cleaned before diffusion from 0.20 to 0.18 $mAcm^{-2}$ for the group with HCl+HF and SPM+HF pre-diffusion cleaning. This might indicate that, apart from the etch back effect, to a small extend the impact of surface-near contamination is also reduced. From the data obtained in **Sec. 4.3.2** it can be assumed that the Fe contamination mostly limits the effective minority carrier lifetime by increasing mostly the emitter and the bulk recombination, resulting in an decreased V_{oc} and J_{sc}. However, it has been shown that a large part of the initial Fe surface contamination is gettered in the PSG and subsequently expected to be removed by the PSG etch. The high Cu contamination of the non cleaned samples, which is expected to be present in the region that is to be etched back by the SPM-step (as Cu appears to enrich in the dead layer as shown before), was responsible for the slightly larger gain by the SPM step after the PSG removal. The generally lower efficiency of the non-cleaned samples could thus be attributed to the presence of remaining Fe and of elevated concentrations of other elements.

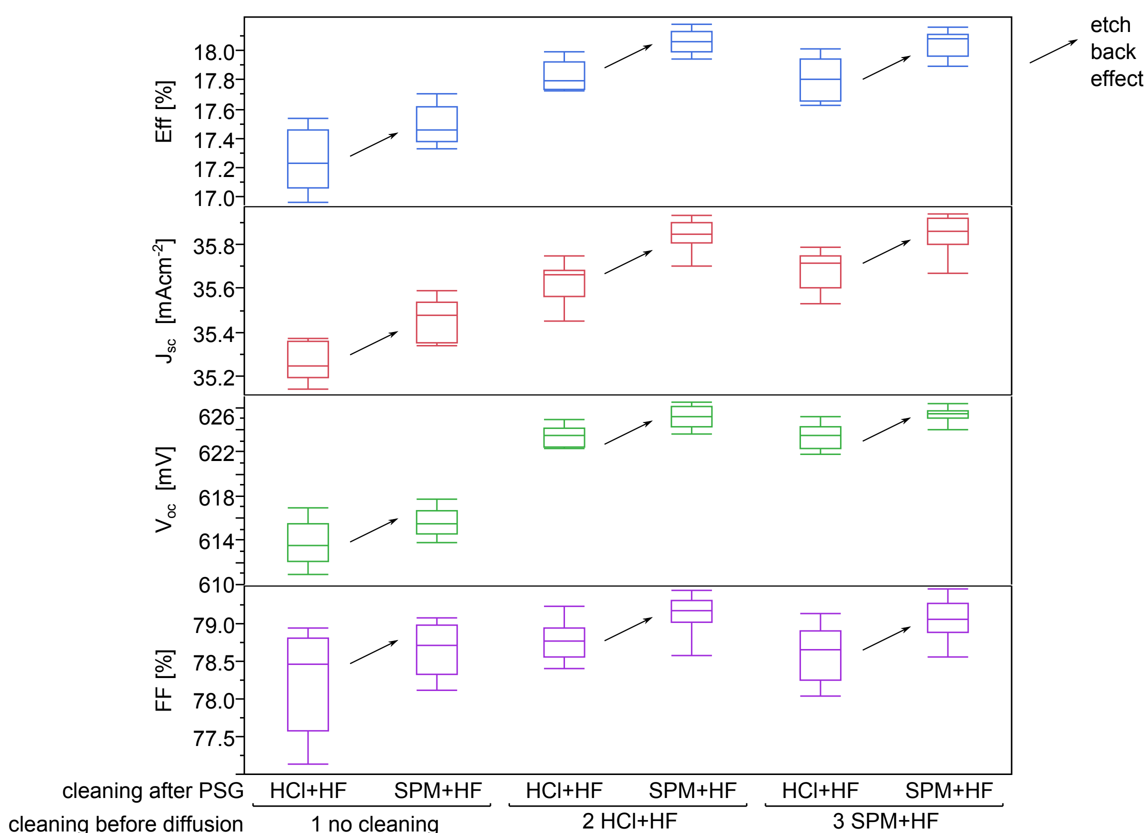

Fig. 5.12: Solar cell parameters from the cleaning variation in the Al-BSF solar cell process.

From this experiment it can be concluded that in standard industrial Al-BSF solar cell processing cleaning is of minor concern. Not cleaning before P-diffusion at all, of course, results in a significant drop in efficiency (about 0.5% absolute in efficiency in this experiment).

More advanced cleaning than a HCl and HF dip sequence on the other hand does not result in a gain in efficiency. Oxidative cleaning after the PSG removal and before the SiN_x deposition does improve solar cell performance in the case of the used emitter. This effect, however, can be mostly attributed to the etch back effect, showing that cleaning systems can also be used for other purposes than removal of surface contamination. In the case of ozone based cleaning this has been further investigated by Moldovan *et al.* in [282].

5.3 Cleaning in high efficiency solar cell processing

The following experiment (run 1076) was designed to shed light on the sensitivity of high efficiency BiSoN solar cell process towards cleaning procedures. Until that point the laboratory-scale production at ISC Konstanz employed high efficiency SPM+HF cleaning before both of the high temperature diffusion steps (detailed description of the applied cleaning sequences can be found in **Fig. 2.21** in **Sec. 2.2.3**). Aiming for the transfer from laboratory scale to large scale mass production, in a first experiment the costly SPM+HF cleaning sequence was stepwise exchanged by the HCl+HF industrial cleaning sequence. The alkaline texturing was followed by the pSC1+HCl+HF cleaning step, in order to remove organic remains of the texturing additive (RENA monoTEX^{TM}) before further SPM+HF wafer cleaning was deployed (summarised as SPM+HF*).

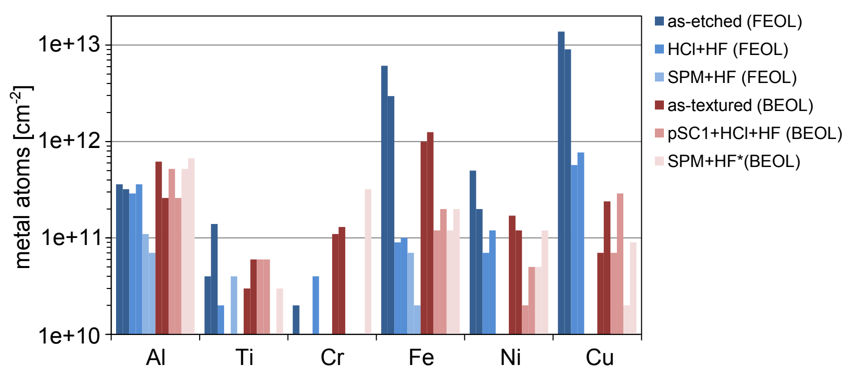

Fig. 5.13: Surface contamination after alkaline etching and the subsequent cleaning steps.

The surface contamination before and after cleaning was measured after both alkaline etching steps (FEOL and BEOL). The results can be found in **Fig. 5.13**. Unfortunately, the surface contamination data are quite noisy. What clearly can be extracted is the much higher initial contamination level after the saw damage etch especially for Fe and Cu. Both are reduced by the HCl+HF cleaning and further reduced (close to or below the limit of quantification) by the SPM+HF cleaning. As expected much lower contamination levels are found after alkaline texturing. Yet, neither of the applied cleaning sequences appears to reduce them much further. Fe, Ni and Cu are even found despite the SPM clean. The Cr peak after SPM+HF of the as-textured wafers is assumed to be an outlier. It appears from the data that the textured surfaces seem to be more challenging to clean, even with lower initial surface contamination before cleaning.

Solar cell parameters for groups of eight to ten cells can be found in **Fig. 5.15**. Both groups with HCl+HF FEOL cleaning show significantly lower efficiencies (as indicated by the non-overlapping rings attributed to the respective groups as determined by the *Student's test*[1]). Each of the possible pairs of groups are compared with each other using the Student's test function implemented in JMP10. Each circle is the graphic representation of the

[1] The student test calculates whether the actual difference of two mean values is greater than their *least significant difference* (LSD). This LSD is the Student's t-statistic multiplied by the standard error of the difference of the two means, with the 0.05 indicating the confidence level (the default value). In simple terms: the Student's test checks, on how the confidence intervals of the respective groups overlap. The Student's test is only fully valid, when distribution of the data follows a Gauss distribution [283].

95% confidence interval (from the confidence level). The larger the variance the larger the circle. The way how the significance of differences between two mean values is determined graphically, is sketched in **Fig. 5.14**.

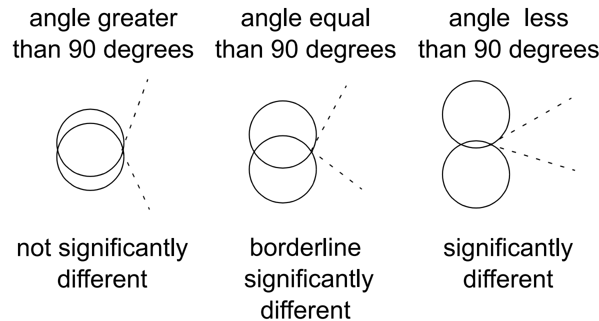

Fig. 5.14: How to read the comparison of groups as determined by Student's test in JMP10 [284].

Means are evaluated by comparing the variance with the respective difference. , despite the fact that surface contamination was found at higher values after BEOL cleaning. When both, FEOL and BEOL cleaning, are replaced by the industrially feasible alternatives, the loss adds up to 0.2% absolute in efficiency compared to the lab-only cleaning group. When only replacing the BEOL post-texture cleaning, no statistically significant loss in efficiency was extracted (the corresponding circles from the student test overlap). A difference in V_{oc} between these groups, however, is already visible but not quite statistically significant.

Concluding from this data, it can be stated that the BiSoN solar cell process sequence is more sensitive to surface contamination present after SDE before the first thermal diffusion than to contamination present after texturing before the second diffusion. Thus more effort has to be taken to replace the FEOL cleaning sequence. The industrial HCl+HF cleaning sequence proved not to be suitable to reach highest efficiencies and alternative procedures suitable for mass production need to be developed.

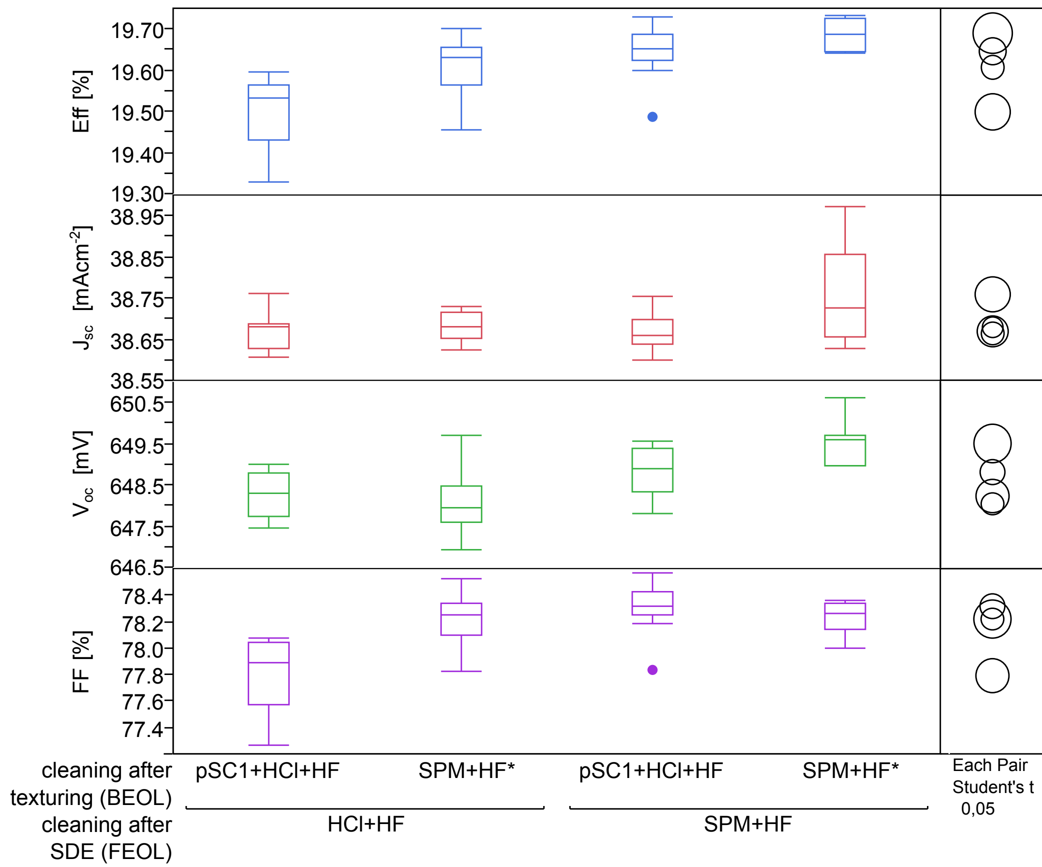

Fig. 5.15: Solar cell parameters from the cleaning variation in the high efficiency BiSoN solar cell process. Statistically significant differences extracted by the *Student's test* between groups are indicated by non-overlapping rings on the right hand side of the graphs.

5.4 Cleaning before high temperature processes

In this section different cleaning approaches from lab-only to industrially feasible are compared in terms of cleaning efficiency. A benchmark process sequence for the qualification of different cleaning was established avoiding the costly surface contamination measurement and solar cell processing. For this purpose the sensitivity of thermal oxidation for surface contamination, as described in **Sec. 4.3.1**, was deployed. The saw damage of p-type wafers is etched in concentrated KOH or the wafers are textured using the respective alkaline solution. The wafers are then cleaned, oxidised and SiN_x is deposited on both sides (using the identical process as described in **Sec. 4.3.1**). After firing, the *implied* V_{oc} of the wafers are measured and the groups compared.

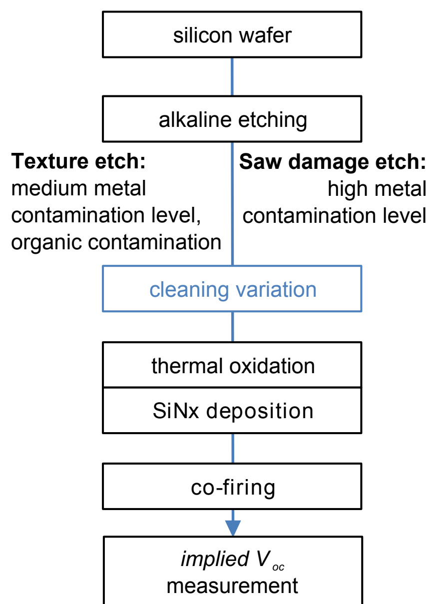

Fig. 5.16: Process sequence for the evaluation and comparison of cleaning processes.

Using the standard high efficiency cleaning sequence (SPM+HF or SPM+HF*) as reference, this sequence allows for the qualitative comparison of different cleaning sequences and methods. In addition to that, results can be immediately transferred to cleaning requirements for p-type back side passivation processes. For further high efficiency processes it can be used for choosing the "best" possible alternative to the costly and not industrially feasible SPM-based reference process. The suitability for the actual high efficiency solar cell process needs then to be tested on lifetime sample and subsequently on solar cell basis.

An example for the comparison of different cleaning methods using thermal oxidation (on p-type wafers) is given in **Fig. 5.17** (left hand side graph). KOH/RENA monoTEX^{TM} textured wafers (without prior treatment) were cleaned using the ISC Konstanz standard cleaning procedures: HCl+HF, pSC1+HCl+HF and pSC1+HCl+HF+SPM+HF (POR).

When comparing the *implied* V_{oc} values obtained after thermal oxidation of the three groups, it can be concluded that the pSC1 step has a vital effect on the surface cleanliness (adding about 50 mV) and that only a small gain is obtained, when the wafers are further cleaned in a subsequent SPM+HF step. The difference between pSC1+HCl+HF and the

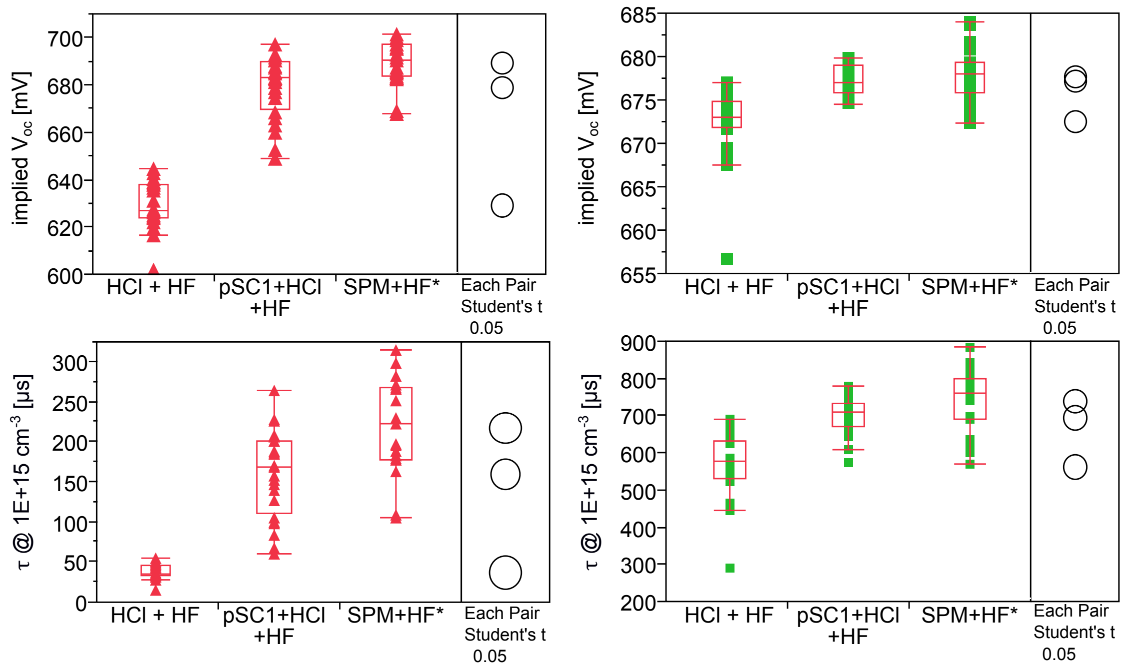

Fig. 5.17: Comparing the cleaning efficiency of ISC Konstanz standard cleaning processes after alkaline texturisation. The impact on *implied* V_{oc} and the respective minority carrier lifetime after thermal oxidation of p-type wafers (left) and on B-diffusion of n-type wafers is studied (run 1113).

POR is small but significant. Before the introduction into the solar cell process every newly developed or optimised cleaning sequence could accordingly individually be tested and compared to the POR.

In order to verify the relevance of the obtained difference in *implied* V_{oc} by the thermal oxidation, in the same experiment identically etched and cleaned n-type wafers were B-diffused. The right hand side graph of **Fig. 5.17** shows the accordingly obtained *implied* V_{oc}. As expected from the previous chapter, the cleaning has a much smaller impact on the *implied* V_{oc}. No significant differences can be detected between the pSC1+HCl+HF and pSC1+HCl+HF+SPM+HF (SPM+HF*) sequence. Differences in effective lifetime (extracted at an injection level of 1e+15 cm^{-3}) can be detected, though, confirming the trend detected by the thermal oxidation process. Median values decrease from 761 to 710 and further to 576 μs for the respective groups. The relative deviation of the lifetime values is large compared to the deviation of the *implied* V_{oc} (as discussed before), which is the reason why for further analysis the *implied* V_{oc} is used. As the differences between the respectively cleaned samples in *implied* V_{oc} are much more pronounced in the case of the thermal oxidation of p-type wafers, due to the high sensitivity to the cleanliness of the surface, it was chosen for the optimisation of cleaning methods. Generally good agreement with other process steps was demonstrated. As indicated in **Fig. 5.16** different requirements in terms of surface contamination (organic contamination and/or metal contamination level) can be taken into account by choosing the respective alkaline etching.

5.5 Development of an industrially feasible ozone-based cleaning process

Cleaning techniques for ultra clean surfaces are hardly feasible for solar cell mass production (RCA sequence, SPM clean). Still, in order to obtain highly clean surfaces for high efficiency solar cell processes, an oxidising cleaning solution is required. A cleaning system containing ozone as oxidising agent has been suggested early in IC manufacturing to replace costly but effective cleaning systems such as the RCA or the SPM cleaning solutions [285, 286]. Ozone can be cheaply and easily generated and has a relatively small half life time in solution so that neither the supply nor the disposal of the waste solution [287] introduce significant extra costs [288]. Good cleaning efficiencies have been shown for IC wafers [289, 290]. Hence, ozone based cleaning solutions appear to fulfill the prerequisites for cost effective solar cell processing.

Several different systems—with and without additives—in ozonated DI water have been investigated in the literature. As shown in the list below, different ozonated mixtures have been reported. The investigated systems (and the respective references) were

- diluted HF [282, 288, 289, 291–293]
- diluted HCl [291]
- a mixture of both [288, 291]
- H_2O only [290, 294, 295].

The studies, in which information about cleaning conditions and cleaning efficiencies was extracted, are summarised in **Tab. 5.1**. All cleanings were followed by a subsequent HF dip unless marked with * (not mentioned in the paper).

Tab. 5.1: Additive concentration used in the literature

additives	concentration range [% wt.]	best cleaning conditions [% wt.]	investigated elements	study
HF *	0.0001 – 1	0.05 ±0.01	Cu	[292]
HF	0.05 – 0.5	for the cleaning of Cu: 0.05 performs better than 0.5	Fe, Cu, Ni	[289]
HF, HCl, HF+HCl	HF 0.1; HCl 0.06; HF 0.1 + HCl 0.06; HF 0.1 + HCl 3.2	@ 95°C; advantage if HCl added	Fe, Cu, Ni	[291]
HF and HCl,	HF 0.25 – 0.5; HCl 0.1 – 1	HF 0.25 + HCl 1 @ 25°C 1 min	Fe, Cu	[282]

Except for [282] all the studies were tests on chemical mechanical polished IC wafers. Furthermore, all the studies cited in **Tab. 5.1** used intentional contamination which does not finally prove whether or not the cleaning would work in a “real” solar cell production environment.

To allow for simple integration into the existing cleaning equipment the sequences were chosen to be similar to the POR, without the initial HCl+HF steps, similar to a cleaning sequence that is often referred to as “IMEC” cleaning sequence (suggested by Meuris *et al.* [97]). As tool for the tests ISC Konstanz’ semi-automated batch wet bench (RENA) was chosen, as it was fitted with an ozone supplied process bath. It was designed to be used as ozone-fed hot water dryer and thus is equipped with a continuous flow heater and recirculation. The ozone is introduced into the process bath via a bubble contactor. Furthermore, the bath is equipped with an optical measurement setup (BMT 964 AQ) so that the effect of ozone enrichment and solubility was investigated and monitored. The ozone generator was operated with 5 bar of oxygen feed and run at a maximal output of 230 g/Sm^3.

5.5.1 Comparison of different cleaning systems

In a first screening experiment (run 954) the effects of different additives and temperatures on the cleaning efficiency was tested. The sequence for qualification of cleaning efficiencies of **Fig. 5.16** was used to compare the tested systems against the process of record (POR), i.e. the SPM-based cleaning sequences (cf. **Sec. 2.2.3**). An overview of the screening experiment is shown in **Tab. 5.2**. The KOH/IPA textured wafers were first dipped into the DI water rinse for two minutes, followed by a ten minutes immersion into the cleaning bath. Each solution was given $>$ 45 minutes for the ozone to saturate. After another dip into DI water (3 min) the oxide was removed in a mixture of diluted HF and HCl (0.8% wt. and 0.2% wt.). Here it turned out, that such low HF concentrations in the subsequent HF/HCl dip are hardly feasible, as it took up to 5 minutes for the wafers to be rendered hydrophobic, indicating a complete removal of the wet oxide created in the O_3-bath. This is the state that is preferred in solar cell processing, since drying of the wafer surface is simplified and watermarks can be avoided.

Tab. 5.2: Tested ozone cleaning systems.

solution	H_2O		HCl		HF/HCl		HF
concentration [%wt.]			0.1		0.05/0.1		0.05
temperature [°C]	25	80	25	80	25	80	25
ozone [ppm wt.]	17.9	1.8	15.9	1.0	18.9	0.5	19.7

Tab. 5.2 shows that the reached concentrations of O_3 varies strongly with temperature. Only very small concentrations were reached when the temperature was as high as 80°C. The relatively high ozone concentration in “only” water group at 25°C can only be explained by insufficient rinsing of the etching bath before filling it with water and thus traces of HF. This was noticed later and corresponds to observations in the literature [296]. At near neutral pH the solubility of ozone is limited to values below 10 ppm wt. For this experiment, however, the small residues of Fe proved to be useful, since all four solutions that were tested at 25°C result in similar O_3 concentrations so that only the influence of the additive on the cleaning performance was compared, not the influence of the ozone solubility. The cleaned wafers were dried in N_2 and subsequently thermally oxidised at 865°C for one hour. Then SiN_x

was deposited on both sides. After firing, the minority carrier lifetimes were measured by QSSPC and the obtained *implied* V_{oc} values were compared against the POR. The results can be found in **Fig. 5.18**. In order to exclude the HF/HCl dip as responsible for the actual cleaning, one set of wafers was only dipped in HF/HCl.

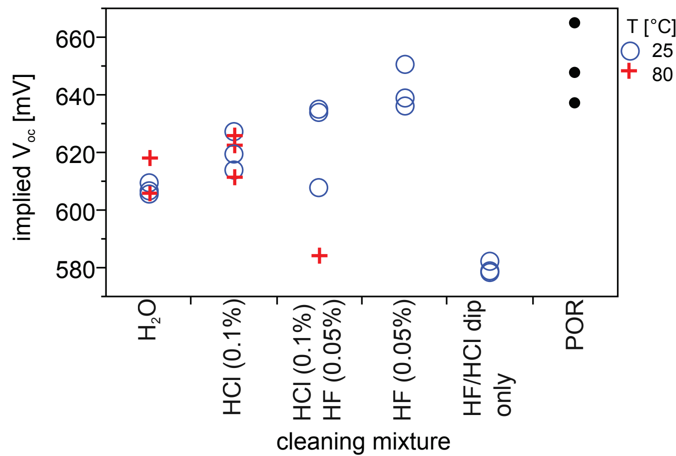

Fig. 5.18: Results of the first HF/O_3 cleaning experiment.

From **Fig. 5.18** it becomes obvious that no additional benefit can be attributed to elevated temperatures. Best cleaning efficiencies were found for the HF/O_3 system with similar values as the POR. Adding HCl or using HCl by itself resulted in similar or lower *implied* V_{oc} values. From these results it was concluded, that the simple three component system $H_2O/HF/O_3$ should be further tested and optimised in order to replace the costly and time consuming POR. Another benefit of such a simple system is that for process control in an production environment the HF concentration can be easily monitored by simple conductivity measurement.

5.6 Optimisation of the HF/ozone cleaning sequence

In the following, the HF/O_3 cleaning sequence, slightly adjusted to the one used in the previous chapter, was tested and further optimised for the cleaning of alkaline etched wafers. The applied sequence and the factors that were kept constant can be found in **Fig. 5.19**. Statistical models were obtained by "Design of Experiment" (DOE) planning and experimenting. The varied factors were immersion time and HF concentration in the HF/O_3 bath. DOE analyses were carried out separately for saw damage etched (**Sec. 5.6.1**) and textured surfaces (**Sec. 5.6.2**). Results were applied and tested for high efficiency solar cell processes in **Sec. 5.7**.

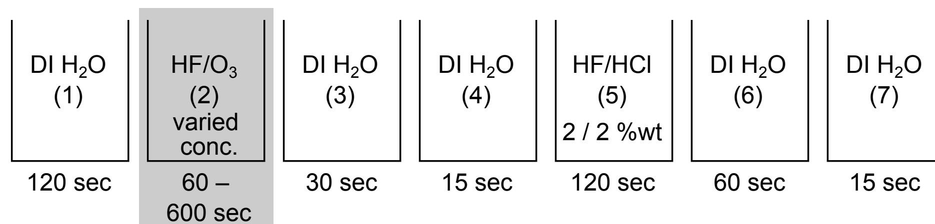

Fig. 5.19: Scheme of the investigated HF/O_3 cleaning sequence including the varied factors.

The wafers, on which the cleaning was optimised, are the same wafers as used for the analysis of alkaline etching in **Sec. 5.1.2**. The etch depth of the saw damage etch was 10 to 10.2 μm for both sawing techniques. The depth of the texturing was 8.7 to 8.8 μm (slurry sawn wafers) and 6.5 to 7.3 μm (diamond wire sawn wafers).

The cleaning time was varied from two to ten minutes, with ten minutes being the highest possible time when process line integration is considered (roughly the same time is required for the saw damage etching or texturing allowing a smooth process flow without the need for a second cleaning bath). The range of the HF concentrations in the HF/O_3 bath was chosen from 0.01% to 1%. For the modelling the negative decadic logarithm $-\log(c(\text{HF}))$ with $c(\text{HF})$ in % was used, as it became apparent that better correlations was obtained this way. HF concentrations of 0.01% to 1% were obtained by adding 10 mL to 1 mL of 50% wt. HF to the 50 L cleaning bath, introducing an error, which grows with concentration (1% as used corresponds to 1.13%).

Each group consisted of six to eight wafers. Slurry and diamond wire sawn wafers were used in order to study the influence of different contamination loads of the etched samples (as discussed in **Sec. 5.1.2**). The overview of the groups according to the testing order can be found in **Tab. 5.3**. After group 14 a new bath was made up (indicated by the dashed line). After the cleaning the wafers were split into two groups: saw damage etched and textured, which were thermally oxidised separately after randomisation.

Groups 33 to 40 were processed a couple of days later. The surface of two pairs of each group (resulting in two samples for each condition) was analysed before and after cleaning. Apart from surface samples, lifetime samples were produced and included into the statistical

Tab. 5.3: Groups of the DOE (run 1273), using both saw damaged etched and textured wafers.

group#	sawing process	etching	c(HF) [%]	time [min]
1	dia	sde	0.3	2
2	dia	sde	0.3	2
3	slurry	sde	0.3	10
4	dia	sde	0.3	2
5	dia	texture	0.3	5
6	slurry	texture	0.3	5
7	slurry	texture	0.3	10
8	slurry	texture	0.3	10
9	dia	texture	1	5
10	slurry	texture	1	2
11	dia	texture	1	10
12	slurry	sde	1	5
13	dia	sde	1	10
14	slurry	sde	1	2
15	slurry	sde	0.01	2
16	dia	texture	0.01	2
17	dia	sde	0.01	10
18	slurry	texture	0.01	5
19	dia	texture	0.01	10
20	slurry	sde	0.01	5
21	dia	sde	0.03	2
22	dia	texture	0.03	10
23	slurry	sde	0.03	10
24	slurry	texture	0.03	2
25	dia	texture	0.03	5
26	slurry	sde	0.03	5
27	dia	texture	0.1	2
28	slurry	texture	0.1	2
29	slurry	sde	0.1	10
30	slurry	sde	0.1	10
31	dia	sde	0.1	5
32	dia	sde	0.1	5
33	slurry	sde	0.1	10
34	slurry	sde	0.01	10
35	dia	sde	0.1	10
36	dia	sde	0.01	10
37	slurry	texture	0.1	10
38	slurry	texture	0.01	10
39	dia	texture	0.1	10
40	dia	texture	0.01	10

model.

5.6.1 Cleaning of saw damage etched surfaces (flat surfaces)

As shown in **Sec. 5.1.2**, as-cut wafers etching in concentrated NaOH results in highly contaminated surfaces. Cleaning these surfaces is challenging, especially if subsequent processes require cleanest possible surfaces, such as the thermal oxidation that was used to produce lifetime samples. The cleaner the surface, the higher is the lifetime and accordingly the *implied* V_{oc}.

The lifetime results of the saw damage etched samples were found to be below the expectations. Not only did the HF/O_3 cleaned samples show low lifetimes but also the SPM reference (REF, as shown in the top right graph of **Fig. 5.20**). While the reference of the diamond wire sawn wafers barely reached 645 mV, the slurry sawn wafers did not even reach 580 mV. The reason for this may be attributed to insufficient removal of the saw damage. The difference between slurry and diamond wire sawn wafers may be explained by different depths of the saw damage. Nevertheless, differences between the respective cleaning conditions, despite the low overall performance, was extracted, when assigning block variables to the different materials.

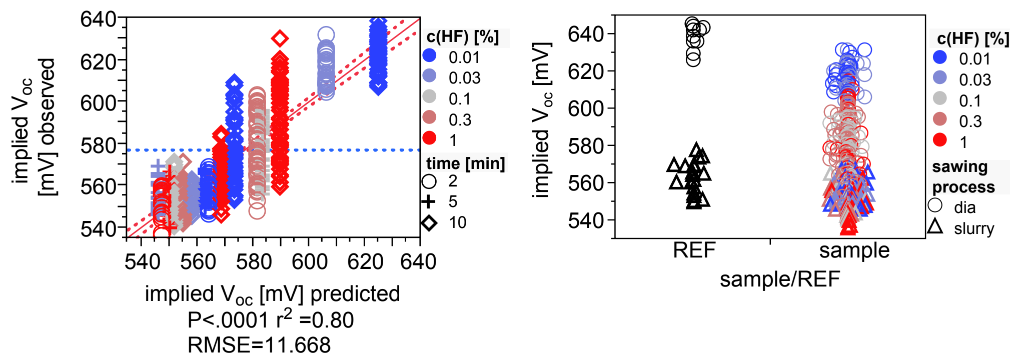

Estimates of parameter

Term	Estimate	Std.-dev.	t-value	Likelihood>|t|
intercept	539.19	2.083	258.83	<.0001*
sawing process[dia]	21.444	0.524	40.93	<.0001*
time [min]	1.405	0.186	7.54	<.0001*
-log(c(HF))	13.081	0.669	19.56	<.0001*
sawing process[dia]*(time [min]-6.793)	-0.985	0.207	-4.77	<.0001*
(time [min]-6.793)*(time [min]-6.793)	0.336	0.092	3.65	0.0003*
sawing process[dia]*(-log(c(HF))-1.015)	7.674	0.661	11.61	<.0001*
(time [min]-6.793)*(-log(c(HF))-1.015)	-0.780	0.197	-3.95	<.0001*
(-log(c(HF))-1.015)*(-log(c(HF))-1.015)	19.297	1.739	11.10	<.0001*

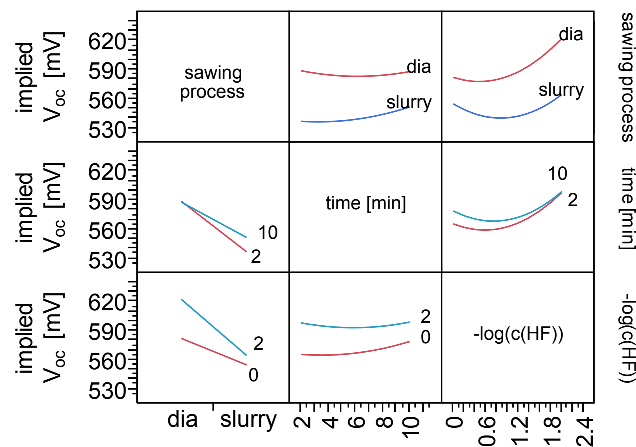

Fig. 5.20: Statistical model for the cleaning efficiency of different HF/O_3 cleaning systems on differently sawn wafers after saw damage removal. Left graph top: Test of predicted data by the model against observed data. Right graph top: Comparison of test samples against the SPM-reference to check for the influence of material properties. Mid: Parameter estimates of the model. Bottom: Interaction profiles of the model.

The statistical model was obtained by stepwise testing all the possible combinations of factors from first to second order (A, B, A*A, A*B, ...) and for the single factors additional

third order influences (A^3, B^3, ...) for statistical relevance. The regression was performed stepwise until the minimum Bayesian Information Criterion (BIC) was reached. The BIC is defined as $-2loglikelihood + k\ln(n)$ with $-2loglikelihood = n*(\ln(2*\pi*sse/n)+1)$; sse is the sum of squares for the current model, k is the number of parameters and n is the sample size [297]. This criterion avoids over-determination of the model as it punishes the addition of further parameters. All possible models were tested against each other and the one with the lowest BIC value was chosen.

The model obtained for the flat surface in run 1273 is depicted in **Fig. 5.20**. The estimates of the parameters determine the impact of the respective term. In this case the "sawing process" had the strongest impact, as was to be expected by the different levels of *implied* V_{oc} observed for the two groups. The negative decadic logarithm as linear and as quadratic factor was of strong impact, resulting in curves that can be found in the top right square of the interaction profiles. The sawing process was found to interrelate with both $-\log(c(HF))$ and the cleaning time. The values for the slurry sawn wafers, however, are to be interpreted carefully, as the lifetime is dominated by the remains of the saw damage. On the other hand, also the diamond wire sawn wafers clearly show a trend towards smaller HF concentration; the maximum values were observed for the group with 0.01% HF ($-\log(c(HF)) = 2$). The influence of the cleaning time is significant but small. The estimates of the parameters considering time are very small compared to the estimates containing the concentration and the sawing process (from the table of estimates of parameters in **Fig. 5.20**).

For a closer analysis the prediction diagrams[1] of the groups 33 to 36 are plotted in **Fig. 5.21**. As chosen conditions for further analysis were: diamond and slurry sawn wafers, immersed for ten minutes in the cleaning baths with the lowest and the highest HF concentration (0.01 and 1%). The surface contamination before and after cleaning under the chosen conditions is shown in **Fig. 5.21**. In both cases, the diamond wire and slurry sawn wafers, the Cu contamination is most effectively removed by lower HF concentration. Also the Fe contamination appears to be lower. In all four cases, however, the value is still relatively high considering the impact of Fe surface contamination as discussed before.

An indication for the suspected incomplete saw damage removal of the diamond wire sawn wafers is the fact that the Ni contamination is still high after cleaning, especially when compared with the slurry sawn wafers. From the surface contamination analysis it can be concluded that the lower the HF concentration, the higher the cleaning efficiency for Cu and Fe. The observation that higher HF concentrations lead to a strong increase in *implied* V_{oc} for the very low level slurry sawn group, despite the fact that higher metal contamination were measured, may be explained by increased etching rate of the cleaning solution with HF concentration. This assumption is confirmed by the significant positive impact of longer etching times. As a similar effect is not visible for the diamond wire sawn group, it can be assumed that the surface damage (remaining saw damage) is still high enough to allow significant etching rates of the HF/O_3 mixture, hence the low lifetimes due to excessive surface

[1]The prediction diagrams are a useful tool to graphically explore the fitted model by changing one parameter and fixing all the others. They can also be used for the detection of maxima and minima in multi-dimensional parameter spaces.

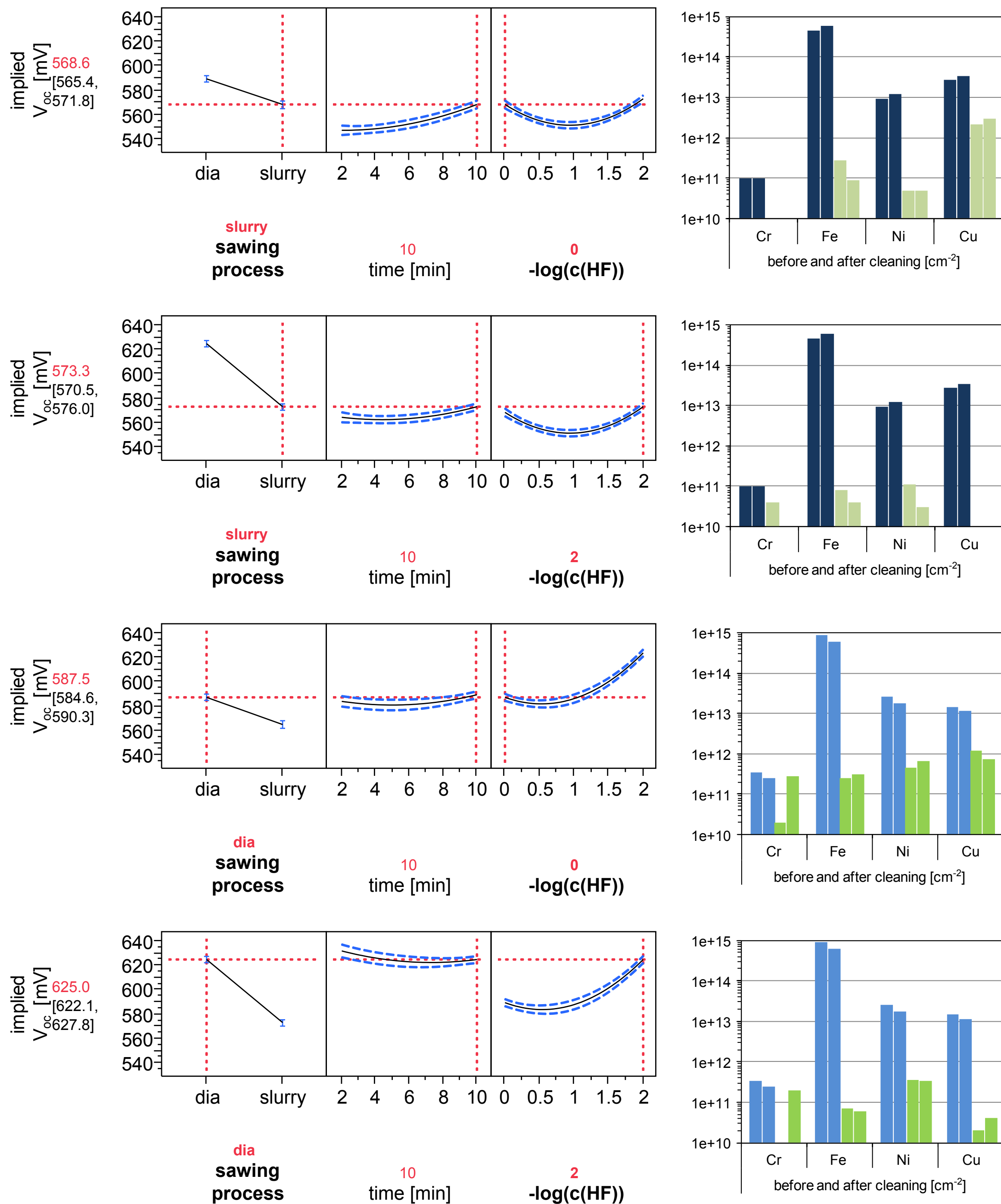

Fig. 5.21: Prediction diagrams for *implied* V_{oc} values for four different cleaning conditions. The respective surface contamination before and after cleaning of saw damage etched slurry and diamond wire sawn wafers is shown in the right hand side graphs. The immersion time was kept constant at 10 min.

recombination.

As discussed above, the level of lifetime obtained was too low for both kind of wafers, indicating remains of saw damage. To get a clearer picture without this limiting factor, a similar experiment was designed, further zooming in on low HF concentrations. A DOE was set up to test HF concentration (0.01; 0.05; 0.1 and 0.5%) against time (1; 5 and 10 minutes) containing twelve groups in run 1332. The groups of the DOE can be found in **Tab. 5.4**.

Three wafers of three different materials from two different suppliers were used per group: the same material as in run 1273 (A-slurry and A-dia) and the current ISC Konstanz reference material B-dia. The saw damage etching time was prolonged to ten minutes resulting in 12.8 μm, 11.0 μm and 11.5 μm per wafer side respectively.

In addition to the twelve DOE cleaning groups, one group of each material was immersed for ten minutes into a bath containing both HCl and HF in the O_3 cleaning bath (0.25 and 1%, respectively) in order to test the effect of additional HCl in HF/O_3 cleaning baths. Apart from the obligatory SPM reference groups of the three different materials (SPM REF I), additional references were included across the oxidation boat to check for cross contamination and, if indicated, to use them for correction of the obtained data. The order, in which the differently cleaned wafers were placed into the oxidation boat, can be found in **Fig. 5.22**. The gas-flow of the oxidation tube is from left to right and accordingly the "clean" SPM references are placed at the very left of the boat.

Tab. 5.4: Second DOE for the optimisation of the cleaning of flat surfaces (run 1332). Each group consisted of three wafers of the three materials (A-slurry, A-dia, B-dia (REF)).

group#	c(HF) [%]	time [min]
1	0.5	10
2	0.5	1
3	0.5	5
4	0.5	10
5	0.01	10
6	0.01	5
7	0.01	1
8	0.01	10
9	0.05	1
10	0.05	10
11	0.1	5
12	0.1	1

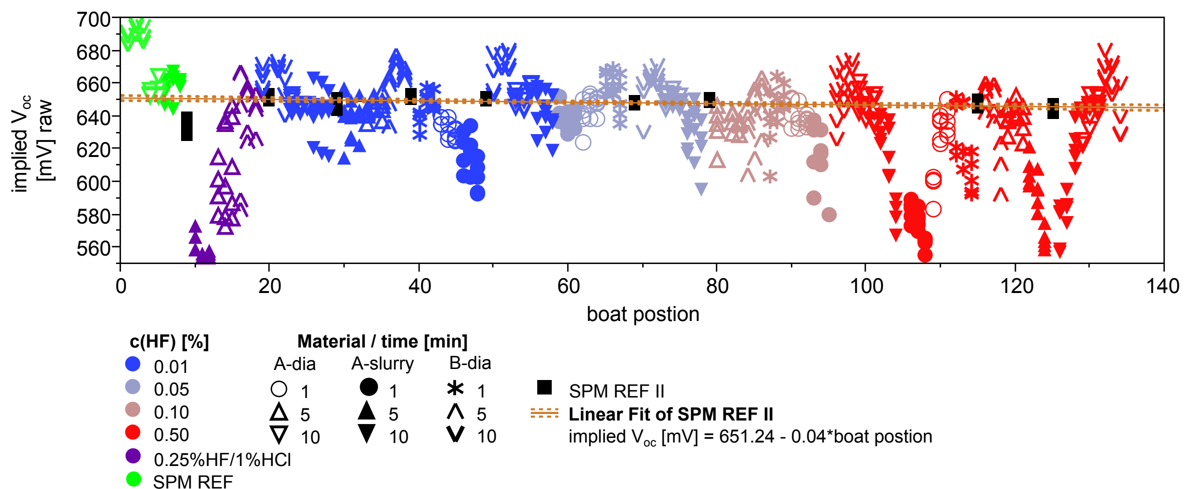

Fig. 5.22: *implied* V_{oc} values of run 1332 (cleaning after SDE) plotted against the position in the boat of the thermal oxidation (gas-flow from left to right). The linear fit of SPM REF II was used for the correction for the boat position.

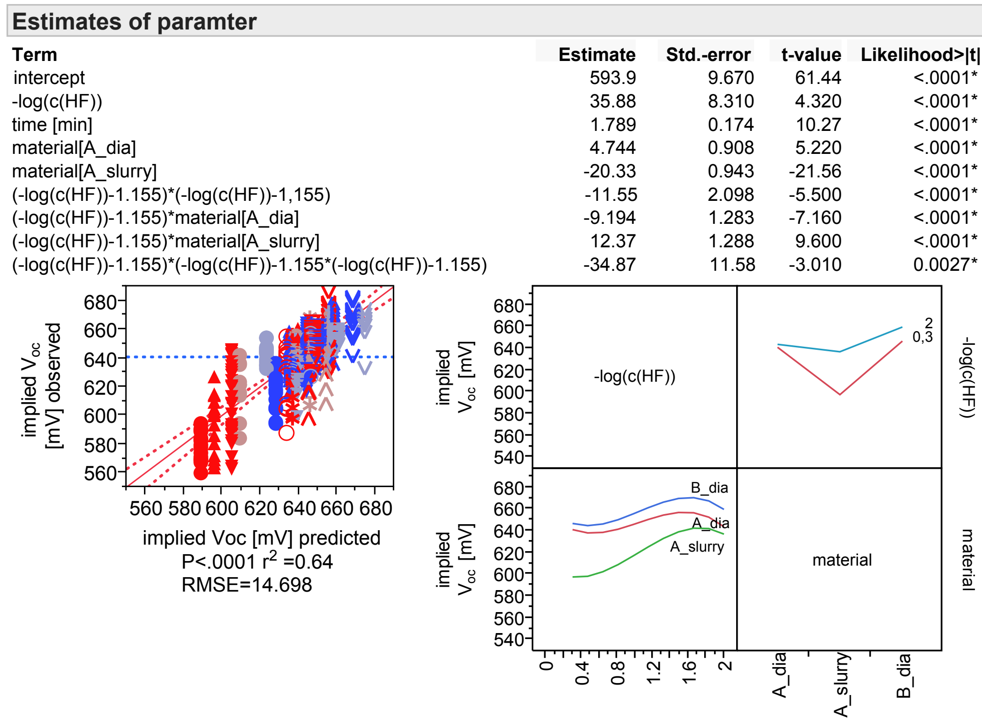

Estimates of paramter

Term	Estimate	Std.-error	t-value	Likelihood>|t|
intercept	593.9	9.670	61.44	<.0001*
-log(c(HF))	35.88	8.310	4.320	<.0001*
time [min]	1.789	0.174	10.27	<.0001*
material[A_dia]	4.744	0.908	5.220	<.0001*
material[A_slurry]	-20.33	0.943	-21.56	<.0001*
(-log(c(HF))-1.155)*(-log(c(HF))-1,155)	-11.55	2.098	-5.500	<.0001*
(-log(c(HF))-1.155)*material[A_dia]	-9.194	1.283	-7.160	<.0001*
(-log(c(HF))-1.155)*material[A_slurry]	12.37	1.288	9.600	<.0001*
(-log(c(HF))-1.155)*(-log(c(HF))-1.155*(-log(c(HF))-1.155)	-34.87	11.58	-3.010	0.0027*

Fig. 5.23: Statistical model of the HF/O_3 cleaning system for material of two different suppliers (A and B), A-dia and A-slurry is the same material as used in the previous experiment. The symbols are the same as used in **Fig. 5.22**.

The linear fit of the references distributed across the boat indicates a relatively small but measurable effect of cross contamination. The fit parameters were used as correction factor for the analysis of the other groups. The statistical model obtained analogous to run 1273 can be found in **Fig. 5.23**. A quite obvious difference in the two models lies in the shape of the HF curve. A third order term becomes statistically significant with an estimate of -34.9 indicating a strong impact. The effect of the third order term (across the investigated concentration range) is mainly bending the asymmetric parabola curve (which is similar to the one detected in run 1273) towards lower concentrations reaching an optimum at around $-\log(c(HF)) = 1.6$ to 1.7%. The cleaning efficiency of slurry sawn wafers shows a much stronger sensitivity to the HF concentration than the diamond wire sawn. This may be due to the higher initial Cu contamination as shown by the surface analysis samples.

The found optimum of the *implied* V_{oc} curve matches nicely the optimal cleaning condition for Cu as reported by Choi *et al.* in [292]. They attribute this relatively small optimum for Cu removal to two factors as plotted in **Fig. 5.24**: In HF/O_3 mixtures with higher HF-concentrations the bare silicon surface allows the tunnelling of electrons to Cu present on the surface favouring the reduction and consequently inhibiting the removal ($c(HF) > 0.1\%$). In very low HF concentrations ($c(HF) < 0.02\%$) the silicon surface is oxidised and the formation of $Cu(OH)_2$ is favoured.

It is observed that time has again a relatively small impact; yet, the singular positive linear factor with the estimate of 1.79 ± 0.17 clearly indicates that longer times are desired, independently of the sawing process or HF concentration. From the model we can conclude

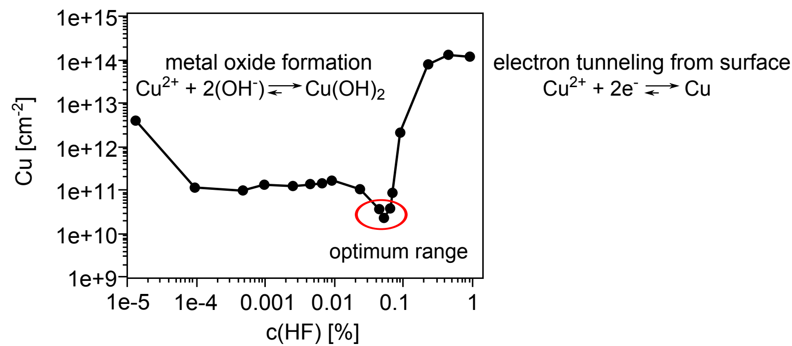

Fig. 5.24: Observed Cu surface contamination after 10 min HF/O_3 cleaning by Choi *et al.* and the presented explanation for the relatively narrow optimum for Cu removal efficiency. Adopted from [292].

that the highest cleaning efficiency is obtained when cleaning for (at least) ten minutes with $-\log(c(HF))$ =1.6 to 1.7 corresponding to 0.025 to 0.02%.

5.6.2 Cleaning of textured surfaces (random pyramids)

Over the time of the work on this thesis, the most common texturing additive isopropyl alcohol (IPA) was more and more replaced by other additives granting more homogeneously textured surfaces and often being more environmentally friendly. One of these commercially available additives is the RENA monoTEX^{TM}, which was used in this study. It has two main components of longer organic molecules replacing the detergent IPA: pectin (a heteropolysaccharide) and carboxymethyl cellulose, CMC, a cellulose (polyglucopyranose) derivative with additional carboxymethyl groups [298]. Both molecules are of varying length with many functional groups. The issue with this texturing additive is that it bonds so effectively to the silicon surface that even long rinsing times and dipping in diluted HCl and HF do not remove it. The surface remains hydrophilic after the HF dip.

Accordingly, it is presumed to either directly interfere with a subsequent process step (introducing carbon to the interface) or to function as mask preventing the cleaning solutions to effectively remove the metal contamination off the surface. In order to remove the remains of the additive that render the surface hydrophilic, an oxidative cleaning step is required. The producer recommends the use of KOH/H_2O_2, also referred to as pseudo SC1 clean. This works quite effectively but has several drawbacks: H_2O_2, which is relatively expensive, is consumed. The decomposition rate increases with metal contamination (bath age) [53] and, if not properly controlled and the H_2O_2 drops below a critical value, the whole solution starts etching the silicon, producing a shiny surface replacing the random pyramids.

In the following the results of the second part of run 1273, treating alkaline textured wafers, is discussed. The wafers were textured without prior treatment for 29.5 minutes resulting in the case of the slurry sawn wafers in an average etching depth of 8.7 μm per side and 35 minutes resulting in an an average etch depth of only 6.5 μm per side. Both kinds of wafers (slurry and diamond) were etched in etching baths with an identical bath age. The much higher etch rate of the slurry sawn wafers indicates the more pronounced damage of the surface (confirming the observations from the previous section). Despite the fact that the overall

etching depths (calculated from the weight loss) are lower for the textured samples than for the SDE etched samples described in the previous part, the lifetimes of both, samples and references, are found at a much higher level. The maximum measured *implied* V_{oc} values are as high as 675 mV. This observation lead to the conclusion that etching of random pyramids preferably "attacks" the structural defects caused by the wire sawing eliminating those as recombination active crystal strains.

Similar to the saw damage etched wafers, first the statistical model for the *implied* V_{oc} values of slurry and diamond wire sawn wafers, depending on HF concentration and immersion time, is presented in **Fig. 5.25** and subsequently the prediction diagrams are interpreted in combination with surface analysis data in **Fig. 5.26**.

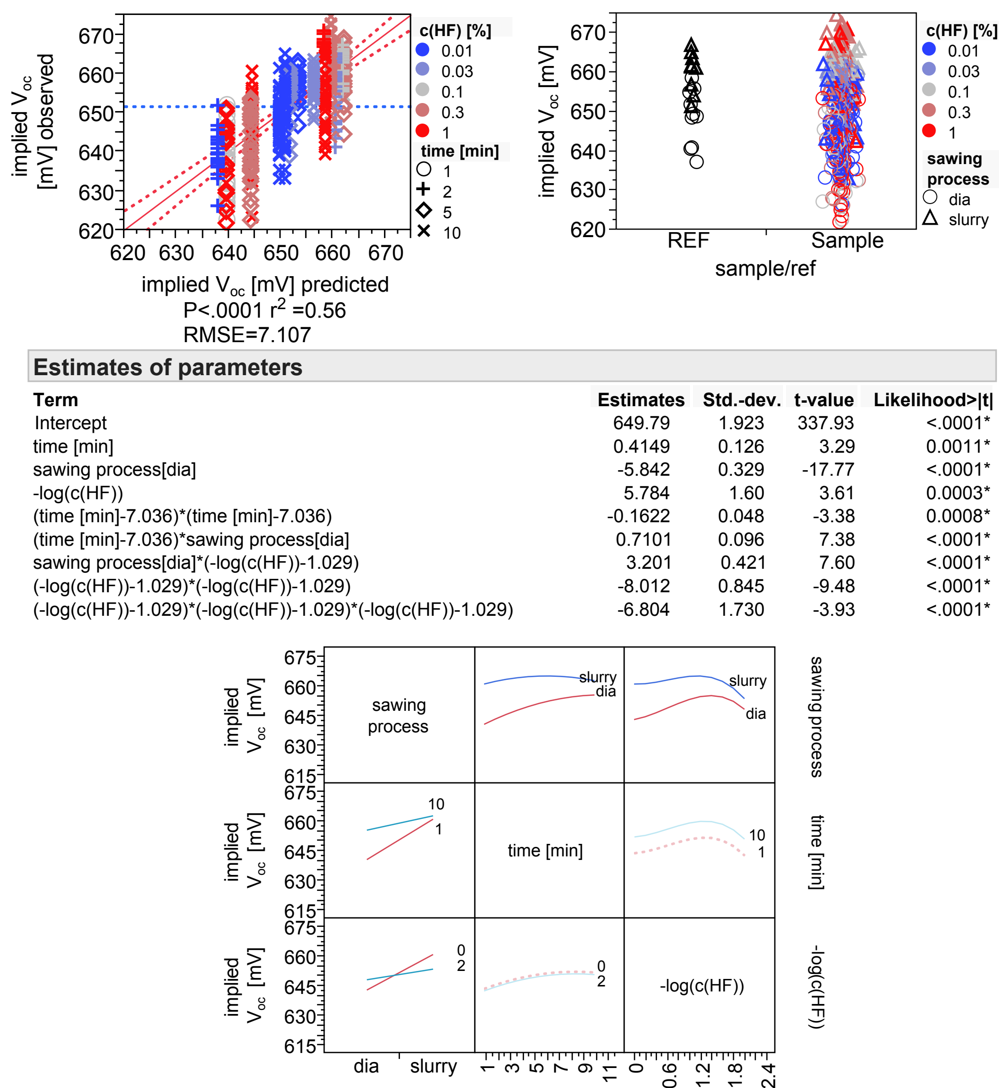

Estimates of parameters

Term	Estimates	Std.-dev.	t-value	Likelihood>|t|
Intercept	649.79	1.923	337.93	<.0001*
time [min]	0.4149	0.126	3.29	0.0011*
sawing process[dia]	-5.842	0.329	-17.77	<.0001*
-log(c(HF))	5.784	1.60	3.61	0.0003*
(time [min]-7.036)*(time [min]-7.036)	-0.1622	0.048	-3.38	0.0008*
(time [min]-7.036)*sawing process[dia]	0.7101	0.096	7.38	<.0001*
sawing process[dia]*(-log(c(HF))-1.029)	3.201	0.421	7.60	<.0001*
(-log(c(HF))-1.029)*(-log(c(HF))-1.029)	-8.012	0.845	-9.48	<.0001*
(-log(c(HF))-1.029)*(-log(c(HF))-1.029)*(-log(c(HF))-1.029)	-6.804	1.730	-3.93	<.0001*

Fig. 5.25: Statistical model for the cleaning efficiency of different HF/O_3 cleaning systems on differently sawn wafers after alkaline texturing. Left graph top: Test of model against observed data. Right graph top: Comparison of test samples against the SPM-reference to check for the influence of material properties. Mid: Parameter estimates of the model. Bottom: Interaction profiles of the model.

The first deduction from the regression model, backed by comparison of the references in the top right graph, is that slurry sawn textured wafers have higher lifetimes than the

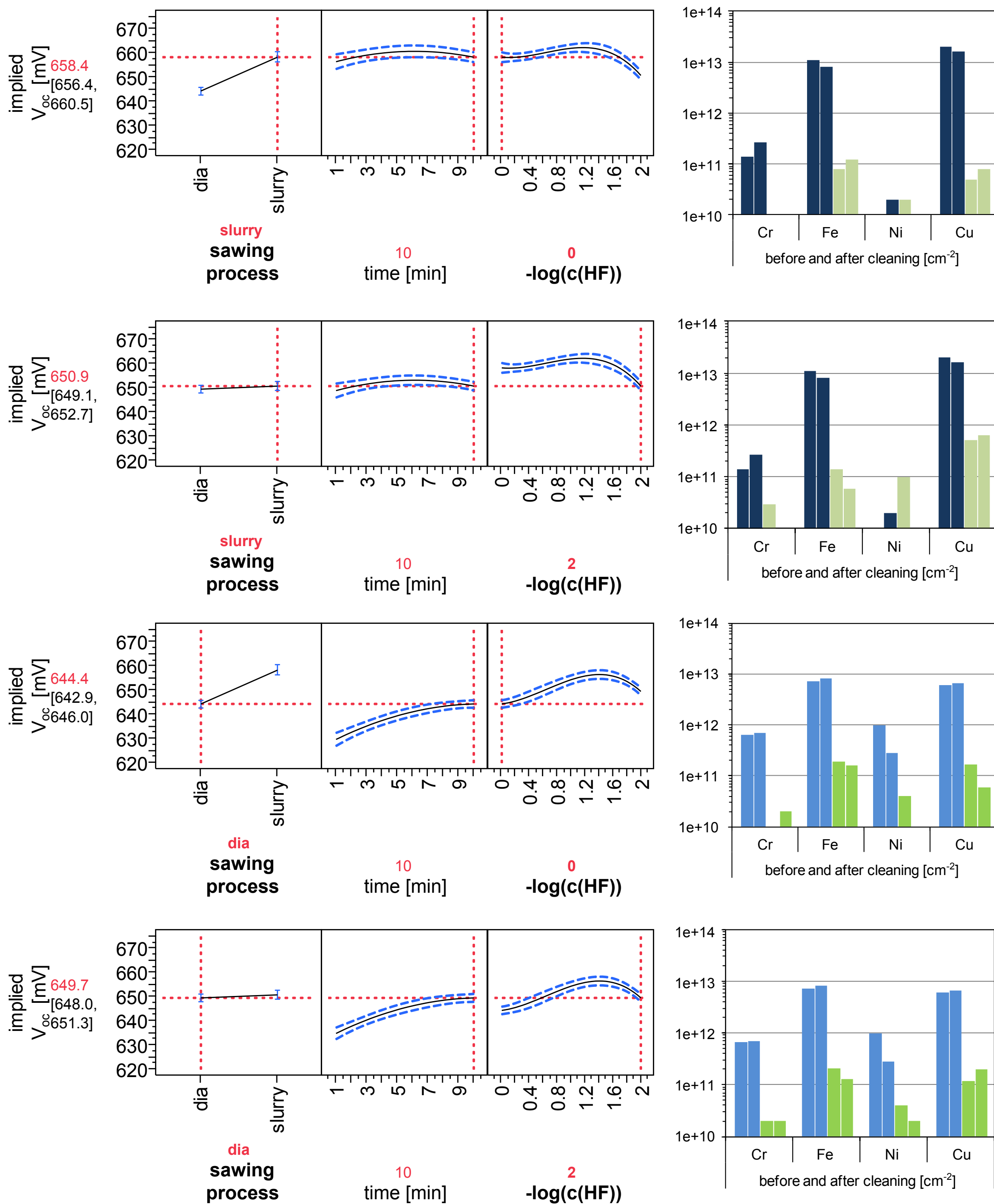

Fig. 5.26: Prediction diagrams for *implied* V_{oc} values for four different cleaning conditions as derived for alkaline textured wafers. The respective surface contamination before and after cleaning is shown in the right hand side graphs. The immersion time was kept constant at 10 min.

diamond sawn textured wafers. The difference in *implied* V_{oc} is about 5 mV. The sawing process is modelled to influence the time and the HF dependence of the cleaning efficiency. A clear time dependency is found for the diamond wire sawn wafers: they show a close to linear trend towards longer cleaning times, while the slurry sawn wafers seem to be hardly affected—this was taken as argument for remains of saw damage in the analysis of the SDE wafers. As the general level lifetime is much higher when the texturing is applied it might

not necessarily have the same reason here.

Interestingly, the HF–*implied* V_{oc} curves look almost identical to the ones modelled in the second experiment with flat surfaces (run 1333). However, the maximum of the cleaning efficiency is slightly shifted to the left. The optima are found between $-\log(c(\mathrm{HF})) = 1.2$ and 1.4 corresponding to 0.06% and 0.04% compared to 0.02% and 0.025% for the SDE wafers. This may be explained by the observations of these experiments that an HF concentration of at least 0.05% was required to render the surfaces hydrophobic after the HF/HCl dip at the end of the cleaning sequence. This indicates that oxidation of the remains of the texturing additive is depending on the pH (which varied from 2.7 to 1.7 for 0.01 to 1% HF respectively) and is favoured by lower pH values.

The remaining film of the additive on the surface could explain the relatively high Cu concentrations for both cases of sawing, when using the 0.01% HF cleaning solution, particularly in the slurry case (≈8e+11 cm^{-2}). The lower Cu concentrations in the diamond wire case (≈2e+11 cm^{-2}) can be attributed to the lower initial surface concentration. Fe, in all four cases, seems to be hardly affected by the HF concentration, the concentration is with 1 to 2e+11 cm^{-2} in a range, in which it would be considered critical for most of the so far investigated process steps. Ni and Cr residues are measured particularly in the case of 0.01% HF. The overall sum of elements for the low HF is mirrored in the *implied* V_{oc} prediction diagram and the relatively steep rise to slightly higher HF concentration indicates that lower metal concentrations are expected when approaching the optimum. Increasing the HF further is expected to be resulting in lower cleaning efficiencies, similar to the case of the flat samples.

5.6.3 Conclusion

The measured surface contamination for low and high HF concentrations (0.01 and 1%) from **Fig. 5.21** and **Fig. 5.26** is summarised in **Tab. 5.5**. It becomes obvious that lower HF concentrations are favourable for the removal of Cr, Fe, Ni and Cu (other elements, such as Al, Ca, K, Na, Ti and Mn were also measured but not found in significant concentrations or to a similar extend on all samples). Values that show unexpected behaviour are highlighted in bold font.

Tab. 5.5: Summary of surface contamination after cleaning of the different surfaces (mean values and standard deviation of the two measurements). Unexpected values are highlighted in bold font.

		Cr		Fe		Ni		Cu	
	c(HF) [%]	0.01	1	0.01	1	0.01	1	0.01	1
SDE slurry	mean [1e+10 cm^{-2}]	2.0±2.8	0.5±0.7	6.0±2.8	18±13	7.0±5.7	5.0±0.0	1.0±0.0	252±57
SDE dia	mean [1e+10 cm^{-2}]	11±13	15±18	6.5±0.7	28±4.2	**35±2.1**	**56±16**	3.0±1.4	98±34
optimum	c(HF) [%]	0.02 – 0.025							
text. slurry	mean [1e+10 cm^{-2}]	1.5±2.1	0.0±0.0	**10±5.7**	10.0±2.8	5.0±7.1	1.0±1.4	**58±8.5**	6.5±2.0
text. dia	mean [1e+10 cm^{-2}]	2.0±0.0	1.5±0.7	**17±5.7**	18±2.1	3.0±1.4	2.5±2.1	**16±5.7**	12±7.8
optimum	c(HF) [%]	0.04 – 0.06							

Cr concentrations are low, measurable for the saw damage etched samples, however. As the saw damage had not been completely removed on these samples this may be connected. Generally, Cr seems to be an "easy to clean" species in the investigated cleaning system. As argued before, Cu requires low HF concentrations to be removed quantitatively to values close to the limit of detection (1e+10 cm^{-2}) and thus allowing the HF/O_3 cleaning to be used for n-type high efficiency solar cells. Unexpectedly, elevated Cu surface coverage at the low HF concentration are found for the textured wafers, which may be explained by remains of the texturing additive interfering with the cleaning. A similar phenomenon is observed for Fe—otherwise Fe is removed to values close to the discussed (cf. **Sec. 4.2.2**) measuring limit in the range of 4e+10 cm^{-2}. Ni appears to be problematic in terms of removal when cleaning saw damage etched diamond wire sawn wafers, here elevated concentrations in the range of several 1e+11 cm^{-2} were measured after cleaning. However, as the lifetime samples indicated, the saw damage had not been completely removed, thus one possible explanation might be remains of Ni from the sawing process that were relatively deeply driven into the silicon.

It can be concluded, that very small HF concentrations (in the range of 0.025 to 0.06%) result in the best cleaning efficiencies when applied for at least ten minutes. Critical metal contamination is removed under these conditions. Strong time dependency is mostly found for insufficiently prepared surfaces and thus may not play such an important role when transferring to well optimised industrial production. The results indicate that HF concentrations of 0.025% are to be preferred in the case of flat NaOH etched samples and 0.06% in the case of textured wafers when using the RENA monoTEX^{TM} texturing additive.

Considering the latest development in terms of high efficiency solar cell devices (PERC and BiSoN), cleaning after alkaline texturing has become less challenging, as the texturing process has shifted towards the BEOL, resulting in slightly cleaner initial surfaces after the texturing step (cf. **Sec. 5.1.2**). On the other hand this produces new restrictions concerning the chemistry in use: SiN_x that easily etches in HF containing solutions must not be affected (i.e. etched) too much by the cleaning. Otherwise its function as diffusion barrier might cease; yet, the texturing additive needs to be removed. In this respect the found concentrations appear to fulfill both requirements, as low HF concentrations are expected to have little impact on SiN_x passivation layers.

Summarising, it can be stated that good cleaning efficiencies were recorded for both saw damage etched and textured wafers. However, especially in the case of the saw damage etched wafers, the reference levels (POR) of the *implied* V_{oc} of thermally oxidised and SiN_x capped wafers were not quite reached in all of the cases. If the observed levels under ideal cleaning conditions suffice for high efficiency solar cells, has to be tested for the different process sequences individually. First test results in the case of p-type PERC and n-type BiSoN solar cell processing will be presented in the following section. Furthermore, process stability for mass-production has to be proven.

5.7 Testing for high efficiency solar cell processes

This short section presents the results of the first tests of the HF/O_3 cleaning sequence as cleaning for high efficiency BiSoN solar cells. As explained above, bificial n-type solar cells require two major cleaning steps after alkaline etching: after saw damage removal (FEOL) and after alkaline texturing (BEOL). The suitability of the HF/O_3 cleaning sequence is tested for both.

5.7.1 N-type BiSoN, FEOL vs. BEOL

The above developed HF/O_3 cleaning sequence (not fully optimised, 0.05% HF, ten minutes at 25°C) was applied in the BiSoN cell process as post-SDE and post-texturing steps and compared to standard cleaning sequences in run 1306. N-type wafers from the same supplier, as used in the previous sections, were used. Of special interest was the cleaning after the initial alkaline etching. Surface contamination before and after cleaning was measured, the data can be found in **Fig. 5.27**. For reasons of comparison, in addition to the SPM+HF and the HF/O_3+HCl/HF cleaning sequence, the industrial HCl+HF cleaning sequence was applied.

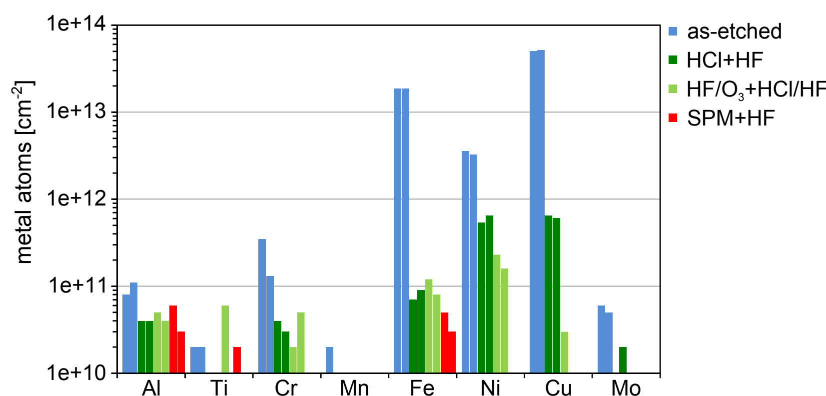

Fig. 5.27: Surface contamination before and after post-SDE cleaning with three different cleaning procedures.

The surface contamination data show good results for the HF/O_3 sequence for the cleaning of Cu and reasonable results for the cleaning of Fe. Ni and Cr appear to be still relatively high. In all cases the HF/O_3 cleaning performs superior to the HCl+HF cleaning.

Not only the FEOL cleaning was replaced by HF/O_3 but also the cleaning after alkaline texturing. Here the standard procedure pSC1+HCl+HF (first from the right in **Fig. 5.28**) was compared to HF/O_3 and an “only” HCl+HF step to confirm the need for oxidising cleaning after alkaline texturing. No clear statistical distinction between the groups was extracted due to a relatively large spreading of the data. The reason for the spreading is one group of an experimental cleaning procedure that utterly failed and as a consequence produced cross contamination in the diffusion tube. As the wafers were shuffled before they were put into the diffusion tube, the effect should affect all groups to a similar extend. The most affected wafers were the neighbouring samples in direction of the diffusion gas flow. They were excluded from the analysis but caused groups to shrink from ten to numbers between

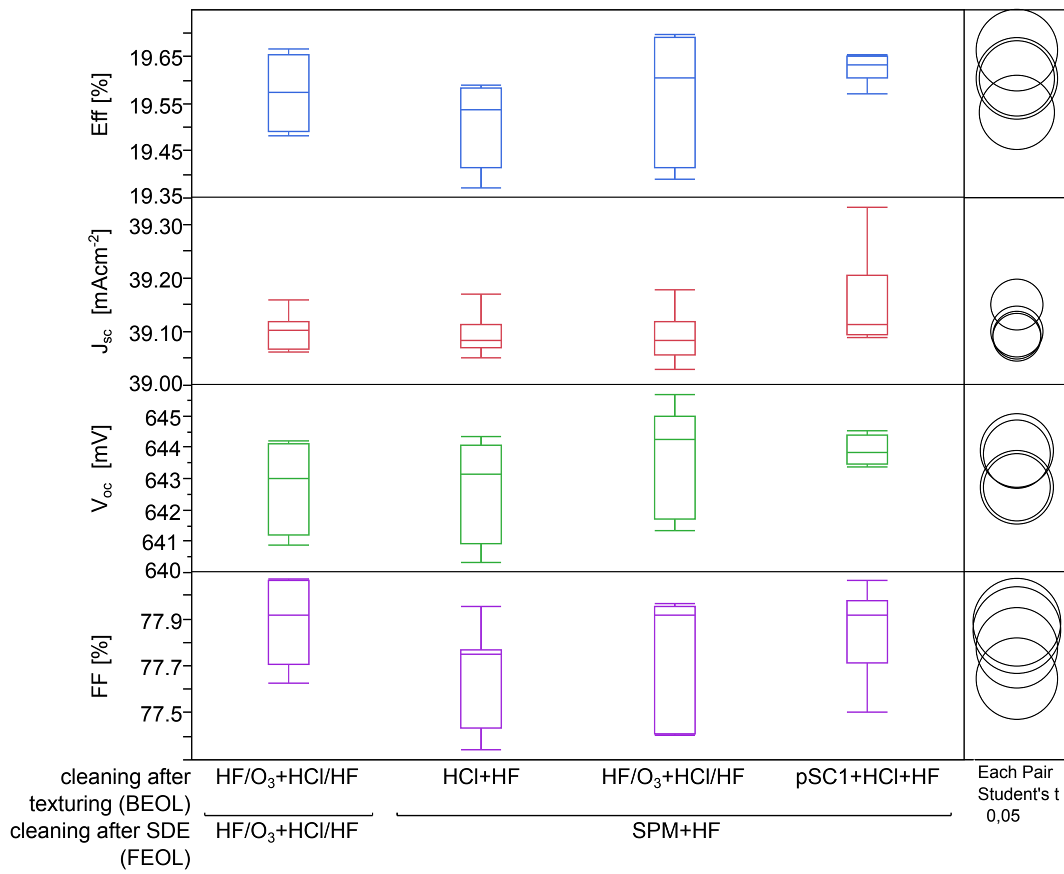

Fig. 5.28: Solar cell results of a first experiment in which HF/O_3 was used to replace the lab cleaning sequences, using the not fully optimised conditions (0.05% HF).

five and ten solar cells per group—which left group sizes too small for statistical comparisons. What can be concluded from the data, however, is that the HF/O_3 group does not show a significant decrease in solar cell efficiency. The spreading of the results when lab-only cleaning procedures are used appears to be smaller, however. An observation that might as well be based on a random effect. The group without oxidative cleaning after texturing appears to be slightly worse compared to the others (although again not statistically proven). This would have to been expected, as organic residues were detected after texturing—the wafers did not render hydrophobic after the final HF-dip.

5.7.2 N-type BiSoN, FEOL cleaning

As shown before (in **Sec. 5.3**) the FEOL etching (post-SDE) step is more sensitive to cleaning variation, therefore in the following experiment (run 1306) the HF/O_3 clean was tested as FEOL cleaning for different type of materials. For this purpose n-type wafers from the two suppliers were used: A-dia, A-slurry and B-dia, with B-dia being the reference material. The BEOL step had been exchanged for HF/O_3 in all three cases.

This time the optimised cleaning conditions (0.03% HF, ten minutes at 25°C) were used. In order to avoid potential cross contamination, the wafers were diffused in three consecutive diffusion runs with SPM+HF cleaned wafers in the gas-zone of the diffusion tube as refer-

ence, in order to detect potential differences between diffusion runs. Unfortunately, all three diffusions turned out to be inhomogeneous due to technical problems (failure of the zone-wise temperature correction, necessary to ensure homogeneous B-diffusion across the boat). As the same gradient for all three diffusions was observed (plotted in **Fig. 5.29**), linear fits were used to implement correction factors. For the linear fits samples of the A-slurry HF/O_3 group were excluded, as they performed exceptionally bad and thus would have biased the linear fit.

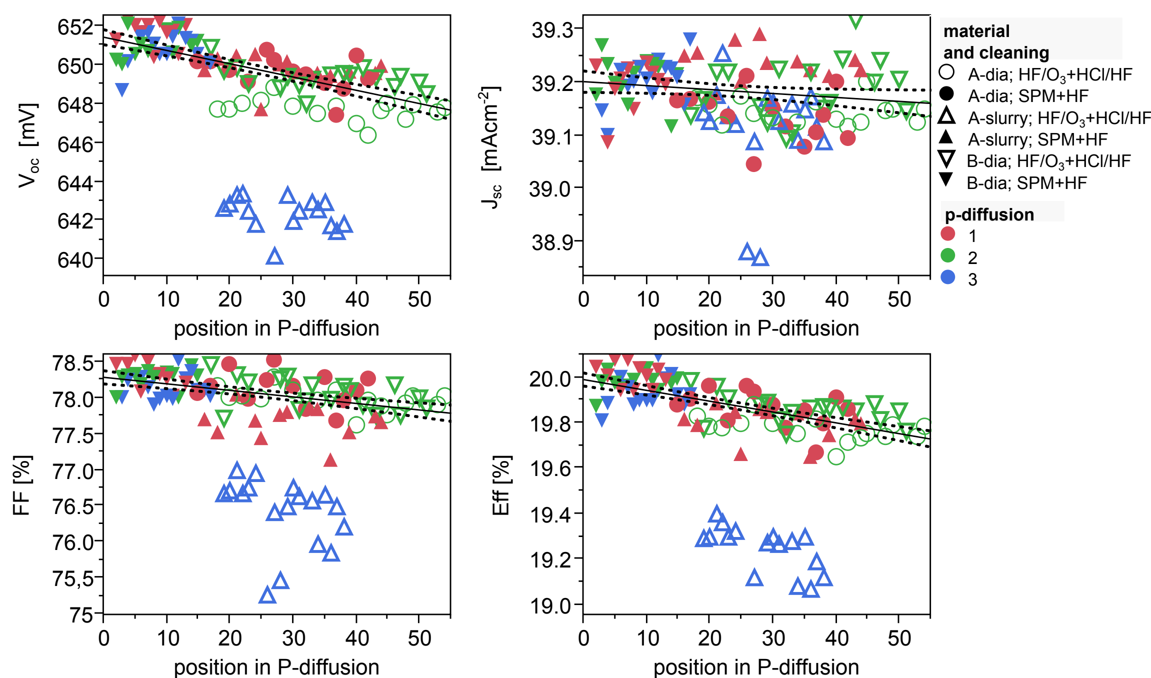

Fig. 5.29: Cell data plotted against position in the P-diffusion boat. Correction factors were obtained from the linear fits.

The correction factors are essential, as, due to the distribution of the wafers in the diffusion boat, without correction all groups would perform much worse than the reference that was always placed in the "good" part of the boat. The corrected cell data are plotted in **Fig. 5.30** and reveal two main points: The difference between the materials used is relatively small and the HF/O_3 clean performs similarly well as the POR, except for the slurry sawn wafers. In this case the HF/O_3 cleaned wafers lose more than 0.5% absolute in efficiency.

In **Fig. 5.31** the efficiencies achieved by HF/O_3+HF/HCl sequence for the different materials are plotted again for the statistical comparison with the efficiencies achieved by the POR as FOEL cleaning step. The student's test (0.05) shows no significant differences for material B (diamond wire sawn wafers). Material A appears to perform slightly worse, yet the circles overlap so that according to the statistical test no definite answer to whether they perform different or not can be give. If a difference was obtained, it is small, in the range of 0.1% absolute in efficiency. All four groups achieve excellent efficiencies of above 20%. The reason for the relatively poor performance of the slurry sawn group cleaned with the HF/O_3 sequence remains unclear. Maybe it is again related to insufficient removal of the saw damage, similarly to the results presented in **Sec. 5.6.1**. The etching effect of the SPM might have

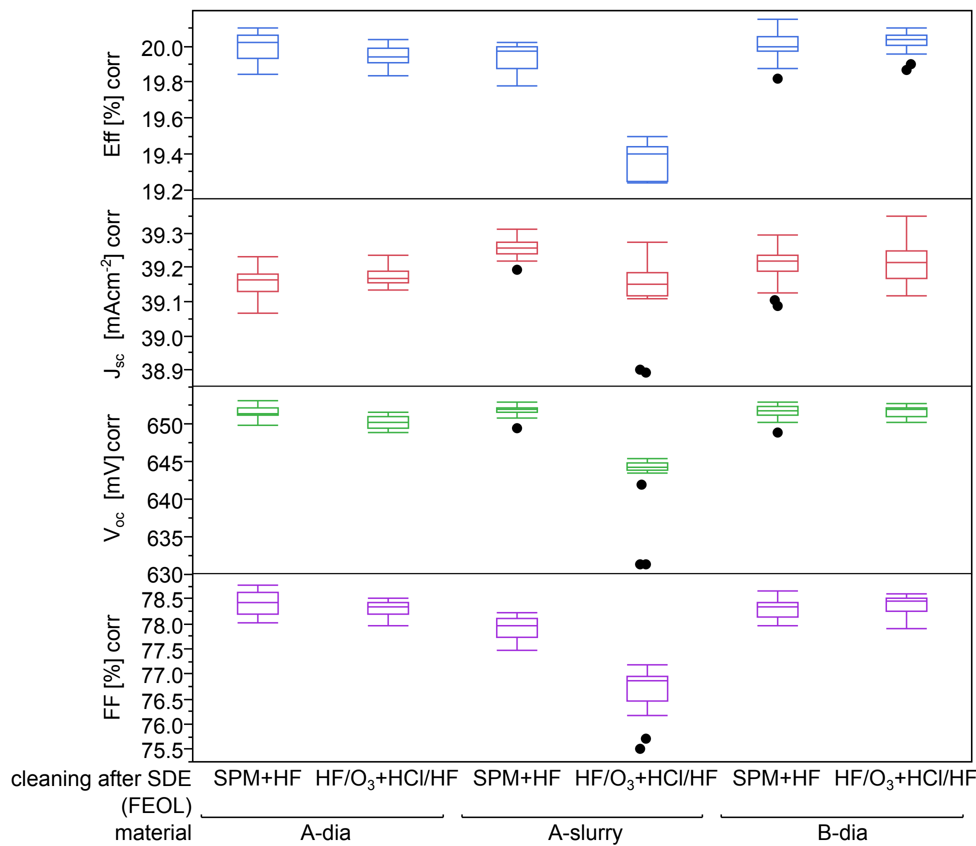

Fig. 5.30: Solar cell data corrected for position in P-diffusion boat comparing the HF/O_3 cleaning sequence against the SPM based on different materials. The black spots are measurement points not covered by the quantiles (outliers).

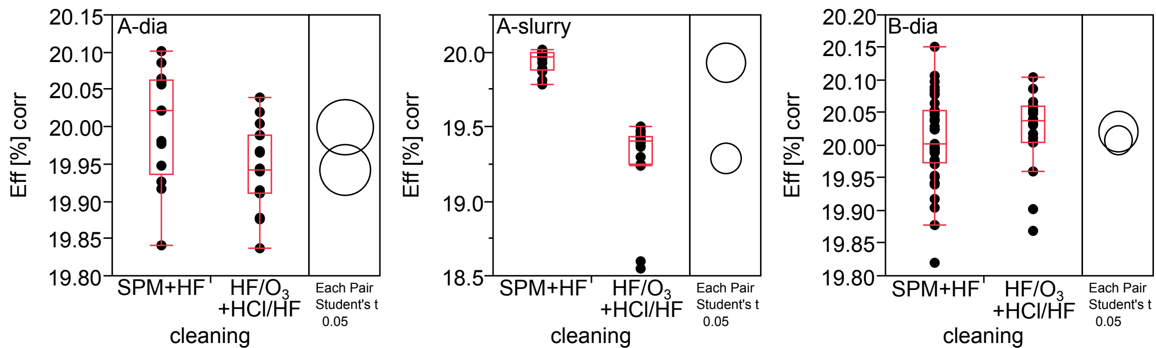

Fig. 5.31: Comparison of the corrected efficiencies achieved with the two different cleaning sequences for the different materials.

removed the last bit of it, while the HF/O_3 solution could not achieve this. When, however, using diamond cut wires, it can be concluded that the straight forward HF/O_3 based cleaning method can be used to produce highly efficient solar cells. Tests for long term performance in a production environment are currently underway [299].

5.8 Surface roughness

It is a well-known fact from IC fabrication that wet chemical steps can contribute to surface roughness of silicon wafers [300–302]. In IC manufacturing surface roughness of flat surfaces is measured routinely either by scanning tunnelling microscope, atomic force microscope, light scattering, optical microscope or interferometric profiler. For IC applications surface roughness in the range of several Å is desired [303, 304]. In solar cell applications the effect of surface roughness has not been considered in the way it has been in IC technology. On the contrary, surface roughness was desired as a surface texture to enhance light coupling. It can, however, be assumed that excessive roughness will increase surface recombination and eventually decrease solar cell performance, especially when the roughness is on such a small scale that no beneficial effect on light coupling can be achieved. From an increased surface roughness an increase in surface recombination and accordingly a decrease in minority carrier lifetime would be expected [301].

Two types of roughness can be distinguished when dealing with (textured) surfaces: Micrometer-scale roughness and nanometer-scale roughness. A scheme of the two types is displayed in **Fig. 5.32**. In addition to the above listed measuring methods for the nano-scale roughness Angermann *et al.* have demonstrated, that reflection measurements can be useful for the detection of nano-roughness [305]. They could model the effect by assigning an increasing effective refractive index with the enlargement of the surface on the nanometer scale.

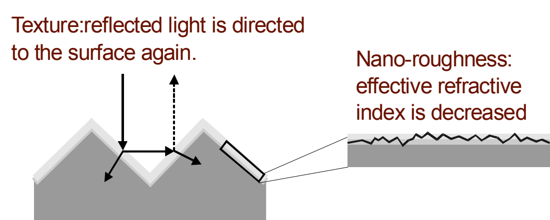

Fig. 5.32: Effect of nano-roughness on random pyramid textured surfaces as predicted by Angermann *et al.* [305].

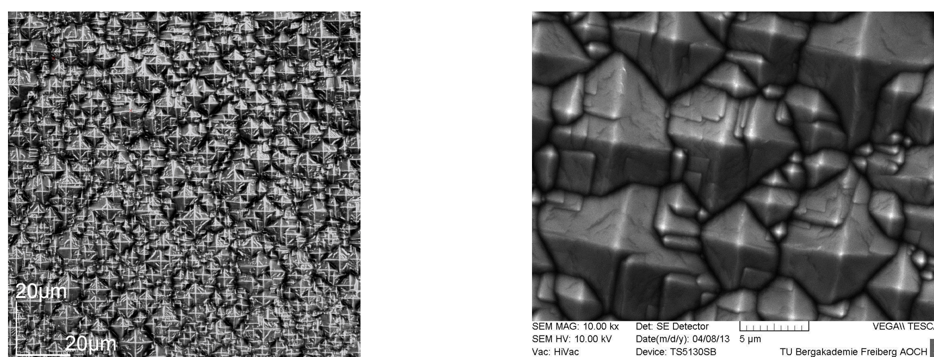

Fig. 5.33: LSM picture of a textured wafer surface (KOH/RENA monoTEX^{TM}) with maximum 100x magnification (left hand side) and SEM picture with 10.000x magnification (right hand side).

The difference between micro-and nano-roughness becomes easily visible when comparing the confocal laser scanning microscope (LSM, Olympus LEXT 4000) picture with a mag-

nification of 100 with a SEM picture with a magnification of 10.000 in **Fig. 5.33**. In the optical laser microscope picture the unevenness on the flanks of the pyramids can only just be detected. The SEM picture reveals a quite pronounced roughness on a scale below one micrometer.

5.8.1 Initial observations

The issue of the effect of surface morphology on the performance of large area silicon devices (namely lifetime samples) was first encountered in a preliminary test on different HF/O_3 cleaning conditions on textured surfaces (run 1013). The six groups in **Tab. 5.6** were tested similar to run 1273 in the previous section (thermal oxidation and both sided SiN_x deposition). Each group consisted of eight wafers and three spots per wafer were measured by QSS-PC. Wafers from two texturing carriers were used and evenly distributed across the groups. The texturing bath had been freshly made up for the first carrier. As-cut wafers were etched for 28 minutes, the resulting etch depth of the first carrier was measured to be 8.4 μm and of the second carrier 9.0 μm per side.

Tab. 5.6: Tested cleaning conditions for HF/O_3 cleaning pretest.

group#	c(HF) [%]	time [min]
1	0.05	10
2	0.05	2
3	0.2	10
4	0.2	2
5	0.5	10
6	0.5	2

When fitting the data in JMP10, the texturing carrier was required as factor to allow a statistical fit. This did not come as a surprise, as a fresh texturing bath had been made up for this experiment and from processing experience a relatively constant output of the texturing bath is obtained only after the second carrier (explaining the different etching depths).

The model extracted from the resulting data can be found in **Fig. 5.34**. Across the investigated concentration range $-\log(c(HF))$ of 0.3 to 1.3 it matches nicely the values from run 1273 (as presented earlier in **Fig. 5.25**). The difference between the two carriers is found to be significant for all groups, including the reference and equals 6 mV in *implied* V_{oc}. From this fact it can be concluded that this deviation is unlikely to be attributed to differences in surface contamination but to surface properties, such as roughness or pyramid structure.

Two wafers from the best (0.05% HF, 10 min) and the worst performing group (0.5%, 2 min) originating from the two carriers and the SPM reference were chosen for further analysis. As no high resolution imaging tool for nano-scale roughness was available, the reflection was used to detect differences in nano-roughness and the LSM for the measurement of the micro-roughness. A spectrophotometer (*Perkin Elmer*) with an integrating sphere was used. The total reflection was averaged across the wavelength range of 400 to 1100 nm. The micrometer scale surface morphology was measured using 3D-LSM imaging with a maximum resolution of 125 nm. The roughness was determined by the *MountainsMap Surface Texture Analy-*

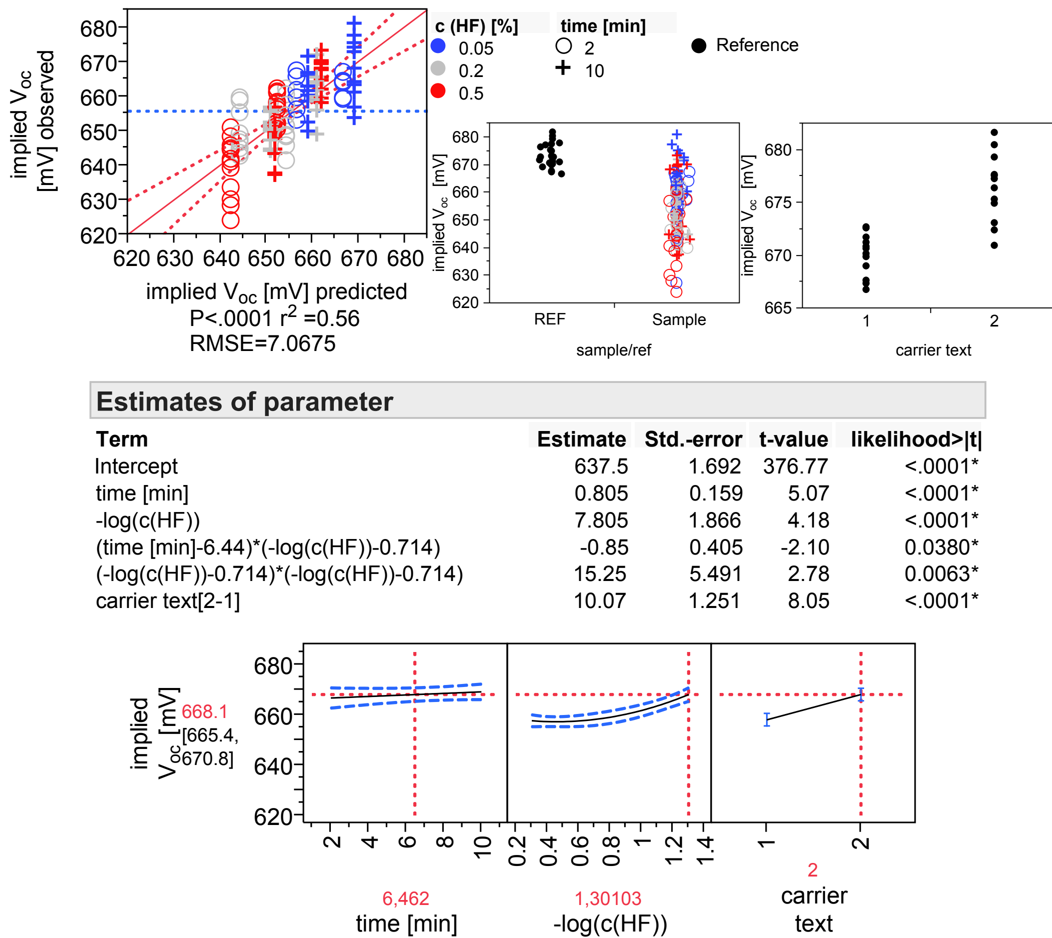

Estimates of parameter

Term	Estimate	Std.-error	t-value	likelihood>|t|
Intercept	637.5	1.692	376.77	<.0001*
time [min]	0.805	0.159	5.07	<.0001*
-log(c(HF))	7.805	1.866	4.18	<.0001*
(time [min]-6.44)*(-log(c(HF))-0.714)	-0.85	0.405	-2.10	0.0380*
(-log(c(HF))-0.714)*(-log(c(HF))-0.714)	15.25	5.491	2.78	0.0063*
carrier text[2-1]	10.07	1.251	8.05	<.0001*

Fig. 5.34: Regression model of pretest including the dependency on the texturing carrier. The difference between the carriers is also detected for the reference, as plotted in the top right hand side graph.

sis Premium 5.1.0.5338 software (following ISO 25178-2:2009). The *sdr* values for surface roughness were calculated by $\frac{(texture\ surface\ area)-(projected\ surface\ area)}{projected\ surface\ area} \cdot 100\%$. The results of the two measurements are displayed in **Fig. 5.35**. The one wafer surface that differs from the rest of the group (with a much higher reflection and lower *sdr* values) is excluded from further analysis. It is considered to be an outlier.

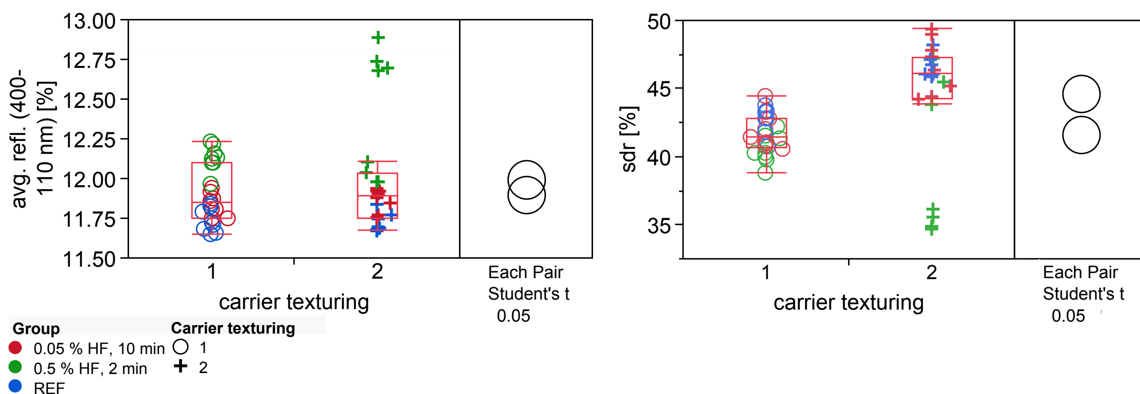

Fig. 5.35: Reflection and surface roughness (*sdr*) of the two texturing groups.

The left hand side graph shows no significant difference between the reflection of the two texturing carriers. The roughness, however, differs by a quite large extend. The observed difference in *sdr* associated with the texturing carriers does not straight forwardly explain the differences in *implied* V_{oc}. As micro-roughness increases, the *implied* V_{oc} does the same. Obviously, the surface passivation is not affected by the enlargement of surface. The reason for the difference in lifetime between the two groups remains unclear.

What had already been indicated by the reflection in **Fig. 5.35** was proven when plotting the reflection against the three cleaning groups, as it was performed in figure **Fig. 5.36**. The reflection differs significantly between the groups. Both HF/O_3 steps increase the reflection of the wafers, the higher the HF concentration, the more pronounced it increases. Following the argumentation by Angermann *et al.* [305], this difference in reflection is caused by a smoothing effect on the nanometer-scale. However, in this case, the effect on lifetime may be superimposed by the cleanliness of the wafers. The group with the lowest reflection (the SPM reference) shows both, the lowest reflection and the highest lifetime (cf. right hand side of **Fig. 5.36**. Most likely the measured lifetime is mainly governed by differences in surface metal contamination, superimposing possible effects of nano-scale roughness.

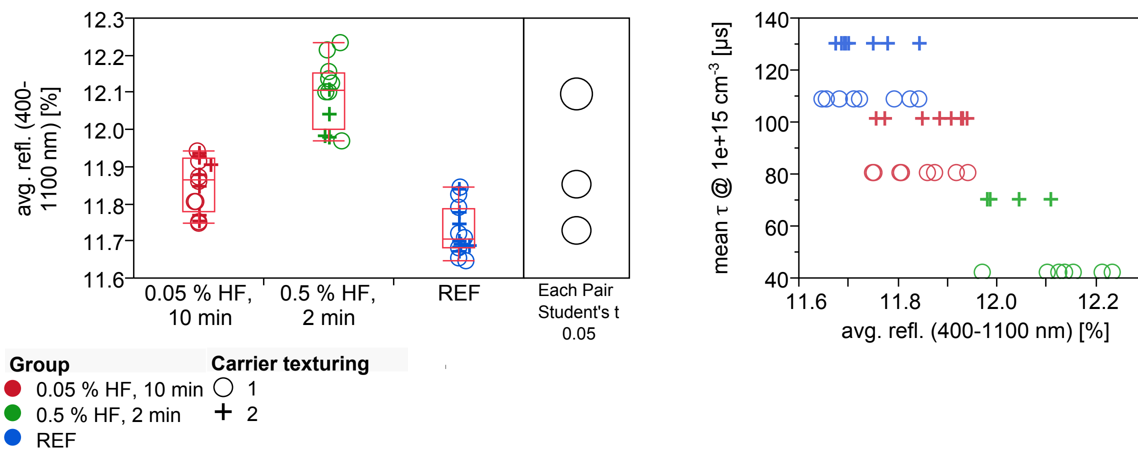

Fig. 5.36: Left hand side: Comparison of the reflection of the the three investigated cleaning groups. Right hand side: Lifetime plotted against the reflection.

Concluding, it can be stated that random pyramid texturing mainly impacts micrometer-scale roughness by varying the pyramid structure. Furthermore, nanometer-scale roughness can be altered by cleaning solutions. Higher HF concentrations in HF/O_3 mixtures show a smoothing effect, while wafers cleaned by the reference SPM+HF* cleaning sequence show lower reflections and thus a rougher surface on the nanometer scale. Differences in lifetime of the lifetime samples passivated by thermal oxide, SiN_x stacks, could not be explained by the observed surface properties.

5.8.2 Impact of etching and cleaning on micro- and nano-roughness

The effect of “micro-roughness” (structure of the texture) and “nano-roughness” (as caused by the cleaning solution) on lifetime sample performance was more systematically investigated by the following experiment (run 1075). In order to vary these parameters the etching depth

and the cleaning sequences were varied.

To avoid interference between surface contamination and surface morphology parameters originating from the as-cut wafer, saw damage etched wafers (10 μm per side) were SPM cleaned and subsequently textured for 12, 28 and 40 min using KOH/monoTEX^{TM} resulting in 4, 6.5 and 10 μm etch depth per side, respectively. Two carriers with 50 wafers were etched for each etching time. Lifetime samples (two per group) were prepared using the process sequence from **Sec. 5.4** and full Al-BSF solar cells were processed (eight per group) using the same diffusion as studied in **Sec. 4.3.2**, targeting efficiencies of 19%. The influence of the two HF/O_3 concentrations from above (0.05% and 0.5% for ten minutes) were compared against the pSC1+HCl+HF sequence, with and without a subsequent piranha step and the SPM+HF by itself.

First, the reflection and surface morphology of each group were measured by the spectrometer and the LSM. The results plotted against the etching depth can be found in **Fig. 5.37**. Obviously, with increasing etching depth both the reflection and the roughness increase. This phenomenon can be explained, when a closer look is taken at an other roughness parameter extracted from the 3D-LSM measurement, namely the *Sz*. *Sz* accounts for the maximum difference in height (from the lowest valley to the highest peak) within the investigated 3D image. This value increases with etching depth indicating that the surface becomes more ragged. As new pyramids tend to grow in the flanks of existing pyramids, "mountain ridge and valley structures" grow on the surface. The open flanks of these structures tend to be less effective in light coupling than the initial surface in which the pyramid tips and valleys in between tended to be in the same range of height (low *Sz*).

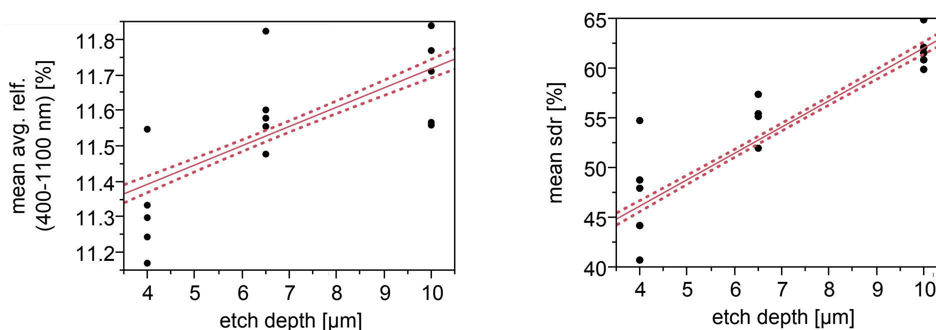

Fig. 5.37: Reflection and roughness plotted against the etching depth.

In order to extract the differences in impact of the cleaning on the wafer surface, taking the etching depth of the different texturing carriers into account, the JMP10 fitting function is used. The texturing carriers are used as ordinal variables. The accordingly fitted data are displayed in **Fig. 5.38**.

As expected, the strongest effect factor on the reflection is the texturing carrier. Interestingly, even when etching similar amounts of silicon (1&2, 3&4, 5&6), the reflection can differ from carrier to carrier. Obviously such factors as texturing bath age and composition due to non-optimised feed/bleed operation (affected by the different etching depths) tend to effect the pyramid structure and in consequence the reflection. The impact of the subsequent clean-

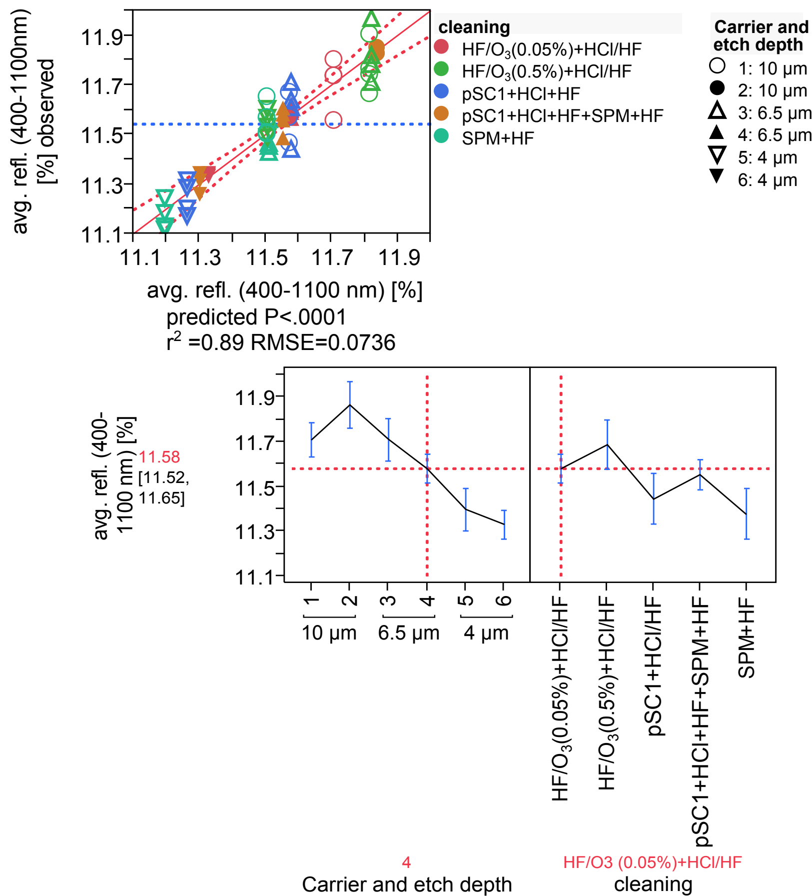

Fig. 5.38: Dependence of the reflection on the texturing carrier and the subsequent cleaning sequence. The steps obtained for the different cleaning systems were used as "reflection due to cleaning" parameter signifying the nano-roughness for the analysis of the following lifetime and cell data.

ing procedure is also evident. As observed in the previous experiment, the highest reflection is measured when cleaning with HF/O_3 with the highest HF concentration. Interestingly, the SPM+HF step itself seems to decrease the reflection, but when applied after KOH/H_2O_2 it rather increases it. Generally speaking, up to 0.3 to 0.4% reflection difference can be attributed to the cleaning, while the etching depth/etching bath composition was found to account for about 0.6%. For the analysis of the effect of the nano-roughness on lifetime and cell parameters the mean value of the reflection (11.657%) was used and modified by the values extracted from the model:

- +0.052% for "HF/O_3(0.05%)+HCl/HF"
- +0.159% for "HF/O_3(0.5%)+HCl/HF"
- –0.084% for "pSC1+HCl+HF"
- +0.025% for "KOH/H_2O_2+HCl/HF+SPM+HF"
- –0.152% for "SPM+HF"

5.8.3 Impact of surface roughness on lifetime samples

Next the results of the lifetime samples are discussed. The samples were manufactured from 1.9 Ωcm p-type Cz silicon by the same supplier taken from several boxes evenly distributed among the groups (as it was prepared for the ISC Konstanz standard run for quality assurance). While the resistivity was within a range of ± 0.1 Ωcm, the lifetime of the wafers varied strongly for the different sections of one or more columns (referred to as "box"). This complicated the matter of comparing the obtained lifetime values after processing. Even within the respective boxes large variations were observed, most likely as they originated from the end of the column (F vs. F-x). As the number of samples was small so that no even distribution of wafers from the respective boxes on the groups of samples was guaranteed, JMP10 fitting was used to compare the cleaning groups. The lifetime levels were taken into account by assigning a nominal variable to the boxes. Ordinal values were assigned to etch texturing carrier (in chronological order, etching depths of carrier **1 & 2: 10 μm**, of carrier **3 & 4: 6.5 μm** and of carrier **5 & 6: 4 μm**). The different cleaning methods were used as nominal variables. The thus obtained model and the prediction diagram can be found in **Fig. 5.39**. The lifetime of minority carriers (at an injection level of $\Delta n = \dot{1}$e+15 cm^{-3}) was used, as the differences between groups in terms of *implied* V_{oc} were relatively small and, as explained in **Sec. 3.2.1**, the lifetime value is more sensitive to small variations.

The differences in lifetime between the carriers were found to be relatively small and mostly within the error bars. Lower etching depths seem to be slightly favourable. The impact of the cleaning can be separated into three main groups: HF/O_3 based (lowest lifetimes), using KOH/H_2O_2 (medium) and SPM+HF (highest). Observed lifetimes correspond to *implied* V_{oc} values of 655 to 706 mV, corresponding to an increase in surface recombination velocity of only about 15 cms^{-1} (calculated from **Eq. 3.18** in **Sec. 3.1.3**). Summarising, in **Fig. 5.40** the lifetime is plotted against the reflection due to cleaning, signifying the differences caused by nano-roughness (as derived in **Sec. 5.8.2**) and the etching depth, signifying the pyramid structure and here referred to as micro-roughness.

From the graphs it becomes clear that no significant effect of the micro- and the nano-roughness was extracted. Differences observed for the various cleaning techniques were most likely caused by slightly different remaining metal surface contamination. Differences in pyramid structure appear to have little to no impact on the surface recombination when thermal oxide/SiN_x passivation stacks are used. Note that these data are not resolved for the differences in bulk performance and might thus be biased.

5.8.4 Impact of surface roughness on solar cell properties

As shown, etch depth and subsequent cleaning have a measurable effect on surface properties, such as nano- and micro-roughness. In the following this impact on solar cell parameters was assessed. The two solar cell parameters that are linked closely to optical properties of the surface are the short circuit current J_{sc}, due to its sensitivity towards light coupling and the V_{oc}, due to its sensitivity towards surface recombination. The more effectively the light is trapped, the higher is the J_{sc}. Inversely, the V_{oc} may decrease with increasing surface

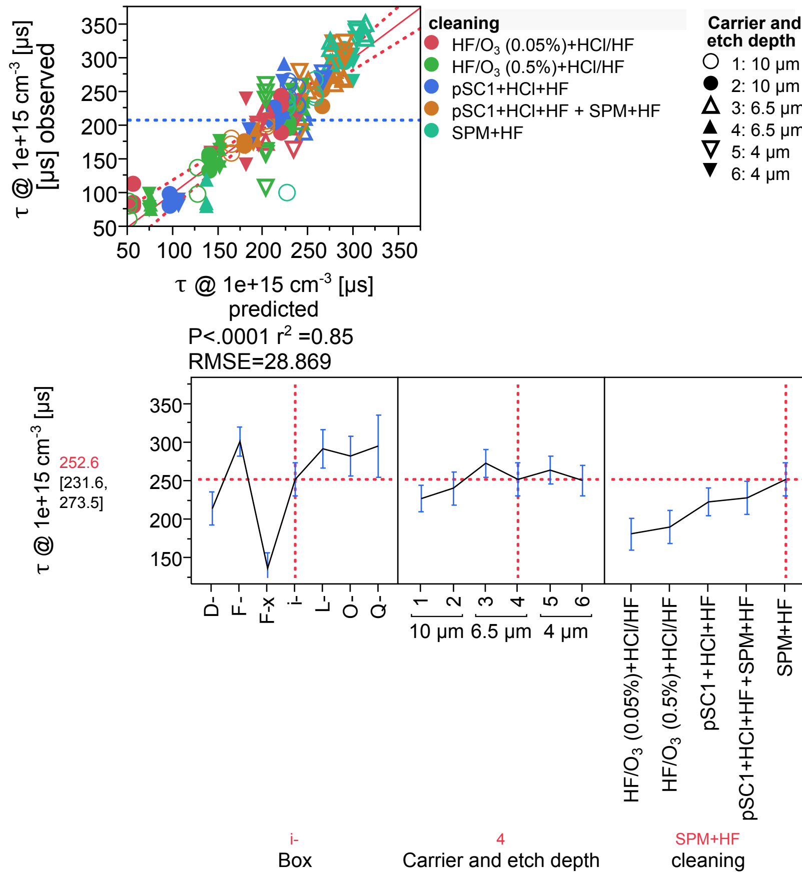

Fig. 5.39: Fit of the obtained lifetimes for the different cleaning procedures and etching carriers, corrected for varying material lifetimes. As only nominal factors are used for the fit, no interaction between the factors is considered so that the interaction diagram can be used to compare the influence of the different factors at any point. Changing one factor changes only the overall level.

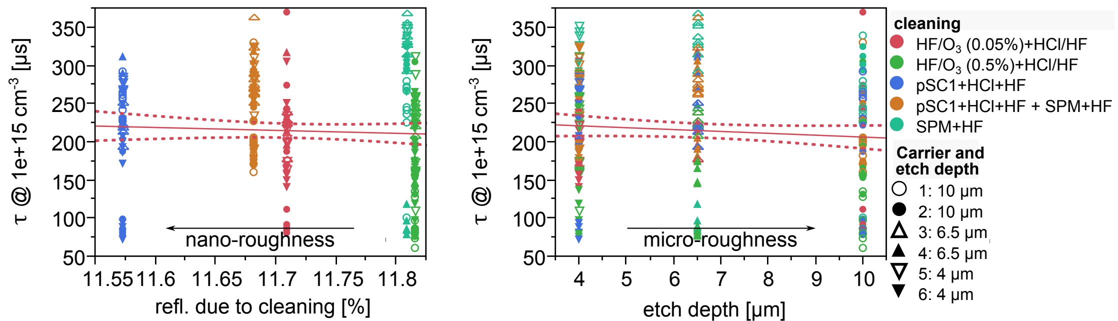

Fig. 5.40: Lifetime plotted against the reflection change due to cleaning (nano-roughness) and the etching depth (micro-roughness).

roughness and surface recombination. In order to study the effect of the nano-roughness the solar cell parameters Eff, V_{oc}, J_{sc} and FF are plotted against the "reflection due to cleaning" as derived in the previous section (cf. **Sec. 5.8.2**).

When analyzing the linear fits of the solar cell parameters against "reflection due to cleaning" only a small, but measurable, influence was detected. With increasing reflection (decreasing nano-roughness) the cell current decreases slightly, so do, most pronounced, fill factor and the efficiency. The effect on solar cell conversion efficiency with a gain of about 0.05%

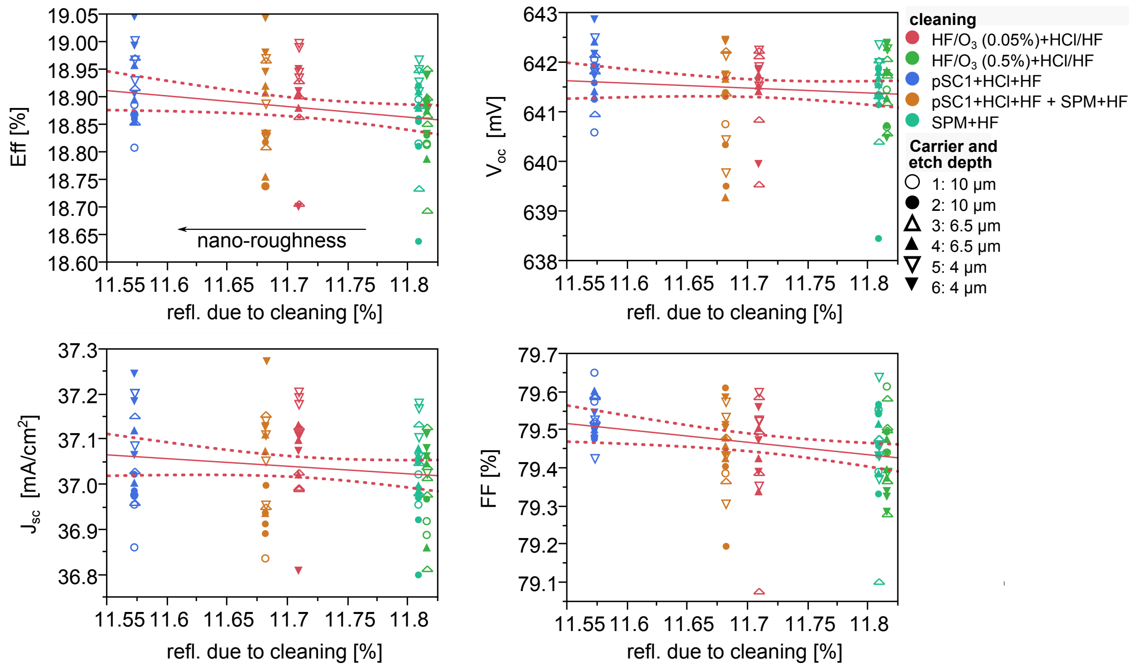

Fig. 5.41: Cell data plotted against reflection caused by nano-roughness.

abs. with increasing nano-roughness across the investigated range is small, though. From this it can be concluded that the nano-roughness does not have a negative effect on the solar cell performance, much rather it improves the contact formation of the silver paste (hence the increased FF) and to a smaller extend the light trapping (hence the increase in J_{sc}).

When plotting the same data against the etching depth in **Fig. 5.42**, using as a measure for the pyramid structure (cf. **Fig. 5.37**), a more pronounced effect is detected. With increasing roughness, most pronouncedly the J_{sc} decreases, which follows the trend of decreasing reflection with increasing roughness. While the V_{oc} decreases by about 1 mV, the fill factor hardly changes. The loss in efficiency accumulates to 0.15% abs..

However, it is a well known fact that thicker solar cells may perform better than thinner cells due to a larger absorber volume. With increasing etching depth thinner wafers are obtained. The solar thickness in this experiment varied between 155 and 175 μm, due to the different etching depths. In order to distinguish these two phenomenons—improved light coupling due to surface properties or due to increasing thickness—a simple PC1D[1] simulation was conducted. The cell parameters were chosen to match the internal quantum efficiency[2] of an average solar cell from this experiment. Then the wafer thickness was varied across the range of wafer thicknesses determined in this experiment and the resulting J_{sc} is plotted and compared with experimental data in **Fig. 5.43**. The two linear fits lead to the conclusion that the differences in J_{sc} between the carriers is mostly due to the variation of the wafer thickness.

Summarising, only very small impact of the two distinguished forms of roughness was detected. The strong decrease in solar cell efficiency observed for the different etching times

[1] PC1D is the standard freeware simulation tool of the PV community [306].

[2] The internal quantum efficiency (IQE) is the wavelength resolved measurement of the cell current corrected for the "external" reflection of the solar cell.

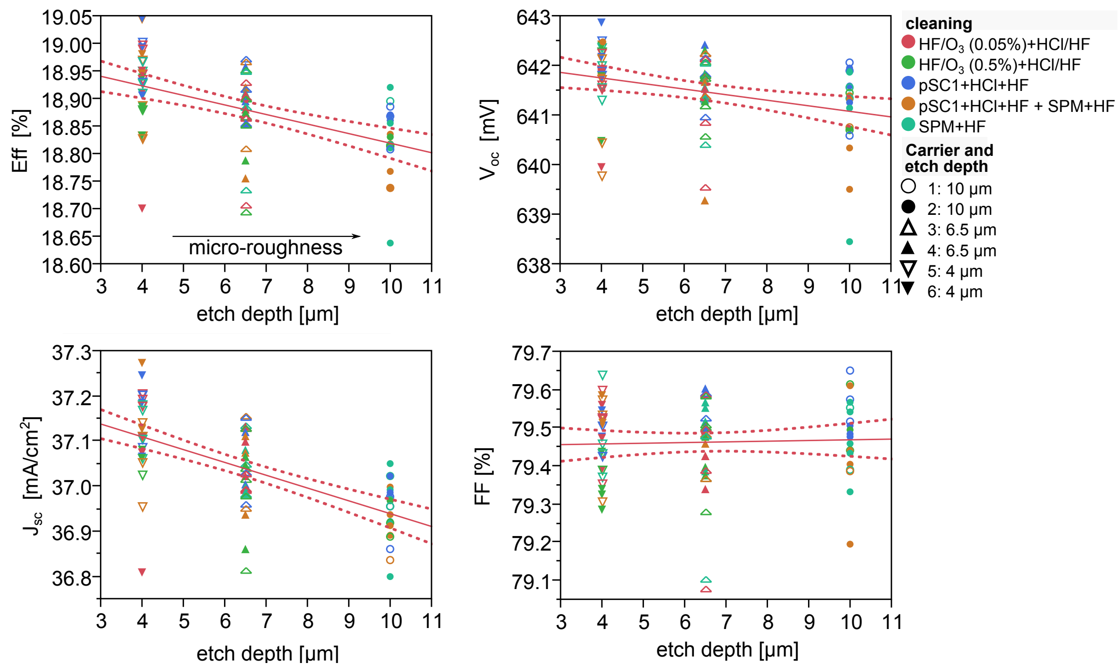

Fig. 5.42: Cell data plotted against the etching depth.

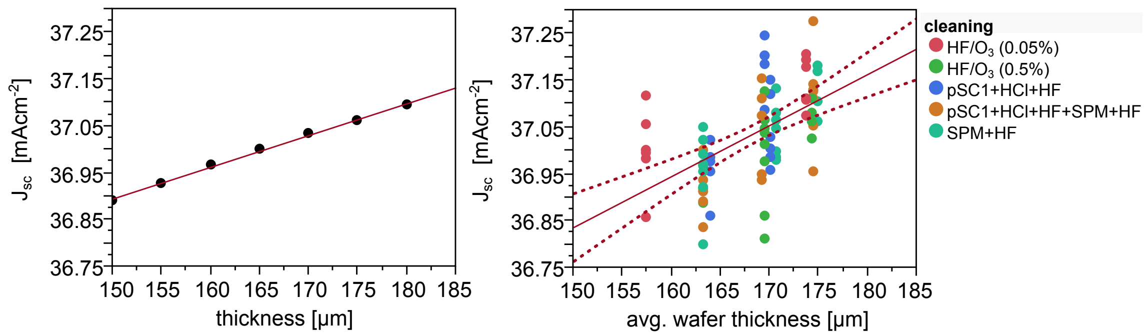

Fig. 5.43: Impact of wafer thickness on J_{sc} as simulated by PC1D and observed in this experiment.

is to a large extend governed by the decrease in wafer thickness.

5.8.5 Conclusion

In summary, it can be stated that wet chemical process steps such as alkaline texturing and cleaning interfere with surface properties such as micro- and nano-scale roughness. Alkaline etching with increasing etching time increases both, the roughness and the reflection. The cleaning mixture and the cleaning sequence were also found to govern the reflection of the silicon surface, an effect that can be attributed to nano-scale roughness. The lowest values for reflection after cleaning were found when using only SPM+HF and only slightly higher values for pSC1+HCl+HF. HF/O_3 mixtures with high HF content (in the range of 0.5%) were found to increase the average reflection and thus smoothing the surface. Interestingly, SPM+HF, if applied after pSC1, increased reflection were found. The difference in reflection due to cleaning was found a useful measure for nano-roughness.

No impact of the differences in surface morphology were detected on thermal oxide/SiN_x

passivation stacks.

The effect of nano- and micro-roughness on Al-BSF solar cells was studied. A small impact of nano-roughness was detected on solar cell conversion efficiencies. A much more pronounced effect, first attributed to the pyramid structure (micro-roughness), turned out to be mainly caused by a variation in thickness. However, surfaces obtained after prolonged etching featuring higher reflection and higher roughness thus seem to be less desirable, as with thickness the J_{sc} decreases, as well as the V_{oc}.

Considering that the highest reached efficiencies were only in the range of 19.1%, it is to be expected that with more efficient solar cells the need for well defined, clean surface features will be required—especially in the case of processing solar cells without front metallisation (IBC cells, cf. **Sec. 2.5**, **Fig. 2.30**) with efficiencies exceeding 22%. Another solar cell concept that has already been shown to be sensitive to surface nano- and micro-roughness are heterojunction solar cells (cf. also **Fig. 2.30**). An amorphous (intrinsic) silicon layer is commonly deposited on the textured silicon surface requiring a highly clean and defined surface [307, 308].

5.9 Summary and outlook

This chapter provided insights into the dynamics of metal surface contamination, with a focus on FEOL wet chemical processing. As-cut wafer surfaces were analysed and differences in metal surface contamination were found depending on the sawing process. The investigated slurry sawn wafers showed higher Cu values (about one order of magnitude), whereas the diamond wire sawn wafers showed higher Cr and Ni concentrations (again in the range of one order of magnitude). Fe surface contamination was found to a similar extend. Generally, transition metal surface concentrations ranged between 1e+14 cm^{-2} (Cu), 1e+13 cm^{-2} (Fe) and 1e+11 to 5e+12 cm^{-2} (Ni, Cr, Mn and Ti). Differences between one end and the other of a column sawn by the same techniques were found especially for the diamond wire sawing technique. Not all observed effects was explained and require further analysis, ideally involving contributions from wafering specialists, such as input on process variations, lifetime of wire saws, et cetera.

Next, the etching of as-cut wafers using highly concentrated NaOH as saw damage etch and lower concentrated KOH with RENA monoTEX^{TM} as texturing additive for the purpose of random pyramid texturing was studied. Surface contamination was measured before and after etching. It was shown that the surface contamination after etching is determined either by the as-cut wafer or the alkaline solutions. High initial base concentration and in consequence high metal concentration lead to higher surface concentration on the wafer after etching than before, and vice versa for low concentrated bases. For example, highly concentrated NaOH is “cleaned” for most of the investigated elements over time, whereas the texturing bath is gradually “contaminated” by the as-cut wafers. Assuming that none of the etching solution is replaced by fresh solution in all cases, it can be assumed that eventually surface concentration after etching will equal initial surface concentration. It has to be stressed that under “real” mass production conditions feed-and-bleed has to be taken into account, as it is expected to de- or increase the surface contamination, depending on whether the feeding solution has a higher or lower contamination load than the ething bath. The data indicate that the said equilibrium is reached quickly in terms of industrial throughput (after a couple of hundred to thousand of wafers). If the alkaline texturing step is moved further down the process line, this behaviour changes, as clean wafers are etched, which in turn get contaminated by the etching solution. Smaller concentrations (about one magnitude lower) were found, when the same type of etching was applied later in the process. Yet, surface concentrations up to 1e+12 cm^{-2} (for Fe) and up to 2e+11 cm^{-2} (for Cr, Ni and Cu) after alkaline texturing were measured.

Surface concentrations after both alkaline etching processes were shown to reach similar magnitudes as found on the wafers before etching, especially FEOL cleaning for high efficiency solar cell processing is a challenging task, particularly when considering large scale mass production. That this assumption holds true was shown when different cleaning sequences were tested for pre-diffusion cleans for standard Al-BSF cells and highly efficient n-type BiSoN solar cells processes. While standard industrial Cz Al-BSF solar cells showed to be unproblematic considering FEOL and BEOL cleaning (HCl+HF was shown to be sufficient),

high efficiency n-tpye BiSoN cells were shown to require highly efficient oxidative solutions.

To overcome this challenge, a cost effective cleaning system, based on ozone containing dilute hydrofluoric acid, was developed, optimised and tested. The procedure used for the comparison and determination of cleaning efficiency consisted of thermally oxidising the cleaned surfaces and measuring the *implied* V_{oc} after SiN_x deposition. The optimisation of the HF/O_3 cleaning system included the factors of surface morphology and sawing (textured, flat, diamond and slurry sawn), as they were found to have a measurable impact on the performance of the cleaning solutions. Furthermore, the variables composition of the oxidative O_3 fed cleaning bath, the immersion time and the process temperature were added. By extensive statistically modelling, it was found that relatively small optimal concentration ranges were required. The ideal HF concentration for flat surface was found to be about 0.025% and slightly higher for textured surface (0.04 to 0.06%). A small dependency on immersion time was found indicating that longer immersion times (up to 10 min were tested) are favourable. Good cleaning efficiencies were achieved at room temperature. After oxidative cleaning, wafer were dipped into 2% HF/HCl mixture for 2 min to remove the sacrifice oxide. If further improvement of the cleaning sequence can be obtained by using different compositions of this step, still has to be tested. Further work in this field may be necessary, as the high efficiency lab scale reference was not quite met in all cases.

Whether the found optima of HF/O_3 based cleaning sequence were sufficient for high efficiency solar cell process, was tested next. Already the not yet fully optimised sequence as FEOL and BEOL pre-diffusion clean showed no significant loss in conversion efficiency of high efficiency BiSoN solar cells, when it was compared to the high efficiency lab cleaning sequence. Finally, at least for diamond-wire sawn wafers, the suitability for BiSoN solar cell processing was shown. The group of slurry sawn wafers showed a lack in efficiency, which may be contributed to the fact that the HF/O_3 cleaning sequence is not as effective in etching remains of the saw damage as the SPM based reference process. Tests for the integration into large scale industrial fabrication of BiSoN are underway and thus experiments about feasibility and long term stability will be much easier to be conducted in “real” production surroundings.

Last, it was shown that texturing and cleaning affects surface properties such as micro- and nano-scale roughness. Cleaning in HF/O_3 turned out to reduce the nano-roughness, depending on the HF concentrations (the higher the HF concentration the stronger). The nano-roughness was indirectly measured by an increase in average reflection. SPM and pSC1 cleaning solutions had either an adverse or little effect. Longer texturing times were found to increase both, roughness, as measured by LSM, and the reflection. This indicates that once the surface is covered with pyramids further etching only increases the ruggedness of the surface without further improving the light coupling. On the investigated lifetime samples no effect of both variation in micro- and in nanoroughness, was conclusively extracted. One reason for this is the fact that small amounts of surface contamination and the nano-roughness were expected to have effects on the minority carrier lifetime to a similar scale.

When varying micro- and nano-roughness for Al-BSF solar cells, several correlations was identified. Increasing nano-roughness showed to be beneficial for the contact formation, as the

FF showed the strongest increase, while the V_{oc} slightly decreased, indicating a small increase in surface recombination. The effect of the increased texturing time was more pronounced. More than a 0.15% abs. decrease in efficiency were observed, when increasing the etching depth from 4 to 10 μm, mainly driven by the J_{sc}. However, from simulation results, it was deduced that this loss was to less extend governed by surface properties than by the decrease in wafer thickness. As the V_{oc} also showed a decrease (it is expected to not be in affected by the wafer thickness), it was concluded that an increase in micro-roughness is not desired. Further work in this field needs to include the effect of surface treatment on higher efficiency solar cells such IBC solar cells, which, due to a lack of front side metallization, feature much higher solar cell currents and hence are expected to be affected to much larger extend.

Summarizing, it can be stated that cleaning is an issue, which is expected to gain even more importance in the future. The solar cell efficiencies reached in this work ranged from 18 to close to 20%, values that have been exceeded many times on lab scale and are about to being exceeded in large scale mass production. The surface concentrations required for highest lifetimes on lifetime samples and for high efficiency solar cells were found in ranges (well) below 1e+11 cm^{-2}, which are in good agreement to the data collected in **Ch. 4**.

6 Experimental section

6.1 Overview runs

Tab. 6.1: Overview of the experiments (runs), from which data were used to write this thesis. The types of material (n-type wafers were P-doped, p-type wafers B-doped), the sawing processes, the doping concentration (resistivity) of the wafers, the sample sizes of the experiment groups (number of wafers) and the topics of each experiments are listed. Large area pseudo-square wafers (156*156 mm^2 with a diagonal of 200 to 210 mm) were used throughout this work.

run	material type	sawing technique	resistivity [Ωcm]	sample type	group size	topic of investigation
700	p-type	slurry	0.55	textured symmetrical lifetime samples	12	cleaning, variation P-diffusion, PSG analysis
824	p-type	slurry	1.6	textured symmetrical lifetime samples and solar cells		cleaning in Al-BSF process, PSG analysis
954	p-type	slurry	2	textured symmetrical lifetime samples	3	first tests O_3 based cleaning
1013	p-type	slurry	1.8–2	textured symmetrical lifetime samples	18	optimisation HF/O_3 clean
1075	p-type	slurry	2.4	solar cells, symmetrical lifetime samples	18	cleaning, surface roughness in Al-BSF process
1076	n-type	slurry	9–10	solar cells	18	cleaning in BiSoN cell process
1113	p-and n-type	slurry	1.9 / 8.5	textured symmetrical lifetime samples	5	cleaning; thermal oxidation
1241	p-type	diamond and slurry	3–4 / 1.9–2	surface analysis	50	saw damage etch and texture etch
1265	n-type	diamond and slurry	5.5	solar cells	9	cleaning in BiSoN cell process, HF/O_3 clean
1273	p-type	diamond and slurry	1.9–2.2	textured and flat symmetrical lifetime samples	3	optimisation HF/O_3 clean
1274	p-type	diamond	1.7–1.9	flat symmetrical lifetime samples	3	contamination from HF and H_2O; MSiN$_x$, thermal oxidation
1288	p-and n-type	diamond	2.0 / 8	flat symmetrical lifetime samples	3	contamination from H_2O; P-diffusion (p-/n-type), B-diffusion, thermal
1306	n-type	diamond and slurry	7.5 (A-slurry); 8.5 (A-dia); 4.5 (B-dia)	solar cells	24	FEOL cleaning variation in BiSoN cell process
1331	p-type	diamond	1.7	surface analysis	50	saw damage etch and texture etch
1332	p-type	diamond	2.1	flat symmetrical lifetime samples	3	optimisation HF/O_3 clean, flat samples
1333	p-and n-type	diamond	2.0 / 8.0	flat symmetrical lifetime samples	3	contamination from H_2O; P-diffusion (p-/n-type), B-diffusion, thermal oxidation
1393	p-type	diamond	1.7	solar cells	7	Test HF/O_3 for PERC solar cell process

6.2 Analytical methods

Two analytical measuring techniques for elemental trace analysis were employed in this work. The sandwich-etch ICP-MS (SE ICP-MS) was used for the extraction and determination of surface contamination. The second technique was implemented to determine Fe and Cu concentrations in aqueous solution in the range of single digit parts per billion by photometric spectroscopy. The two techniques are discussed briefly in the following. While in the case of the SE ICP-MS method only the sampling was performed at ISC Konstanz. The case of the spectrophotometric determination of Fe and Cu the tool was available at ISC Konstanz and part of the optimisation was performed within the scope of this thesis.

6.2.1 Sandwich-etch ICP-MS

Inductively coupled plasma mass spectroscopy (ICP-MS) is a multi-element analytical technique, which uses a high temperature (argon-) plasma source to decompose, dissociate, atomise and ionise the elements of interest in a sample. It can handle small amounts of sample solution (< 1 mL) of highly aggressive chemicals. The detection limit for a variety of metals lies in the range of $0.01 - 0.05$ ppb (for silicon-free samples).

Therefore, it is the method of choice for surface sample analysis. In the sample solutions, few interferences obscure the measurement of the trace elements of interest; primarily by polyatomic ions derived from the sample solvent and the plasma gas (O, H, Ar, C, N), which overlap the specific mass of interest, but also from the sample matrices (HF, HNO_3 and Si). In this work a reaction cell ICP-MS located and operated at *Analytik für Technik und Umwelt (ATU) GmbH* in Herrenberg was used. The reaction cell allowed to attenuate interferences either by reaction with H_2-gas or by collision with He-gas. A scheme of such a device is shown in **Fig. 6.1**.

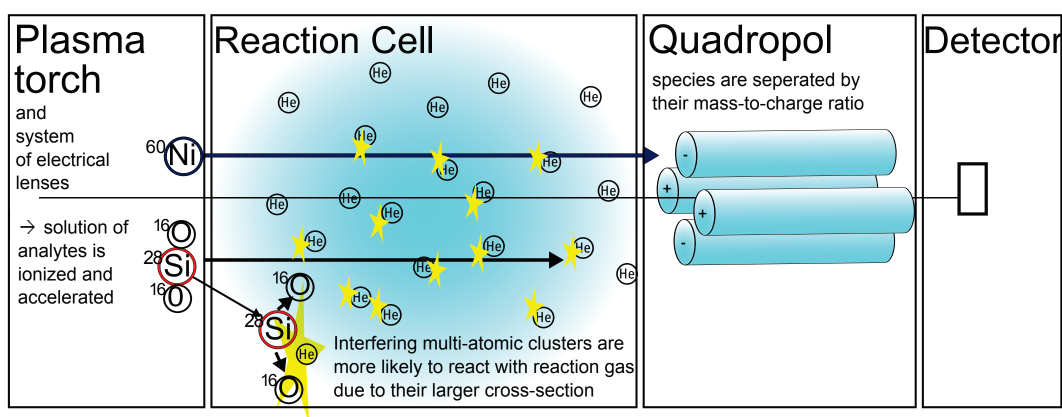

Fig. 6.1: Scheme of a reaction cell ICP-MS.

For the surface samples of the experiments, the solutions were diluted by a factor of ten in order to decrease the silicon content of the sample solution which in turn increased the detection limit by the same factor to 0.1 to 0.5 ppb (or 0.1 to 2 e+10 cm^{-2}). For lower detection limits silicon would have to be removed by evaporation previous to the measurement.

It is a well-known fact that the quantitative dilution of noble transition metals is relatively

challenging. In contact with Si they tend to be reduced and therefore need to be oxidised before they can be dissolved. Cu is the most problematic contaminant in terms of solubility. Therefore, different oxidising sampling solutions were applied and compared in terms of Cu collection efficiency. The solutions were made up from highly pure H_2O_2 or HNO_3 and HF. The latter was believed to be required to dissolve the native silicon oxide. The measurement results from a whole set of consecutive wafers, which were sampled by the sandwich etch technique (as described in detail in **Sec. 4.1.1**) are shown in **Fig. 6.2**. In addition to values obtained by the sandwich etch sampling techniques, values are shown as obtained by vapor phase decomposition (VPD), a surface contamination extraction method commonly used in IC processing. For the VPD technique the wafer was placed in a HF vapour containing chamber. The HF vapour then condensates on the cooled wafer surface. Subsequently, the wafer surface is scanned with a HF/H_2O_2 droplet, which is then analysed.

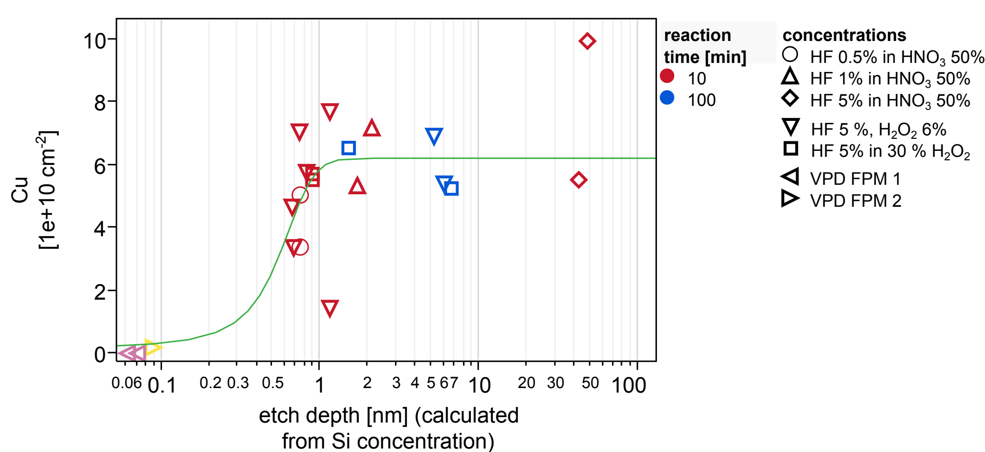

Fig. 6.2: Several solutions and reaction times were tested for Cu detection. The 5% HF in 30% H_2O_2 was chosen and used throughout this work. A set of subsequent multicrystalline wafers after acidic texturisation wafers were used in this experiment.

In **Fig. 6.2** the Cu contamination obtained by different methods, using different chemical mixtures and reaction times, of a hole set of consecutive multicrystalline wafers after acidic texturing, is plotted against the etch depth, estimated from the silicon concentration in the sample matrix. It shows that the sandwich etch method detects much higher concentrations compared to the IC standard method. The different solutions and reaction times used for the sandwich etch approach result in different etching depths. The Cu concentration saturates just below one nanometer at about 6e+10 cm^{-2}, which can be assumed to be the "true" value. For further experiments the most practical solution—in terms of handling—was chosen, which proved also to be the one showing the least spread of values: 5%(wt.) HF in 30%(wt.) H_2O_2. In contrast to most of the mixtures, it is made up from only two components (no UPW needs to be used for dilution). Furthermore, in contrast to the HNO_3 containing solutions, the reaction of the HF/H_2O_2 was not exothermic and did not produce caustic gases.

During this work, the HF/H_2O_2 solution was freshly made up from the chemicals every time before sampling up to 40 sets of wafers. With every set of samples a blank sample (sampling solution only, handled similarly) was taken to ensure the quality of the chemicals, pipette tips and vessels. In order to minimise the use of chemicals and number of samples,

usually the sampling of several experiments was combined.

The volume of the sampling solution for textured wafers was 1 mL and for flat samples 0.7 mL, which were found to be the ideal amounts for 156x156 cm^2 wafers, covering the whole surface and not causing sampling solution to protrude from the sandwich. The reaction time was chosen to be ten minutes, which resulted in sufficiently deep etching. Only when textured surfaces were extracted, the reaction time needed to be increased to 20 minutes in order to produce hydrophobic surfaces. The reason for this was the fact that the surfaces still contained the remains of the texturing additive. Hydrophobic surfaces were required for complete collection of the metal contamination. This was another issue complicating the collection of sampling solution after separating the wafer pair. When highly contaminated samples, such as wafers after SDE, were analysed, the etching solution produced hydrophilic porous silicon due to the catalytic effect of the metal surface contamination. After separation of the wafers, the sampling solution formed a film on the surface and could only be collected after the solution was accumulated by blowing it to one end of the wafer with the help of a nitrogen gun.

To ensure that no contamination was left behind after sampling the method was repeated, in an experiment, on the same set of wafers (acidic textured multicrystalline wafers) for a number of times. After each scan the droplets that had not been collected were rinsed off with ultrapure water and the wafers were dried with a nitrogen gun. The results of this experiment are shown in **Fig. 6.3**. Background contamination or matrix effects are detected for Fe and to a much smaller extend for Ni. In the case of Fe, the measured minimum contamination level saturated at a level of 5e+10 cm^{-2} as minimum measuring range/level of quantification.

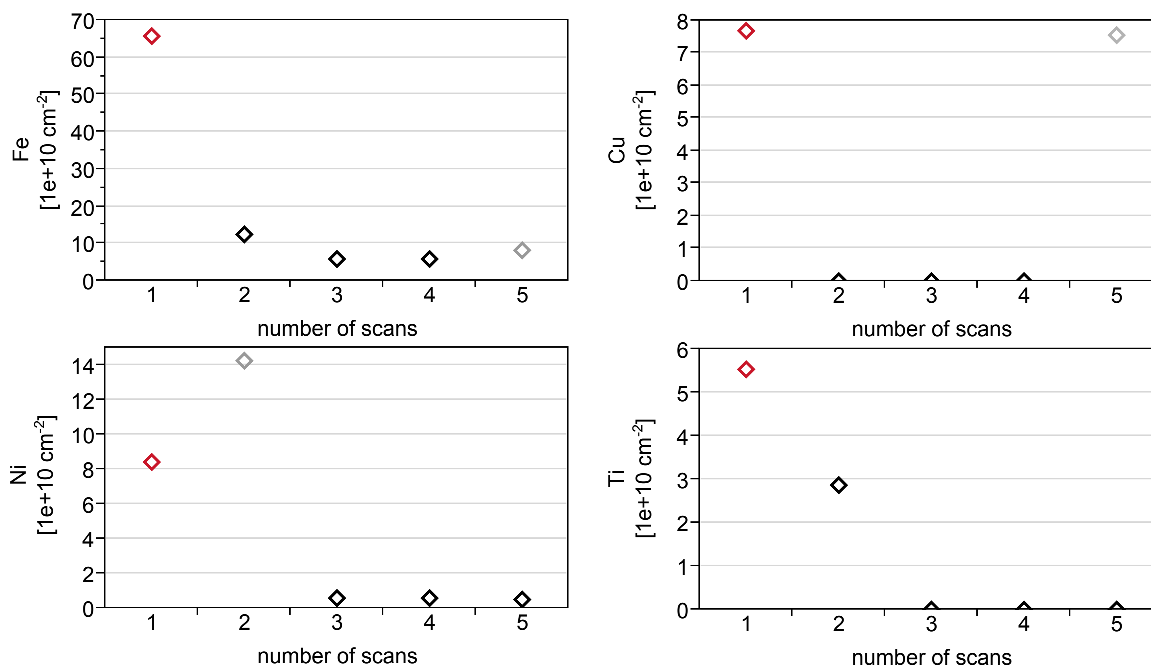

Fig. 6.3: Repeated scanning of the same wafer. After each scan the droplets that had not been collected were rinsed off with ultrapure water and the wafer was dryed with nitrogen. Initial concentrations are indicated in red, outliers in gray.

From the thus obtained concentrations the recovery rate (RR) was estimated, which is

defined as the ratio of detected surface concentration over true concentration [309, 310]. As the "true" concentration level is not known, the recovery rate can be estimated according to the following equation

$$RR_{estimated} = \frac{c_1}{c_1 + c_2(+.. + c_i)} \times 100\%, \qquad (6.1)$$

with $c_{1..i}$ being the concentrations measured in the subsequent surface extractions. In the first experiment the recovery rate for four elements was determined and found to be 90% for Fe, 100% for Cu and only about 50% for Ti, yet on a very low initial level. The recovery rate for Ni could not be determined, as the second scan most likely produced an outlier.

In a second experiment, two subsequent surface extractions were performed on two pairs of wafers (Cz-wafers, saw damage etched in KOH, HCl+HF cleaned). Unfortunately, the second extraction of the first wafer produced an outlier. While Cu and Ni values were consistent, Fe was affected, as were Ti, Cr and Mo, with the last only being detected in this sample, strongly indicating an external contamination (maybe the surface to be extracted was touched by a steel part of the vacuum tweezers). Ignoring this outlier, the elements shown in **Fig. 6.4** prove to be consistent with the first experiment: Ni, Cu and Cr have excellent recovery rates close to or equal 100%. Fe also has a good recovery rate, if the "limit of quantification" is taken into account. As discussed before, the noise of the Fe measurement is with 4e+10 cm^{-2} relatively high.

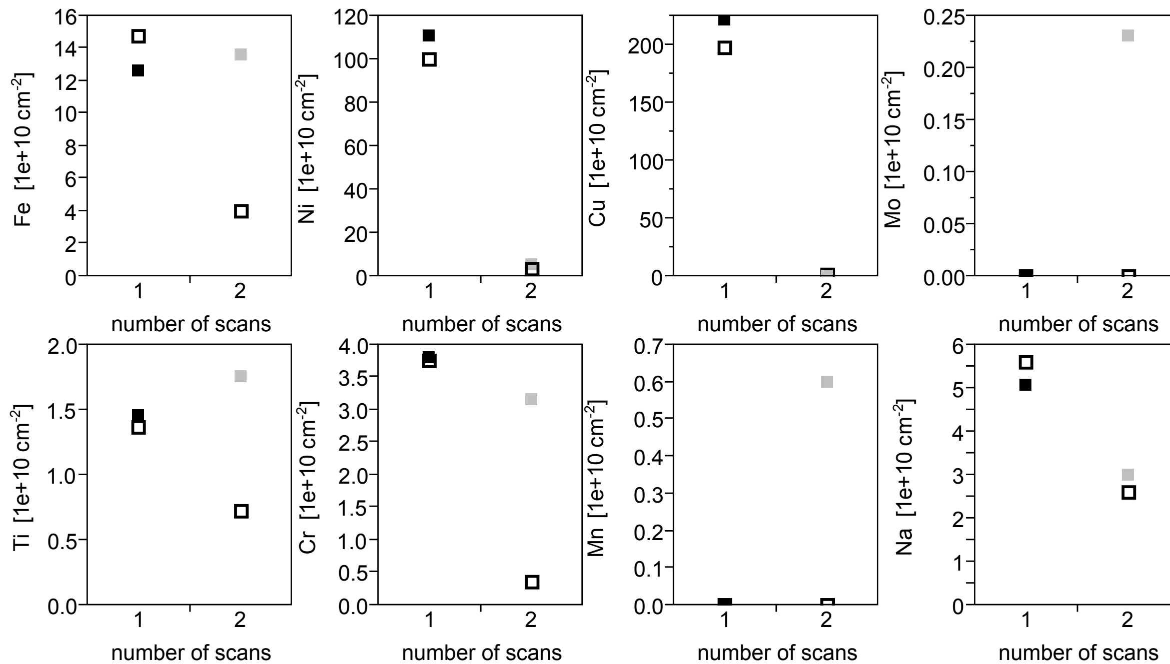

Fig. 6.4: Repeated scanning of two wafers, same symbols refer to the same wafer. After each scan the droplets that had not been collected were rinsed off with ultrapure water and the wafer was dryed with nitrogen. Flat, alkaline etched Cz-wafers were used in this experiment.

Blank concentrations as caused by the sampling solution, pipettes and vessels were measured for every set of samples and—if necessary—the obtained concentration values were corrected accordingly. Low blank values were obtained by decocting the pipette tips and

PFA sample cups in a 1:1 mixture of HCl (32%) and methanol for one hour in a PFA beaker. The cleaning solution was then removed and replaced by fresh ultrapure water, which in turn was replaced by ultrapure water after decocting for another hour.

6.2.2 Spectrophotometric determination of Fe and Cu

In cooperation with *Deutsche METROHM Prozessanalytik* methods for the trace analysis of Fe and Cu based on quantitative spectrophotometry of chromophoric ion-specific complexes were developed and optimised. The methods were integrated into a fully automated METROHM ProcessLab system.

Samples were prepared by adding the ion specific complexing agent (1,10-phenanthroline hydrochloride monohydrate for Fe and bathocuproindisulfonic acid bisodium salt for Cu, see **Fig. 6.5**), a reducing agent and in the case of HF a masking agent was added. Due to the higher complexing constant of the masking agent for F^-, Fe was made accessible to the species-selective complexing agent. Lastly, the pH of the solution was adjusted. Subsequently, the so prepared solution was transferred to a 10 cm quartz glass cuvette. The sample was then analysed using a photospectrometer within the wavelength range of 350 to 1100 nm with an integration time of 52 ms, the number of averaged spectra is 300. The Cu complex was analysed at 510 nm and the Fe complex was 480 nm.

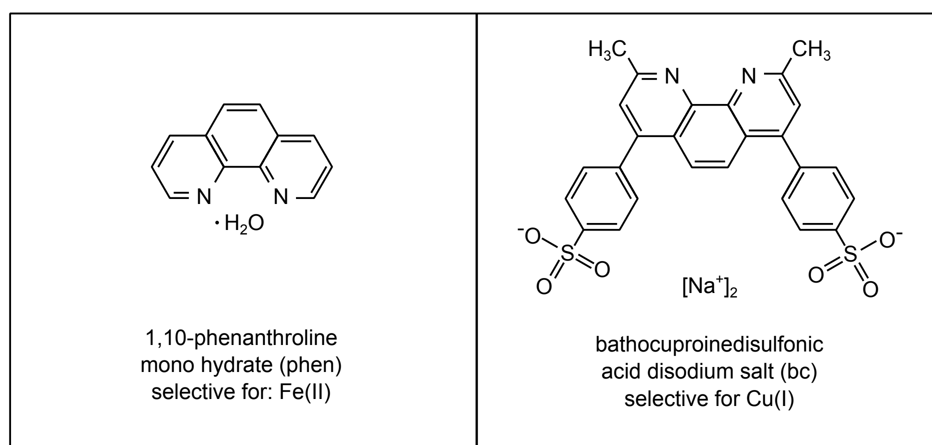

Fig. 6.5: Ion selective complexing agents used for the determination of Fe and Cu.

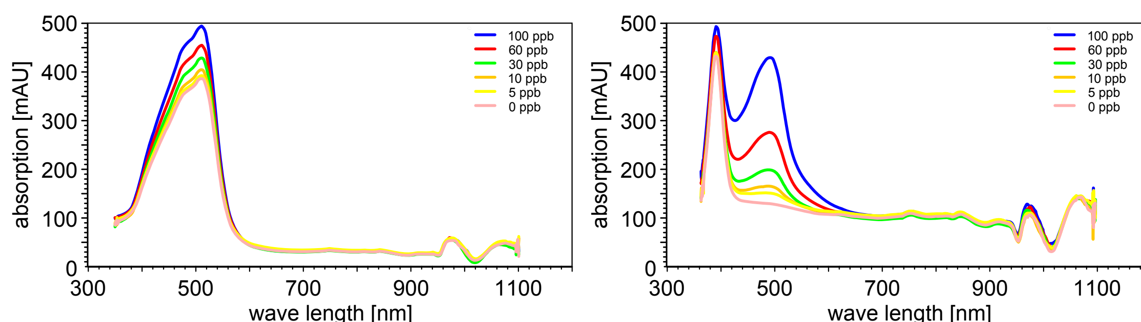

Fig. 6.6: Calibration spectra of Fe (left) and Cu (right) in 2% HF.

The whole sample preparation procedure was run by a liquid handling module that was controlled by *tiamo*^{TM}, the METROHM software for titration. It controls the modules and data handling, processes and stores the collected data. Before and after every analysis the whole system cleaned itself automatically. The calibration of the system was performed by adding defined amounts of a Fe/Cu mixture to a blank solution. The system, so far, has been optimised and calibrated for measurements of water, diluted HF (0.5 to 2%) and HCl (up to 3%). Calibration spectra can be found in **Fig. 6.6**. The obtained limits of detection (LOD) and limits of quantification (LOQ) are displayed in **Tab. 6.2**.

Tab. 6.2: Detection and quantification limits according to [311] of the METROHM analysis system.

	Fe in H_2O	Cu in H_2O	Fe in HF (2%)	Cu in HF (2%)	Fe in HCl (3%)	Cu in HCl (3%)
Limit of detection (LOD) [ppb]	2.2	2.2	2.7	1.1	0.5	6.6
Limit of quantification (LOQ) [ppb]	7.0	7.0	9.5	3.8	1.6	23

In order to demonstrate the applicability of this method, several cleaning baths were analysed, when freshly made up and when in use for up to several weeks. The measured Fe and Cu concentrations were checked against by ICP-MS. The measured contractions in relation to the LOD and LOQ, including the standard deviation of the measured values, can be found in **Tab. 6.3**. Excellent agreement for measured values above the LOD with the ICP-MS data were obtained.

Tab. 6.3: Fe and Cu concentrations in cleaning baths measured by the described method and checked by ICP-MS.

	Fe			Cu		
	x [ppb]	std. dev. [%]	x [ppb] (ICP-MS)	x [ppb]	std. dev. [%]	x [ppb] (ICP-MS)
1 HF ≈2%; fresh bath	$x_{\mathrm{LOD}} \leq x < x_{\mathrm{LOQ}}$	46	5	$x_{\mathrm{LOD}} \leq x < x_{\mathrm{LOQ}}$	124	0.3
2 HF ≈2%; bath in use	147	1	146	6	1	7.1
3 HF ≈2%; fresh bath	$x \leq x_{\mathrm{LOD}}$	116	0.9	$x \leq x_{\mathrm{LOD}}$	42	0.5
4 HCl ≈3%; bath in use	91	1	92.5	$x \leq x_{\mathrm{LOD}}$	7	7

6.3 Chemicals used in this work

Tab. 6.4: Chemicals used in this work.

used for	chemical	formula	conc. [%wt.]	molar mass [$gmol^{-1}$]	density [gcm^{-3}]
Processing of wafers	Hydrofluoric acid (Honeywell, Puranal)	HF	50	20.01	1.17
	Hydrochloric acid (Honeywell, Puranal)	HCl	32	36.46	1.16
	Sulfuric acid (Honeywell, Puranal)	H_2SO_4	95–97	98.08	1.84
	Hydrogen peroxide (Honeywell, Puranal)	H_2O_2	30	34.01	1.11
	Sodium hydroxide pellets (Honeywell, Puranal)	$NaOH$		40.00	2.13
	Potassium hydroxide (Honeywell, Puranal)	KOH	50	56.11	1.51
Sampling of surfaces and preparation of vessels	Hydrofluoric acid (Merck, Suprapur)	HF	40	20.01	1.13
	Hydrogen peroxide (Fluka, TraceSELECT Ultra)	H_2O_2	30	34.01	1.11
	Ultra Pure Water (C. Roth, Ultra Qualität)	H_2O	100	18.02	1.00
	Hydrochloric acid (C. Roth, Supra Qualität)	HCl	35	36.46	1.16
	Methanol (C. Roth, Ultra LC-MS)	CH_3OH	>99.98	32.04	0.79
Contamination of surfaces	Iron(III) nitrate nonahydrate (Merck, Emsure ACS, Reag. PH Eur)	$Fe(NO_3)_3 \cdot 9\,H_2O$	>99	404.00	1.68
	Copper(II) nitrate trihydrate (C. Roth, p. a. ACS)	$Cu(NO_3)_2\,3\,H_2O$	>99	241.60	2.32
Spectrophometric determination of Fe and Cu	Bathocuproine sulphonate disodium salt hydrate (C. Roth)	$C_{26}H_{18}N_2Na_2O_6S_2 \cdot xH_2O$	>98	564.55+ xH_2O	
	1.10-Phenanthroline hydrochloride monohydrate (C. Roth)	$C_{12}H_8N_2 \cdot HCl \cdot H_2O$	>99	234.69	
	Ammonium hydroxide (C. Roth, Rotipuran p. a.)	NH_4OH	25	35.04	0.91
	Hydroxylammonium chloride (VWR Prolabo, AnalaR Normapur)	$HONH_2\,HCl$		69.49	
	1.000 gL^{-1}Cu in 2% HNO_3, AAS standard solution (C. Roth, Rotistar)	Cu		63.55	
	1.000 gL^{-1} Fe in 2% HNO_3, AAS standard solution (C. Roth, Rotistar)	Fe		55.85	

7 Simulation models

In the following section details about the simulation software, parameters and models that were used to simulate the impact of surface contamination on high temperature diffusion processes in **Sec. 4.5** are presented.

7.1 EDNA 2 simulation of heavily doped regions

The web-based free-to-access EDNA 2 simulation software is programmed to simulate highly doped semiconductor regions, in particular for solar cell devices. It can calculate the saturation current densities J_0 and internal quantum efficiency for arbitrary dopant profiles. It is suitable for the determination of the surface recombination velocity S_r from experimentally determined J_0 values.

The key assumption of the EDNA 2 simulation tool is the principle of quasi-neutrality, from which follows $\Delta n = \Delta p$ throughout the whole simulated part of the device, which is only the respective highly doped region—greatly simplifying the calculations. The assumption of quasi-neutrality has been introduced for the measurement of lifetime samples in **Sec. 3.1.1**. It simplifies many calculations, as the three differential equations for the carrier concentrations n, p and the electrical field E of the device can be combined to one single equation. This assumption holds valid for the state of no or small electrical fields. It becomes invalid for the depletion region and thus the error increases significantly. The chosen approach, however, shows good agreement to state-of-the-art emitter solar cell device modelling as demonstrated by McIntosh *et al.* in [273]. They demonstrate that the closer one approaches the surface, the more exact this method becomes, making it suitable for the presented modelling task, as the key simplification is that the recombination takes place at the surface. Recombination in the emitter (based on SRH statistics) is possible to be taken into account by EDNA 2. This, however, is not recommended as the doping and injection level in a gradually doped region complicate matters of SRH calculations strongly.

The effective surface recombination velocity is extracted using experimental J_0 data by producing an additional recombination current of recombination at the surface, J_s, introduced by the initial surface contamination x from which follows:

$$J_0(x) = J_{0,ref} + J_s(x) \ , \tag{7.1}$$

with the recombination current of the reference, $J_{0,ref}$. The surface recombination current can be expressed via the surface recombination rate $R_{surface}$ multiplied by the elemental charge q:

$$J_s = q \cdot R_{surface} = q \cdot S_{eff} \cdot \Delta n_d. \quad (7.2)$$

Δn_d denotes the excess carrier density near the surface, that is no longer affected by band bending due to surface charge. In case of a neutral dielectric layer $\Delta n_d = \Delta n_s$. S_{eff} is the effective surface recombination velocity. The surface recombination rate can be described by the *SRH* recombination mechanism as it has been introduced by **Eq. 3.19** in **Sec. 3.1.3**, for the sake of argumentation it is printed again below:

$$R_{surface} = \frac{p_s n_s - n_i^2}{\frac{p_s + p_1}{S_{n0}} + \frac{n_s + n_1}{S_{p0}}}. \quad (7.3)$$

If the *SRH* equation is applied to highly doped n-type silicon, it can be very much simplified (the same applies for highly doped p-type silicon just with opposite symbols) following the argumentation by McIntosh *et al.* in [274]. First, $n_s \gg n_1$ and $(n_s + n_1)/S_{p0} \gg (p_s + p_1)/S_{n0}$ are assumed which applies to a situation in which the defect is not close to the band edges, where there is no great asymmetry in the capture cross sections and the surface charge Q_{tot} is negligible. Furthermore, $p_s n_s \gg n_i^2$ applies, which holds true for highly doped regions under mid to high injection. Accordingly **Eq. 7.3** boils down to

$$R_{surface} = S_{p0} \cdot p_s. \quad (7.4)$$

Combining **Eq. 7.2** and **Eq. 7.4** results in

$$S_{eff} = S_{p0} \cdot \frac{p_s}{\Delta n_d} \quad (7.5)$$

and due to the high doping at the surface (cf. **Fig. 7.1** and **7.2**) $p_d \approx \Delta n_d$ which simplifies **Eq. 7.5** in the aforementioned case in which $n_s = n_d$ (which is a reasonable assumption for the considered case, as all of the chosen diffused regions were passivated by the oxide-like glass layer) to

$$S_{eff} = S_{p0}. \quad (7.6)$$

When band bending occurs and $Q_{tot} \neq 0$, the electrical field at the surface has to be considered and complicates matters, find more details in [274]. The so defined effective surface recombination velocity combines the surface recombination properties such as capture cross section and defect density. The effective surface recombination velocity was extracted in dependence of the Fe and Cu surface contamination for the P-diffused region of the considered Al-BSF and BiSoN solar cells using the data shown provided below.

The diffusion profile used for the simulation profile is obtained by the same diffusion as used in runs 1075, 1288 and 1333. The fits displayed in **Fig. 7.1** were used as input into EDNA 2. The summary of the other input parameters and chosen models required for the extraction of the effective *SRV* is displayed in **Tab. 7.1**. Details about the chosen models can be found in **Sec. 7.2**.

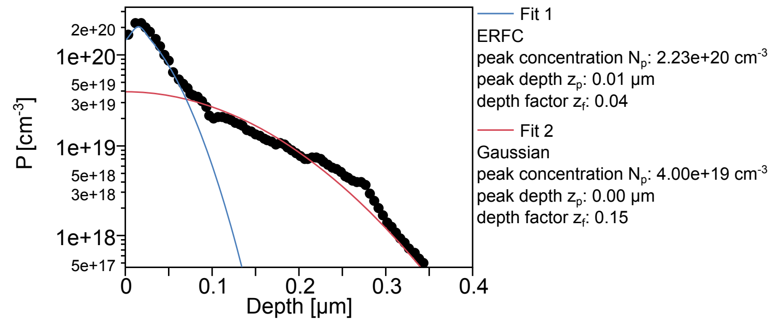

Fig. 7.1: Fits used to model the emitter of the p-type solar cells. The data points were obtained by ECV measurement of the electrical active dopant concentration [312].

Tab. 7.1: Models and parameters chosen in EDNA 2 for the simulation of P-emitter (of p-type cells).

input	value
EDNA Version	2.5.2
Date & time	28.05.2015 08:23:24
Temperature [K]	300
Junction voltage [V]	0.55
Background dopant species	Boron
Background dopant conc. [cm^{-3}]	7.2e+15
Background resistivity [Ωcm]	1.99
Emitter dopant species	Phosphorus
Emitter dopant profile	Generated
Emitter function 1	ERFC
Function 1 N_p [cm^{-3}]	2.23e+20
Function 1 z_p [μm]	0.01
Function 1 z_f [μm]	0.04
Emitter function 2	Gaussian
Function 2 N_p [cm^{-3}]	4e+19
Function 2 z_p [μm]	0
Function 2 z_f [μm]	0.15
Radiative recombination model	Altermatt2005
Auger recombination model	Richter2012
SRH at surface	Effective SRV
SRH in emitter	None
Spectrum	Monochromatic light
Wavelength [nm]	300
Incident intensity [mA/cm^2]	40
Transmission fraction	1
Propagation angle [°]	0
Mobility model	Klaassen1992
Intrinsic band gap model	Sentaurus2008
Band gap multiplier	1.00547
Density of states model	Sentaurus2008 DOS Form. 2
Dopant ionisation model	Altermatt2006
Carrier statistics model	Fermi-Dirac
Band gap narrowing model	Schenk1998
Definition of z_f	PC1D
Emitter depth condition 1	10
Emitter depth condition 2	1

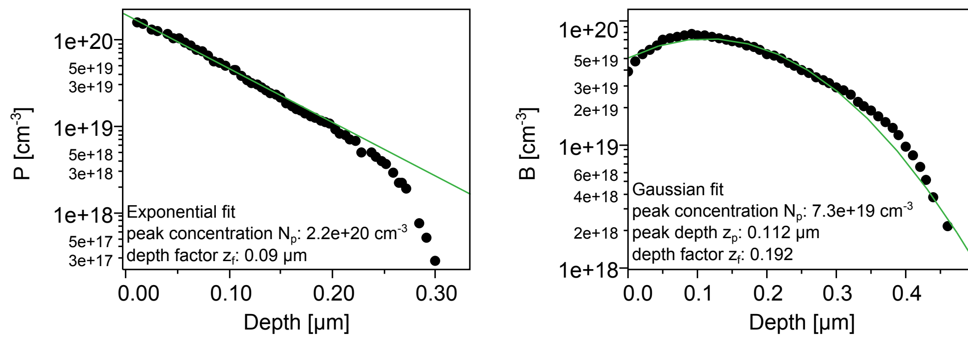

Fig. 7.2: Emitter and back surface field diffusion profiles and fit parameters.

Tab. 7.2: Models and parameters chosen in EDNA 2 for the simulation of emitter and BSF of the n-type cells.

	emitter	BSF
input	value	value
EDNA Version	2.5.2	2.5.2
Temperature [K]	300	300
Junction voltage [V]	0.55	0.55
Background dopant species	Phosphorus	Phosphorus
Background dopant conc. [cm^{-3}]	5.6e+14	5.6e+14
Background resistivity [Ωcm]	8.08	8.08
Emitter dopant species	Phosphorus	Boron
Emitter dopant profile	Generated	Generated
Emitter function 1	Exponential	Gaussian
Function 1 N_p [cm^{-3}]	2.2e+20	7.3e+19
Function 1 z_p [μm]	0	0.112
Function 1 z_f [μm]	0.09	0.192
Radiative recombination model	Altermatt2005	Altermatt2005
Auger recombination model	Richter2012	Richter2012
SRH at surface	Effective SRV	Effective SRV
SRH in emitter	None	None
Spectrum	Monochromatic light	Monochromatic light
Wavelength [nm]	300	300
Incident intensity [mA/cm^2]	40	40
Transmission fraction	1	1
Propagation angle [°]	0	0
Mobility model	Klaassen1992	Klaassen1992
Intrinsic band gap model	Sentaurus2008	Sentaurus2008
Band gap multiplier	1.00547	1.00547
Density of states model	Sentaurus2008 DOS Form. 2	Couderc2014 (Eqs 4.5.18.19)
Dopant ionisation model	Altermatt2006	Altermatt2006
Carrier statistics model	Fermi–Dirac	Fermi–Dirac
Band gap narrowing model	Schenk1998	Schenk1998
Definition of z_f	PC1D	PC1D
Emitter depth condition 1	10	10
Emitter depth condition 2	1	1

7.2 Models and input parameters used for consistent simulation

A comprehensive summary of issues related to the modelling of solar cells can be found in an overview paper by Prof. Altermatt in [270]. He claims that, despite being a relatively straight forward semiconductor device structure, the solar cell performance usually cannot be described by analytical theories but requires numerical solutions of the coupled semiconductor equations. A list of required parameters and used models can be found below. Since most of the models and parametrisations tend to be quite extensive and would exceed the scope of this work, only a summary is kept short, but it is including the references of the relevant literature, which are recommended for further reading.

- **Temperature**: The temperature of the solar cell has a strong impact on the efficiency, due to the strong temperature dependence of carrier concentrations. From the perspective of calculations, this is mirrored by the strong temperature dependency of the intrinsic carrier density (n_i). Standard testing conditions specify 25°C/298.15 K. Yet, many assumptions and simulations in the literature are performed at 300 K (e.g. as recommended by Altermatt in [270]). However, as the data in this work were extracted at 25°C, the ATLAS simulation was run at this temperature. It was not possible to switch temperatures in EDNA 2 and thus the SRV is off, as EDNA 2 calculates it at 300 K. A temperature correction for the emitter simulation is required for future simulations.

- **Radiative recombination model**: An improved description of the radiative recombination has been reported by Altermatt *et al.* in [313] (2005) and is used in both simulations.

- **Auger recombination model**: An improved description of Auger recombination, which becomes lifetime limiting especially in highly doped regions and under high injection conditions, is presented by Richter *et al.* in [314] (2012) and was also used throughout the simulation task.

- **Mobility model**: A unified model for the mobility of minority and majority carriers, holes and electrons depending on temperature and doping density has been introduced by Klaassen in [315, 316] (1992). Exact values for the mobility of carriers are required to accurately describe their drift diffusion behaviour.

- **Intrinsic band gap**: The temperature dependence of the intrinsic band gap is introduced in both, EDNA 2 (based on the SENTAURUS simulation software) and in the ATLAS software, by the formula

$$E_g(T) = E_g(0) - \frac{\alpha T^2}{T + \beta} \tag{7.7}$$

  with $\alpha = 4.73\text{e–}4\,\text{eVK}^{-1}$ and $\beta = 636\,\text{K}$ and $E_g(0) = 1.18\,\text{eV}$.

- **Density of states**: The calculation of the density of states is required for the determination n_i and is performed in both, EDNA 2 and ATLAS, via the formulas

$N_C(T) = N_C(300K)\left(\frac{T_n}{300K}\right)^{3/2}$ and $N_V(T) = N_V(300K)\left(\frac{T_p}{300K}\right)^{3/2}$, with hole and electron temperatures calculated from the effective hole and electron masses, for more details refer to [33, 317]. At 298.15 K n_i equals 8.30e+9 cm^{-3} and at 300 K n_i equals 9.65e+9 cm^{-3}. The only case in which the common model for n_i did not apply was the B-diffusion. Using standard carrier statistics the experimentally observed J_0 values was not be met, thus a more advanced model was recommended by Couderc *et al.* in [318] (2014), who were able to combine several attempts to calculate n_i.

- **Dopant ionisation model**: Details about the used dopant ionisation model by Altermatt *et al.* can be found in [319, 320] (2006).
- **Carrier statistics**: Fermi-Dirac statistics are implemented in EDNA 2 and ATLAS.
- **Band gap narrowing model**: The band gap of a semiconductor is not constant with doping but becomes smaller with increased doping, which needs to be taken into account, when dealing with heavily doped regions. The most common way to calculate the so-called band gap narrowing (BGN) has been suggested by Schenk in [321] (1998).

7.3 Atlas Simulation

The Silvaco ATLAS simualation tool provides general capabilities for physically-based two-(2D) and three-dimensional (3D) simulation of semiconductor devices. It predicts the electrical behaviour of specified semiconductor structures and provides insight into the internal physical mechanisms associated with device operation. At ISC Konstanz, it is used for 2D simulation of solar cells. In the scope of this work, it has only been used for 1D simulation but allowed the incorporation of several defect levels at the same time. Its capability of modelling variation in heavily doped regions has not fully been explored, yet, which is the reason that the “detour” via EDNA 2 was necessary.

7.4 Effective lifetime fits

The effective lifetime fits in this section were used in **3.** of **Fig. 4.43** for the calculation of the average excess carrier density.

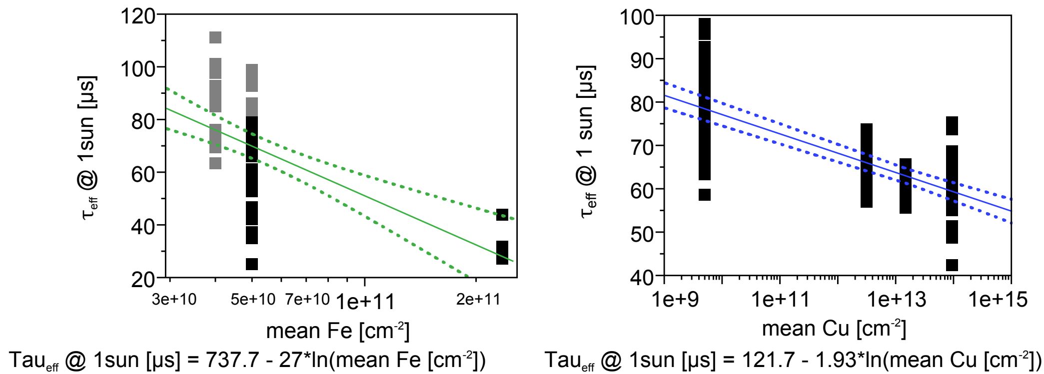

Fig. 7.3: Effective lifetime after phosphorus diffusion as a function of Fe and Cu surface contamination. With an optical factor $OF = 0.8$, a base doping of $2\,\Omega$cm, and a thickness of $155\,\mu$m.

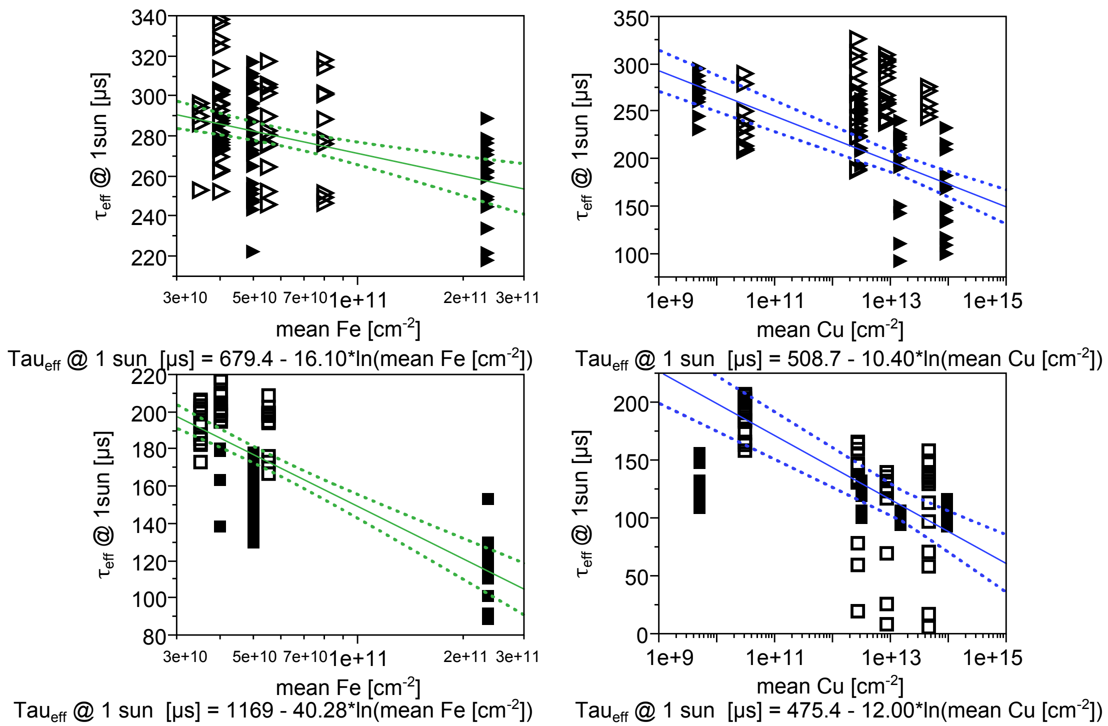

Fig. 7.4: Effective lifetime after P- (top row) and B-diffusion (bottom row) as a function of Fe and Cu surface concentration. Filled symbols are from run 1288, hollow from run 1333. The fit from Cu before B-diffusion is only taking run 1288 and the fit from Cu before P-diffusion is only taking run 1333 into account, which are the groups in which temporary gettering was observed. With an optical factor of 0.8, a base resistivity of 8 Ωcm, a thickness of $165\,\mu$m.

Bibliography

1. Hernàndez-Moro, J. & Martínez-Duart, J. Analytical model for solar PV and CSP electricity costs: present LCOE values and their future evolution. *Renewable and Sustainable Energy Reviews* **20,** 119–132 (2013).
2. Hutchby, J. A. A "Moore's Law"-like approach to roadmapping photovoltaic technologies. *Renewable and Sustainable Energy Reviews* **29,** 883–890 (2014).
3. Fischer, M., Metz, A. & S., R. *SEMI International Technology Roadmap for Photovoltaics (ITRPV) - Challenges in c-Si Technology for Suppliers and Manufacturers* in *Proc. 27th European Photovoltaic Solar Energy Conference* (Frankfurt, 2012).
4. Fischer, M., Julsrud, S., Metz, A., Xing, G. & Yong, L. *International Technology Roadmap for Photovoltaic (ITRPV) Results 2012* tech. rep. (SEMI - Solar/PV, 2013).
5. Istratov, A. A., Hieslmair, H. & Weber, E. R. Iron Contamination in Silicon Technology. *Applied Physics A: Materials Science and Processing* **70,** 489–534 (2000).
6. Istratov, A. A. & Weber, E. R. Physics of copper in silicon. *Journal of the Electrochemical Society* **149,** G21–G30 (2002).
7. Buchholz, F., Wefringhaus, E., Eisert, S., Egenolf, H. & Groß, A. *Measurement and impact of surface transition metal contamination of textured multicrystalline silicon wafers* in *Proc. 26th European Photovoltaics Solar Energy Conference* (Hamburg, 2011), 1187–1190.
8. Schweckendiek, J., Hoyer, R., Patzig-Klein, S., Delahaye, F., Knoch, G. & Nussbaumer, H. Cleaning in crystalline Si solar cell manufacturing. *Solid State Phenomena* **195,** 283–288 (2013).
9. Bidiville, A., Wasmer, K., Kraft, R. & Ballif, C. *Diamond wire-sawn silicon wafers - from the lab to the cell production* in *Proc. 24th European Photovoltaics Solar Energy Conference* (Hamburg, 2009), 1400–1405.
10. Coletti, G., Bronsveld, P., Hahn, G., Warta, W., Macdonald, D., Ceccaroli, B., Wambach, K., Le Quang, N. & Fernandez, J. M. Impact of metal contamination in silicon solar cells. *Advanced Functional Materials* **21,** 879–890 (2011).
11. Buchholz, F., Galbiati, G., Edler, A., Wefringhaus, E., Ferstl, B. & Ross, M. *Comparison of wafer cleaning procedures for high efficiency n-type solar cells* in *Proc. 28th European Photovoltaics Solar Energy Conference* (Paris, 2013), 793–796.
12. Graff, K. *Metal Impurities in Silicon-Device Fabrication* 2nd ed. (Springer-Verlag Berlin, 1999).

13. Macdonald, D. Impact of nickel contamination on carrier recombination in n- and p-type crystalline silicon wafers. *Applied Physics A: Materials Science and Processing* **81,** 1619–1625 (2005).

14. Zhong, L. & Shimura, F. Dependence of lifetime on surface concentration of copper and iron in silicon wafers. *Applied Physics Letters* **61,** 1078–1080 (1992).

15. Macdonald, D., Cuevas, A., McIntosh, K., Barbosa, L. & De Ceuster, D. *Impact of Cr, Fe, Ni, Ti and W surface contamination on diffused and oxidised n-type crystalline silicon wafers* in *Proc. 20th European Photovoltaics Solar Energy Conference* (Barcelona, Spain, 2005), 627–630.

16. Breitenstein, O., Bauer, J., Bothe, K., Kwapil, W., Lausch, D., Rau, U., Schmidt, J., Schneemann, M., Schubert, M. C., Wagner, J.-M. & Warta, W. Understanding junction breakdown in multicrystalline solar cells. *Journal of Applied Physics* **109,** 071101–10 (2011).

17. Rothschild, A, Penaud, J, Toman, J, Jaffrennou, P, Choulat, P, Cornagliotti, E, Payo, M. R., Pawlak, B, Das, J & Uruena, A. *Impact of surface preparation prior to ALD-Al_2O_3 deposition for PERC type solar cell* in *Proc. 27th European Photovoltaics Solar Energy Conference* (2012), 1974–1977.

18. Danel, A., Nolan, T., Souche, F., Le Tiec, Y. & Ribeyron, P. J. HF last passivation for high efficiency a-Si/c-Si heterojunction solar cells. *Solid State Phenomena* **187,** 345–348 (2012).

19. Bentzen, A., Holt, A., Kopecek, R., Stokkan, G., Christensen, J. S. & Svensson, B. G. Gettering of transition metal impurities during phosphorus emitter diffusion in multicrystalline silicon solar cell processing. *Journal of Applied Physics* **99,** 093509 (2006).

20. Buchholz, F., Wefringhaus, E. & Schubert, G. Metal surface contamination during phosphorus diffusion. *Energy Procedia* **27,** 287–292 (2012).

21. Macdonald, D., Mackel, H. & Cuevas, A. Effect of gettered iron on recombination in diffused regions of crystalline silicon wafers. *Applied Physics Letters* **88,** 092105–092105–3 (2006).

22. Phang, S. P. & Macdonald, D. Direct comparison of boron, phosphorus, and aluminum gettering of iron in crystalline silicon. *Journal of Applied Physics* **109,** 073521 (2011).

23. Glunz, S. High-efficiency crystalline silicon solar cells. *Advances in Optoelectronics,* 97370 (2007).

24. Mortimer, C. E. & Müller, U. *Das Basiswissen der Chemie* 8th ed., 452 (Thieme-Verlag, Stuttgart, 2003).

25. Hull, R. *Properties of Crystalline Silicon* 91 (Institution of Engineering and Technology, London, 1999).

26. Rössler, U. *Solid state theory: An introduction* 148 (Springer, Berlin, Heidelberg, 2009).

27. Noffsinger, J., Kioupakis, E., Van de Walle, C. G., Louie, S. G. & Cohen, M. L. Phonon-assisted optical absorption in silicon from first principles. *Physical Review Letters* **108,** 167402 (2012).

28. Rössler, U. *Solid State Theory: An Introduction* 7 (Springer, Berlin, Heidelberg, 2009).

29. Chelikowsky, J. R. & Cohen, M. L. Electronic structure of silicon. *Physical Review B* **10,** 5095 (1974).

30. Hoffmann, R. How chemistry and physics meet in the solid state. *Angewandte Chemie International Edition in English* **26,** 846–878 (1987).

31. Steigerwald, M. L. & Brus, L. E. Semiconductor crystallites: A class of large molecules. *Accounts of Chemical Research* **23,** 183–188 (1990).

32. Atkins, P. W., Höpfner, A., Schleitzer, A. & Bär, M. *Physikalische Chemie* 471 (VCH Weinheim, 1987).

33. Sze, S. M. *Physics of Semiconductor Devices* 2nd ed., 16–23 (John Wiley & Sons, New York, 1981).

34. Gribov, B. G. & Zinov'ev, K. V. Preparation of high-purity silicon for solar cells. *Inorganic Materials* **39,** 653–662 (2003).

35. Goodrich, A., Hacke, P., Wang, Q., Sopori, B., Margolis, R., James, T. L. & Woodhouse, M. A wafer-based monocrystalline silicon photovoltaics road map: Utilizing known technology improvement opportunities for further reductions in manufacturing costs. *Solar Energy Materials and Solar Cells* **114,** 110–135 (2013).

36. Fischer, M., Julsrud, S., Metz, A., Xing, G. & Yong, L. *International Technology Roadmap for Photovoltaic (ITRPV) 2013 Results* tech. rep. (SEMI - Solar/PV, 2014).

37. Braga, A., Moreira, S., Zampieri, P., Bacchin, J. & Mei, P. New processes for the production of solar-grade polycrystalline silicon: A review. *Solar Energy Materials and Solar Cells* **92,** 418–424 (2008).

38. Kato, Y., Hanazawa, K., Baba, H., Nakamura, N., Yuge, N., Sakaguchi, Y., Hiwasa, S. & Aratani, F. Purification of metallurgical grade silicon to solar grade for use in solar cell wafers. *Tetsu-to-Hagane (Journal of the Iron and Steel Institute of Japan)* **86,** 717–724 (2000).

39. Möller, H. J. Basic mechanisms and models of multi-wire sawing. *Advanced Engineering Materials* **6,** 501–513 (2004).

40. Liedke, T. & Kuna, M. A macroscopic mechanical model of the wire sawing process. *International Journal of Machine Tools and Manufacture* **51,** 711–720 (2011).

41. Radet, M., Jaffrennou, P., Habka, N., Takchi, C., Abric, E., Penaud, J. & Lombardet, B. *Comparative analysis of slurry and diamond sawing methods using Raman spectroscopy on monocrystalline silicon wafers* in *Proc. 27th European Photovoltaic Solar Energy Conference* (Frankfurt, 2012), 794–797.

42. Patterson, J. D. & Bailey, B. C. *Solid-state physics: introduction to the theory* 2nd ed., 31 (Springer Science & Business Media, Berlin Heidelberg, 2007).

43. Bauza, D. in *Handbook of Surfaces and Interface of Materials* (ed Nalwa, H. S.) 140f (Academic Press, San Diego, 2001).

44. Neergaard Waltenburg, H. & Yates, J. Surface chemistry of silicon. *Chemical Reviews* **95,** 1589–1673 (1995).

45. Angermann, H., Henrion, W. & Roseler, A. in *Silicon-Based Material and Devices* (ed Nalwa, H. S.) (Academic Press, New York, 2001).

46. Konecny, R. & Doren, D. J. Adsorption of water on Si (100)-(2-1): A study with density functional theory. *The Journal of Chemical Physics* **106,** 2426–2435 (1997).

47. Andersohn, L & Köhler, U. In situ observation of water adsorption on Si (100) with scanning tunneling microscopy. *Surface Science* **284,** 77–90 (1993).

48. Gräf, D., Grundner, M. & Schulz, R. Reaction of water with hydrofluoric acid treated silicon (111) and (100) surfaces. *Journal of Vacuum Science and Technology A* **7,** 808–813 (1989).

49. Morita, M., Ohmi, T., Hasegawa, E., Kawakami, M. & Ohwada, M. Growth of native oxide on a silicon surface. *Journal of Applied Physics* **68,** 1272–1281 (1990).

50. Takahagi, T., Ishitani, A., Kuroda, H., Nagasawa, Y., Ito, H. & Wakao, S. Control of the chemical reactivity of a silicon single-crystal surface using the chemical modification technique. *Journal of Applied Physics* **68,** 2187–2191 (1990).

51. Angermann, H., Henrion, W., Rebien, M., Zettler, J. T. & Roseler, A. Characterization of chemically prepared Si-surfaces by uv-vis and IR spectroscopic ellipsometry and surface photovoltage. *Surface Science* **388,** 15–23 (1997).

52. Knotter, D. M. in *Handbook of Silicon Wafer Cleaning Technology* (eds Reinhardt, K. A. & Reidy, R. F.) 2nd ed. (William Andrew Inc., Norwich, NY, 2008).

53. Knotter, D. M., de Gendt, S., Baeyens, M., Mertens, P. W. & Heyns, M. M. Hydrogen peroxide decomposition in ammonia solutions. *Journal of the Electrochemical Society* **146,** 3476–3481 (1999).

54. Spierings, G. A. C. M. Wet chemical etching of silicate glasses in hydrofluoric acid based solutions. *Journal of Materials Science* **28,** 6261–6273 (1993).

55. Kern, W. & Deckert, C. A. in *Thin Film Processes* (eds Vossen, J. L. & Kern, W.) 401–496 (Academic Press, New York, 1978).

56. Verhaverbeke, S., Teerlinck, I., Vinckier, C., Stevens, G., Cartuyvels, R. & Heyns, M. M. The etching mechanisms of SiO_2 in hydrofluoric acid. *Journal of the Electrochemical Society* **141,** 2852–2857 (1994).

57. Braddy, R., McTigue, P. T. & Verity, B. Equilibria in moderately concentrated aqueous hydrogen fluoride solutions. *Journal of fluorine chemistry* **66,** 63–67 (1994).

58. O'Donnell, T. A. On the acidity of hydrogen fluoride. *Journal of Fluorine Chemistry* **25,** 75–82 (1984).

59. Trucks, G. W., Raghavachari, K., Higashi, G. S. & Chabal, Y. J. Mechanism of HF etching of silicon surfaces: A theoretical understanding of hydrogen passivation. *Physical Review Letters* **65,** 504 (1990).

60. Einhaus, R., Vazsonyi, E., Szlufcik, J., Nijs, J. & Mertens, R. *Isotropic texturing of multicrystalline silicon wafers with acidic texturing solutions* in *Proc. 26th IEEE Photovoltaic Specialists Conference* (New York, 1997), 167–170.

61. Hauser, A., Melnyk, I., Wefringhaus, E., Delahaye, F., Vilsmeier, G. & Fath, P. *Acidic texturisation of mc-Si using a high throughput in-line prototype system with no organic chemistry* in *Proc. 19th European Photovoltaic Solar Energy Conference* (Paris, 2004), 1094–1097.

62. Macdonald, D., Cuevas, A., Kerr, M. J., Samundsett, C., Ruby, D., Winderbaum, S. & Leo, A. Texturing industrial multicrystalline silicon solar cells. *Solar Energy* **76,** 277–283 (2004).

63. Cornagliotti, E., Ngamo, M., Tous, L., Russell, R., Horzel, J., Hendrickx, D., Douhard, B., Prajapati, V., Janssens, T. & Poortmans, J. Integration of inline single-side wet emitter etch in PERC cell manufacturing. *Energy Procedia* **27,** 624–630 (2012).

64. Cornagliotti, E., Uruena, A., Horzel, J., John, J., Tous, L., Hendrickx, D., Prajapati, V., Singh, S. N., Hoyer, R. & Delahaye, F. *How much rear side polishing is required? A study on the impact of rear side polishing in PERC solar cells* in *Proc. 27th European Photovoltaic Solar Energy Conference* (2012), 561–566.

65. Bailey, W. L., Coleman, M. G., Harris, C. B. & Lesk, I. A. *Patent* US 4.137.123 (US). <http://patft.uspto.gov/>(1979).

66. Löwe, H., Keppel, P. & Zach, D. *Halbleiterätzverfahren* (Akademie-Verlag, Berlin, 1990).

67. Kolasinski, K. W. Etching of silicon in fluoride solutions. *Surface Science* **603,** 1904–1911 (2009).

68. Bertagna, V., Plougonven, C., Rouelle, F. & Chemla, M. P-and n-Type silicon electrochemical properties in dilute hydrofluoric acid solutions. *Journal of The Electrochemical Society* **143,** 3532–3538 (1996).

69. Hauser, H., Voisin, P., Guttowski, A., Mick, J., Pfeifer, M., Müller, C., Hermle, M., Glunz, S. W. & Bläsi, B. *Honeycomb textured multicrystalline silicon via Nanoimprint Lithography* in *Proc. 24th European Photovoltaic Solar Energy Conference* (Hambug, 2009), 1118–1122.

70. Nievendick, J., Specht, J., Zimmer, M., Zahner, L., Glover, W., Stüwe, D. & Rentsch, J. Formation of a honeycomb texture for multicrystalline silicon solar cells using an inkjetted mask. *Physica Status Solidi - Rapid Research Letters* **6,** 7–9 (2012).

71. Gabor, A. & van Mierlo, F. The self aligned cell: Scaling up manufacture of a cost effective cell architecture for multicrystalline silicon photovoltaics. *National Renewable Energy Laboratory; Subcontract Report* **NAT-9-88012-01,** 1–15 (2010).

72. Patzig-Klein, S. *Untersuchungen zum Reaktionsverhalten kristalliner Siliziumoberflächen in HF-basierten Ätzlösungen* PhD thesis (Technischen Universität Bergakademie Freiberg, 2009).

73. Röver, I., Roewer, G., Bohmhammel, K. & Wambach, K. *Reactivity of crystalline silicon in the system HF-HNO_3-H_2O (a novel study)* in *Proc. 19th European Photovoltaic Solar Energy Conference* (Paris, 2004), 895–898.

74. Lippold, M. *Beiträge zum Verständnis des sauren nasschemischen Ätzens von Silicium* PhD thesis (Technischen Universität Bergakademie Freiberg, 2014).

75. Zubel, I., Barycka, I., Kotowska, K. & Kramkowska, M. Silicon anisotropic etching in alkaline solutions IV: The effect of organic and inorganic agents on silicon anisotropic etching process. *Physical Sensors and Actuators A* **87,** 163–171 (2001).

76. Seidel, H., Csepregi, L., Heuberger, A. & Baumgärtel, H. Anisotropic etching of crystalline silicon in alkaline solutions II. Influence of dopants. *Journal of the Electrochemical Society* **137,** 3626–3632 (1990).

77. Zhang, X. G. *Electrochemistry of Silicon and its Oxide* (Springer, New York, 2001).

78. Fahlman, B. D. *Materials Chemistry* 251–321 (Springer Netherlands, Dordrecht, 2011).

79. Seidel, H., Csepregi, L., Heuberger, A. & Baumgärtel, H. Anisotropic etching of crystalline silicon in alkaline solutions I. Orientation dependence and behavior of passivation layers. *Journal of the Electrochemical Society* **137,** 3612–3626 (1990).

80. Palik, E. D., Gray, H. F. & Klein, P. B. A Raman study of etching silicon in aqueous KOH. *Journal of the Electrochemical Society* **130,** 956–959 (1983).

81. Bean, K. E. Anisotropic etching of silicon. *25th IEEE Transactions on Electron Devices* **25,** 1185–1193 (1978).

82. Williams, K. R. & Muller, R. S. Etch rates for micromachining processing. *Journal of Microelectromechanical Systems* **5,** 256–269 (1996).

83. Campbell, P. & Green, M. A. Light trapping properties of pyramidally textured surfaces. *Journal of Applied Physics* **62,** 243–249 (1987).

84. Bressers, P. M. M. C., Kelly, J. J., Gardeniers, J. G. E. & Elwenspoek, M. Surface morphology of p-Type (100) silicon etched in aqueous alkaline solution. *Journal of The Electrochemical Society* **143,** 1744–1750 (1996).

85. Lamb, W. R. & E., L. J. *Patent* US 4918030 (US). <http://patft.uspto.gov/>(1990).

86. King, D. L. & Buck, M. E. *Experimental optimization of an anisotropic etching process for random texturization of silicon solar cells* in *Proc. 22nd IEEE Photovoltaic Specialists Conference* (Las Vegas, 1991), 303–308 vol.1.

87. Vazsonyi, E., De Clercq, K., Einhaus, R., Van Kerschaver, E., Said, K., Poortmans, J., Szlufcik, J. & Nijs, J. Improved anisotropic etching process for industrial texturing of silicon solar cells. *Solar energy materials and solar cells* **57,** 179–188 (1999).

88. Singh, P. K., Kumar, R., Lal, M., Singh, S. N. & Das, B. K. Effectiveness of anisotropic etching of silicon in aqueous alkaline solutions. *Solar Energy Materials and Solar cells* **70,** 103–113 (2001).

89. Kern, W. *Handbook of Semiconductor Wafer Cleaning Technology - Science, Technology, and Application* (Noyes, Park Ridge, NJ, 2011).

90. *Handbook of Silicon Wafer Cleaning Technology* 2nd ed. (eds Reinhardt, K. & Kern, W.) (William Andrew Inc., Norwich, NY, 2008).

91. Leachman, R. C. & Hodges, D. A. Benchmarking semiconductor manufacturing. *IEEE Transactions on Semiconductor Manufacturing* **9,** 158–169 (1996).

92. Kern, W. & Puotinen, D. The RCA-clean. *RCA Review* **31,** 197 (1970).

93. Martin, A. R., Baeyens, M., Hub, W., Mertens, P. W. & Kolbesen, B. O. Alkaline cleaning of silicon wafers: additives for the prevention of metal contamination. *Microelectronic Engineering* **45,** 197–208 (1999).

94. Anttila, O. J. & Tilli, M. V. Metal contamination removal on silicon wafers using dilute acidic solutions. *Journal of The Electrochemical Society* **139,** 1751–1756 (1992).

95. Anttila, O. *Patent* US 5.382.296 (US). <`http://patft.uspto.gov/`>(1995).

96. Lin, S.-S. & Gurol, M. D. Catalytic decomposition of hydrogen peroxide on iron oxide: kinetics, mechanism, and implications. *Environmental Science & Technology* **32,** 1417–1423 (1998).

97. Meuris, M., Mertens, P. W., Opdebeeck, A., Schmidt, H. F., Depas, M., Vereecke, G., Heyns, M. M. & Philipossian, A. The IMEC clean - a new concept for particle and metal removal on Si surfaces. *Solid State Technology* **38,** 109 (1995).

98. Ferstl, B., Rajagopalan, S., Thate, S., Ross, M., Cornagliotti, E., Haslinger, M. & John, J. *Investigation on wet chemical solutions performing pre-diffusion and pre-passivation cleans in next generation PERC-type silicon solar cells* in *Proc. 28th European Photovoltaics Solar Energy Conference* (Paris, 2013), 1295–1299.

99. *Handbook of Preparative Inorganic Chemistry* 2nd ed. (ed Brauer, G.) 388–389 (Academic Press Inc., New York, 1963).

100. Reinhardt, K. A. & Reidy, R. F. *Handbook of Cleaning for Semiconductor Manufacturing - Fundamentals and Applications* (eds Reinhardt, K. A. & Reidy, R. F.) 37 (John Wiley and Sons, Inc. - Scrivener Publishing LLC, 2011).

101. Heyns, M., Bearda, T., Cornelissen, I., De Gendt, S., Loewenstein, L., Mertens, P., Mertens, S., Meuris, M., Schaekers, M., Teerlinck, I., Vos, R. & Wolke, K. *Advanced cleaning strategies for ultra-clean silicon surfaces* in *Proc. 6th International Symposium Cleaning Technology in Semiconductor Device Manufacturing* **99** (Honolulu, 1999), 2–15.

102. O'Sullivan, B., Haslinger, M., Singh, S., Bearda, T., Debucquoy, M. & Szlufcik, J. *Ozone base cleaning: Impact on high efficiency interdigitated back contact solar cells* in *Solid State Phenomena* **219** (Trans Tech Publ, 2014), 312–316.

103. Sharma, V. *Study of charges present in silicon nitride thin films and their effect on silicon solar cell efficiencies* PhD thesis (Arizona State University, Tempe, 2013).

104. Schultz, O., Mette, A., Hermle, M. & Glunz, S. W. Thermal oxidation for crystalline silicon solar cells exceeding 19% efficiency applying industrially feasible process technology. *Progress in Photovoltaics: Research and Applications* **16,** 317–324 (2008).

105. Benick, J., Zimmermann, K., Spiegelman, J., Hermle, M. & Glunz, S. W. Rear side passivation of PERC-type solar cells by wet oxides grown from purified steam. *Progress in Photovoltaics: Research and Applications* **19,** 361–365 (2011).

106. Hoex, B., Heil, S. B. S., Langereis, E., Van de Sanden, M. C. M. & Kessels, W. M. M. Ultralow surface recombination of c-Si substrates passivated by plasma-assisted atomic layer deposited Al_2O_3. *Applied Physics Letters* **89,** 042112 (2006).

107. Schmidt, J., Merkle, A., Brendel, R., Hoex, B., Van de Sanden, M. C. M. & Kessels, W. M. M. Surface passivation of high-efficiency silicon solar cells by atomic-layer-deposited Al_2O_3. *Progress in Photovoltaics: Research and Applications* **16,** 461–466 (2008).

108. Dingemans, G. & Kessels, W. M. M. Status and prospects of Al_2O_3-based surface passivation schemes for silicon solar cells. *Journal of Vacuum Science and Technology A* **30,** 040802 (2012).

109. Leguijt, C., Lölgen, P., Eikelboom, J. A., Weeber, A. W., Schuurmans, F. M., Sinke, W. C., Alkemade, P. F. A., Sarro, P. M., Marée, C. H. M. & Verhoef, L. A. Low temperature surface passivation for silicon solar cells. *Solar Energy Materials and Solar Cells* **40,** 297–345 (1996).

110. Mark, K. J. & Andres, C. Recombination at the interface between silicon and stoichiometric plasma silicon nitride. *Semiconductor Science and Technology* **17,** 166 (2002).

111. Schroder, D. K. Carrier lifetimes in silicon. *IEEE Transactions on Electron Devices* **44,** 160–170 (1997).

112. Richter, A., Henneck, S., Benick, J., Hörteis, M., Hermle, M. & Glunz, S. *Firing stable Al_2O_3/SiN_x layer stack passivation for the front side boron emitter of n-type silicon solar cells* in *Proc. 25th European Photovoltaic Solar Energy Conference* (Valencia, 2010), 1453–1459.

113. Winderbaum, S., Yun, F. & Reinhold, O. Application of plasma enhanced chemical vapor deposition silicon nitride as a double layer antireflection coating and passivation layer for polysilicon solar cells. *Journal of Vacuum Science and Technology A* **15,** 1020–1025 (1997).

114. Angermann, H., Henrion, W., Rebien, M. & Röseler, A. Wet-chemical passivation and characterization of silicon interfaces for solar cell applications. *Solar Energy Materials and Solar Cells* **83,** 331–346 (2004).

115. Deal, B. E. & Grove, A. S. General relationship for the thermal oxidation of silicon. *Journal of applied physics* **36,** 3770–3778 (1965).

116. Mihailetchi, V., Komatsu, Y. & Geerligs, L. J. Nitric acid pretreatment for the passivation of boron emitters for n-type base silicon solar cells. *Applied Physics Letters* **92,** 063510–063510–3 (2008).

117. Aberle, A. G. Overview on SiN surface passivation of crystalline silicon solar cells. *Solar Energy Materials and Solar Cells* **65,** 239–248 (2001).

118. Aberle, A. G. Surface passivation of crystalline silicon solar cells: A review. *Progress in Photovoltaics: Research and Applications* **8,** 473–487 (2000).

119. Duerinckx, F. & Szlufcik, J. Defect passivation of industrial multicrystalline solar cells based on PECVD silicon nitride. *Solar Energy Materials and Solar Cells* **72,** 231–246 (2002).

120. Soppe, W., Rieffe, H. & Weeber, A. Bulk and surface passivation of silicon solar cells accomplished by silicon nitride deposited on industrial scale by microwave PECVD. *Progress in Photovoltaics: Research and Applications* **13,** 551–569 (2005).

121. Lelièvre, J. F., Fourmond, E., Kaminski, A., Palais, O., Ballutaud, D. & Lemiti, M. Study of the composition of hydrogenated silicon nitride SiN_x:H for efficient surface and bulk passivation of silicon. *Solar Energy Materials and Solar Cells* **93,** 1281–1289 (2009).

122. El Amrani, A., Menous, I., Mahiou, L., Tadjine, R., Touati, A. & Lefgoum, A. Silicon nitride film for solar cells. *Renewable Energy* **33,** 2289–2293 (2008).

123. Wright, D. N., Marstein, E. S., Rognmo, A. & Holt, A. Plasma-enhanced chemical vapour-deposited silicon nitride films: The effect of annealing on optical properties and etch rates. *Solar energy materials and solar cells* **92,** 1091–1098 (2008).

124. Queisser, S., Wefringhaus, E., Lichtner, M., Saule, W., Heeren, A., Delahaye, F. & Schweckendiek, J. *Novel precursor deposition method for inline diffusion* in *Proc. 23rd European Photovoltaic Solar Energy Conference* (Valencia, 2008), 1991–1994.

125. Voyer, C., Biro, D., Wagner, K., Benick, J. & Preu, R. *Fabrication of textured solar cells using sprayed phosphoric acid as the dopant source for the in-line emitter diffusion* in *Proc. 21st European Photovoltaic Solar Energy Conference* (Dresden, 2006), 1157–1160.

126. Kwon, T. Y., Yang, D. H., Ju, M. K., Jung, W. W., Kim, S. Y., Lee, Y. W., Gong, D. Y. & Yi, J. Screen printed phosphorus diffusion for low-cost and simplified industrial mono-crystalline silicon solar cells. *Solar Energy Materials and Solar Cells* **95,** 14–17 (2011).

127. Recart, F., Freire, I., Perez, L., Lago-Aurrekoetxea, R., Jimeno, J. C. & Bueno, G. Screen printed boron emitters for solar cells. *Solar energy materials and solar cells* **91,** 897–902 (2007).

128. Antoniadis, H. *Silicon ink high efficiency solar cells* in *Proc. 34th IEEE Photovoltaic Specialists Conference* (IEEE, Philadelphia, PA, 2009), 000650–000654.

129. Seiffe, J., Pillath, F., Trogus, D., Brand, A. A., Savio, C., Hofmann, M. & Rentsch, J. *Multifunctional PECVD layers: Dopant source, passivation, and optics* in *Proc. 38th IEEE Photovoltaic Specialists Conference* **2** (IEEE, Austin, Texas, 2012), 1–6.

130. Rohatgi, A., Meier, D. L., McPherson, B., Ok, Y.-W., Upadhyaya, A. D., Lai, J.-H. & Zimbardi, F. High-throughput ion-implantation for low-cost high-efficiency silicon solar cells. *Energy Procedia* **15,** 10–19 (2012).

131. Bentzen, A. *Phosphorus Diffusion and Gettering in Silicon Solar Cells* PhD thesis (University of Oslo, 2006), 7–8.

132. Pignatel, G. U. & Queirolo, G. Further insight on boron diffusion in silicon obtained with Auger electron spectroscopy. *Thin Solid Films* **67,** 233–238 (1980).

133. Kessler, M. A., Ohrdes, T., Wolpensinger, B. & Harder, N.-P. Charge carrier lifetime degradation in Cz silicon through the formation of a boron-rich layer during BBr3 diffusion processes. *Semiconductor Science and Technology* **25,** 055001 (2010).

134. Arai, E., Nakamura, H. & Terunuma, Y. Interface reactions of B2O3-Si system and boron diffusion into silicon. *Journal of The Electrochemical Society* **120,** 980–987 (1973).

135. Sze, S. M. *Physics of Semiconductor Devices* 2nd ed., 63–132 (John Wiley & Sons, New York, 1981).

136. Goetzberger, A., Voß, B. & Knobloch, J. *Sonnenenergie: Photovoltaik - Physik und Technologie der Solarzelle* 2nd ed., 80–91 (Teubner, 1997).

137. McIntosh, K. *Lumps, Humps and Bumps: Three Detrimental Effects in the Current-voltage Curve of Silicon Solar Cells* PhD thesis (University of New South Wales, Sydney, 2001).

138. Neuhaus, D.-H. & Münzer, A. Industrial silicon wafer solar cells. *Advances in Opto-Electronics* **2007** (2008).

139. Muller, J., Bothe, K., Gatz, S., Plagwitz, H., Schubert, G. & Brendel, R. Contact formation and recombination at screen-printed local aluminum-alloyed silicon solar cell base contacts. *IEEE Transactions on Electron Devices* **58,** 3239–3245 (2011).

140. Rudiger, M., Schmiga, C., Rauer, M., Hermle, M. & Glunz, S. W. Efficiency potential of n-type silicon solar cells with aluminum-doped rear emitter. *IEEE Transactions on Electron Devices* **59,** 1295–1303 (2012).

141. Chapin, D. M., S., F. C. & Pearson, G. L. *Patent* US 2780765 (US). <`http://patft.uspto.gov/`>(1957).

142. Macdonald, D. & Geerligs, L. J. Recombination activity of interstitial iron and other transition metal point defects in p-and n-type crystalline silicon. *Applied Physics Letters* **85,** 40–61 (2004).

143. Geerligs, L., Manshanden, P., Solheim, I., Ovrelid, E. & Waernes, A. *Impact of common metallurgical impurities on mc-Si solar cell efficiency: p-type versus n-type doped ingots* in *Proc. 21st European Photovoltaic Solar Energy Conference* **1** (2006).

144. Cotter, J. E., Guo, J. H., Cousins, P. J., Abbott, M. D., Chen, F. W. & Fisher, K. C. P-type versus n-type silicon wafers: prospects for high-efficiency commercial silicon solar cells. *IEEE Transactions on Electron Devices* **53,** 1893–1901 (2006).

145. Green, M. A. Silicon solar cells: state of the art. *Philosophical Transactions of the Royal Society A: Mathematical, Physical and Engineering Sciences* **371** (2013).

146. Hieslmair, H., Balasubramanian, S., Istratov, A. A. & Weber, E. R. Gettering simulator: physical basis and algorithm. *Semiconductor Science and Technology* **16,** 567 (2001).

147. Kveder, V, Schröter, W, Sattler, A & Seibt, M. Simulation of Al and phosphorus diffusion gettering in Si. *Materials Science and Engineering: B* **71,** 175–181 (2000).

148. Shabani, M., Yamashita, T. & Morita, E. Study of gettering mechanisms in silicon: Competitive gettering between phosphorus diffusion gettering and other gettering sites. *Solid State Phenomena* **131,** 399–404 (2008).

149. Bentzen, A. & Holt, A. Overview of phosphorus diffusion and gettering in multicrystalline silicon. *Materials Science and Engineering: B* **159-160,** 228–234 (2009).

150. Buonassisi, T., Istratov, A. A., Marcus, M. A., Lai, B., Cai, Z., Heald, S. M. & Weber, E. R. Engineering metal-impurity nanodefects for low-cost solar cells. *Nature Material* **4,** 676–679 (2005).

151. Istratov, A. A., Buonassisi, T., Pickett, M. D., Heuer, M. & Weber, E. R. Control of metal impurities in "dirty" multicrystalline silicon for solar cells. *Materials Science and Engineering: B* **134,** 282–286 (2006).

152. Metz, A. *et al.* Industrial high performance crystalline silicon solar cells and modules based on rear surface passivation technology. *Solar Energy Materials and Solar cells* **120, Part A,** 417–425 (2014).

153. Schmiga, C., Rauer, M., Rüdiger, M., Meyer, K., Lossen, J., Krokoszinski, H.-J., Hermle, M. & Glunz, S. W. *Aluminium-doped p+ silicon for rear emitters and back surface fields: results and potentials of industrial n-and p-type solar cells* in *Proc. 25th European Photovoltaic Solar Energy Conference* (Valencia, 2010), 1163–1168.

154. Glunz, S. W., Preu, R., Schaefer, S., Schneiderlochner, E., Pfleging, W., Ludemann, R. & Willeke, G. *New simplified methods for patterning the rear contact of RP-PERC high-efficiency solar cells* in *Proc. 28th IEEE Photovoltaic Specialists Conference* (IEEE, 2000), 168–171.

155. Uruena, A., John, J., Beaucarne, G., Choulat, P., Eyben, P., Agostinelli, G., Van Kerschaver, E., Poortmans, J. & Mertens, R. *Local Al-alloyed contacts for next generation Si solar cells* in *Proc. 24th European Photovoltaic Solar Energy Conference* (Hamburg, 2009), 1483–1486.

156. Münzer, A., Schöne, J., Teppe, A., Hein, M., Schlosser, R. E., Hanke, M., Varner, K., Mäckel, H., Keller, S. & Fath, P. Physical properties of industrial 19% rear side passivated Al-LBSFR-solar cells. *Energy Procedia* **8,** 415–420 (2011).

157. Weber, T., Fischer, G., Oehlke, A., Kusterer, C., Strauch, K., Schiepe, R., Mühlbauer, M., Möller, M., Wolny, F., Köhler, R., Grupp-Mueller, G., Schneiderlächner, E., Stegemann, K. H. & Neuhaus, H. High volume pilot production of high efficiency PERC solar cells-analysis based on device simulation. *Energy Procedia* **38,** 474–481 (2013).

158. Gassenbauer, Y., Ramspeck, K., Bethmann, B., Dressler, K., Moschner, J. D., Fiedler, M., Brouwer, E., Drossler, R., Lenck, N. & Heyer, F. Rear-surface passivation technology for crystalline silicon solar cells: a versatile process for mass production. *IEEE Journal of Photovoltaics* **3,** 125–130 (2013).

159. Edler, A., Mihailetchi, V., Kopecek, R., Harney, R., Böscke, T., Stichtenoth, D., Lossen, J., Meyer, K., Hellriegel, R. & Aichele, T. Improving screen printed metallization for large area industrial solar cells based on n-type material. *Energy Procedia* **8,** 493–497 (2011).

160. Song, D., Xiong, J., Hu, Z., Li, G., Wang, H., An, H., Yu, B., Grenko, B., Borden, K. & Sauer, K. *Progress in n-type Si solar cell and module technology for high efficiency and low cost* in *Proc. 38th IEEE Photovoltaic Specialists Conference* (IEEE, Austin, Texas, 2012), 003004–003008.

161. Boscke, T. S., Kania, D., Helbig, A., Schollhorn, C., Dupke, M., Sadler, P., Braun, M., Roth, T., Stichtenoth, D. & Wutherich, T. Bifacial n-type cells with >20% front-side efficiency for industrial production. *IEEE Journal of Photovoltaics* **3,** 674–677 (2013).

162. Mihailetchi, V. D., Jourdan, J., Edler, A., Kopecek, R., Harney, R., Stichtenoth, D., Lossen, J., Böscke, T. S. & Krokoszinski, H.-J. *Screen printed n-type silicon solar cells for industrial application* in *Proc. 25th European Photovoltaic Solar Energy Conference* (2010), 6–10.

163. Lanterne, A., Le Perchec, J., Gall, S., Coig, M., Tauzin, A. & Veschetti, Y. 20.5% efficiency on large area n-type PERT cells by ion implantation. *Energy Procedia* **55,** 437–443 (2014).

164. Yang, L., Ye, Q. H., Ebong, A., Song, W. T., Zhang, G. J., Wang, J. X. & Ma, Y. High efficiency screen printed bifacial solar cells on monocrystalline Cz silicon. *Progress in Photovoltaics: Research and Applications* **19,** 275–279 (2011).

165. Kopecek, R., Veschetti, Y., Gerritsen, E., Schneider, A., Comparotto, C., Mihailetchi, V. D., Lossen, J. & Libal, J. Bifaciality: One small step for technology, one giant leap for kWh cost reduction. *Photovoltaics International* **26** (2015).

166. Goetzberger, A., Voß, B. & Knobloch, J. *Sonnenenergie: Photovoltaik - Physik und Technologie der Solarzelle* 2nd ed. (Teubner, 1997).

167. Schroder, D. K. *Semiconductor Material and Device Characterization* 392 (John Wiley and Sons, Inc., New York, 2006).

168. Weber, E. R. *Efficiency Improvement of Crystalline Solar Cells, Final Subcontract Report* (National Renewable Energy Laboratory, Golden, Colorado, 2007).

169. Shockley, W. & Read, W. T. Statistics of the recombinations of holes and electrons. *Physical Review* **87,** 835 (1952).

170. Hall, R. N. Electron-hole recombination in germanium. *Physical Review* **87,** 387 (1952).

171. Cuevas, A. & Macdonald, D. Measuring and interpreting the lifetime of silicon wafers. *Solar Energy* **76,** 255–262 (2004).

172. Misiakos, K. & Tsamakis, D. Accurate measurements of the silicon intrinsic carrier density from 78 to 340 K. *Journal of Applied Physics* **74,** 3293–3297 (1993).

173. Auger, P. Sur les rayons beta secondaires produits dans un gaz par des rayons x. *C.R.A.S.* **177,** 168–171 (1923).

174. Schroder, D. K. *Semiconductor Material and Device Characterization* (John Wiley and Sons, Inc., New York, 2006).

175. Macdonald, D., Geerligs, L. & Azzizi, A. Iron detection in crystalline silicon by carrier lifetime measurements for arbitrary injection and doping. *Journal of Applied Physics* **95,** 1021–1028 (2004).

176. Kerr, M. J. *Surface, emitter and bulk recombination in silicon and development of silicon nitride passivated solar cells* PhD thesis (Australian National University, Canberra, 2002), 18.

177. Kane, D. E. & Swanson, R. M. *Measurement of the emitter saturation current by a contactless photoconductivity decay method* in *Proc. 18th IEEE Photovoltaic Specialists Conference* (IEEE, Las Vegas, 1985), 578–583.

178. Cuevas, A. The effect of emitter recombination on the effective lifetime of silicon wafers. *Solar Energy Materials and Solar Cells* **57,** 277–290 (1999).

179. Kimmerle, A., Wolf, A., Belledin, U. & Biro, D. Modelling carrier recombination in highly phosphorus-doped industrial emitters. *Energy Procedia* **8,** 275–281 (2011).

180. Schroder, D. K. Carrier lifetimes in silicon. *IEEE Transactions on Electron Devices* **44,** 396 (1997).

181. Sinton, R. A. & Cuevas, A. Contactless determination of current-voltage characteristics and minority-carrier lifetimes in semiconductors from quasi-steady-state photoconductance data. *Applied Physics Letters* **69,** 2510–2512 (1996a).

182. Sinton, R. A., Cuevas, A. & Stuckings, M. *Quasi-steady-state photoconductance, a new method for solar cell material and device characterization* in *Proc. 25th IEEE Photovoltaic Specialists Conference* (IEEE, 1996), 457–460.

183. Sinton, R. A. & Macdonald, D. *WCT-120 Photoconductance Lifetime Tester and optional Suns-Voc Stage User Manual* 2006.

184. Olibet, S. *Properties of interfaces in amorphous/crystalline silicon heterojunctions* PhD thesis (Université de Neuchâtel, 2008), 14–15.

185. Cuevas, A. & Sinton, R. A. Prediction of the open-circuit voltage of solar cells from the steady-state photoconductance. *Progress in Photovoltaics: Research and Applications* **5,** 79–90 (1997).

186. De Wolf, S., Descoeudres, A., Holman, Z. C. & Ballif, C. High-efficiency silicon heterojunction solar cells: A review. *Green* **2,** 7–24 (2012).

187. Olibet, S. *Properties of interfaces in amorphous/crystalline silicon heterojunctions* PhD thesis (Université de Neuchâtel, 2008), 111.

188. Schmidt, J., Veith, B., Werner, F., Zielke, D. & Brendel, R. *Silicon surface passivation by ultrathin Al_2O_3 films and Al_2O_3/SiN_x stacks* in *Proc. 35th IEEE Photovoltaic Specialists Conference* (IEEE, 2010), 885–890.

189. Borrego, J. M., Gutmann, R. J., Jensen, N. & Paz, O. Non-destructive lifetime measurement in silicon wafers by microwave reflection. *Solid-State Electronics* **30,** 195–203 (1987).

190. Wilson, M., Savtchouk, A., Lagowski, J., Kis-Szabo, K., Korsos, F., Toth, A., Kopecek, R. & Mihailetchi, V. QSS-uPCD measurement of lifetime in silicon wafers: advantages and new applications. *Energy Procedia* **8,** 128–134 (2011).

191. Wilson, M., Edelman, P., Lagowski, J., Olibet, S. & Mihailetchi, V. Improved QSS-uPCD measurement with quality of decay control: Correlation with steady-state carrier lifetime. *Solar energy materials and solar cells* **106,** 66–70 (2012).

192. Basore, P. A. & Hansen, B. R. *Microwave-detected photoconductance decay* in *Proc. 21st IEEE Photovoltaic Specialists Conference* (IEEE, 1990), 374–379.

193. Zoth, G. & Bergholz, W. A fast, preparation-free method to detect iron in silicon. *Journal of Applied Physics* **67,** 6764–6771 (1990).

194. Lagowski, J., Edelman, P., Kontkiewicz, A. M., Milic, O., Henley, W., Dexter, M., Jastrzebski, L. & Hoff, A. M. Iron detection in the part per quadrillion range in silicon using surface photovoltage and photodissociation of iron-boron pairs. *Applied Physics Letters* **63,** 3043–3045 (1993).

195. Wilson, M., D'Amico, J., Savtchouk, A., Edelman, P., Findlay, A., Jastrzebski, L., Lagowski, J., Kis-Szabo, K., Korsos, F. & Toth, A. *Multifunction metrology platform for photovoltaics* in *Proc. 37th IEEE Photovoltaic Specialists Conference* (IEEE, 2011), 001748–001753.

196. Wilson, M., Lagowski, J., Savtchouk, A., Jastrzebski, L. & D'Amico, J. COCOS (corona oxide characterization of semiconductor) metrology: Physical principal and applications. *ASTM Special Technical Publication* **1382,** 74–90 (2000).

197. Wilson, M., Marinskiy, D., Byelyayev, A., D'Amico, J., Findlay, A., Jastrzebski, L. & Lagowski, J. The present status and recent advancements in corona-Kelvin non-contact electrical metrology of dielectrics for IC-manufacturing. *ECS Transactions* **3,** 3–24 (2006).

198. Wilson, M. *PV-2000 Operation Manual* (SemilabSDI, Tampa, FL, December 23, 2010).

199. Sze, S. M. *Physics of Semiconductor Devices* 2nd ed., 272 (John Wiley & Sons, New York, 1981).

200. Wilson, M., Lagowski, J., Jastrzebski, L., Savtchouk, A. & Faifer, V. *COCOS (corona oxide characterization of semiconductor) non-contact metrology for gate dielectrics* in *Proc. Characterization and Metrology for ULSI Technology* **550** (AIP Publishing, 2001), 220–225.

201. Wostyn, K., Baekelant, W., Rip, J., Haslinger, M., Kenis, K., Struyf, H., Claes, M., Mertens, P. W. & De Gendt, S. "Just clean enough": wet cleaning for solar cell manufacturing applications. *Solid State Phenomena* **195,** 293–296 (2013).

202. Pianetta, P., Baur, K., Singh, A., Brennan, S., Kerner, J., Werho, D. & Wang, J. Application of synchrotron radiation to TXRF analysis of metal contamination on silicon wafer surfaces. *Thin Solid Films* **373,** 222–226 (2000).

203. Krushevska, A., Tan, S., Passer, M. & Liu, X. R. Advances in trace element analysis of silicon wafer surfaces by vapor phase decomposition (VPD) and inductively coupled plasma mass spectrometry (ICP-MS). *Journal of Analytical Atomic Spectrometry* **15,** 1211–1216 (2000).

204. Chung, H. Y., Kim, Y. H., Cho, H. Y., Lee, B. Y., Yoo, H. D. & Lee, S. H. Collection efficiency of metallic contaminants on Si wafer by vapor-phase decomposition-droplet collection. *Analytical Sciences* **17,** 653–658 (2001).

205. Chung, H., Lee, S., Kim, Y., Lee, K. & Kim, D. Determination of metallic impurities in a silicon wafer by local etching and electrothermal atomic absorption spectrometry. *Analytical Sciences* **19,** 1051–1054 (2003).

206. Beebe, M. & Anderson, S. Monitoring wafer cleanliness and metal contamination via VPD ICP-MS: Case studies for next generation requirements. *Microelectronic Engineering* **87,** 1701–1705 (2010).

207. Shimizu, H. & Ishiwari, S. Pack-extraction method combined with inductively coupled plasma mass spectroscopy to monitor metal contaminants on surfaces of silicon wafers. *Semiconductor Science and Technology* **15,** 776 (2000).

208. Buchholz, F. *Oberflächenanalytik von Metallverunreinigungen auf Si-Wafern für Solarzellen* Wissenschaftliche Arbeit für das Staatsexamen für Höheres Lehramt (Universität Konstanz, 2010).

209. Shabani, M., Yoshimi, T., Okuuchi, S. & Kaniava, A. A Quantitative Method of Metal Impurities Depth Profiling for Gettering Evaluation in Silicon Wafers. *Solid State Phenomena* **57,** 81–90 (1997).

210. Kirihara, K. Production technology of wire rod for high tensile strength steel cord. *Kobelco Technology Review* **No. 30,** 62–65 (2011).

211. Buonassisi, T., Istratov, A. A., Pickett, M. D., Heuer, M., Kalejs, J. P., Hahn, G., Marcus, M. A., Lai, B., Cai, Z. & Heald, S. M. Chemical natures and distributions of metal impurities in multicrystalline silicon materials. *Progress in Photovoltaics* **14,** 513 (2006).

212. Buonassisi, T., Marcus, M., Istratov, A., Heuer, M., Ciszek, T., Lai, B., Cai, Z. & Weber, E. Analysis of copper-rich precipitates in silicon: Chemical state, gettering, and impact on multicrystalline silicon solar cell material. *Journal of Applied Physics* **97,** 063503 (2005).

213. Pickett, M. & Buonassisi, T. Iron point defect reduction in multicrystalline silicon solar cells. *Applied Physics Letters* **92,** 122103–122103–3 (2008).

214. Istratov, A. A., Buonassisi, T., McDonald, R. J., Smith, A. R., Schindler, R., Rand, J. A., Kalejs, J. P. & Weber, E. R. Metal content of multicrystalline silicon for solar cells and its impact on minority carrier diffusion length. *Journal of Applied Physics* **94,** 6552 (2003).

215. Hourai, M., Naridomi, T., Oka, Y., Murakami, K., Sumita, S., Fujino, N. & Shiraiwa, T. A method of quantitative contamination with metallic impurities of the surface of a silicon wafer. *Japanese Journal of Applied Physics* **27,** L2361–L2363 (1988).

216. Loewenstein, L. M. & Mertens, P. W. Adsorption of metal ions onto hydrophilic silicon surfaces from aqueous solution: effect of pH. *Journal of the Electrochemical Society* **145,** 2841–2847 (1998).

217. Loewenstein, L. M., Charpin, F. & Mertens, P. W. Competitive adsorption of metal ions onto hydrophilic silicon surfaces from aqueous solution. *Journal of the Electrochemical Society* **146,** 719–727 (1999).

218. Bearda, T., de Gendt, S., Loewenstein, L., Knotter, M., Mertens, P. & Heyns, M. Behaviour of metallic contaminants during MOS processing. *Solid State Phenomena* **65-6,** 11–14 (1999).

219. Ohmi, T., Imaoka, T., Sugiyama, I. & Kezuka, T. Metallic impurities segregation at the interface between Si wafer and liquid during wet cleaning. *Journal of the Electrochemical Society* **139,** 3317–3335 (1992).

220. Ryuta, J., Yoshimi, T., Kondo, H., Okuda, H. & Shimanuki, Y. Adsorption and desorption of metallic impurities on Si wafer surface in SC1 solution. *Japanese Journal of Applied Physics* **31,** 2338–2342 (1992).

221. Atsumi, J., Ohtsuka, S., Munehira, S. & Kajiyama, K. Metallic contamination on Si wafers from cleaning solutions. *Proceedings of the Electrochemcial Society* **90,** 59–66 (1990).

222. Hoelzl, R., Range, K.-J., Fabry, L. & Huber, D. Calibrated contamination spiking method for silicon wafers in the 10^{10} - 10^{12} atoms/cm^2 range. *Journal of The Electrochemical Society* **146,** 2245–2253 (1999).

223. Norga, G. J., Platero, M., Black, K. A., Reddy, A. J., Michel, J. & Kimerling, L. C. Mechanism of copper deposition on silicon from dilute hydrofluoric acid solution. *Journal of the Electrochemical Society* **144,** 2801 (1997).

224. Hsu, E., Parks, H. G., Craigin, R., Tomooka, S., Ramberg, J. S. & Lowry, R. K. Deposition characteristics of metal contaminants from HF-based process solutions onto silicon-wafer surfaces. *Journal of the Electrochemical Society* **139,** 3659–3664 (1992).

225. Pourbaix, M. *Atlas of electrochemical equilibria in aqueous solutions* 2nd ed. (National Association of Corrosion Engineers, Houston, Tex, 1974).

226. Pesterfield, L. L., Maddox, J. B., Crocker, M. S. & Schweitzer, G. K. Pourbaix (E-pH-M) diagrams in three dimensions. *Journal of Chemical Education* **89,** 891–899 (2012).

227. Lim, S. W., Mo, R. T., Pianetta, P. A. & Chidsey, C. E. D. Effect of silicon surface termination on copper deposition in deionized water. *Journal of the Electrochemical Society* **148,** C16–C20 (2001).

228. Kim, J., Morita, H., Choi, G. & Ohmid, T. Cleaning efficiencies of various chemical solutions for noble metals such as Cu, Ag, and Au on Si wafer surfaces. *Journal of the Electrochemical Society* **146,** 4281 (1999).

229. Costine, A. & Thurgate, S. Iron adsorption on SiO_2/Si(111). *Surface and Interface Analysis* **39,** 711–714 (2007).

230. Miyashita, M., Kubota, H., Matsushita, Y., Yoshimura, R. & Tada, T. Quantum Chemical Analysis of Metal Adsorption Mechanism onto Silicon Surface in Cleaning Solution. *Japanese Journal of Applied Physics* **34,** L288 (1995).

231. Buchholz, F. & Wefringhaus, E. *Impact of Fe and Cu surface contamination on high efficiency solar cell processes* in *Proc. Ultra Clean Processing of Semiconductor Surfaces* (Brussels, 2014), 305–311.

232. Blakers, A. W., Wang, A., Milne, A. M., Zhao, J. & Green, M. A. 22.8% efficient silicon solar cell. *Applied Physics Letters* **55,** 1363–1365 (1989).

233. Dauwe, S., Mittelstädt, L., Metz, A. & Hezel, R. Experimental evidence of parasitic shunting in silicon nitride rear surface passivated solar cells. *Progress in Photovoltaics: Research and Applications* **10,** 271–278 (2002).

234. Glunz, S. W., Biro, D., Rein, S. & Warta, W. Field-effect passivation of the SiO_2Si interface. *Journal of Applied Physics* **86,** 683–691 (1999).

235. Agostinelli, G., Delabie, A., Vitanov, P., Alexieva, Z., Dekkers, H. F. W., De Wolf, S. & Beaucarne, G. Very low surface recombination velocities on p-type silicon wafers passivated with a dielectric with fixed negative charge. *Solar Energy Materials and Solar Cells* **90,** 3438–3443 (2006).

236. Vermang, B., Goverde, H., Uruena, A., Lorenz, A., Cornagliotti, E., Rothschild, A., John, J., Poortmans, J. & Mertens, R. Blistering in ALD Al_2O_3 passivation layers as rear contacting for local Al BSF Si solar cells. *Solar energy materials and solar cells* **101,** 204–209 (2012).

237. Glatz-Reichenbach, J., Buchholz, F., Díaz-Pérez, P., Preis, P., Theobald, J., Wefring-haus, E. & Peter, K. *Development of high efficient p-type industrial PERC-solar cells* in *Proc. 28th European Photovoltaic Solar Energy Conference* (Frankfurt, 2013), 1842–1845.

238. Schmitt, S., Peter, C., Olibet, S., Theobald, J. & Schneider, A. *Influence of various process variations on the fabrication of PERC solar cells* in *Proc. 28th European Photovoltaic Solar Energy Conference* (Frankfurt, 2013), 2059–2062.

239. Hong, J., Kessels, W. M. M., Soppe, W. J., Weeber, A. W., Arnoldbik, W. M. & Van de Sanden, M. C. M. Influence of the high-temperature "firing" step on high-rate plasma deposited silicon nitride films used as bulk passivating antireflection coatings on silicon solar cells. *Journal of Vacuum Science and Technology B* **21,** 2123–2132 (2003).

240. Hull, R. *Properties of Crystalline Silicon* (Institution of Engineering and Technology, London, 1999).

241. Istratov, A. A., Flink, C., Hieslmair, H., McHugo, S. A. & Weber, E. R. Diffusion, solubility and gettering of copper in silicon. *Materials Science and Engineering: B* **72,** 99–104 (2000).

242. Istratov, A. A., Hieslmair, H. & Weber, E. R. Advanced gettering. *MRS Bulletin* **June,** 33 (2000).

243. Ramappa, D. A. & Henley, W. B. Diffusion of iron in silicon dioxide. *Journal of the Electrochemical Society* **146,** 3773–3777 (1999).

244. Huang, Z., Geyer, N., Werner, P., De Boor, J. & Gösele, U. Metal-assisted chemical etching of silicon: A review. *Advanced materials* **23,** 285–308 (2011).

245. Sachdeva, R., Istratov, A. A. & Weber, E. R. Recombination activity of copper in silicon. *Applied Physics Letters* **79,** 2937–2939 (2001).

246. Macdonald, D., Mackel, H. & Cuevas, A. *Recombination in n-and p-type silicon emitters contaminated with iron* in *Proc. IEEE 4th World Conference on Photovoltaic Energy Conversion* **1** (IEEE, 2006), 952–955.

247. Phang, S. P. & Macdonald, D. *Boron, phosphorus and aluminum gettering of iron in crystalline silicon: Experiments and modelling* in *Proc. 35th IEEE Photovoltaic Specialists Conference* (IEEE, 2010), 000352–000356.

248. Joge, T., Araki, I., Uematsu, T., Warabisako, T., Nakashima, H. & Matsukuma, K. Low-temperature boron gettering for improving the carrier lifetime in Fe-contaminated bifacial silicon solar cells with n+ pp+ back-surface-field structure. *Japanese Journal of Applied Physics* **42,** 5397 (2003).

249. Haarahiltunen, A., Talvitie, H., Savin, H., Yli-Koski, M., Asghar, M. I. & Sinkkonen, J. Modeling boron diffusion gettering of iron in silicon solar cells. *Applied Physics Letters* **92,** 021902 (2008).

250. Weber, T., Zechner, C., Macdonald, D. & Altermatt, P. *Numerical simulation of gettering and recombination in iron-contaminated boron emitters* in *Proc. 21st European Photovoltaic Solar Energy Conference* (Dresden, 2006), 1486–1489.

251. Dubois, S., Palais, O., Pasquinelli, M., Martinuzzi, S. & Jaussaud, C. Influence of substitutional metallic impurities on the performances of p-type crystalline silicon solar cells: The case of gold. *Journal of Applied Physics* **100,** 123502 (2006).

252. Schmidt, J. Effect of dissociation of iron-boron pairs in crystalline silicon on solar cell properties. *Progress in Photovoltaics: Research and Applications* **13,** 325–331 (2005).

253. Hofstetter, J., Fenning, D. P., Bertoni, M. I., Lelièvre, J. F., del Canizo, C. & Buonassisi, T. Impurity-to-efficiency simulator: Predictive simulation of silicon solar cell performance based on iron content and distribution. *Progress in Photovoltaics: Research and Applications* **19,** 487–497 (2011).

254. Coletti, G. Sensitivity of state-of-the-art and high efficiency crystalline silicon solar cells to metal impurities. *Progress in Photovoltaics: Research and Applications* **21,** 1163–1170 (2012).

255. Coletti, G., Bronsveld, P. C. P., Hahn, G., Warta, W., Macdonald, D., Ceccaroli, B., Wambach, K., Le Quang, N. & Fernandez, J. M. Impact of metal contamination in silicon solar cells. *Advanced Functional Materials* **21,** 879–890 (2011).

256. Schmidt, J., Lim, B., Walter, D., Bothe, K., Gatz, S., Dullweber, T. & Altermatt, P. P. *Impurity-related limitations of next-generation industrial silicon solar cells* in *Proc. 38th IEEE Photovoltaic Specialists Conference* **2** (IEEE, 2012), 1–5.

257. Shabani, M. B., Yoshimi, T. & Abe, H. Low-temperature out-diffusion of Cu from silicon wafers. *Journal of the Electrochemical Society* **143,** 2025–2029 (1996).

258. Istratov, A. A., Flink, C., Hieslmair, H., Weber, E. R. & Heiser, T. Intrinsic diffusion coefficient of interstitial copper in silicon. *Physical Review Letters* **81,** 1243 (1998).

259. Rotondaro, A. L. P., Hurd, T. Q., Kaniava, A., Vanhellemont, J., Simoen, E., Heyns, M. M., Claeys, C. & Brown, G. Impact of Fe and Cu contamination on the minority carrier lifetime of silicon substrates. *Journal of the Electrochemical Society* **143,** 3014–3019 (1996).

260. Macdonald, D., Brendle, W., Cuevas, A. & Istratov, A. A. *Injection-dependent lifetime studies of copper precipitates in silicon* in *Proc. 12th Workshop on Crystalline Silicon Solar Cell Material and Processes* (National Renewable Energy Laboratory (NREL), Breckenridge, CO, 2002).

261. Walz, D. & Kamarinos, G. On the recombination behaviour of iron in moderately boron-doped p-type silicon. *Applied Physics A* **62,** 345–353 (1996).

262. Schmidt, J. & Cuevas, A. Electronic properties of light-induced recombination centers in boron-doped Czochralski silicon. *Journal of Applied Physics* **86,** 3175–3180 (1999).

263. Glunz, S., Rein, S., Lee, J. & Warta, W. Minority carrier lifetime degradation in boron-doped Czochralski silicon. *Journal of Applied Physics* **90,** 2397–2404 (2001).

264. Bothe, K., Hezel, R. & Schmidt, J. Recombination-enhanced formation of the metastable boron-oxygen complex in crystalline silicon. *Applied Physics Letters* **83,** 1125–1127 (2003).

265. Bothe, K., Sinton, R. & Schmidt, J. Fundamental boron-oxygen-related carrier lifetime limit in mono-and multicrystalline silicon. *Progress in Photovoltaics: Research and Applications* **13,** 287–296 (2005).

266. Bothe, K. & Schmidt, J. Fast-forming boron-oxygen-related recombination center in crystalline silicon. *Applied Physics Letters* **87,** 262108 (2005).

267. Du, M.-H., Branz, H. M., Crandall, R. S. & Zhang, S. B. Bistability-mediated carrier recombination at light-induced boron-oxygen complexes in silicon. *Physical Review Letters* **97,** 256602 (2006).

268. Murin, L. I., Tolkacheva, E. A., Markevich, V. P., Peaker, A. R., Hamilton, B., Monakhov, E., Svensson, B. G., Lindstrom, J. L., Santos, P. & Coutinho, J. The oxygen dimer in Si: Its relationship to the light-induced degradation of Si solar cells. *Applied Physics Letters* **98,** 182101–182101–3 (2011).

269. Green, M. A. Self-consistent optical parameters of intrinsic silicon at 300 K including temperature coefficients. *Solar Energy Materials and Solar Cells* **92,** 1305–1310 (2008).

270. Altermatt, P. P. Models for numerical device simulations of crystalline silicon solar cells-a review. *Journal of Computational Electronics* **10,** 314–330 (2011).

271. Koduvelikulathu, L. J., Mihailetchi, V. D., Olibet, S., Rudolph, D., Cabrera, E. & Kopecek, R. Two-dimensional modeling of the metallization-induced recombination losses of screen-printed solar cells. *IEEE Journal of Photovoltaics* **5,** 159 –165 (2013).

272. McIntosh, K. R. & Altermatt, P. P. *A freeware 1D emitter model for silicon solar cells* in *Proc. 35th IEEE Photovoltaic Specialists Conference (PVSC)* (IEEE, Hawaii, 2010), 002188–002193.

273. McIntosh, K. R., Altermatt, P. P., Ratcliff, T. J., Fong, K. C., Black, L. E., Baker-Finch, S. C. & Abbott, M. D. *An examination of three common assumptions used to simulate recombination in heavily doped silicon* in *Proc. 28th European Photovoltaic Solar Energy Conference* (Paris, 2013), 1672–1679.

274. McIntosh, K. R. & Black, L. E. On effective surface recombination parameters. *Journal of Applied Physics* **116,** 014503 (2014).

275. Edler, A., Mihailetchi, V. D., Koduvelikulathu, L. J., Comparotto, C., Kopecek, R. & Harney, R. Metallization-induced recombination losses of bifacial silicon solar cells. *Progress in Photovoltaics: Research and Applications* **23,** 620–627 (2014).

276. Graff, K. & Pieper, H. The properties of iron in silicon. *Journal of The Electrochemical Society* **128,** 669–674 (1981).

277. Brotherton, S., Bradley, P. & Gill, A. Iron and the iron-boron complex in silicon. *Journal of Applied Physics* **57,** 1941–1943 (1985).

278. Reiss, J. H., King, R. R. & Mitchell, K. W. Characterization of diffusion length degradation in Czochralski silicon solar cells. *Applied Physics Letters* **68,** 3302–3304 (1996).

279. Davis, J. R., Rohatgi, A., Hopkins, R. H., Blais, P. D., Rai-Choudhury, P., McCormick, J. R. & Mollenkopf, H. C. Impurities in silicon solar cells. *IEEE Transactions on Electron Devices* **27,** 677–687 (1980).

280. Feitknecht, W. & Schindler, P. Solubility constants of metal oxides, metal hydroxides and metal hydroxide salts in aqueous solution. *Pure and Applied Chemistry* **6,** 125–206 (1963).

281. Hahn, G. *Status of selective emitter technology* in *Proc. 25th European Photovoltaic Solar Energy Conference* (Valencia, 2010), 6–10.

282. Moldovan, A., Birmann, K., Rentsch, J., Zimmer, M., Gitte, T. & Fittkau, J. Combined ozone/HF/HCl based cleaning and adjusted Emitter etch-back for silicon solar cells. *Solid State Phenomena* **195,** 305–309 (2013).

283. Sall, J., Lehman, A., Stephens, M. L. & Creighton, L. *JMP start statistics: a guide to statistics and data analysis using JMP* 7th ed., 128 (SAS Institute Inc., Cary, NC, USA, 2007).

284. Sall, J., Lehman, A., Stephens, M. L. & Creighton, L. *JMP start statistics: a guide to statistics and data analysis using JMP* 7th ed., 144–146 (SAS Institute Inc., Cary, NC, USA, 2007).

285. Ohmi, T., Isagawa, T., Kogure, M. & Imaoka, T. Native oxide growth and organic impurity removal on Si surface with ozone-injected ultrapure water. *Journal of the Electrochemical Society* **140,** 804–810 (1993).

286. De Smedt, F., De Gendt, S., Claes, M., Heyns, M. M., Vankerckhoven, H. & Vinckier, C. The increasing importance of the use of ozone in the microelectronics industry. *Ozone-Science and Engineering* **24,** 379–390 (2002).

287. Nelson, S. *Reducing environmental impact with ozone based processes* in *Proc. 4th International Symposium on Environmental Issues with Materials and Processes for the Electronics and Semiconductor Industries* (The Electrochemical Society, Washington, DC, 2001), 126–133.

288. Bergman, E. & Lagrange, S. Process and environmental benefits of HF-ozone cleaning chemistry. *Solid State Technology* **44,** 115 (2001).

289. Fukazawa, Y., Miyazaki, H. & Ogawa, Y. *Direct replacement cleaning technology based on ozonated water using a single processing tank* in *Proc. International Symposium on Cleaning Technology in Semiconductor Device Manufacturing* (Electrochemical Society, Paris, 1998), 264–271.

290. Pipia, F., Bellandi, E., Crivelli, B. & Alessandri, M. Fe and Cu removal efficiency in HF-DIW/O_3 cleaning sequence. *Solid State Phenomena* **65,** 109–112 (1998).

291. Bergman, E., Lagrange, S., Claes, M., De Gendt, S. & Röhr, E. Pre-Diffusion cleaning using ozone and HF. *Solid State Phenomena* **76,** 85–88 (2001).

292. Choi, G. M., Yokoi, I. & Ohmi, T. *The role of oxidant in HF-based solution for noble metal removal from substrate* in *Proc. Ultra Clean Processing of Silicon Surfaces* (eds Heyns, M., Mertens, P. & Meuris, M.) **76-77** (2001), 267–270.

293. Gottschalk, C. & Schweckendiek, J. Using dissolved ozone in semiconductor cleaning applications. *Micro* **22,** 81–84 (2004).

294. Choi, G.-M. & Ohmi, T. Removal efficiency of metallic impurities on various substrates in HF-based solutions. *Journal of The Electrochemical Society* **148,** G241–G248 (2001).

295. Chen, G. *The applications of DI-O_3 water on wafer surface preparation* in *Proc. International Conference on Wafer Rinsing, Water Reclamation and Environmental Technology for Semiconductor Manufacturing* (Hsinchu, Taiwan, 1999), 100–123.

296. De Smedt, F., De Gendt, S., Heyns, M. M. & Vinckier, C. The application of ozone in semiconductor cleaning processes: the solubility issue. *Journal of The Electrochemical Society* **148,** G487 (2001).

297. SAS Institute Inc. *Fitting Linear Models; Stepwise Regression Models; Example Using Stepwise Regression* <`http://www.jmp.com/support/help/The_Stepwise_Report.shtml`> (2014).

298. El Jaouhari, A. A. & Schweckendiek, J. *Patent: Verfahrung zum Ätzen von Siliziumoberflächen* GER, 2009.

299. Lossen, J., Buchholz, F., Comparotto, C., Eisert, S., Libal, J., Mihailetchi, V., Wefringhaus, E., Rossetto, M., Discato, D. & Traverso, F. *From lab to fab: Bifacial n-type cells entering industrial production* in *Proc. 31th European Photovoltaic Solar Energy Conference* (Hamburg, 2015), 965 –968.

300. Ohmi, T., Miyashita, M., Itano, M., Imaoka, T. & Kawanabe, I. Dependence of thin-oxide films quality on surface microroughness. *IEEE Transactions on Electron Devices* **39,** 537–545 (1992).

301. M'saad, H., Michel, J., Reddy, A. & Kimerling, L. C. Monitoring and optimization of silicon surface quality. *Journal of the Electrochemical Society* **142,** 2833–2835 (1995).

302. Heyns, M., Hasenack, C., De Keersmaecker, R. & Falster, R. Impact of silicon surface characteristics on MOS device yield for ULSI. *Microelectronic Engineering* **10,** 235–257 (1991).

303. Pietsch, G., Köhler, U. & Henzler, M. Direct observation of silicon surface etching by water with scanning tunneling microscopy. *Chemical Physics Letters* **197,** 346–351 (1992).

304. Malik, I. J., Pirooz, S., Shive, L. W., Davenport, A. J. & Vitus, C. M. Surface toughness of silicon wafers on different lateral length scales. *Journal of the Electrochemical Society* **140,** L75–L77 (1993).

305. Angermann, H., Uredat, S. & Zettler, J. T. *Surface Texturization and Interface Passivation of Mono- and Polycrystalline Silicon Substrates: Evaluation of the Wet Chemical Treatments by UV-NIR-Reflectance* in *Proc. 24th European Photovoltaic Solar Energy Conference* (Hamburg, 2009), 1954–1957.

306. Clugston, D. A. & Basore, P. A. *PC1D version 5: 32-bit solar cell modeling on personal computers* in *Proc. 26th IEEE Photovoltaic Specialists Conference* (IEEE, 1997), 207–210.

307. Angermann, H., Korte, L., Rappich, J., Conrad, E., Sieber, I., Schmidt, M., Huebener, K. & Hauschild, J. Optimisation of electronic interface properties of a-Si:H/c-Si heterojunction solar cells by wet-chemical surface pre-treatment. *Thin Solid Films* **516,** 6775–6781 (2008).

308. Korte, L., Conrad, E., Angermann, H., Stangl, R. & Schmidt, M. Advances in a-Si:H/c-Si heterojunction solar cell fabrication and characterization. *Solar Energy Materials and Solar Cells* **93,** 905–910 (2009).

309. Burns, D., Danzer, K. & Townshend, A. Use of the terms "recovery" and "apparent recovery" in analytical procedures. *Pure and Applied Chemistry* **74,** 2201–2205 (2002).

310. Tanner, S., Baranov, V. & Instruments, P. Theory, design, and operation of a dynamic reaction cell for ICP-MS. *Atomic Spectroscopy,* 45 (1999).

311. Kolb, M., Bahr, A., Hippich, S. & Schulz, W. Calculation of detection limit, identification limit and determination limit according to DIN 32645 with the aid of a computer program. *Acta Hydrochimica et Hydrobiologica* **21,** 308–311 (1993).

312. Peiner, E., Schlachetzki, A. & Krüger, D. Doping profile analysis in Si by electrochemical capacitance-voltage measurements. *Journal of the Electrochemical Society* **142,** 576–580 (1995).

313. Altermatt, P. P., Geelhaar, F., Trupke, T., Dai, X., Neisser, A. & Daub, E. *Injection dependence of spontaneous radiative recombination in c-Si: experiment, theoretical analysis, and simulation* in *Proc. 5th International Conference on Numerical Simulation and Optoelectronic Devices* (Berlin, 2005), 47–48.

314. Richter, A., Glunz, S. W., Werner, F., Schmidt, J. & Cuevas, A. Improved quantitative description of Auger recombination in crystalline silicon. *Physical Review B* **86,** 165202 (2012).

315. Klaassen, D. B. M. A unified mobility model for device simulation-I. Model equations and concentration dependence. *Solid-State Electronics* **35,** 953–959 (1992).

316. Klaassen, D. B. M. A unified mobility model for device simulation-II. Temperature dependence of carrier mobility and lifetime. *Solid-State Electronics* **35,** 961–967 (1992).

317. Manual, A. U. Device simulation software. *Silvaco Int., Santa Clara, CA* (2014).

318. Couderc, R., Amara, M. & Lemiti, M. Reassessment of the intrinsic carrier density temperature dependence in crystalline silicon. *Journal of Applied Physics* **115,** 093705 (2014).

319. Altermatt, P. P., Schenk, A. & Heiser, G. A simulation model for the density of states and for incomplete ionization in crystalline silicon. I. Establishing the model in Si: P. *Journal of Applied Physics* **100,** 113714 (2006).

320. Altermatt, P., Schenk, A, Schmithüsen, B & Heiser, G. A simulation model for the density of states and for incomplete ionization in crystalline silicon. II. Investigation of Si: As and Si: B and usage in device simulation. *Journal of Applied Physics* **100,** 113715 (2006).

321. Schenk, A. Finite-temperature full random-phase approximation model of band gap narrowing for silicon device simulation. *Journal of Applied Physics* **84,** 3684–3695 (1998).

Glossary

Symbols, units and conversion factors

symbol/unit	description	unit/ conversion factor
A	area (of the wafer)	cm^2
Å	Angstroms	1e–10 m
AM	air mass (see STC)	
B	radiative recombination constant	$\mathrm{cm}^3\mathrm{s}^{-1}$
$C_{n/p}$	*Auger* recombination coefficients for electrons/holes	$\mathrm{cm}^6\mathrm{s}^{-1}$
c_i	concentration (with i=SF for surface concentration)	cm^{-3}, (cm^{-2})
D	diffusivity	$\mathrm{cm}^2\mathrm{s}^{-1}$
ΔQ_c	applied amount of corona charge	$\mathrm{q\,cm}^{-2}$
ΔQ_{it}	amount of charge required to fill the interface traps	$\mathrm{q\,cm}^{-2}$
ΔQ_{sc}	surface space charge	$\mathrm{q\,cm}^{-2}$
D_{it}	density of interface states	$\mathrm{cm}^{-2}\mathrm{eV}^{-1}$
Δn	excess carrier density (injection level), excess carrier density of electrons (as minority carriers)	cm^{-3}
Δn_{av}	average excess carrier density across the sample	cm^{-3}
Δp	excess carrier density of holes (as minority carriers)	cm^{-3}
E	energy	eV
E_A	energy level of acceptor state	eV
E_C	energy of the conduction band	eV
E_D	energy level of donor state	eV
E_F	Fermi energy	eV
E_g	energy of the band gap	eV
E_i	Fermi level in the intrinsic state	eV
E_T	trap energy level	eV
E_V	energy of the valence band	eV
η	efficiency, also abbreviated as eff.	%
eV	electron volts	1.60218e–19 J
FF	fill factor	%
Γ, X	crystal vectors	
G	generation rate	$\mathrm{cm}^{-2}\mathrm{s}^{-1}$
implied V_{oc}	implied open circuit voltage as obtained by QSS-PC measurement	mV
J_{mpp}	maximum power point current density	mAcm^{-2}
J_0	recombination current density of highly doped regions	fAcm^{-2}
J_{0E}	emitter recombination current density	fAcm^{-2}
J_{ph}	photocurrent	mAcm^{-2}
J_{sc}	short circuit current density	mAcm^{-2}
L_{eff}	effective minority carrier diffusion length	μm

symbol/unit	description	unit/ conversion factor
M	molar mass	$\mathrm{g\,mol^{-1}}$
μm	micrometer	1e–6 m
$\mu_{n/p}$	mobility of electrons/holes	$\mathrm{cm^2V^{-1}s^{-1}}$
n	“negatively” doped region	
n	electron concentration	$\mathrm{cm^{-3}}$
N_A	density of acceptor states	$\mathrm{cm^{-3}}$
N_C	effective density of states in the conduction band	$\mathrm{cm^{-3}}$
N_D	density of donor states	$\mathrm{cm^{-3}}$
n_i	intrinsic carrier concentration	$\mathrm{cm^{-3}}$
N_{it}	number of interface states	$\mathrm{cm^{-2}}$
nm	nanometer	1e–9 m
n^+	highly negatively doped region	
N_T	density of traps (concentration)	$\mathrm{cm^{-3}}$
N_V	effective density of states in the valence band	$\mathrm{cm^{-3}}$
OF	optical factor for texture correction	
p	“positvely” doped region	
p	hole concentration	$\mathrm{cm^{-3}}$
P	probability	
Φ_{ms}	work function difference between the metal of the Kelvin probe and the semiconductor	V
$\Phi_{n/p}$	quasi-Fermi levels (electron/hole distribution under non-equilibrium conditions)	eV
p^+	highly “negatively” doped region	
ppb	parts per billion	μg/kg
ppm	parts per million	mg/kg
Q_{tot}	total amount of fixed charges of a dielectric layer	$\mathrm{q\,cm^{-2}}$
Q_s	applied charge to the surface	$\mathrm{q\,cm^{-2}}$
Q_{sc}	space charge	$\mathrm{q\,cm^{-2}}$
R	recombination rate	$\mathrm{cm^3s^{-1}}$
r^2	coefficient of determination	
RR	recovery rate	%
S	solubility	$\mathrm{cm^{-3}}$
sdr	relative increase in total surface	%
σ_L	photoconductance	S
σ_n	capture cross section for electrons	$\mathrm{cm^2}$
σ_p	capture cross section for holes	$\mathrm{cm^2}$
s_q	the root mean squared of Z(x,y) in the measured area	μm
S_r	surface recombination velocity (SRV)	$\mathrm{cm\ s^{-1}}$
sun	light intensity	$\mathrm{100\,mWcm^{-2}}$
S_z	maximum height within the examined area	μm
T	absolute temperature	K
τ	lifetime	μs
τ_{eff}	effective minority carrier lifetime	μs or s
τ_{n0}	capture time constant for electrons	μs or s
τ_{p0}	capture time constant for holes	μs or s
V_D	electrical field within the dielectric	V
V_{FB}	flat band voltage	V
V_{mpp}	maximum power point voltage	V
V_{oc}	open circuit voltage	V

List of constants

Symbol	constant	value/unit
k_B	Boltzmann constant	8.61733e–5 eVK^{-1}
N_A	Avogadro's number	6.02214 mol^{-1}
q	elementary charge	1.60218e–19 C

List of abbreviations

abbreviation	meaning
ALD	atomic layer deposition
ALID	accelerated light induced degradation
ATLAS	electronic device simulation software
BiSoN	bifacial industrial solar cell on n-type substrate
BEOL	back end of line
BGN	band gap narrowing
BRL	boron rich layer
BSF	back surface field
BSG	boron silicate glass
c-Si	crystalline silicon
CVD	chemical vapor deposition
Cz	Czochralski grown crystal
dia	fixed diamond abrasive particle wire sawn wafers
ECV	electrochemical capacity voltage
EDNA 2	web based simulation software for highly doped regions
ERFC	complementary error function $erfc(x) = \frac{2}{\sqrt{\pi}} \int_x^\infty \exp(-t^2)\mathrm{d}t$
fcc	face centered cubic
FBR	fluid bed reactor
FEOL	front end of line
HOMO	highest occupied molecular orbital
IBC cell	interdigitated back contact solar cell
IC	integrated circuits
ICP-MS	inductively coupled plasma mass spectroscopy
IQE	internal quantum efficiency
IMEC	Interuniversity Microelectronics Centre, Leuven (Belgium)
ISC (Konstanz)	International Solar Energy Research Center Konstanz
ITRPV	international roadmap for photovoltaic
JMP10	software for statistical data analysis (by SAS)
LCOE	levelised costs of energy
LOD	limit of determination
LOQ	limit of quantification
LSD	least significant difference
LSM	laser scanning microscope (confocal microscope)
LUMO	lowest occupied molecular orbital
mAU	milli-absorbance-unit
mc	multicrystalline

abbreviation	meaning
MO	molecular orbital
mono	monocrystalline
mSiN_x	"magic" silicon nitride passivation stack
PERC	passivated emitter and rear cell
PC1D	open source 1-D simulation software for solar cells
PECVD	plasma enhanced chemical vapor deposition
PERT	passivated emitter, rear totally diffused cell
PFA	perfluoroalkoxy alkanes
pH	negative decadic log of the H^+ concentration
POR	process of record
pSC1	pseudo SC1 ($NaOH+H_2O_2$ mixture)
PSG	phosphorus silicate glass
QSS-μPCD	quasi-steady state microwave-detected photoconductance decay
QSS-PC	quasi-steady state photoconductance
RAM	random access memory
RCA clean	cleaning procedure developed by the Radio Corperation of America (SC1+SC2)
RIE	reactive ion etching
RMSE	root-mean-square error
SDE	saw damage etching
SE-ICP-MS	sandwich etch ICP-MS
SEM	scanning electron microscope
SC1	standard clean 1 ($NH_3+H_2O_2$ mixture)
SC2	standard clean 2 ($HCl+H_2O_2$ mixture)
SEMI	Semiconductor Equipment and Materials International
SiN_x	amorphous silicon nitride
slurry	loose abrasive particle slurry sawn wafers
SPM	sulfuric acid peroxide mixture
SRH	*Shockely Read Hall* recombination theory
SRV	surface recombination velocity
STC	standard testing conditions (25°C, 1000 W/m^2, 1.5 AM spectrum)
t-value	the ratio of the parameter estimate to its standard error
TMAH	tetramethyl ammonium hydroxide
ULSI	ultra large integration scale
UPW	ultra pure water
VPD	vapor phase decomposition

Acknowledgments

Finally it has been completed. As all works in science this work would not have been possible with the help of colleagues. First of all, I would like to thank my supervisor *Dr. Eckard Wefringhaus* for the trust and support during last five years. Despite all the ups and downs of the solar industry and the consequential unsteadiness of the financial support by several projects, he and his colleagues of the board of directors of the *International Solar Energy Research Center Konstanz* managed to provide me the best possible working conditions under the circumstances.

I would like to acknowledge my academic supervisor *Prof. Dr. Edwin Kroke*, who was willing to take me as his student despite the long distance. Thank you for the support and the thorough reading of this work. Of course, I would also like to thank *Prof. Dr. Johannes Heitmann* for his willingness to take the job as second reviewer.

Not to forget are the other current and former colleagues that have become friends over the year. *Jens Theobald*, *Dr. Alexander Edler*, *Pirmin Preis*, *Corrado Comparotto*, *Haifeng Cu*, and all the others: I know that it must have been hard listening to me constantly claiming I would finish soon for the last two to three years. However, I would like to thank you very much for the fruitful discussions and the technical and scientific help. ISC has been a great and invaluable pool of knowledge of all kind. Of course, a central part of my work at ISC was the “Brotzeit/Kaffee” group. Thank you for the never boring, always extended lunch breaks.

Thank you *Lejo Koduvelikulathu* for the running and re-running the simulations based on my constantly updated input data.

Furthermore, I would like to thank all the technical staff at ISC, *Lejlja Hildebrand*, *Rafael Marzcak*, *Annette Helfricht* and the others, for their patience and their helping hands in performing my experiments. With their steady hands many more of my wafers and cells would have broken and the efficiencies of my solar cells would not have been nearly as good.

Invaluable for the outcome of my work was the always reliable and highly professional help by *Markus Reutz* from *ATU Herrenberg*, who constantly provided the results of my ICP-MS samples in record-breaking time.

Far away locally, but absolutely essential for the completion of this work was the support from the “locals” in Freiberg, *Christoph Gondek*, *Marcus Lippold* and the others from the former grad school of photovoltaics. Always good for a nice meal at the Stadtwirtschaft and very helpful in all sorts of administrative and uni-related things.

Last but not least, thank you *Lena*, my love, for your infinite patients and love. I know I was not always easy to deal with in the last couple of years. And of course, I thank my *family* for always being there for me, even when I did not call for a long time.

List of publications by the author

Oral Presentations

1. Buchholz, F., Wefringhaus, E., Eisert, S., Egenolf, H. & Groß, A. *Measurement and impact of surface transition metal contamination of textured multicrystalline silicon wafers* in *Proc. 26th European Photovoltaic Solar Energy Conference and Exhibition* (Hamburg, 2011), 1187-1190.

2. Buchholz, F., Galbiati, G., Edler, A., Wefringhaus, E., Ferstl, B. & Ross, M. *Comparison of wafer cleaning procedures for high efficiency n-type solar cells in Proc. 28th European Photovoltaic Solar Energy Conference and Exhibition* (Paris, 2013), 793-796.

3. Buchholz, F. & Wefringhaus, E. *Impact of Fe and Cu surface contamination on high efficiency solar cell processes* in *Proc. of the Ultra Clean Processing of Semiconductor Surfaces XII; Solid State Phenomena Vol. 219* (Brussels, 2014), 305-311.

4. Wilson, M., Savtchouk, A., Olibet, S., Buchholz, F., Kopecek, R., Peter, K. & Lagowski, J. *Monitoring of incoming silicon PV wafers with modified surface photovoltage (SPV) minority carrier diffusion length method* in *Proc. 26th European Photovoltaic Solar Energy Conference and Exhibition* (Hamburg, 2011), 05-09.

Poster Presentations

5. Buchholz, F., Wefringhaus, E. & Schubert, G. M*etal Surface Contamination During Phosphorus Diffusion* in *Proc. Silicon PV* (Leuven, 2012) *Energy Procedia* **27**, 287-292.

6. Buchholz, F., Wefringhaus, E., Moron, L., Lukesch, M. & Weber, W. *Spectrophotometric monitoring of iron and copper contamination of cleaning baths for solar cell processing* in *Proc. 28th European Photovoltaic Solar Energy Conference and Exhibition* (Paris, 2013), 1813-1815.

7. Gondek, C., Hanich, R., Lippold, M., Buchholz, F., Röver, I. & Kroke, E., *HF-O_3-H_2O-mixtures for cleaning and etching sg-silicon materials - removal of metal contaminations* in *Proc. 28th European Photovoltaic Solar Energy Conference and Exhibition*

(Paris, 2013), 1813-1815.

8. Glatz-Reichenbach, J., Buchholz, F., Díaz-Pérez, P., Preis, P., Theobald, J., Wefringhaus, E. & Peter K. *Development of high efficient p-type industrial PERC-solar cells* in *Proc. 28th European Photovoltaic Solar Energy Conference and Exhibition* (Paris, 2013), 1842-1845.

9. Lossen, J., Buchholz, F., Comparotto, C., Eisert, S., Libal, J., Mihailetchi, V., Wefringhaus, E., Rossetto, M., Discato, D. & Traverso, F. *From lab to fab: Bifacial n-type cells entering industrial production* in *Proc. 31th European Photovoltaic Solar Energy Conference* (Hamburg, 2015), 965-968.

Articles

10. Buchholz, F. & Wefringhaus, E. Cleaning for high efficiency solar cell processing. *Photovoltaics International* **22**, 47-54, (2013).

11. Lippold, M., Buchholz, F., Gondek, C., Honeit, F., Wefringhaus, E. & Kroke, E. Texturing of SiC-slurry and diamond wire sawn silicon wafers by HF-HNO_3-H_2SO_4 mixtures. *Solar Energy Materials and Solar Cells* **127**, 104-110 (2014).